Elucidation of dynamics of neuronal functions by molecular analyses of Ca^{2+} channel complexes

Takafumi Miki

2009

Kyoto University

Contents

General introduction

Intracellular Ca^{2+} concentration

Ionized calcium (Ca^{2+}) is a highly versatile intracellular signal that can regulate many different cellular functions. For example, neurotransmitter release, membrane excitability, muscle contraction, fertilization, gene expression, cell proliferation, programmed cell death, cell migration, cell damage repair, and synaptic plasticity[1,2]. In the steady-state cell, intracellular Ca^{2+} concentration is ~100 nM, which is 10000 times lower than the extracellular concentration of ~1 mM[3]. Once the Ca^{2+} influx from extracellular to intracellular, intracellular Ca^{2+} concentration increase and function as a second messenger. And then, the proteins, which can bind Ca^{2+} ion and change the conformations of the proteins, mediated various kinds of cellular function[4]. By contrast, the Ca^{2+} influx deregulations cause many diseases, for example ischemic cell death, neural degeneration, malignant hyperthermia, cerebellar ataxia, familial hemiplegic migraine, epilepsy, vasospasm, hypoKK, and polycystic kidney disease. These facts indicate that Ca^{2+} influx regulate to cell fate regulation.

The intracellular Ca^{2+} concentration is derived either from the internal strores or external medium mediated by various kinds of proteins, for example channels, pumps, and exchangers. The release of Ca^{2+} from the internal store, the endoplasmic reticulum or sarcoplasmic reticulum, is controlled by inositol 1,4,5-triphosphate receptor or ryanodine receptors[5,6]. In the case of Ca^{2+} influx from external medium, there are mainly three types of channels, voltage-dependent Ca^{2+} channel (VDCC), ligand-gated Ca^{2+} channel, and transient receptor potential (TRP) channels. Changes in plasma membrane voltage induce Ca^{2+} entry through plasma membrane channels by controlling the gating of VDCC. The ligand-gated ion channels are opened or closed

in response to binding of a chemical messenger. Ca^{2+} influx via TRP channels is induced by various kinds of stimuli that include noxious stimuli, intracellular messengers and the depletion of intracellular stores.

VDCCs

VDCCs are comprised by α_1, α_2/δ, β, and γ subunits. α_1 subunit has 4 repeats of 6 transmembrane domains, including voltage sensor regions, and pore regions. There are ten isoforms in α_1 subunit, α_{1A}, $_{1B}$, $_{1C}$, $_{1D}$, $_{1E}$, $_{1F}$, $_{1G}$, $_{1H}$, and $_{1I}$ (ref. 7,8). Electrophysiological and pharmacological analyses categorize α_{1A} as P- and Q-type, α_{1B} as N-type, α_{1C}, $_{1D}$, $_{1F}$ and $_{1S}$ as L-type, α_{1E} as R-type, and α_{1G}, $_{1H}$, and $_{1I}$ as T-type (ref. 2,9-11). Classified the threshold of activation voltage, L-, N-, P-, Q-, R-type Ca^{2+} channels are categorized as high-threshold VDCCs, and T-type Ca^{2+} channel is categorized as low-threshold VDCC. The auxiliary subunits α_2/δ, β, and γ modulate channel activity[13-16]. Especially, the β-subunit interacts with the α_1-subunit to induce enhancement of functional channel trafficking to the plasma membrane[17,18] and to modify multiple kinetic properties[19]. In addition, β-subunits have been shown to interact with several proteins[20-22]. Therefore, it is intriguing to investigate whether β-subunits are involved in targeting VDCC complexes to specific subcellular machinery for functional activity of VDCC by interacting with other proteins.

P/Q-type Ca^{2+} channel

In 1991, P/Q-type Ca^{2+} channel, α_{1A} subunit gene (*CACNA1A*), were first identified primary structure and functional expression[17]. The channel is a high voltage-activated calcium channel that is insensitive both to L-type Ca^{2+} channel inhibitor nifedipine and to N-type Ca^{2+} channel inhibitor ω-conotoxin[17]. It is expressed predominantly in

cerebellum, olfactory bulb, cerebral cortex, hippocampus, inferior colliculus, and auditory brain stem[23,24]. The Ca^{2+} influx via P/Q-type Ca^{2+} channels trigger the neurotransmitter release in presynapse and Ca^{2+} spike in cerebellum[25-29].

Missense mutations in the human *CACNA1A* gene underlie several neurological disorders, including familial hemiplegic migraine, spinocerebellar ataxia type6, and episodic ataxia type2 (ref. 30-32). And the *CACNA1A* mutant animals, *tottering* mouse, *rolling* mouse Nagoya, *leaner* mouse, *rocker* mouse, *Wobbly* mouse, and *groggy* rat were reported as the human disease models[33-41]. These studies appeared the functional impact of the missense mutation in molecular level. However the effect of the mutation on the higher brain functions has been remain unclear.

Survey of this thesis

This thesis consists of five chapters on VDCCs. The first three chapters describe the physiological role of novel VDCC complexes, focused on VDCC-β interacting proteins. The next two chapters describe the functional impact of the missense mutation of *CACNA1A* on brain morphology and higher brain functions.

References

1. Tsien, R.W. & Tsien, R.Y. Calcium channels, stores, and oscillations. *Annu Rev Cell Biol* **6**, 715-60 (1990).
2. Tsien, R.W., Ellinor, P.T. & Horne, W.A. Molecular diversity of voltage-dependent Ca^{2+} channels. *Trends Pharmacol Sci* **12**, 349-54 (1991).
3. Clapham, D.E. Calcium signaling. *Cell* **80**, 259-268(1995).
4. Heizmann, C.W. & Hunziker, W. Intracellular calcium-binding proteins: more sites than insights. *Trends Biochem Sci* **16**, 98-103 (1991).
5. Furuichi, T. et al. Primary structure and functional expression of the inositol 1,4,5-trisphosphate-binding protein P400. *Nature* **342**, 32-38 (1989).
6. Takeshima, H. et al. Primary structure and expression from complementary DNA of skeletal muscle ryanodine receptor. *Nature* **339**, 439-445 (1989).
7. Birnbaumer, L. et al. The naming of voltage-gated calcium channels. *Neuron* **13**, 505-506 (1994).
8. Lee, J. et al. Cloning and expression of a novel member of the low voltage-activated T-type calcium channel family. *J. Neurosci.* **19**, 1912-1921 (1999).
9. Bean, B.P. Classes of calcium channels in vertebrate cells. *Annu Rev Physiol* **51**, 367-84 (1989).
10. Llinás, R. et al. Distribution and functional significance of the P-type, voltage-dependent Ca^{2+} channels in the mammalian central nervous system. *Trends Neurosci* **15**, 351-5 (1992).
11. Zhang, J.F. et al. Distinctive pharmacology and kinetics of cloned neuronal Ca^{2+} channels and their possible counterparts in mammalian CNS neurons. *Neuropharmacology* **32**, 1075-88 (1993).
12. Kobayashi, T. & Mori, Y. Ca^{2+} channel antagonists and neuroprotection from

cerebral ischemia. *European Journal of Pharmacology* **363**, 1-15 (1998).

13. Campbell, K.P., Leung, A.T. & Sharp, A.H. The biochemistry and molecular biology of the dihydropyridine-sensitive calcium channel. *Trends Neurosci* **11**, 425-30 (1988).
14. Ahlijanian, M.K., Westenbroek, R.E. & Catterall, W.A. Subunit structure and localization of dihydropyridine-sensitive calcium channels in mammalian brain, spinal cord, and retina. *Neuron* **4**, 819-832 (1990).
15. Witcher, D.R. et al. Subunit identification and reconstitution of the N-type Ca^{2+} channel complex purified from brain. *Science* **261**, 486-9 (1993).
16. Letts, V.A. et al. The mouse stargazer gene encodes a neuronal Ca^{2+}-channel γ subunit. *Nat Genet* **19**, 340-347 (1998).
17. Mori, Y. et al. Primary structure and functional expression from complementary DNA of a brain calcium channel. *Nature* **350**, 398-402 (1991).
18. Bichet, D. et al. The I-II Loop of the Ca^{2+} channel $\alpha 1$ subunit contains an endoplasmic reticulum retention signal antagonized by the β subunit. *Neuron* **25**, 177-190 (2000).
19. Varadi, G. et al. Acceleration of activation and inactivation by the β subunit of the skeletal muscle calcium channel. *Nature* **352**, 159-162 (1991).
20. Beguin, P. et al. Regulation of Ca^{2+} channel expression at the cell surface by the small G-protein kir/Gem. *Nature* **411**, 701-706 (2001).
21. Hibino, H. et al. Direct interaction with a nuclear protein and regulation of gene silencing by a variant of the Ca^{2+}-channel β_4 subunit. *Proc Natl Acad Sci U S A.* **100**, 307–312 (2003).
22. Vendel, A.C. et al. Alternative splicing of the voltage-gated Ca^{2+} channel β_4 subunit creates a uniquely folded N-terminal protein binding domain with cell-specific

expression in the cerebellar cortex. *J. Neurosci.* **26**, 2635-2644 (2006).

23. Fletcher, C.F. et al. Absence epilepsy in tottering mutant mice is associated with calcium channel defects. *Cell* **87**, 607-617 (1996).
24. Tsujimoto, T. et al. Neuronal calcium sensor 1 and activity-dependent facilitation of P/Q-Type calcium currents at presynaptic nerve terminals. *Science* **295**, 2276-2279 (2002).
25. Hirning, L.D. et al. Dominant role of N-type Ca^{2+} channels in evoked release of norepinephrine from sympathetic neurons. *Science* **239**, 57-61 (1988).
26. Turner, T.J., Adams, M.E. & Dunlap, K. Calcium channels coupled to glutamate release identified by omega-Aga-IVA. *Science* **258**, 310-3 (1992).
27. Takahashi, T. & Momiyama, A. Different types of calcium channels mediate central synaptic transmission. *Nature* **366**, 156-158 (1993).
28. Artalejo, C.R., Adams, M.E. & Fox, A.P. Three types of Ca^{2+} channel trigger secretion with different efficacies in chromaffin cells. *Nature* **367**, 72-76 (1994).
29. Regehr, W.G. & Mintz, I.M. Participation of multiple calcium channel types in transmission at single climbing fiber to Purkinje cell synapses. *Neuron* **12**, 605-613 (1994).
30. Ophoff, R.A. et al. Familial hemiplegic migraine and episodic ataxia type-2 are caused by mutations in the Ca^{2+} channel gene CACNL1A4. *Cell* **87**, 543-552 (1996).
31. Yue, Q. et al. Progressive ataxia due to a missense mutation in a calcium-channel gene. *The American Journal of Human Genetics* **61**, 1078-1087 (1997).
32. Zhuchenko, O. et al. Autosomal dominant cerebellar ataxia (SCA6) associated with small polyglutamine expansions in the α_{1A}-voltage-dependent calcium channel. *Nat Genet* **15**, 62-69 (1997).

33. GREEN, M.C. & SIDMAN, R.L. Tottering--a neuromusclar mutation in the mouse. And its linkage with oligosyndacylism. *J Hered* **53**, 233-7 (1962)

34. Meier, H. & MacPike, A.D. Three syndromes produced by two mutant genes in the mouse. Clinical, pathological, and ultrastructural bases of tottering, leaner, and heterozygous mice. *J Hered* **62**, 297-302 (1971)

35. Oda, S. The observation of rolling mouse Nagoya (rol), a new neurological mutant and its maintenance. *Exp. Anim.* **22**, 281-288 (1973).

36. Noebels, J.L. & Sidman, R.L. Inherited epilepsy: spike-wave and focal motor seizures in the mutant mouse tottering. *Science* **204**, 1334-6 (1979).

37. Doyle, J. et al. Mutations in the Cacnl1a4 calcium channel gene are associated with seizures, cerebellar degeneration, and ataxia in tottering and leaner mutant mice. *Mammalian Genome* **8**, 113-120 (1997).

38. Mori, Y. et al. Reduced voltage sensitivity of activation of P/Q-type Ca^{2+} channels is associated with the ataxic mouse mutation rolling Nagoya (tgrol). *J. Neurosci.* **20**, 5654-5662 (2000).

39. Zwingman, T.A. et al. Rocker is a new variant of the voltage-dependent calcium channel gene Cacna1a. *J. Neurosci.* **21**, 1169-1178(2001).

40. Tokuda, S. et al. The ataxic groggy rat has a missense mutation in the P/Q-type voltage-gated Ca^{2+} channel α_{1A} subunit gene and exhibits absence seizures. *Brain Research* **1133**, 168-177 (2007).

41. Xie, G. et al. Forward genetic screen of mouse reveals dominant missense mutation in the P/Q-type voltage-dependent calcium channel, CACNA1A. *Genes, Brain and Behavior* **6**, 717-727 (2007).

Chaptor 1

RIM1 confers sustained activity and neurotransmitter vesicle anchoring to presynaptic Ca^{2+} channels

Abstract

The molecular organization of presynaptic active zones (AZs) is central to neurotransmitter release triggered by depolarization-induced Ca^{2+} influx. Here, we demonstrate a novel interaction between AZ components, RIM1 and voltage-dependent Ca^{2+} channels (VDCCs), that controls neurotransmitter release. RIM1 associates with VDCC β-subunits via its C-terminus to markedly suppress voltage-dependent inactivation among different neuronal VDCCs. Consistently, in neuroendocrine PC12 cells, acetylcholine release is significantly potentiated by the full-length and C-terminal RIM1 constructs, but membrane docking of vesicles is enhanced only by the full-length RIM1. The dominant negative β construct BADN, that disrupts the RIM1-β association, accelerates inactivation of native VDCC currents, and suppresses vesicle docking and acetylcholine release in PC12 cells, and inhibits glutamate release in cultured cerebellar neurons. Thus, RIM1 association with β in the AZ supports release via two distinct mechanisms: sustaining Ca^{2+} influx through inhibition of channel inactivation; and anchoring of neurotransmitter-containing vesicles in the vicinity of VDCCs.

Introduction

The presynaptic active zone (AZ) is the specific site for impulse-evoked exocytosis of neurotransmitters at neuronal synapses of the nervous system across species[1,2]. Fine regulation of AZ neurotransmitter release is integral to nervous system adaptive functions including learning, memory, and cognition. The molecular organization of AZs, where synaptic vesicles are docked in close vicinity to VDCCs at the presynaptic membrane, is essential for the control of neurotransmitter release triggered by depolarization-induced Ca^{2+} influx. The spacing between VDCCs and vesicles at AZ is particularly thought to influence the dynamic properties of synaptic transmission[3]. However, molecular determinants that maintain or regulate synaptic vesicles and VDCCs within a physiologically appropriate distance have remained elusive.

The Rab3-interacting molecule RIM1 was originally identified as a putative effector for the synaptic vesicle protein Rab3 (ref. 4), and is part of the RIM superfamily whose members share a common C_2B domain at their C-termini[5]. RIM1 interacts with several other AZ protein components, including Munc13, ELKS/CAST, RIM-BP, or Liprins, to form a protein scaffold in the presynaptic nerve terminal[6-10]. Mouse knockouts revealed that, in different types of synapses, RIM1 is essential for different forms of synaptic plasticity[9,11]. In the CA1-region Schaffer-collateral excitatory synapses and in GABAergic synapses, RIM1 is required for maintaining normal neurotransmitter release and short-term synaptic plasticity. In contrast, in excitatory CA3-region mossy fibre synapses and cerebellar parallel fibre synapses, RIM1 is necessary for presynaptic long-term, but not short-term, synaptic plasticity. In autaptic neurons, the deletion of RIM1 causes a significant reduction in the readily releasable pool of vesicles, alters short-term plasticity, and changes the properties of evoked asynchronous release[12]. However, in spite of the progress in understanding

RIM1 mediated effects, the mechanisms by which RIM1 acts remain unknown. Moreover, the physiological roles played by other RIM isoforms (RIM2, RIM3, and RIM4)[5] remain unclear.

Multiple types of VDCCs distinguished on the basis of biophysical and pharmacological properties coexist in neurons[13]. High voltage-activated types of VDCCs known for their essential involvement in neurotransmitter release include N-, P/Q-, R-, and L-types[14-16]. In terms of subunit composition, it has been accepted that VDCCs are heteromultimeric protein complexes comprised of the pore-forming α_1, designated as Ca_v, and auxiliary subunits such as α_2/δ, β, and γ (ref. 17). The α_1-subunit is encoded by at least 10 distinct genes, whose correspondence with functional types is largely elucidated[13,17]. Many reports have also documented the association of VDCC complexes with presynaptic and postsynaptic proteins including syntaxin, SNAP-25, synaptotagmin, CASK, and Mint primarily via interactions with the α_1 subunit[18-25]. The β-subunit interacts with the α_1-subunit to induce enhancement of functional channel trafficking to the plasma membrane[26,27] and to modify multiple kinetic properties[28]. In addition, β-subunits have been shown to interact with several proteins[29-31]. Therefore, it is intriguing to investigate whether β-subunits are involved in targeting VDCC complexes to specific subcellular machinery at AZs for functional neurotransmitter release by interacting with other proteins. Here, we demonstrate a novel molecular interaction between RIM1 and neuronal VDCC β-subunits, both of which are considered to be essential AZ proteins. The RIM1-β interaction supports the function of RIM1 in neurotransmitter release via two distinct mechanisms: the anchoring of neurotransmitter-containing vesicles in the vicinity of VDCCs; and sustaining Ca^{2+} influx through the inhibition of voltage-dependent inactivation.

Results

VDCC β-subunits directly interact with RIM1

To identify β-subunit interacting proteins that regulate the AZ organization, we performed yeast two-hybrid screening with the combination of a mouse brain complementary DNA library using the full amino acid sequence of the rat β_{4b}-subunit as a bait protein. The β_4-subunit was chosen because spontaneous β_4-mutant mice *lethargic*[32] have clear neurological defects suggesting that β_4-containing VDCCs are physiologically significant in the brain. Screening with VDCC β_{4b}-subunit identified a clone (#2-5) encoding the C-terminal region (1079-1463) of the mouse RIM1 protein[4] including the C_2B domain (**Fig. 1a**). Subsequent two-hybrid assays using a series of deletion and point mutants of β_{4b} revealed that residues 49-410 containing major structural motifs such as Src homology 3 (SH3) domain, α_1-interacting domain known as BID, and guanylate kinase (GK) domain, are required for the interaction of β_{4b} with the RIM1 C-terminus (**Fig. 1b**). *in vitro* pulldown assays using GST fusion proteins for different regions of RIM1 identified the C-terminus (residues 1079-1463) as a major β_4-interaction domain likely formed in concert by two adjacent subdomains (1079-1257 and 1258-1463) in RIM1 (**Fig. 1c** and **Supplementary Fig. 1**). An *in vitro* binding assay using purified recombinant constructs for β_4 and RIM subfragments revealed a dissociation constant (K_d) of 35.1 nM for RIM1(1079-1463) significantly lower than 481 nM for RIM1(1079-1257) and 717 nM for RIM1(1258-1463) (**Fig. 1d** and **Supplementary Fig. 2**). These results, as well as the successful coimmunoprecipitation of full-length RIM1 with β_{4b} (**Fig. 1e**), suggest a direct protein-protein interaction between RIM1 and β_4.

RIM1 physically associates with native VDCCs in the brain

Association between native VDCC β-subunits and RIM1 association was characterized biochemically using VDCC complexes enriched from mouse brains through microsome preparation, KCl wash, solubilization, heparin purification, and sucrose density gradient fractionation[23]. Western blot analysis of sucrose gradient fractions showed cosedimentation of RIM1 with $Ca_v2.1$ and β_4 (**Fig. 2a**). Statistical analysis of cosedimentation data plotting the normalized density of each protein as a function of the sucrose density fraction number reveals complete overlap of $Ca_v2.1$ and β_4, confirming their association in the VDCC complex (**Fig. 2b**). RIM1 sedimented in overlapping minor and major peaks. The major peak completely overlapped with VDCC subunits, whereas the smaller peak did not cosediment with VDCC and likely represents a subset of RIM1 in a smaller, non-VDCC complex. Syntaxin, a VDCC interacting protein, showed similar cosedimentation with RIM1 (**Fig. 2a**). To confirm that the cosedimentation of RIM1 is due to its specific interaction with VDCC subunits, heparin purified samples were subjected to immunoprecipitation analysis (**Fig. 2c**). Anti-β_4 antibody precipitated RIM1 from wild-type mice but not from *lethargic* mice that express truncated β_4 protein lacking the C-terminal region responsible for α_1 interaction[32,33]. It is unlikely that the β_4 isoform exclusively mediates the RIM1-VDCC association in the brain, since wild-type and *lethargic* mice were indistinguishable in the sucrose gradient profile (**Fig. 2d**). A β_{4b} fusion construct was designed as a dominant negative (beta-AID dominant negative (BADN)) suppressor mutant to dissociate the activity of β-binding proteins such as RIM1 from the functional VDCC complex (**Supplementary Fig. 3a-c**). BADN contains the full-length β_{4b} structure with the β-interacting AID region from $Ca_v2.1$ buried at the α_1-binding site [33]. As residues 49-410 of the entire 519 amino acid sequence of β_{4b} are required for RIM1 binding (**Fig. 1b**), we utilized the "full-length" β_{4b} in order to efficiently quench RIM1.

The ability of BADN to bind RIM1 was confirmed by *in vitro* binding assay (**Supplementary Fig. 3d**). Coimmunoprecipitation experiments also showed binding of BADN to RIM1 but not to the AID-containing I-II linker region of $Ca_v2.1$ in HEK cells (**Supplementary Fig. 3e**). Since the intermolecular association of BADN with VDCC α_1 is thus inhibited by the intramolecular occlusion of the α_1-binding site in BADN, BADN overexpression should deprive native β-subunits of RIM1 without affecting their association with α_1. Importantly, coimmunoprecipitation experiments revealed that the native β-RIM1 association in partially purified brain VDCCs was disrupted by 8 hr coincubation with 100 nM GST fusion proteins for BADN or RIM1(1079-1463) (**Fig. 2e**). Binding of β_4 to RIM(1079-1463) rapidly decayed with the addition of excessive recombinant BADN protein (200 nM) indicating that this disruption is attributable to displacement of binding partners in native association (**Supplementary Fig. 3f**). These results provide evidence for a physiological association between native RIM1 and P/Q-type VDCCs via the β-subunit in brain.

RIM1 targets to VDCC via the β-subunit at the plasma membrane

In recombinant HEK293 cells, β_{4b} and RIM1 were concentrated at the plasma membrane by coexpression of the P/Q-type $Ca_v2.1$ α_1-subunit, whereas they were diffusively colocalized throughout the intracellular area in the absence of $Ca_v2.1$ (**Fig. 3**; **Supplementary Fig. 4**): F_{PM}/F_{CYT} (ratio of the fluorescent intensity at the plasma membrane to that in the cytoplasm) was 0.52 ± 0.07 and 0.48 ± 0.07 in the presence of $Ca_v2.1$ and 0.10 ± 0.02 and 0.08 ± 0.02 in the absence of $Ca_v2.1$ for β_{4b} and RIM1, respectively. Importantly, RIM1 localization to the plasma membrane via a membrane-targeted β-binding domain comprised of CD8 and the $Ca_v2.1$ I-II linker was elicited only after β_{4b} coexpression (**Fig. 3b** and **Supplementary Fig. 4**). F_{PM}/F_{CYT}

was 0.29 ± 0.03 and 0.27 ± 0.02 in the presence of β_{4b} and 0.08 ± 0.01 and 0.08 ± 0.02 in the absence of β_{4b} for the $Ca_v2.1$ I-II linker and RIM1, respectively. Notably, the plasma membrane colocalization of RIM1 and β_{4b} via $Ca_v2.1$ or the β_{4b}-mediated colocalization of RIM1 and the $Ca_v2.1$ I-II linker was efficiently disrupted by BADN (**Fig. 3a,b**). In the presence of BADN, F_{PM}/F_{CYT} was 0.56 ± 0.11 and 0.19 ± 0.04 for β_{4b} and RIM1, respectively; and F_{PM}/F_{CYT} was 0.33 ± 0.04 and 0.13 ± 0.04 for the $Ca_v2.1$ I-II linker and RIM1, respectively. Thus, the RIM1-β_{4b} interaction is likely to be essential for assembly of RIM1 with VDCC at the plasma membrane. In cultured mouse hippocampal neurons, RIM1 and β_{4b} both became enriched near presynaptic termini, in parallel with the clustering of $Ca_v2.1$. These events had a substantially later onset than synaptogenesis indicated by synapsin I clustering observed at 8 days *in vitro* (**Fig. 3c,d**). Quantitative analysis using confocal imaging demonstrated that overexpression of either BADN or the RIM1 C-terminal domain impaired the clustering of the $Ca_v2.1$ α_1-subunit in presynaptic varicosities in cultured hippocampal neurons, (**Fig. 3e,f**). The coincident targeting of RIM1 and β_{4b}, as well as the blockade of the $Ca_v2.1$ enrichment in presynaptic varicosities by quenching of RIM1 and βs, suggests that the RIM1-β interaction regulates localization of VDCCs at the presynaptic membrane. Since RIM1 is known to interact with multiple proteins (**Fig. 1a**) (ref. 6-10), we cannot exclude the possibility that the RIM1 effect observed in neurons using BADN and the RIM1 C-terminus was due to the quenching of other RIM-dependent interactions at different subcellular locations. However, recent immunostaining at the giant calyx-type synapse of the chick ciliary ganglion by Khanna et al.[34] revealed that the staining intensities for $Ca_v2.2$ and RIM co-vary. This is consistent with the idea that they are both components of transmitter release sites.

RIM1-β interaction modulates inactivation properties of VDCCs

To elucidate the functional significance of direct RIM1-β_4 coupling, we characterized whole-cell Ba^{2+} currents through recombinant VDCCs expressed as $\alpha_1\alpha_2/\delta\beta$ complexes in BHK cells. RIM1 was tested with VDCC containing various neuronal α_1-subunits, N-type $Ca_v2.2$, P/Q-type $Ca_v2.1$, R-type $Ca_v2.3$, and L-type $Ca_v1.2$. The most prominent RIM1 effect on VDCC currents was observed on inactivation parameters. The rate of inactivation was dramatically decelerated in N-, P/Q-, R-, and L-type channels (**Fig. 4a,b**). The same set of VDCC types also showed a significant depolarizing shift in the voltage dependence of inactivation (**Fig. 4c,d**). In P/Q-types ($Ca_v2.1$ + β_{4b}), RIM1 coexpression shifted the half inactivation potential by +24.6 mV eliciting an inactivation curve with a component susceptible to inactivation induced at high voltages ($V_{0.5}$ (vector) = –45.9 mV, $V_{0.5}$ (RIM1) = –21.3 mV; $V_{0.5}$ is the potential to give a half-value of inactivation) and a non-inactivating component (**Supplementary Table 1**). In N- and R-types, RIM1 coexpression provoked a switch in the major phase of a biphasic inactivation curves from low voltage-induced ($V_{0.5}$ and ratio; –64.5 mV and 0.91 for N, and –78.2 mV and 0.91 for R) to high voltage-induced ($V_{0.5}$ and ratio; –20.8 mV and 0.61 for N, and –27.9 mV and 0.53 for R). L-type inactivation curve remained monophasic, however the non-inactivating component was significantly augmented by RIM1 (from 0.07 to 0.25). In P/Q-type channels, RIM1 effects on kinetics and voltage-dependent equilibrium of inactivation were observed with all other β-subunits tested (**Fig. 4a,c; Supplementary Table 2**). Furthermore, the C-terminal truncated mutants RIM1(1079-1463) and RIM1(1258-1463), but not RIM1(1079-1257), successfully slowed P/Q-type (with β_{1a}) current inactivation (**Fig. 4a,c**; **Supplementary Table 3**). After RIM1 coexpression, single-channel currents clearly demonstrated prolongation of mean time between first channel opening and last closing within a trace

during 750-ms depolarizations to 20 mV without significant changes in single-channel amplitude (0.59 pA) (**Fig. 4e**). This observation corresponds well with the whole-cell data and suggests that RIM1 predominantly stabilizes the non-inactivating mode[35] in P/Q-type channels. Currents evoked by trains of action potential (AP) waveforms, a more physiological voltage-clamp protocol used particularly to reveal closed-state inactivation[36], further support the profound suppression of voltage-dependent inactivation by RIM1 (**Fig. 4f**). The observed effect of RIM1 on VDCC inactivation is attributable to its association with the β-subunit, since replacement of β_4 with a C-terminal truncation construct β_4-GK, that directly interacts with α_1[37] but lacks the SH3 domain necessary for the RIM binding (**Fig. 1b; Supplementary Fig. 5a,b**), failed to significantly affect inactivation in N-type channels (**Supplementary Fig. 5c,d**; **Supplementary Table 4**). In addition, BADN, the dominant negative form to quench RIM1 interaction with the β-subunit, significantly diminished the effect of RIM1 on P/Q channel inactivation (**Supplementary Fig. 5e,f**; **Supplementary Table 5**). When 5 mM Ca^{2+} was used as a physiological charge carrier capable of inducing both Ca^{2+}-dependent and voltage-dependent inactivation[38], RIM1 still exerted prominent suppressive effects on inactivation, slowing the speed and shifting the voltage dependence toward depolarizing potentials in P/Q-type currents expressed in HEK cells (**Fig 5a,b**; **Supplementary Table 6**). Importantly, in rat pheochromocytoma PC12 neuroendocrine cells, BADN or co-application of siRNAs specific for RIM1 and RIM2 accelerated inactivation and shifted the inactivation curve toward the hyperpolarizing direction (**Fig. 5c,d**; **Supplementary Table 7**; see **Supplementary Fig. 7a** for the expression suppression of RIMs in PC12 cells). This supports a physiologically significant role for RIM-mediated VDCC modulation via the β subunit. Notably, as observed in RIM1-expressing cells, voltage-dependent inactivation of presynaptic

VDCC currents at membrane potentials ≥ –40 mV was demonstrated in a previous report[39]. Thus, RIM1 exerts strong effects on the kinetics and voltage dependence of inactivation of VDCC currents.

RIM1 effects on other functional current parameters such as voltage dependence of activation (**Fig. 6a**), activation kinetics (**Fig. 6b**), and current densities at different voltages in current-voltage relationships (**Fig. 6c,d**), distinguish VDCCs into two different groups (**Supplementary Table 1**). In β_{4b}-expressing BHK cells, the current densities of N- and P/Q-type channels were significantly augmented by RIM1 (**Fig. 6c,d**), while those of the R- and L-type ($Ca_v1.2$) channels were unaffected by RIM1 (**Fig. 6d**). In P/Q-type, the RIM1 C-terminal region (1079-1463), that carries the β-association site, was sufficient to enhance current density (**Fig. 6c**). By contrast, activation speeds were significantly decelerated (**Fig. 6b)** and activation curves were shifted toward positive potentials by RIM1 in R- and L-type, but not in N- and P/Q-type currents (**Fig. 6a**). When β_{4b} was replaced with other β isoforms, the augmentation of P/Q-type current densities by RIM1 was abolished (**Supplementary Fig. 6a**), whereas the effect of RIM1 on activation speed of P/Q-type was induced by the β-subunits other than β_{4b} (**Supplementary Table 2**): activation was decelerated in the presence of β_{1a}, β_{2a}, and β_3 (**Fig. 6b**, left panel). The effect of RIM1 shifting the activation curve toward positive potentials was also elicited by β_{2a} in P/Q-type (**Supplementary Fig. 6b**). Thus, N- and P/Q-type currents responded differently than R- and L-type ($Ca_v1.2$) currents to RIM1 in terms of activation kinetics, voltage dependence of activation, and current densities, perhaps reflecting different subcellular localizations or functions of these channel subsets.

RIM1-β interaction anchors neurotransmitter vesicles to VDCC

We directly observed vesicles docked to the plasma membrane using evanescent wave microscopy, which illuminates only the subcellular area from the surface to a depth of less than 100 nm by total internal reflection[40]. Dense-core vesicles were identified by a fusion protein of neuropeptide Y (NPY) and the fluorescent protein Venus in rat pheochromocytoma PC12 neuroendocrine cells. The overlapping distribution of NPY-Venus, VAMP-DsRedmonomer, and RIM1-DsRedmonomer indicates that the identification of transmitter-filled synaptic vesicles is possible using fluorescent signals of NPY-Venus (**Fig. 7a**). The co-distribution is likely specific for RIM1, since caveolin-1-EGFP failed to colocalize with VAMP-DsRedmonomer, that showed colocalization with NPY-Venus (Fig. 7a). As demonstrated in **Fig. 7b** and **7c**, the number of docked vesicles containing NPY-Venus was increased significantly by expression of the full-length RIM1, whereas it was unaffected by the RIM1 N-terminal Zn^{2+} finger subfragment (11-399), that has been reported to form a ternary complex with Rab3 and Munc13 critical for neurotransmitter release[41]. The number of docked vesicles was also unaffected by the middle subfragment (400-1078), or by the C-terminal β-interacting subfragment (1079-1463) (**Supplementary Fig. 7b**). Importantly, the dominant negative mutant BADN significantly attenuated the number of docked vesicles (**Fig. 7b,c**). Furthermore, RIM1(1079-1463) also decreased docked vesicles compared to the control vector. These inhibitory effects of BADN and RIM1(1079-1463) on vesicle docking are most likely to be exerted by quenching endogenous full-length RIMs, or by saturating RIM1 interaction sites on VDCC β subunits, respectively. The BADN-induced decrease in vesicle docking is not due to a reduction in the densities of VDCCs in PC12 cells, as BADN failed to significantly affect current densities (**Fig. 5c**). Thus, the full-length RIM1 structure carrying the Rab3-interacting N-terminus, the β-interacting C-terminus, and the middle linker region

is likely to be essential for RIM1 to anchor neurotransmitter vesicles to VDCCs.

RIM1-β interaction enhances neurotransimitter release from PC12 cells and cultured neurons.

To gain insight into the physiological relevance of RIM1 interactions with the VDCC complex, we assessed neurotransmitter release from PC12 cells in which diverse high voltage-activated types of VDCCs have been characterized in detail[35,42] (**Supplementary Fig. 7c,d**). PC12 cells were transfected with RIM1 construct cDNAs along with the choline acetyltransferase (ChAT) gene that synthesizes ACh for synaptic vesicles[43]. ACh release, triggered by Ca^{2+} influx in response to high-K^+ (elevation of extracellular K^+ concentration from 4.7 mM to 49.9 mM) membrane depolarization, was significantly potentiated by full-length RIM1 (**Fig. 8a** and **Supplementary Fig. 7e**). ACh release was also enhanced by the Rab3-interacting N-terminal Zn^{2+} finger RIM1 subfragment (11-399) and by the C-terminal β-interacting RIM1 domain (1079-1463) that maintains VDCC currents, but not by the middle subfragment RIM1(400-1078) (**Fig. 8a**). In contrast, BADN significantly suppressed ACh release in PC12 cells (**Fig. 8a**). In cultured cerebellar neurons, similar suppression by BADN and potentiation by the full-length RIM1 were observed for glutamate release induced by high-K^+ stimulation (**Fig. 8b**). The results suggest that RIM1 potentiates neurotransmitter release through its interaction with VDCC β in neuronal and neuron-like cells.

Discussion

The present investigation reveals a novel physical association between the presynaptic AZ proteins RIM1 and VDCC β-subunits. The results of yeast two hybrid assay, *in*

vitro binding assay, and coimmunoprecipitation experiments have identified a RIM1-VDCC complex formed by direct protein-protein interaction of the β-subunit with the α_1-subunit AID region and the RIM C-terminus 1079-1463 (**Fig. 1**). The identification of native RIM1-VDCC complexes in brain (**Fig. 2**), the colocalization of RIM1 with VDCC subunits at the plasma membrane and the presynapse, and the disruption of such localization and complex formation by the BADN protein (**Fig. 3**) strongly support a physiological roles for the RIM1-VDCC β-subunit complex. Further biochemical and functional analyses (**Fig. 1** and **Fig. 4**) suggest that RIM1(1079-1257) and RIM1(1258-1463) are the primary β-subunit binding site and modulatory region, respectively, in the RIM1 protein. While the RIM1-β_4 interaction was shown in our experiments, RIM1 of wild-type and *lethargic* brains was indistinguishable by sucrose gradient profile (**Fig. 2a,d**). It has been previously reported that immunolocalization of $Ca_v2.1$ and $Ca_v2.2$ in the brain and properties of P-type VDCC currents in Purkinje neurons are indistinguishable between wild-type and *lethargic* mice[44]. This has been attributed to the rescue of β_4 deficiency by reshuffling of remaining β_1, β_2, and β_3. We expect a similar compensatory mechanism may also occur in the RIM1-β interaction in *lethargic* mice. Therefore, the β_4 isoform is unlikely to exclusively mediate the RIM1-VDCC association in the brain.

The RIM1-β association enables RIM1 to play a dual physiological role in neurotransmitter release: sustaining Ca^{2+} influx through the functional regulation of VDCCs and anchoring vesicles to VDCCs (**Fig. 8c**). Among the functional parameters of VDCCs, those which are related to voltage-dependent inactivation are most prominently modified by RIM1 through the β interaction (**Fig. 4**). Inactivation kinetics are markedly decelerated resulting in the predominance of high voltage inactivation and an inactivation-resistant current component in the 2-s prepulse protocol.

Similarly modulated inactivation properties of P/Q-type VDCC by other RIM family members such as RIM2α, RIM3γ, or RIM4γ (unpublished results), which all carry the C_2B domain, suggest that this function is a common feature for the RIM family[5]. Suppression by BADN of the RIM1-mediated inactivation in both the recombinant (**Supplementary Fig. 5e,f**) and native VDCCs (**Fig. 5c**) provides evidence that the RIM1 effect is in fact exerted through the RIM1-β association, as described in our model (**Fig. 8c**). This is supported by our finding that the C-terminal β construct, which binds to α_1 (ref. 37) but not to RIM1, failed to mediate RIM1 effects on N-type channels (**Supplementary Fig. 5**). Although detailed molecular mechanisms underlying inactivation are yet to be elucidated, previous mapping of the molecular determinants for voltage-dependent inactivation kinetics to segment S6 of repeat I (IS6)[45] may suggest that RIM1-β complexes bound to the I-II linker AID further act on adjacent IS6 to hinder its conformational transition to inactivation the inactivated state. Alternatively, RIM1 may immobilize the β-subunit and the process of inactivation by slowing the movement of the I-II loop[46,47]. When voltage-dependent inactivation is thus suppressed, VDCCs would be regulated predominantly by Ca^{2+}-dependent inactivation[48] and only weakly by membrane potential depolarization. RIM1 suppression of inactivation may potentiate responses of Ca^{2+} sensors such as synaptotagmins to Ca^{2+} influx at depolarizing membrane potentials that induce voltage-dependent inactivation when RIM1 is absent. Interestingly, since RIM1 virtually abolished VDCC inactivation elicited by a train of AP waveforms (**Fig. 4f**), certain forms of synaptic depression via closed-state inactivation[36] may be minimized by the presence of RIM1 at AZs. Furthermore, the impact of the RIM1-β association to delay VDCC inactivation may explain recent findings using the RIM1α knockout mouse demonstrating that RIM1 is important for the late stage asynchronous

neurotransmitter release[12] whereas synaptotagmin I is involved in the earlier synchronous release[49]. With P/Q- and N-type channels, the RIM1-β association significantly affected channel activity as well: current densities were nearly doubled by RIM coexpression (**Fig. 6c**). Thus, RIM1 can maintain and enhance depolarization-induced Ca^{2+} influx to support neurotransmitter release at presynaptic AZs.

Regarding the role of RIM1 in vesicle anchoring, our model (**Fig. 8c**) proposes that synaptic vesicles may be situated in close proximity to VDCC complexes through simultaneous interactions of RIM1 with vesicle-associated Rab3 / Munc13 via the N-terminal Zn^{2+}-finger domain[41] and with the VDCC β-subunit via the C-terminal C_2B domain. Hence, full-length RIM1 is required to mediate vesicle anchoring to VDCC at the plasma membrane, in contrast to the RIM1 suppression of VDCC inactivation which only requires the C-terminal C_2B domain. Taking into consideration the direct RIM1-Rab3 association and the regulation of tethering and/or priming of synaptic vesicles by Rab3 (ref. 41), it is likely that the RIM1-β interaction underlies, at least in part, the maintenance of a close proximity between VDCCs and vesicles, thereby regulating the dynamic properties of synaptic transmission[3]. Supporting this idea, BADN and the C-terminal RIM1 subfragment significantly suppressed vesicle docking in PC12 cells (**Fig. 7c**). In our experiments, the RIM1-β interaction prompted vesicle anchoring to VDCCs in AZs, however RIM1 and β-subunit targeting to the presynaptic site was observed after early synapse formation (**Fig. 3**). It is important to note that the interaction of Mint and CASK with VDCC α_1-subunits via their C-termini have been implicated[24,25] and may direct early channel targeting that precedes RIM1-β-subunit complex formation. Notably, our observation is consistent with a previous report[50] stating that the loss of UNC10/RIM caused a reduction in

membrane-contacting synaptic vesicles within 30 nm of the dense projection at *Caenorhabditis elegans* neuromuscular junctions. Furthermore, in RIM1α-defecient mice, the decay of excitatory postsynaptic currents (EPSCs) during 14 Hz trains of presynaptic stimulation is abolished[12], while the rate at which the readily releasable vesicle pool is refilled is indistinguishable between the wild-type and RIM1α mutant mice[12]. These data suggest that RIM1-mediated vesicle anchoring to VDCCs may enable a rapid depletion of vesicle pools such that available vesicles are exhausted leading to EPSC decay. In this scenario, RIM1 knockout would minimize rapid vesicle release enabling the readily releasable pool to be maintained and thus prevent EPSC decay. More recently, Schoch *et al.*[51] have reported mice deficient in both RIM1α and RIM2α show lethality due to, at least in part, defects in Ca^{2+}-triggered release despite normal AZ length and normal spontaneous neurotransmitter release. Combined, these studies support our model (**Fig. 8c**), predicting a dual function for RIM1 in neurotransmitter release by coordinating the molecular constituents and Ca^{2+} signaling at presynaptic AZs via the VDCC β interaction.

Previous reports have demonstrated the functional impact of syntaxin, synaptosome-associated protein (SNAP-25), and synaptotagmin on VDCCs through physical association with the 'synprint' region in the II-III linker of α_1-proteins[19-21]. Physical association of RIM directly via the C_2A domain with the synprint[10] (**Fig. 1a**) and indirectly via the RIM-binding protein (RIM-BP) with the C-terminal tail of α_1 have been also reported[52]. However, RIM1 regulation of VDCCs may be independent of the synprint-mediated regulation or the RIM-BP-mediated association, because RIM1(1079-1463), which lacks both the C_2A domain necessary for synprint binding[10] and the PXXP motif for the RIM-BP binding is still sufficient to inhibit VDCC inactivation (**Fig. 4a,c**). This is supported by our observation that the dominant

negative β construct BADN (**Supplementary Fig. 5e,f**) or replacement of wild-type β with a C-terminal truncation construct (**Supplementary Fig. 5a-d**), is sufficient to disrupt RIM1 effects on inactivation. Syntaxin and SNAP-25 have been proposed to exert inhibition of VDCC-mediated Ca^{2+} influx via a hyperpolarizing shift of the inactivation curve in the absence of vesicle docking at VDCC sites[19,21], while our finding by contrast implies enhancement or maintenance of the Ca^{2+} influx via interaction with RIM1 during the docking of vesicles. Importantly, previous reports suggest that RIM1 is involved in the modification of the release apparatus at a late stage in the vesicle cycle[9], particularly in the post-docking step[53]. Thus, the protein associations of VDCC α_1 and the VDCC β-RIM1 association may be distinct interactions that contribute at different stages of vesicle cycling to control the Ca^{2+} supply from the source, namely the VDCC, in addition to regulating the proximity between the Ca^{2+} source VDCC and the target Ca^{2+} sensors at the presynaptic AZ.

Methods

Yeast two-hybrid screening and β-galactosidase assay

Rat β_{4b}-subunit (GenBank accession number XM_215742) subcloned into pGBK-T7 was used as a bait to screen a mouse brain pACT2 library (Clontech) in the yeast strain AH109 according to the manufacturer's instructions (Clontech). 1.5 x 10^6 transformants plated to synthetic medium lacking adenine, histidine, leucine, and tryptophan. His^+ colonies were assayed for β-galactosidase activity by a filter assay. Of the transformants, 103 were His^+, of which 21 were also $LacZ^+$. Prey clone #2-5 encoding RIM1 (amino acids 1079-1463) (NM_053270) was isolated. Expression plasmids pGBK-T7 carrying β_{4b} or its mutants were constructed by PCR.

Molecular modeling of BADN

Molecular building and molecular dynamics calculations were performed with Insight II / Discover packaged in the context of the Molecular Simulations Inc (MSI) under the consistent valence force field (CVFF). Biopolymer modules based on the X-ray crystallographic data of β_2-subunit and AID complex (PDB ID: 1T3L) in RSCB protein data bank (PDB) were used. During molecular dynamics minimization around 1000 K, most of the structure except for hexa-peptide (GELNGG, see **Supplementary Fig. 2b**) was restrained. An energetically stabilized conformation was chosen.

Molecular cloning and construction of expression vectors

RIM1 (NM_053270) was cloned from mouse brain Marathon-Ready cDNA (Clontech) using PCR, and was subcloned into pCI-neo (Promega), the FLAG-tagged vector pCMV-tag2 (Stratagene), the myc-tagged vector pCMV-tag3 (Stratagene), the pDsRed-Monomer-N1 (Clontech), and the pIRES2-EGFP (Clontech). Rat β_{4b}

(XM_215742) was subcloned into the same vectors. The rat β_{4b} construct, BADN, that carries ELNG (amino acid residues 388-391 of rabbit $Ca_v2.1$) with G flanking on both the N- and C-terminal sides for ENQ (380-382 of rat β_{4b}) (**Supplementary Fig.3**), was created by using PCR, and was subcloned into PCI-neo. $Ca_v2.1$(I-II linker) (1-435) was constructed by PCR using pK4KBI-2 (ref. 54), and was subcloned into pCMV-tag2. Mouse VAMP (NM_009497) was cloned using PCR from mouse brain Marathon-Ready cDNA (Clontech), and was subcloned into pEGFP-N1 (Clontech). Human caveolin-1 (NM_001753) was cloned using PCR from human lung Marathon-Ready cDNA (Clontech), and was subcloned into pEGFP-N1 (Clontech).

Cell culture and recombinant expression in HEK293 cells

HEK293 cells were cultured in Dulbecco's modified Eagle's medium (DMEM) containing 10% fetal bovine serum, 30 units/ml penicillin, and 30 μg/ml streptomycin. Transfection of cDNA plasmids was carried out using SuperFect Transfection Reagent (QIAGEN). The cells were subjected to electrophysiological measurements and confocal imaging (see below) 48-72 h after transfection.

Expression of recombinant Ca^{2+} channels in BHK cells

Rabbit β_{2a}-subunit (X64297) and rabbit β_3-subunit (X64300) were subcloned into pCI-neo to yield pCI-β_{2a} and pCI-β_3, respectively. BHK cells cultured as previously described[53] were transfected with pAGS-3a2 (ref. 54) and pCI-β_{2a} or pCI-β_3 using SuperFect (Qiagen), and were cultured in DMEM containing Geneticin (600 μg/ml) (Sigma) and Zeocin (600 μg/ml) (invitrogen), to establish BHK lines stably expressing α_2/δ and β_{2a}, or β_3. BHK lines stably expressing α_2/δ and β_{1a}, or β_{4b} and BHK6-2 stably expressing $Ca_v2.1$, α_2/δ and β_{1a} were described previously[54]. These BHK cell

lines were co-transfected with pK4K plasmids[54] containing cDNAs for α_1-subunits (pK4KBI-2, pK4KBII, pK4KBIII, pK4KC1) and expression plasmids carrying RIM1 constructs (pIRES2-EGFP-vector, pIRES2-EGFP-RIM1, pIRES2-EGFP-RIM1(1079-1463), pIRES2-EGFP-RIM1(1079-1257), pIRES2-EGFP-RIM1(1258-1463)), using Effectene Transfection Regent (Qiagen). The cells were subjected to measurements 72-96 h after transfection.

Production of GST fusion proteins and purified recombinat β_4-subunit proteins.

For production of GST fusion proteins for RIM1, cDNAs for RIM1 constructs and the GST were subcloned together into the pET23 vector (Novagen). The Rosetta strain (Novagen) of *Escherichia coli* was transformed by the expression vectors, and protein expression/purification was performed according to the manufacturer's instruction (Novagen, GE Healthcare). For production of recombinant β_4-subunits, the gene encoding residues 47-475 of rat β_{4b}-subunit and the GST were subcloned into the pET23 vector (Novagen). The GST-β_4 proteins were purified by glutathione-Sepharose affinity column (GE Healthcare), and the GST tag was cleaved by incubation with thrombin (4 units/ml, Sigma) for 6 h at 4 °C. Resultant GST and thrombin were removed by glutathione-Sepharose and benzamidine-beads (Sigma) to obtain purified recombinant β_4-subunits. The purified recombinant of residues 47-410 (for disruption experiments) or 47-475 (for *in vitro* binding assay) of BADN was obtained using the same protocol as that for the β_4-subunit. These proteins were stored at –80 °C.

***in vitro* binding of the purified RIM1 GST fusion and recombinant β_4 proteins**

RIM1 GST fusion proteins at various concentrations were incubated with 50 pM

purified recombinant β_4-subunits for 3 h at 4 °C in PBS buffer containing 0.1 % NP40 and 50 μg/ml BSA, and then with glutathione-Sepharose beads for 1 h. The beads were centrifuged and washed twice with the PBS buffer. Proteins were boiled in SDS sample buffer and subject to 10 % SDS-PAGE, followed by western blotting (WB) with the anti-β_4 antibody raised against the peptide containing ENYHNERARKSRNRLS, and detected by enhanced chemiluminescence (Pierce). The densities of protein signals, obtained using NIH image under the linear relationship with the applied amount of proteins (**Supplementary Fig.2a**), were normalized to the densities from the maximal binding. Three independent experiments were performed.

GST-pulldown assay, and coimmunoprecipitation in HEK293 cells.

48 h after transfection, HEK293 cells were solubilized in NP40 buffer containing 150 mM NaCl, 1 % NP40, 50 mM Tris, 1 mM PMSF, 10 μg/ml leupeptin (pH8.0), then centrifuged at 17400 x *g* for 20 min. For pulldown assay, the cell lysate was incubated with glutathione-Sepharose beads bound with purified fusion proteins, then the beads were washed with NP40 buffer at 4 °C. The proteins retained on the beads were characterized by WB with anti-myc antibody (invitrogen). For coimmunoprecipitation, the cell lysate was incubated with anti-FLAG M2 monoclonal antibody (Sigma), then the immunocomplexes were incubated with protein A-agarose beads (Santa Cruz) and washed with NP40 buffer. Immunoprecipitated proteins were characterized by WB with anti-myc antibody.

Partial purification, sucrose density fractionation, and immunoprecipitation of neuronal Ca^{2+} channel complexes from mouse brains

The Ca^{2+} channel complexes were partially purified from brains of C57B6 mice or

lethargic mice (B6EiC3Sn-*a*/*A*-*Cacnb4*^{lh}/J, Jackson Laboratory) as previously reported[23]. From the 50 mg microsomes, the complexes were extracted with solubilization buffer containing 50 mM Tris, 500 mM NaCl, a mixture of protease inhibitors, 1 % digitonin (Biochemica & Synthetica) (pH 7.4). After centrifugation at 142,000 x *g* for 37 min, solubilized proteins in the supernatant were then mixed with Heparin-agarose beads (Sigma). After washing with Buffer I containing 20 mM HEPES, 300 mM NaCl, a mixture of protease inhibitors, 0.1 % digitonin (pH7.4), and Buffer II containing 20 mM HEPES, 400 mM NaCl, a mixture of protease inhibitors, 0.1 % digitonin (pH 7.4), heparin-bound proteins were eluted with Buffer III containing 20 mM HEPES, 700 mM NaCl, a mixture of protease inhibitors, 0.1 % digitonin (pH 7.4). After elution, concentration of NaCl was diluted to 150 mM by addition of Buffer IV containing 20 mM HEPES, a mixture of protease inhibitors, 0.1 % digitonin (pH 7.4), then the sample was concentrated to 4 ml in an Ultrafree-15 centrifugal filter device (millipore).

The samples were applied to 5-40 % sucrose density gradient (Buffer V containing 50 mM Tris, 150 mM NaCl, a mixture of protease inhibitors, 0.1 % digitonin + 5-40 % sucrose (pH 7.4)). The gradients were centrifuged at 215,000 x *g* for 90 min. WB was performed using anti-RIM antibody (BD bioscience), anti-$Ca_v2.1$ antibody (Alomone), anti-syntaxin antibody (Sigma), or anti-β_4 antibody. The density of protein signals measured using NIH image were normalized through four to five independent experiments.

Anti-RIM1 antibody was prepared according to the paper by Wang *et al.*[4]. For immunoprecipitation, partially purified neuronal VDCC complexes were incubated with anti-β_4 or anti-RIM1 antibody-bound protein A-agarose beads. Immunoprecipitated proteins were subject to WB with anti-RIM antibody or anti-$Ca_v2.1$ antibody. To

disrupt physiological association of native RIM1 with VDCC β_4, the partially purified VDCC complexes above were incubated with 200 nM GST fusion proteins for BADN and RIM1(1079-1463) for 8h at 4 °C, and subjected to the immunoprecipitation experiment.

Confocal imaging

PC12 cells were cultured as described previously[43]. 32 h after transfection, HEK293 cells or PC12 cells were plated onto poly-L-lysine coated glass coverslips. 56 h after transfection, Hoechst 33342 (1 μg/ml, Dojindo) was added for 30 min to stain nuclei. The imaging was performed in modified Ringer's buffer that contained 130 mM NaCl, 3 mM KCl, 5 mM $CaCl_2$, 1.5 mM $MgCl_2$, 10 mM glucose, 10 mM HEPES (pH 7.4). Fluorescence images were acquired with a confocal laser-scanning microscope (Olympus FV500) using the 405-nm line of an laser diode for excitation and a 430-nm to 460-nm band-pass filter for emission (Hoechst 33342), the 488-nm line of an argon laser for excitation and a 505-nm to 525-nm band-pass filter for emission (EGFP or Venus), or the 543-nm line of a HeNe laser for excitation and a 560-nm long-pass filter for emission (DsRedmonomer). The specimens were viewed at high magnification using plan oil objectives (x60, 1.40 numerical aperture (NA), Olympus).

Total internal reflection fluorescence (TIRF) microscopy

PC12 cells co-transfected with 1 μg pVenus-N1-NPY and of expression plasmids for RIM1 constructs at the equal molar quantity (5.0 μg of RIM1(11-399), 5.7 μg of RIM1(400-1078), 5.0 μg of RIM1(1079-1463), or 7.5 μg of RIM1) and BADN (10 μg) using OptiFect (invitrogen) were plated onto poly-L-lysine-coated coverslips. PCR analysis of the transfection level reveals that the RIM plasmids are transfected at the

equal level (**Supplemetary Fig. 7b**). The imaging was performed in modified Ringer's buffer. Fluorescence images of NPY-Venus were observed at the single vesicle level as previously reported[40]. In brief, a high numerical aperture objective lens (Plan Apochromatic, 100x, numerical aperture = 1.45, infinity-corrected, Olympus) was mounted on an inverted microscope (IX71, Olympus), and incident light for total internal reflection illumination was introduced from the high numerical objective lens through a single mode optical fiber. A diode-pumped solid state 488-nm laser (kyma488, 20 milliwatt, MELLES GRIOT) was used for total internal fluorescence illumination and 510-nm long pass filter as an emission filter. Images were captured by a cooled CCD camera (EM-CCD, Hamamatsu Photonics) operated with Metamorph (Molecular Devices). Area calculations and counting the number of fluorescent spots were performed using Metamorph softwares. We omitted the cells with disruption of distribution of vesicles by a dark spot with area > 10 μm^2 were omitted, to select the cells, in which vesicles were uniformly distributed, for the analyses. 10 μm^2 was adopted, because 10 μm^2 was the maximal dark circle area that can be located in between vesicles in the images from BADN-transfected cells with uniform vesicle distribution. The statistical analyses were performed using ANOVA followed by Fisher's test.

Immunostaining of cultured hippocampal neurons

Mouse hippocampal neurons were cultured as described[55]. Myc-tagged RIM1, FLAG-tagged β_{4b} or EGFP-tagged $Ca_v2.1$ were transfected to neurons by lipofection at either 6 or 7 days *in vitro* (div), and 2 or 16 days later, the cells were fixed and immunostained using anti-FLAG M2 monoclonal and anti-myc polyclonal (Cell Signaling) antibodies, with Alexa488- and Alexa594-conjugated secondary antibodies

(Molecular Probes). For quantification of $Ca_v2.1$ accumulation at varicosities, neurons were co-transfected, at 6 or 7 div, with EGFP-tagged $Ca_v2.1$ and mCherry (provided to H.B. by R.Y. Tsien). Immunofluorescent z-stack images for EGFP and mCherry were acquired using a Zeiss LSM510META confocal microscope, and a projection image was obtained from each of confocal z-stack images for EGFP and mCherry using a simple summation algorithm in order to retain all pixel fluorescence information. Somata and varicosities were manually cropped on the projection image of mCherry fluorescence to define individual regions of interests (ROIs). At least 10 adjacent varicosities were selected from a randomly chosen axonal process that could be traced directly from a mCherry-positive soma. Subsequently, fluorescence values of all pixels within each ROI in the image were integrated to calculate the total fluorescence for EGFP-$Ca_v2.1$ and mCherry. Integrated fluorescence at each varicosity was then normalized by dividing against the integrated soma fluorescence, in order to estimate the relative expression per each varicosity. Because this "relative expression factor" is heavily dependent on the sizes of the varicosities and the soma, we further calculated a ratio between the "relative expression factor" for $Ca_v2.1$ and the "relative expression factor" for mCherry at each varicosity, and designated the ratio as "$Ca_v2.1$ accumulation index". Since mCherry is a space-filling volume marker, this ratio is indicative of volume-independent $Ca_v2.1$ enrichment at each varicosity. Statistical analysis was carried out by a Kolmogorov-Smirnov test between either 22 div and + RIM1(1079-1463) samples, or between 22 div and + BADN samples.

Whole-cell recordings

Whole-cell mode of the patch-clamp technique was performed on BHK cells or PC12 cells at room temperature (22-25 °C) as previously described[54]. Pipette resistance

ranged from 2 to 3.5 megohm. The series resistance was electronically compensated, and both the leakage and the remaining capacitance were subtracted by a –P/4 method. Currents were sampled at 100 kHz after low pass filtering at 8.4 kHz (3 db) in the experiments of activation kinetics, otherwise sampled at 10 kHz after low pass filtering at 2.9 kHz (3 db). An external solution contained 3 mM $BaCl_2$, 155 mM tetraethylammonium chloride (TEA-Cl), 10 mM HEPES, 10 mM glucose (pH adjusted to 7.4 with tetraethylammonium-OH). For current recordings in PC12 cells, an external solution contained 10 mM $BaCl_2$, 153 mM TEA-Cl, 10 mM HEPES, 10 mM glucose (pH adjusted to 7.4 with TEA-OH). The pipette solution contained 95 mM CsOH, 95 mM Aspartate, 40 mM CsCl, 4 mM $MgCl_2$, 5 mM EGTA, 2 mM $ATPNa_2$, 5 mM HEPES, 8 mM creatine phosphate (pH adjusted to 7.2 with CsOH). To characterize Ca^{2+}-dependent inactivation of $Ca_v2.1$ expressed in HEK cells, external solutions contained 5 mM $CaCl_2$ or $BaCl_2$, 153 mM TEA-Cl, 10 mM HEPES, 10 mM glucose (pH adjusted to 7.4 with tetraethylammonium-OH (TEA-OH)). The pipette solution contained 135 mM Cs-$MeSO_3$, 5 mM CsCl, 0.5 mM EGTA, 5 mM $MgCl_2$, 4 mM $ATPNa_2$ and 10 mM HEPES (pH adjusted to 7.2 with CsOH). Details of voltage dependence of inactivation, AP train, and voltage dependence of activation are described in Supplementary Methods.

Single-channel recording

The cell-attached patch recording technique was performed[54]. Patch electrodes had resistance of 5-8 megohms. The bath solution contained 150 mM KCl, 5 mM HEPES, 0.2 mM EGTA, 10 mM glucose (pH adjusted to 7.4 with KOH). The composition of the pipette solution was 110 mM $BaCl_2$ and 10 mM HEPES (pH adjusted to 7.4 with $Ba(OH)_2$). Voltage steps with duration of 750 ms were given every 5 s from a V_h of

–100 mV. The data, low-passed filtered at 1 kHz (3 db, 8-pole Bessel filter), were digitized at 10 kHz and analyzed using the pCLAMP 6.02 software. The records were corrected for capacitative and leakage currents by subtraction of the average of records without channel activity.

Release assay and RNA analysis in PC12 cells

RNA expression of the α_1-subunits, β-subunits, RIM1, or RIM2 in PC12 cells was determined by RT-PCR (**Supplemetary Fig. 7a,c**) using specific primers listed in **Supplementary Table 5**. ACh secretion experiments were performed as previously reported with slight modifications[43]. PC12 cells were plated in poly-D-lysine-coated 35-mm dishes (BD bioscience) with 5 x 10^5 cells per dish. Cells were co-transfected with 1 μg of pEFmChAT encoding mouse ChAT cDNA and RIM1 plasmids at equal molar quantity (3.4 μg of RIM1(11-399), 3.8 μg of RIM1(400-1078), 3.4 μg of RIM1(1079-1463), or 5.0 μg of RIM1) and BADN (10 μg) using Lipofectamine^{TM} 2000 (invitrogen). Three days after transfection, PC12 cells were washed with a low-K^+ solution that contained 10 μM eserine, 140 mM NaCl, 4.7 mM KCl, 1.2 mM KH_2PO_4, 2.5 mM $CaCl_2$, 1.2 mM $MgSO_4$, 11 mM glucose, 15 mM HEPES-NaOH (pH 7.4) and incubated for 30 s with the low-K^+ solution at 37 °C. The release of ACh during this period was considered as basal release. To measure K^+-stimulated release of ACh, the cells were then incubated for 30 s with a high-K^+ solution that contained 10 μM eserine, 94.8 mM NaCl, 49.9 mM KCl, 1.2 mM KH_2PO_4, 2.5 mM $CaCl_2$, 1.2 mM $MgSO_4$, 11 mM glucose, 15 mM HEPES-NaOH (pH 7.4). Supernatant from cells solubilized in NP40 buffer and centrifuged at 17400 x *g* for 20 min at 4 °C was taken as the cellular ACh that was not secreted. ACh was measured using HPLC with electrochemical detection (HTEC-500, EiCOM). ANOVA followed by Fisher's test was employed for

statistical analyses.

Suppression of the action of endogenous RIM1 and RIM2 using specific siRNAs and BADN in PC12 cells

The sense siRNA sequences 5'-AAGAATGGACCACAAATGCTT-3' and 5'-AAGGTGATTGGATGGTATAAA-3' for rat RIM1, and 5'-AAGGCCCAGATACTCTTAGAT-3' and 5'-AAGAACTATCCAACATGGTAA-3' for rat RIM2 were used. To construct siRNA oligomers, the Silencer siRNA Construction Kit (Ambion) was used. The GAPDH siRNA (siControl) used was the control provided with the kit. We transfected the mixture of RIM1 and RIM2 siRNAs to PC12 cells using Lipofectamine^{TM} 2000. Suppression of RNA expression was confirmed using RT-PCR analyses (**Supplemetary Fig. 7a**). 8.0 μg pCI-neo-BADN or 8.0 μg pCI-neo-RIM1 was transfected as described above in the TIRF imaging. The cells treated with siRNAs or cDNA constructs were subjected to patch clamp measurements 72-96 h after transfection.

Preparation of cerebellar neuron primary cultures

As described previously[56], following decapitation of 7–9-day-old Wister rats, cerebella were removed and transferred into ice-cold DMEM immediately. After eliminating meninges, the tissues were cut into 1-mm pieces and incubated in PBS containing 1% (w/v) trypsine (Difco), 12.5 mM glucose (Difco), 0.02 % (w/v) DNase (Sigma) for 20 min at 37 °C, with occasional agitation. The trypsin solution was removed after a brief centrifugation and the tissue was mechanically dissociated by repeated pipetting in DMEM containing 10 % (v/v) FCS (GIBCO). The cell suspension obtained was left for 10 min at room temperature to let the remaining tissues precipitate. The cell

suspension was then collected carefully and spun at 200 x *g* for 3 min. After washing once by centrifugation, the pellet was resuspended in 10 ml of culture medium composed of DMEM with 10 % FCS, 26 mM KCl, 60 U/ml penicillin, and 60 μg/ml streptomycin. After filtering through a cell strainer (70 μm, BD Falcon), the cells were plated on polyethylenimine-coated 35-mm diameter culture dishes (BD Falcon) at a density of 4.5–5.0 x 10^6 cells/dish, and maintained at 37 °C in 10 % CO_2. Between 2 and 4 div, the medium was replaced with fresh medium containing 1 μM cytosine arabinofuranoside to inhibit the replication of non-neuronal cells, and thereafter no further medium change was carried out before experiments.

Preparation and infection of Sindbis viruses

The plasmid pSinEGdsp/BADN and pSinEGdsp/RIM1 were generated from the plasmid pSinEGdsp (kindly provided by S. Ozawa) containing the second subgenomic promoter followed by the cDNA of GFP[57]. The cDNA of BADN or RIM1 was ligated into the cloning site immediately downstream of the first subgenomic promoter. The recombinant RNA was transcribed from the linearized pSinEGdsp, pSinEGdsp/BADN or pSinEGdsp/RIM1 with an InvitroScript CAP SP6 *in vitro* transcription kit (Ambion). This recombinant RNA was co-transfected together with 'helper' RNA encoding the structural proteins of the Sindbis virus into BHK cells using the Gene Pulser II electroporation system (Bio-Rad Laboratories). The virions thus produced and released into the extracellular medium were harvested 36-48 h postinfection and centrifuged at 128690 x *g* for 3 h. The pellet was resuspended with PBS and kept at –80 °C. Cerebellar neurons were infected with recombinant Sindbis viruses on 8–10 div. By 48 h after the infection, 60–80% of the neurons appeared positive for EGFP.

Glutamate release assay

As described previously[56], 24 h after the infection with Sindbis viruses, cerebellar neurons (9–11 div) were washed briefly with pre-warmed low-K^+ solution that contained 140 mM NaCl, 4.7 mM KCl, 1.2 mM KH_2PO_4, 2.5 mM $CaCl_2$, 1.2 mM $MgSO_4$, 11 mM glucose, and 15 mM HEPES-NaOH (pH 7.4), and were incubated for 1 min with the low-K^+ solution at 37 °C. The release of Glutamate during this period was considered as basal release. To measure K^+-stimulated release of Glutamate, the cells were then incubated for 1 min with a high-K^+ solution that contained 94.8 mM NaCl, 49.9 mM KCl, 1.2 mM KH_2PO_4, 2.5 mM $CaCl_2$, 1.2 mM $MgSO_4$, 11 mM glucose, 15 mM HEPES-NaOH (pH 7.4). Glutamate was determined by reverse-phase HPLC on an Eicompak SC-5ODS (EiCOM), using precolum derivatization with *o*-phthalaldehyde and electrochemical detection (HTEC-500, EiCOM).

Statistical analysis

All data were expressed as means ± S.E.M. The data were accumulated under each condition from at least three independent experiments. The statistical analyses were performed using Student's *t*-test, Kolmogorov-Smirnov test, or ANOVA followed by Fisher's test.

References

1. Zhai, R. G. & Bellen, H. J. The architecture of the active zone in the presynaptic nerve terminal. *Physiology* **19**, 262-270 (2004).
2. Atwood, H. L. Gatekeeper at the synapse. *Science* **312**, 1008-1009 (2006).
3. Neher, E. Vesicle pools and Ca^{2+} microdomains: New tools for understanding their roles in neurotransmitter release. *Neuron* **20**, 389-399 (1998).
4. Wang, Y., Okamoto, M., Schmitz, F., Hofmann, K. & Südhof, T. C. Rim is a putative Rab3 effector in regulating synaptic-vesicle fusion. *Nature* **388**, 593-598 (1997).
5. Wang, Y. & Südhof, T. C. Genomic definition of RIM proteins: evolutionary amplification of a family of synaptic regulatory proteins. *Genomics* **81**, 126-137 (2003).
6. Wang, Y., Sugita, S. & Südhof, T. C. The RIM/NIM family of neuronal C_2 domain proteins. *J. Biol. Chem.* **275**, 20033-20044 (2000).
7. Betz, A. et al. Functional interaction of the active zone proteins Munc13-1 and RIM1 in synaptic vesicle priming. *Neuron* **30**, 183-196 (2001).
8. Ohtsuka, T. et al. CAST: a novel protein of the cytomatrix at the active zone of synapses that forms a tenary complex with RIM1 and Munc13-1. *J. Cell Biol.* **158**, 577-590 (2002).
9. Schoch, S. et al. RIM1α forms a protein scaffold for regulating neurotransmitter release at the active zone. *Nature* **415**, 321-326 (2002).
10. Coppola, T. et al. Direct interaction of the Rab3 effector RIM with Ca^{2+} channels, SNAP-25, and synaptotagmin. *J. Biol. Chem.* **276**, 32756-32762 (2001).
11. Castillo, P. E., Schoch, S., Schmitz, F., Südhof, T. C. & Malenka, R. C. RIM1α is required for presynaptic long-term potentiation. *Nature* **415**, 327-330 (2002).
12. Calakos, N., Schoch, S., Südhof, T. C. & Malenka, R. C. Multiple roles for the

active zone protein RIM1α in late stages of neurotransmitter release. *Neuron* **42**, 889-896 (2004).

13. Tsien, R. W., Ellinor, P. T. & Horne, W. A. Molecular diversity of voltage-dependent Ca^{2+} channels. *Trends Pharmacol. Sci.* **12**, 349-354 (1991).
14. Takahashi, T & Momiyama, A. Different types of calcium channels mediate central synaptic transmission. *Nature* **366**, 156-158 (1993).
15. Wheeler, D. B., Randell, A. & Tsien, R. W. Roles of N-type and Q-type Ca^{2+} channels in supporting hippocampal synaptic transmission. *Science* **264**, 107-111 (1994).
16. Catterall, W. A. Structure and function of neuronal Ca^{2+} channels and their role in neurotransmitter release. *Cell Calcium* **24**, 307-323 (1998).
17. Ertel, E. A. et al. Nomenclature of voltage-gated calcium channels, *Neuron* **25**, 533-535 (2000).
18. Sheng, Z.-H., Rettig, J., Takahashi, M. & Catterall, W. A. Identification of a syntaxin-binding site of N-type calcium channels. *Neuron* **13**, 1303-1313 (1994).
19. Bezprozvanny, I., Scheller, R. H. & Tsien, R. W. Functional impact of syntaxin on gating of N-type and Q-type calcium channels. *Nature* **378**, 623-626 (1995).
20. Zhong, H., Yokoyama, C. T., Scheuer, T. & Catterall, W. A. Reciprocal regulation of P/Q-type Ca^{2+} channels by SNAP-25, syntaxin and synaptotagmin. *Nat. Neurosci.* **2**, 939-941 (1999).
21. Spafford, J. D. & Zamponi, G. W. Functional interactions between presynaptic calcium channels and the neurotransmitter release machinery. *Curr. Opin. Neurobiol.* **13**, 308-314 (2003).
22. Nishimune, H., Sanes, J. R. & Carlson, S. S. A synaptic laminin-calcium channel interaction organizes active zones in motor nerve terminals. *Nature* **432**, 580-587

(2004).

23. Kang, M. G. et al. A functional AMPA receptor-calcium channel complex in the postsynaptic membrane. *Proc. Natl. Acad. Sci. USA* **103**, 5561-5566 (2006).
24. Maximov, A., Südhof, T. C. & Bezprozvanny I. Association of neuronal calcium channels with modular adaptor proteins. *J. Biol. Chem.* **274**, 24453-24456 (1999).
25. Maximov, A. & Bezprozvany I. Synaptic targeting of N-type calcium channels in hippocampal neurons. *J. Neurosci.* **22**, 6939-6952 (2002).
26. Mori, Y. et al. Primary structure and functional expression from complementary DNA of a brain calcium channel. *Nature* **350**, 398-402 (1991).
27. Bichet, D. et al. The I-II loop of the Ca^{2+} channel α_1 subunit contains an endoplasmic reticulum retention signal antagonized by the β subunit. *Neuron* **25**, 177-190 (2000).
28. Varadi, G., Lory, P., Schultz, D., Varadi, M. & Schwartz, A. Acceleration of activation and inactivation by the β subunit of the skeletal muscle calcium channel. *Nature* **352**, 159-162 (1991).
29. Béguin, P. et al. Regulation of Ca^{2+} channel expression at the cell surface by the small G-protein kir/Gem. *Nature* **411**, 701-706 (2001).
30. Hibino, H. et al. Direct interaction with a nuclear protein and regulation of gene silencing by a variant of the Ca^{2+}-channel β_4 subunit. *Proc. Natl. Acad. Sci. USA* **100**, 307-312 (2003).
31. Vendel, A. C. et al. Alternative splicing of the voltage-gated Ca^{2+} channel β_4 subunit creates a uniquely folded N-terminal protein binding domain with cell-specific expression in the cerebellar cortex. *J. Neurosci.* **26**, 2635-2644 (2006).
32. Burgess, D. L., Jones, J. M., Meisler, M. H. & Noebels, J. L. Mutation of the Ca^{2+} channel β subunit gene *Cchb4* is associated with ataxia and seizures in the lethargic

(*lh*) mouse. *Cell* **88**, 385-392 (1997).

33. Opatowsky, Y., Chen, C. C., Campbell, K. P. & Hirsch, J. A. Structural analysis of the voltage-dependent calcium channel β subunit functional core and its complex with the α_1 interaction domain. *Neuron* **42**, 387-399 (2004).
34. Khanna, R., Li, Q., Sun, L., Collins, T. J. & Stanley, E. F. N type Ca^{2+} channels and RIM scaffold protein covary at the presynaptic transmitter release face but are components of independent protein complexes. *Neuroscience* **140**, 1201-1208 (2006).
35. Plummer, M. R., Logothetis D. E. & Hess, P. Elementary properties and pharmacological sensitivities of calcium channels in mammalian peripheral neurons *Neuron* **2**, 1453-1463 (1989).
36. Patil, P. G., Brody, D. L. & Yue, D. T. Preferential closed-state inactivation of neuronal calcium channels. *Neuron* **20**, 1027-1038 (1998).
37. De Waard, M., Pragnell, M. & Campbell, K. P. Ca^{2+} channel regulation by a conserved β subunit domain. *Neuron* **13**, 495-503 (1994).
38. DeMaria, C. D., Soong, T. W., Alseikhan, B. A., Alvania, R. S. & Yue, D. T. Calmodulin bifurcates the local Ca^{2+} signal that modulates P/Q-type Ca^{2+} chanels. *Nature* **411**, 484-489 (2001).
39. Stanley, E. F. Syntaxin I modulation of presynaptic calcium channel inactivation revealed by botulinum toxin C1. *Eur. J. Neurosci.* **17**, 1303-1305 (2003)
40. Tsuboi, T. & Fukuda, M. Rab3A and Rab27A cooperatively regulate the docking step of dense-core vesicle exocytosis in PC12 cells. *J. Cell Sci.* **119**, 2196-2203 (2006).
41. Dulubova, I. et al. A Munc13/RIM/Rab3 tripartite complex: from priming to plasticity? *EMBO J.* **24**, 2839-2850 (2005).

42. Liu, H. et al. Expression and subunit interaction of voltage-dependent Ca^{2+} channels in PC12 cells. *J. Neurosci.* **16**, 7557-7565 (1996).

43. Nishiki, T. et al. Comparison of exocytotic mechanisms between acetylcholine- and catecholamine-containing vesicles in rat pheochromocytoma cells. *Biochem. Biophys. Res. Commun.* **239**, 57-62 (1997).

44. Burgess, D. L. et al. β subunit reshuffling modifies N- and P/Q-type Ca^{2+} channel subunit compositions in lethargic mouse brain. *Mol. Cell. Neurosci.* **13**, 293-311 (1999).

45. Zhang, J. F., Ellinor, P. T., Aldrich, R. W. & Tsien, R. W. Molecular determinants of voltage-dependent inactivation in calcium channels. *Nature* **372**, 97-100 (1994).

46. Stotz, S. C., Hamid, J., Spaetgens, R. L., Jarvis, S. E. & Zamponi, G. W. Fast inactivation of voltage-dependent calcium channels. *J. Biol. Chem.* **275**, 24575-24582 (2000).

47. Geib, S. et al. The interaction between the I-II loop and the III-IV loop of $Ca_v2.1$ contributes to voltage-dependent inactivation in a β-dependent manner. *J. Biol. Chem.* **277**, 10003-10013 (2002).

48. Brehm, P. & Eckert, R. Calcium entry leads to inactivation of calcium channel in *Paramecium*. *Science* **202**, 1203-1206 (1978).

49. Maximov, A. & Südhof, T. C. Autonomous function of synaptotagmin 1 in triggering synchronous release independent of asynchronous release. *Neuron* **48**, 547-554 (2005).

50. Weimer, R. M. et al. UNC-13 and UNC-10/Rim localize synaptic vesicles to specific membrane domains. *J. Neurosci.* **26**, 8040-8047 (2006).

51. Schoch, S. et al. Redundant functions of RIM1α and RIM2α in Ca^{2+}-triggered neurotransmitter release. *EMBO J.* **25**, 5852-5863 (2006).

52. Hibino, H. et al. RIM binding proteins (RBPs) couple Rab3-interacting molecules (RIMs) to voltage-gated Ca^{2+} channels. *Neuron* **34**, 411-423 (2002).

53. Koushika, S. P. et al. A post-docking role for active zone protein Rim, *Nat. Neurosci.* **4**, 997-1005 (2001).

54. Wakamori, M. et al. Single tottering mutations responsible for the neuropathic phenotype of the P-type calcium channel. *J. Biol. Chem.* **273**, 34857–34867 (1998).

55. Nonaka, M., Doi, T., Fujiyoshi, Y., Takemoto-Kimura, S. & Bito, H. Essential contribution of the ligand-binding βB/βC loop of PDZ1 and PDZ2 in the regulation of postsynaptic clustering, scaffolding, and localization of postsynaptic density-95. *J. Neurosci.* **26**, 763-774 (2006).

56. Koga, T., Kozaki, S. & Takahashi, M. Exocytotic release of alanine from cultured cerebellar neurons. *Brain Res.* **952**, 282-289 (2002).

57. Okada, T. et al. Sindbis viral-mediated expression of Ca^{2+}-permeable AMPA receptors at hippocampal CA1 synapses and induction of NMDA receptor-independent long-term potentiation. *Eur. J. Neurosci.* **13**, 1635-1643 (2001).

Supplementary Methods

cDNA cloning and construction of expression vectors

RIM1 (NM_053270) was cloned from mouse brain Marathon-Ready cDNA (Clontech) using PCR, and was subcloned into pCI-neo (Promega), the FLAG-tagged vector pCMV-tag2 (Stratagene), the myc-tagged vector pCMV-tag3 (Stratagene), the pDsRed-Monomer-N1 (Clontech), and the pIRES2-EGFP (Clontech). Rat β_{4b} (XM_215742) was subcloned into the same vectors. The rat β_{4b} construct, BADN, that carries ELNG (amino acid residues 388–391 of rabbit $Ca_v2.1$) with G flanking on both the N- and C-terminal sides for ENQ (380–382 of rat β_{4b}) (**Supplementary Fig.3**), was created by using PCR, and was subcloned into PCI-neo. $Ca_v2.1$(I-II linker) (1–435) was constructed by PCR using pK4KBI-2 (ref. 1), and was subcloned into pCMV-tag2. Mouse VAMP (NM_009497) was cloned using PCR from mouse brain Marathon-Ready cDNA (Clontech), and was subcloned into pEGFP-N1 (Clontech). Human caveolin-1 (NM_001753) was cloned using PCR from human lung Marathon-Ready cDNA (Clontech), and was subcloned into pEGFP-N1 (Clontech). Expression plasmids pGBK-T7 carrying β_{4b} or its mutants were constructed by PCR.

Cell culture and cDNA expression in HEK293 cells

HEK293 cells were cultured in Dulbecco's modified Eagle's medium (DMEM) containing 10% fetal bovine serum, 30 units/ml penicillin, and 30 μg/ml streptomycin. Transfection of cDNA plasmids was carried out using SuperFect Transfection Reagent (QIAGEN). The cells were subjected to electrophysiological measurements and confocal imaging 48–72 h after transfection.

cDNA expression of Ca2+ channels in BHK cells

Rabbit β_{2a} subunit (X64297) and rabbit β_3 subunit (X64300) were subcloned into pCI-neo to yield pCI-β_{2a} and pCI-β_3, respectively. BHK cells cultured as previously described2 were transfected with pAGS-3a2 and pCI-β_{2a} or pCI-β_3 using SuperFect (Qiagen), and were cultured in DMEM containing Geneticin (600 μg/ml) (Sigma) and Zeocin (600 μg/ml) (invitrogen), to establish BHK lines stably expressing α_2/δ and β_{2a}, or β_3. BHK lines stably expressing $\alpha 2/\delta$ and β_{1a}, or β_{4b} and BHK6-2 stably expressing $Ca_v2.1$, α_2/δ and β_{1a} were described previously[2]. These BHK cell lines were co-transfected with pK4K plasmids containing cDNAs for α_1-subunits (pK4KBI-2, pK4KBII, pK4KBIII, pK4KC1) and expression plasmids carrying RIM1 constructs (pIRES2-EGFP-vector, pIRES2-EGFP-RIM1, pIRES2-EGFP-RIM11079–1463, pIRES2-EGFP-RIM11079–1257, pIRES2-EGFP-RIM11258–1463), using Effectene Transfection Regent (Qiagen). The cells were subjected to measurements 72–96 h after transfection.

Production of GST fusion proteins and purified recombinat β_4 subunit proteins.

For production of GST fusion proteins for RIM1, cDNAs for RIM1 constructs and the GST were subcloned together into the pET23 vector (Novagen). The Rosetta strain (Novagen) of *Escherichia coli* was transformed by the expression vectors, and protein expression/purification was performed according to the manufacturer's instruction (Novagen, GE Healthcare). For production of recombinant β_4 subunits, the gene encoding residues 47–475 of rat β_{4b} subunit and the GST were subcloned into the pET23 vector (Novagen). The GST-β_4 proteins were purified by glutathione-Sepharose affinity column (GE Healthcare), and the GST tag was cleaved by incubation with thrombin (4 units/ml, Sigma) for 6 h at 4 °C. Resultant GST and

thrombin were removed by glutathione-Sepharose and benzamidine-beads (Sigma) to obtain purified recombinant β_4 subunits. The purified recombinant of residues 47–410 (for disruption experiments) or 47–475 (for *in vitro* binding assay) of BADN was obtained using the same protocol as that for the β_4 subunit. These proteins were stored at –80 °C.

Molecular modeling of BADN

Molecular building and molecular dynamics calculations were performed with Insight II / Discover packaged in the context of the Molecular Simulations Inc (MSI) under the consistent valence force field (CVFF). Biopolymer modules based on the X-ray crystallographic data of β_2 subunit and AID complex (PDB ID: 1T3L) in RSCB protein data bank (PDB) were used. During molecular dynamics minimization around 1000 K, most of the structure except for hexa-peptide (GELNGG, see **Supplementary Fig. 3b**) was restrained. An energetically stabilized conformation was chosen.

***in vitro* binding of the purified RIM1 GST fusion and recombinant β_4 proteins**

RIM1 GST fusion proteins at various concentrations were incubated with 50 pM purified recombinant β_4 subunits for 3 h at 4 °C in PBS buffer containing 0.1% NP40 and 50 μg/ml BSA, and then with glutathione-Sepharose beads for 1 h. The beads were centrifuged and washed twice with the PBS buffer. Proteins were boiled in SDS sample buffer and subject to 10% SDS-PAGE, followed by western blotting (WB) with the anti- β_4 antibody raised against the peptide containing ENYHNERARKSRNRLS, and detected by enhanced chemiluminescence (Pierce). The densities of protein signals, obtained using NIH image under the linear relationship with the applied amount of proteins (**Supplementary Fig. 2a**), were normalized to the densities from the

maximal binding. Three independent experiments were performed.

GST-pulldown assay, and coimmunoprecipitation in HEK293 cells.

48 h after transfection, HEK293 cells were solubilized in NP40 buffer (**Supplementary Table 8**), then centrifuged at 17400 x *g* for 20 min. For pulldown assay, the cell lysate was incubated with glutathione-Sepharose beads bound with purified fusion proteins, then the beads were washed with NP40 buffer at 4 °C. The proteins retained on the beads were characterized by WB with anti-myc antibody (invitrogen). For coimmunoprecipitation, the cell lysate was incubated with anti-FLAG M2 monoclonal antibody (Sigma), then the immunocomplexes were incubated with protein A-agarose beads (Santa Cruz) and washed with NP40 buffer. Immunoprecipitated proteins were characterized by WB with anti-myc antibody.

Confocal imaging

PC12 cells were cultured as described previously[3]. 32 h after transfection, HEK293 cells or PC12 cells were plated onto poly-L-lysine coated glass coverslips. 56 h after transfection, Hoechst 33342 (1 μg/ml, Dojindo) was added for 30 min to stain nuclei. The imaging was performed in modified Ringer's buffer that contained (in mM): 130 NaCl, 3 KCl, 5 $CaCl_2$, 1.5 $MgCl_2$, 10 glucose, 10 HEPES (pH 7.4). Fluorescence images were acquired with a confocal laser-scanning microscope (Olympus FV500) using the 405-nm line of an laser diode for excitation and a 430-nm to 460-nm band-pass filter for emission (Hoechst 33342), the 488-nm line of an argon laser for excitation and a 505-nm to 525-nm band-pass filter for emission (EGFP or Venus), or the 543-nm line of a HeNe laser for excitation and a 560-nm long-pass filter for emission (DsRedmonomer). The specimens were viewed at high magnification using

plan oil objectives (x60, 1.40 numerical aperture (NA), Olympus).

Total internal reflection fluorescence (TIRF) microscopy

PC12 cells co-transfected with 1 μg pVenus-N1-NPY and of expression plasmids for RIM1 constructs at the equal molar quantity (5.0 μg of RIM111–399, 5.7 μg of RIM1400–1078, 5.0 μg of RIM11079–1463, or 7.5 μg of RIM1) and BADN (10 μg) using OptiFect (invitrogen) were plated onto poly-L-lysine-coated coverslips. PCR analysis of the transfection level reveals that the RIM plasmids are transfected at the equal level (**Supplemetary Fig. 7b**). The imaging was performed in modified Ringer's buffer. Fluorescence images of NPY-Venus were observed at the single vesicle level as previously reported[4]. In brief, a high numerical aperture objective lens (Plan Apochromatic, 100x, numerical aperture = 1.45, infinity-corrected, Olympus) was mounted on an inverted microscope (IX71, Olympus), and incident light for total internal reflection illumination was introduced from the high numerical objective lens through a single mode optical fiber. A diode-pumped solid state 488-nm laser (kyma488, 20 milliwatt, MELLES GRIOT) was used for total internal fluorescence illumination and 510-nm long pass filter as an emission filter. Images were captured by a cooled CCD camera (EM-CCD, Hamamatsu Photonics) operated with Metamorph (Molecular Devices). Area calculations and counting the number of fluorescent spots were performed using Metamorph softwares. We omitted the cells with disruption of distribution of vesicles by a dark spot with area > 10 μm^2 were omitted, to select the cells, in which vesicles were uniformly distributed, for the analyses. 10 μm^2 was adopted, because 10 μm^2 was the maximal dark circle area that can be located in between vesicles in the images from BADN-transfected cells with uniform vesicle distribution. The statistical analyses were performed using ANOVA followed by

Fisher's test.

Quantification of presynaptic $Ca_v2.1$ accumulation

For quantification of $Ca_v2.1$ accumulation at presynaptic varicosities, neurons were co-transfected, at 6 or 7 DIV, with EGFP-tagged $Ca_v2.1$ and mCherry. Immunofluorescent z-stack images for EGFP and mCherry were acquired using a Zeiss LSM510META confocal microscope, and a projection image was obtained from each of confocal z-stack images for EGFP and mCherry using a simple summation algorithm in order to retain all pixel fluorescence information. Somata and varicosities were manually cropped on the projection image of mCherry fluorescence to define individual regions of interests (ROIs). At least 10 adjacent varicosities were selected from a randomly chosen axonal process that could be traced directly from a mCherry-positive soma. Subsequently, fluorescence values of all pixels within each ROI in the image were integrated to calculate the total fluorescence for EGFP-$Ca_v2.1$ and mCherry. Integrated fluorescence at each varicosity was then normalized by dividing against the integrated soma fluorescence, in order to estimate the relative expression per each varicosity. Because this "relative expression factor" is heavily dependent on the sizes of the varicosities and the soma, we further calculated a ratio between the "relative expression factor" for $Ca_v2.1$ and the "relative expression factor" for mCherry at each varicosity, and designated the ratio as "$Ca_v2.1$ accumulation index". Since mCherry is a space-filling volume marker, this ratio is indicative of volume-independent $Ca_v2.1$ enrichment at each varicosity. Statistical analysis was carried out by a Kolmogorov-Smirnov test between either 22 DIV and + RIM11079–1463 samples, or between 22 DIV and + BADN samples.

Current recordings

Whole-cell mode of the patch-clamp technique was performed on BHK cells or PC12 cells at room temperature (22–25 °C) as previously described[2]. Pipette resistance ranged from 2 to 3.5 megohm. The series resistance was electronically compensated, and both the leakage and the remaining capacitance were subtracted by a –P/4 method. Currents were sampled at 100 kHz after low pass filtering at 8.4 kHz (3 db) in the experiments of activation kinetics, otherwise sampled at 10 kHz after low pass filtering at 2.9 kHz (3 db). An external solution contained (in mM): 3 $BaCl_2$, 155 tetraethylammonium chloride (TEA-Cl), 10 HEPES, 10 glucose (pH adjusted to 7.4 with tetraethylammonium-OH). For current recordings in PC12 cells, an external solution contained (in mM): 10 $BaCl_2$, 153 TEA-Cl, 10 HEPES, 10 glucose (pH adjusted to 7.4 with TEA-OH). The pipette solution contained (in mM): 95 CsOH, 95 Aspartate, 40 CsCl, 4 $MgCl_2$, 5 EGTA, 2 $ATPNa_2$, 5 HEPES, 8 creatine phosphate (pH adjusted to 7.2 with CsOH). To characterize Ca^{2+}-dependent inactivation of $Ca_v2.1$ expressed in HEK293 cells, external solutions contained (in mM): 5 $CaCl_2$ or $BaCl_2$, 153 TEA-Cl, 10 HEPES, 10 glucose (pH adjusted to 7.4 with tetraethylammonium-OH (TEA-OH)). The pipette solution contained (in mM): 135 Cs-$MeSO_3$, 5 CsCl, 0.5 EGTA, 5 $MgCl_2$, 4 $ATPNa_2$ and 10 HEPES (pH adjusted to 7.2 with CsOH). Single-channel currents were recored using cell-attached patch mode[2]. Patch electrodes had resistance of 5–8 megohms. The bath solution contained (in mM): 150 KCl, 5 HEPES, 0.2 EGTA, 10 glucose (pH adjusted to 7.4 with KOH). The pipette solution contained (in mM): 110 $BaCl_2$ and 10 HEPES (pH adjusted to 7.4 with $Ba(OH)_2$). Voltage steps with duration of 750 ms were given every 5 s from a V_h of –100 mV. The data, low-passed filtered at 1 kHz (3 db, 8-pole Bessel filter), were digitized at 10 kHz and analyzed using the pCLAMP 6.02 software. The records were

corrected for capacitative and leakage currents by subtraction of the average of records without channel activity.

Voltage dependence of inactivation

To determine the voltage dependence of inactivation (inactivation curve) of VDCCs, Ba^{2+} currents were evoked by 20-ms test pulse to 5 mV after the 10-ms repolarization to –100 mV (–110 mV for $Ca_v2.3$, –80 mV for PC12) following 2-s *V*h displacement (conditioning pulse) from –110 mV to 20 mV (from –80 mV to 20 mV for PC12) with 10-mV increments. Amplitudes of currents elicited by the test pulses were normalized to those elicited by the test pulse after a 2-s V_h displacement to –110 mV (–80mV for PC12). The mean values were plotted against potentials of the 2-s V_h displacement. When the inactivation curve was monophasic, the mean values were fitted to the single Boltzmann's equation:

$$h(V_h) = (1-a)+a\ /\{1+\exp[(V_{0.5}{}^{1st}-V_h)/k^{1st}]\}$$

where a is the rate of inactivating component, $V_{0.5}{}^{1st}$ is the potential to give a half-value of inactivation, and k^{1st} is the slope factor. Otherwise, the mean values were fitted to the sum of two (1st and 2nd) Boltzmann's equations:

$$h(V_h) = (1-a-b)+a/\{1+\exp[(V_{0.5}{}^{1st}-V_h)/k^{1st}]\}+b\{1+\exp[(V_{0.5}{}^{2nd}-V_h)/k^{2nd}]\}$$

where a and b are the ratios of 1st and 2nd inactivating phases, $V_{0.5}{}^{1st}$ and $V_{0.5}{}^{2nd}$ are the potentials give a half-value of 1st and 2nd inactivation phases, and k^{1st} and k^{2nd} are the slope factors for 1st and 2nd inactivating phases, respectively. The AP train was the same as Patil *et al.*[5]. APs began at −80 mV and peaked at 33 mV. Maximal rising and falling slopes were 300 V/s and −100 V/s, respectively. Leaks and capacitive transients were subtracted by a –P/6 protocol. External solution contained 3 mM Ba^{2+}.

Voltage dependence of activation

Tail currents were elicited by repolarization to –60 mV after 5-ms test pulse from –50 to 50 mV with 5-mV increments. Currents were sampled at 100 kHz after low pass filtering at 8.4 kHz. Amplitude of tail currents were normalized to the tail current amplitude obtained with a test pulse to 50 mV. The mean values were plotted against test pulse potentials, and fitted to the Boltzmann's equation:

$n(V_m) = 1/\{1+\exp[(V_{0.5}-V_m)/k]\}$

where V_m is membrane potential, $V_{0.5}$ is the potential to give a half-value of conductance, and k is the slope factor.

Release assay and RNA analysis in PC12 cells

RNA expression of the α_1-subunits, β subunits, RIM1, or RIM2 in PC12 cells was determined by RT-PCR (**Supplemetary Fig. 7a,c**) using specific primers listed in **Supplementary Table 9**. ACh secretion experiments were performed as previously reported with slight modifications3. PC12 cells were plated in poly-D-lysine-coated 35-mm dishes (BD bioscience) with 5 x 105 cells per dish. Cells were co-transfected with 1 μg of pEFmChAT encoding mouse ChAT cDNA and RIM1 plasmids at equal molar quantity (3.4 μg of RIM111–399, 3.8 μg of RIM1400–1078, 3.4 μg of RIM11079–1463, or 5.0 μg of RIM1) and BADN (10 μg) using LipofectamineTM 2000 (invitrogen). Three days after transfection, PC12 cells were washed with a low-K^+ solution that contained (in mM): 0.01 eserine, 140 NaCl, 4.7 KCl, 1.2 KH_2PO_4, 2.5 $CaCl_2$, 1.2 $MgSO_4$, 11 glucose, 15 HEPES-NaOH (pH 7.4) and incubated for 30 s with the low-K^+ solution at 37 °C. The release of ACh during this period was considered as basal release. To measure K^+-stimulated release of ACh, the cells were then incubated for 30 s with a high-K^+ solution that contained (in mM): 0.01 eserine, 94.8 NaCl, 49.9

KCl, 1.2 KH_2PO_4, 2.5 $CaCl_2$, 1.2 $MgSO_4$, 11 glucose, 15 HEPES-NaOH (pH 7.4). Supernatant from cells solubilized in NP40 buffer and centrifuged at 17400 x *g* for 20 min at 4 °C was taken as the cellular ACh that was not secreted. ACh was measured using HPLC with electrochemical detection (HTEC-500, EiCOM). ANOVA followed by Fisher's test was employed for statistical analyses.

Suppression of the action of endogenous RIM1 and RIM2 using specific siRNAs and BADN in PC12 cells

The sense siRNA sequences 5'-AAGAATGGACCACAAATGCTT-3' and 5'-AAGGTGATTGGATGGTATAAA-3' for rat RIM1, and 5'-AAGGCCCAGATACTCTTAGAT-3' and 5'-AAGAACTATCCAACATGGTAA-3' for rat RIM2 were used. To construct siRNA oligomers, the Silencer siRNA Construction Kit (Ambion) was used. The GAPDH siRNA (siControl) used was the control provided with the kit. We transfected the mixture of RIM1 and RIM2 siRNAs to PC12 cells using LipofectamineTM 2000. Suppression of RNA expression was confirmed using RT-PCR analyses (**Supplemetary Fig. 7a**). 8.0 μg pCI-neo-BADN or 8.0 μg pCI-neo-RIM1 was transfected as described above in the TIRF imaging. The cells treated with siRNAs or cDNA constructs were subjected to patch clamp measurements 72–96 h after transfection.

Preparation of cerebellar neuron primary cultures

As described previously[6], following decapitation of 7–9-day-old Wister rats, cerebella were removed and transferred into ice-cold DMEM immediately. After eliminating meninges, the tissues were cut into 1-mm pieces and incubated in PBS containing 1%

(w/v) trypsine (Difco), 12.5 mM glucose (Difco), 0.02% (w/v) DNase (Sigma) for 20 min at 37 °C, with occasional agitation. The trypsin solution was removed after a brief centrifugation and the tissue was mechanically dissociated by repeated pipetting in DMEM containing 10% (v/v) FCS (GIBCO). The cell suspension obtained was left for 10 min at room temperature to let the remaining tissues precipitate. The cell suspension was then collected carefully and spun at 200 x *g* for 3 min. After washing once by centrifugation, the pellet was resuspended in 10 ml of culture medium composed of DMEM with 10% FCS, 26 mM KCl, 60 U/ml penicillin, and 60 μg/ml streptomycin. After filtering through a cell strainer (70 μm, BD Falcon), the cells were plated on polyethylenimine-coated 35-mm diameter culture dishes (BD Falcon) at a density of 4.5–5.0 x 106 cells/dish, and maintained at 37 °C in 10% CO_2. Between 2 and 4 DIV, the medium was replaced with fresh medium containing 1 μM cytosine arabinofuranoside to inhibit the replication of non-neuronal cells, and thereafter no further medium change was carried out before experiments.

Preparation and infection of Sindbis viruses

The plasmid pSinEGdsp/BADN and pSinEGdsp/RIM1 were generated from the plasmid pSinEGdsp (kindly provided by S. Ozawa) containing the second subgenomic promoter followed by the cDNA of GFP[7]. The cDNA of BADN or RIM1 was ligated into the cloning site immediately downstream of the first subgenomic promoter. The recombinant RNA was transcribed from the linearized pSinEGdsp, pSinEGdsp/BADN or pSinEGdsp/RIM1 with an InvitroScript CAP SP6 *in vitro* transcription kit (Ambion). This recombinant RNA was co-transfected together with 'helper' RNA encoding the structural proteins of the Sindbis virus into BHK cells using the Gene Pulser II electroporation system (Bio-Rad Laboratories). The virions thus produced and

released into the extracellular medium were harvested 36–48 h postinfection and centrifuged at 128690 x *g* for 3 h. The pellet was resuspended with PBS and kept at –80 °C. Cerebellar neurons were infected with recombinant Sindbis viruses on 8–10 DIV. By 48 h after the infection, 60–80% of the neurons appeared positive for EGFP.

Glutamate release assay

As described previously[6], 24 h after the infection with Sindbis viruses, cerebellar neurons (9–11 DIV) were washed briefly with pre-warmed low-K^+ solution that contained (in mM): 140 NaCl, 4.7 KCl, 1.2 KH_2PO_4, 2.5 $CaCl_2$, 1.2 $MgSO_4$, 11 glucose, and 15 HEPES-NaOH (pH 7.4), and were incubated for 1 min with the low-K^+ solution at 37 °C. The release of Glutamate during this period was considered as basal release. To measure K^+-stimulated release of Glutamate, the cells were then incubated for 1 min with a high-K^+ solution that contained (in mM): 94.8 NaCl, 49.9 KCl, 1.2 KH_2PO_4, 2.5 $CaCl_2$, 1.2 MgSO4, 11 glucose, 15 HEPES-NaOH (pH 7.4). Glutamate was determined by reverse-phase HPLC on an Eicompak SC-5ODS (EiCOM), using precolum derivatization with *o*-phthalaldehyde and electrochemical detection (HTEC-500, EiCOM).

References

1. Niidome T. et al. Stable expression of the neuronal BI (class A) calcium channel in baby hamster kidney cells. *Biochem. Biophys. Res. Commun.* **203**, 1821-1827 (1994).
2. Wakamori, M. et al. Single tottering mutations responsible for the neuropathic phenotype of the P-type calcium channel. *J. Biol. Chem.* **273**, 34857−34867 (1998).
3. Nishiki, T. et al. Comparison of exocytotic mechanisms between acetylcholine- and catecholamine-containing vesicles in rat pheochromocytoma cells. *Biochem. Biophys. Res. Commun.* **239**, 57-62 (1997).
4. Tsuboi, T. & Fukuda, M. Rab3A and Rab27A cooperatively regulate the docking step of dense-core vesicle exocytosis in PC12 cells. *J. Cell Sci.* **119**, 2196-2203 (2006).
5. Patil, P. G., Brody, D. L. & Yue, D. T. Preferential closed-state inactivation of neuronal calcium channels. *Neuron* **20**, 1027-1038 (1998).
6. Koga, T., Kozaki, S. & Takahashi, M. Exocytotic release of alanine from cultured cerebellar neurons. *Brain Res.* **952**, 282-289 (2002).
7. Okada, T. et al. Sindbis viral-mediated expression of Ca^{2+}-permeable AMPA receptors at hippocampal CA1 synapses and induction of NMDA receptor-independent long-term potentiation. *Eur. J. Neurosci.* **13**, 1635-1643 (2001).

Figure 1

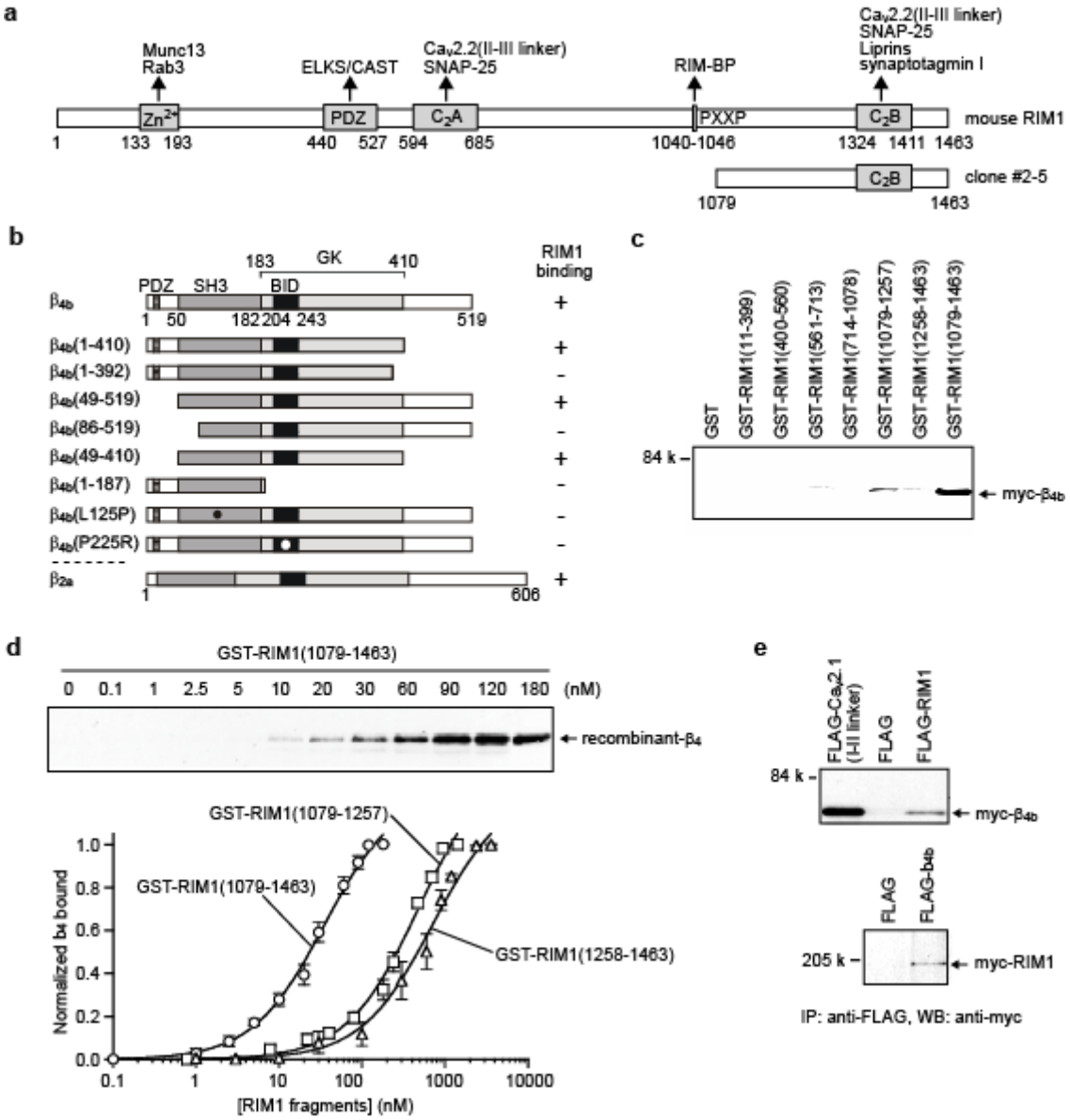
a
Munc13
Rab3
ELKS/CAST
Cav2.2(II-III linker)
SNAP-25
RIM-BP
Cav2.2(II-III linker)
SNAP-25
Liprins
synaptotagmin I
Zn2+
PDZ
C2A
PXXP
C2B
mouse RIM1
1
133
193
440
527
594
685
1040-1046
1324
1411
1463
C2B
clone #2-5
1079
1463
b
183
GK
410
RIM1
binding
PDZ
SH3
BID
β4b
1
50
182
204
243
519
β4b(1-410)
β4b(1-392)
β4b(49-519)
β4b(86-519)
β4b(49-410)
β4b(1-187)
β4b(L125P)
β4b(P225R)
β2a
606
c
GST
GST-RIM1(11-399)
GST-RIM1(400-560)
GST-RIM1(561-713)
GST-RIM1(714-1078)
GST-RIM1(1079-1257)
GST-RIM1(1258-1463)
GST-RIM1(1079-1463)
84 k
myc-β4b
d
GST-RIM1(1079-1463)
0
0.1
1
2.5
5
10
20
30
60
90
120
180
(nM)
recombinant-β4
GST-RIM1(1079-1257)
GST-RIM1(1079-1463)
GST-RIM1(1258-1463)
Normalized b4 bound
1.0
0.8
0.6
0.4
0.2
0.0
0.1
1
10
100
1000
10000
[RIM1 fragments] (nM)
e
FLAG-Cav2.1
(I-II linker)
FLAG
FLAG-RIM1
84 k
myc-β4b
FLAG
FLAG-b4b
205 k
myc-RIM1
IP: anti-FLAG, WB: anti-myc

Figure 1 Direct interaction of RIM1 with the VDCC β_{4b}-subunit.

(**a**) Domain structure of mouse RIM1. Arrows indicate molecules interacting with RIM1 at the following domains: Zn^{2+}, Zn^{2+}-finger like domain; PDZ, PDZ domain; C_2A and C_2B, first and second C_2 domains; PXXP, proline-rich region[4,6-10]. The protein region encoded by clone #2-5 is also indicated. (**b**) Mapping of RIM1 binding sites on β_{4b} by the yeast two-hybrid assay. Full-length and various mutant β-subunits in bait vectors are tested with RIM1 in the prey vector. The interactions are scored by β-galactosidase activity and His^+ prototrophy. (**c**) Pulldown assay of β_{4b} with GST fusion RIM1 mutants. GST fusion proteins immobilized on glutathione-Sepharose beads are incubated with cell lysate obtained from myc-β_{4b} cDNA plasmid-transfected HEK293 cells. Bound proteins are analyzed by western blotting (WB) using anti-myc antibody. (**d**) *in vitro* association between the purified preparations of GST-RIM1 fusion constructs and the recombinant β_4-subunit (amino acid residues 47-475). GST-RIM1 proteins at various concentrations, incubated with VDCC β_4 (50 pM), are captured by glutathione-Sepharose beads. Captured β_4 proteins are examined by WB. The bottom panel shows the quantitative densitometric analysis of bands shown in the upper panel and in **Supplementary Figure 2**. The saturation curves are subjected to the nonlinear least-squares curve-fitting method to evaluate the apparent dissociation constant (K_d). (**e**) Interaction of recombinant β_{4b} and RIM1 in HEK293 cells. The interaction is evaluated by immunoprecipitation (IP) with anti-FLAG antibody, followed by WB with anti-myc antibody. Top: physical association of myc-β_{4b} with FLAG-RIM1 is examined in comparison to a positive control FLAG-$Ca_v2.1$(I-II linker). Bottom: physical association of FLAG-β_{4b} with myc-RIM1 is examined.

Figure 2

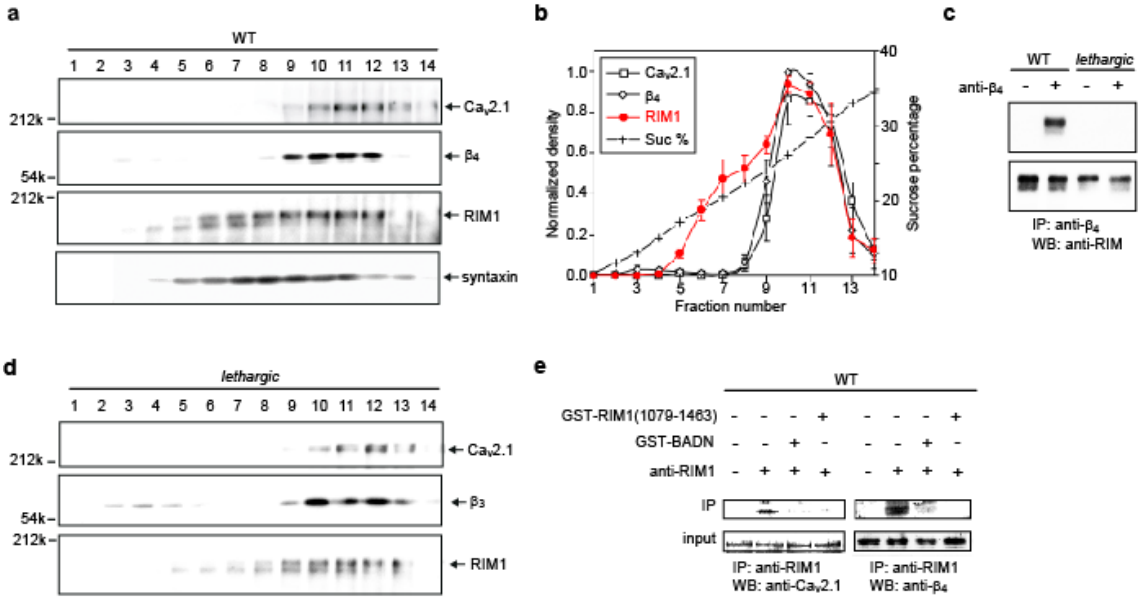

Figure 2 Association of RIM1 with native neuronal VDCC complexes.

(**a**) Sucrose gradient fractionation of neuronal VDCC complexes from wild-type (WT) mouse brains and subsequent WB demonstrate cosedimentation of RIM1 with $Ca_v2.1$ and β_4. Syntaxin showed similar cosedimentation with RIM1. (**b**) Densitometry of $Ca_v2.1$, β_4, and RIM1 from western blots of sucrose gradient fractions. (**c**) Coimmunoprecipitation of RIM1 with the β_4-subunit. Immunoprecipitation (IP) using an anti-β_4 antibody and subsequent WB for RIM1 is performed on heparin purified samples. As a negative control, a preparation from *lethargic* mice is used. (**d**) Sucrose gradient fractionation of neuronal VDCC complexes from *lethargic* mouse brains. (**e**) Coimmunoprecipitation of $Ca_v2.1$ with RIM1. The immunocomplexes are disrupted by GST-BADN or GST-RIM1(1079-1463). IP using anti-RIM1 antibody and subsequent WB for $Ca_v2.1$ is performed.

Figure 3

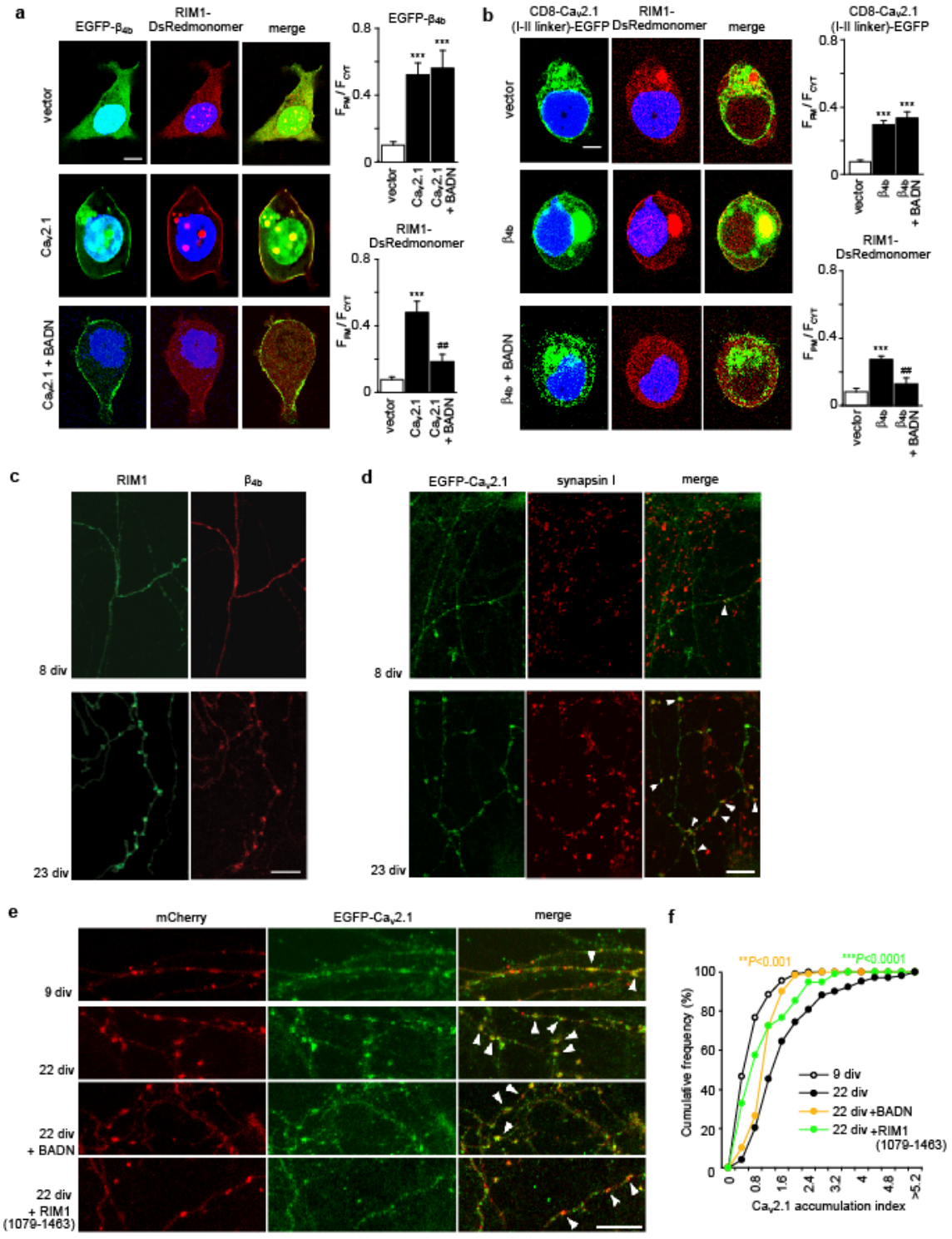
a
EGFP-β4b
RIM1-DsRedmonomer
merge
vector
CaV2.1
CaV2.1 + BADN
EGFP-β4b
RIM1-DsRedmonomer
vector
CaV2.1
CaV2.1 + BADN
b
CD8-CaV2.1 (I-II linker)-EGFP
RIM1-DsRedmonomer
merge
vector
β4b
β4b + BADN
CD8-CaV2.1 (I-II linker)-EGFP
RIM1-DsRedmonomer
vector
β4b
β4b + BADN
c
RIM1
β4b
8 div
23 div
d
EGFP-CaV2.1
synapsin I
merge
8 div
23 div
e
mCherry
EGFP-CaV2.1
merge
9 div
22 div
22 div + BADN
22 div + RIM1 (1079-1463)
f
**P<0.001
***P<0.0001
Cumulative frequency (%)
9 div
22 div
22 div +BADN
22 div +RIM1 (1079-1463)
CaV2.1 accumulation index

Figure 3 RIM1 clusters with the VDCC α_1- and β-subunits near presynaptic termini in cultured hippocampal neurons.

(**a**) The $Ca_v2.1$ α_1-subunit elicits colocalization of β_{4b} with RIM1 at the plasma membrane. The colocalization is disrupted by BADN. Left: confocal imaging of HEK293 cells co-transfected with EGFP-β_{4b} and RIM1-DsRedmonomer in the presence vector (top), $Ca_v2.1$ (middle), or $Ca_v2.1$ plus BADN (bottom). Scale bar: 5 μm. Nuclei are stained with Hoechst 33342. Right: statistical analysis of subcellular location of EGFP-β_{4b} or RIM1-DsRedmonomer distributed in 1 μm widths plasma membrane regions (PM) and in the cytosolic area (CYT) (n = 5 cells in each). $^{***}P <$ 0.001 vs vector. $^{\#\#}P < 0.01$ vs $Ca_v2.1$. (**b**) The β_{4b}-subunit elicits colocalization of $Ca_v2.1$(I-II linker) and RIM1 on the plasma membrane. The colocalization is disrupted by BADN. Left: confocal imaging of HEK293 cells co-transfected with CD8-$Ca_v2.1$(I-II linker)-EGFP and RIM1-DsRedmonomer in the presence vector (top), β_{4b} (middle), or β_{4b} and BADN (bottom). Scale bar: 5 μm. Right: stastical analysis of subcellular location of CD8-$Ca_v2.1$(I-II linker)-EGFP or RIM1-DsRedmonomer (n = 5 cells in each). $^{***}P < 0.001$ vs vector. $^{\#\#}P < 0.01$ vs β_{4b}. (**c**) Immunolocalization studies of tagged-RIM1 and β_{4b} in mouse hippocampal neurons. Clustering of RIM1 and β_{4b} not detected at 8 days *in vitro* (div), but is present at a substantially later stage at 23 div in cultured mouse hippocampal neurons. Scale bar: 10 μm. (**d**) Comparison of localization of EGFP-$Ca_v2.1$ with that of intrinsic synapsin I in hippocampal neurons. Like RIM1 and β_{4b}, $Ca_v2.1$ clusters much later than the onset of synaptogenesis which occurs earlier than 8 div, as synapsin I-positive puncta are already in abundance at 8 div, while $Ca_v2.1$ distribution is still diffuse. (**e, f**) Enrichment of EGFP-$Ca_v2.1$ in presynaptic varicosities is achieved between 9 div and 22 div. However, this maturation process is impaired by coexpression of a C-terminal fragment of RIM1 (+

RIM1(1079-1463)), or a dominant negative β construct with occluded α_1-binding pocket (+ BADN), indicating that the local concentration of presynaptic Ca^{2+} channels at AZs may be influenced by RIM1- β-subunit interaction during a postsynaptogenic maturation period, although contributions from other RIM1-C-terminus-interacting proteins cannot be excluded.

Figure 4

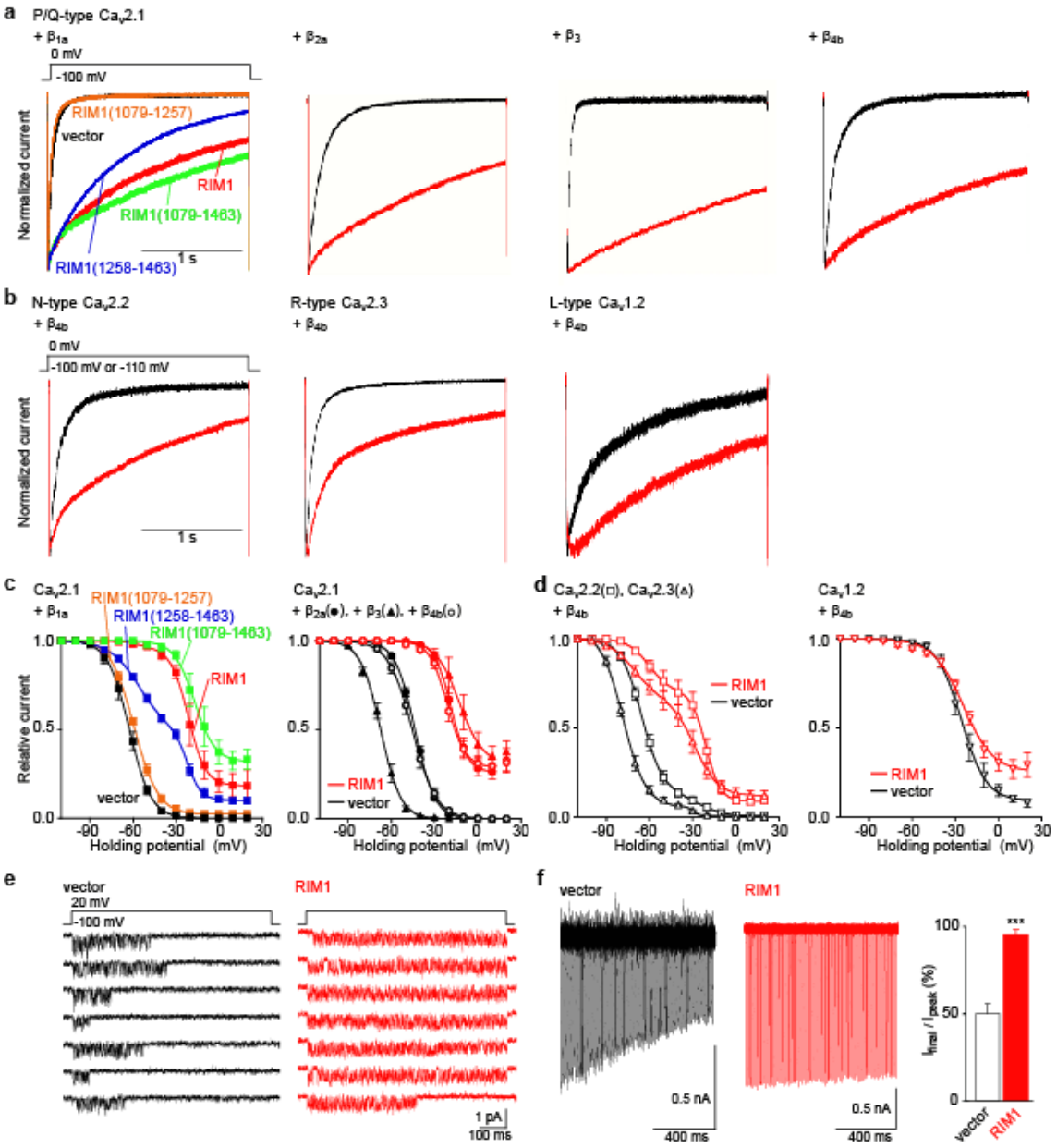
a
P/Q-type Cav2.1
+ β1a
+ β2a
+ β3
+ β4b
0 mV
-100 mV
RIM1(1079-1257)
vector
RIM1
RIM1(1079-1463)
RIM1(1258-1463)
1 s
Normalized current
b
N-type Cav2.2
+ β4b
R-type Cav2.3
+ β4b
L-type Cav1.2
+ β4b
0 mV
-100 mV or -110 mV
1 s
Normalized current
c
Cav2.1
+ β1a
RIM1(1079-1257)
RIM1(1258-1463)
RIM1(1079-1463)
RIM1
vector
Relative current
Holding potential (mV)
Cav2.1
+ β2a(●), + β3(▲), + β4b(○)
RIM1
vector
Holding potential (mV)
d
Cav2.2(□), Cav2.3(△)
+ β4b
RIM1
vector
Holding potential (mV)
Cav1.2
+ β4b
RIM1
vector
Holding potential (mV)
e
vector
20 mV
-100 mV
RIM1
1 pA
100 ms
f
vector
RIM1
0.5 nA
400 ms
0.5 nA
400 ms
100
50
0
***
Irmi / Ipeak (%)
vector
RIM1

Figure 4 Effects of RIM1 on the inactivation properties of recombinant neuronal VDCCs.

(**a**) Inactivation of P/Q-type $Ca_v2.1$ currents in BHK cells expressing α_2/δ and β-subunits. For comparison of inactivation time courses before and after expression of RIM1 constructs, the peak amplitudes are normalized for Ba^{2+} currents elicited by 2-s pulses to 0 mV from a holding potential (V_h) of –100 mV. (**b**) Inactivation of N-type $Ca_v2.2$, R-type $Ca_v2.3$, or L-type $Ca_v1.2$ currents in BHK cells expressing α_2/δ and β_{4b}. The V_h is –100 mV for $Ca_v2.2$ or $Ca_v1.2$, and –110 mV for $Ca_v2.3$. (**c**) Left: inactivation curves (see Supplementary Methods for the detail) for $Ca_v2.1$ in BHK cells expressing α_2/δ and β_{1a}. See **Supplementary Table 3** for statistical significance of the differences between vector and RIM1, RIM1(1079-1463), or RIM1(1258-1463). Right: inactivation curves for $Ca_v2.1$ in BHK cells expressing α_2/δ and different β-subunits. See **Supplementary Table 2** for statistical significance of the differences between vector and RIM1 in the presence of β_{2a}, β_3, or β_{4b}. (**d**) Inactivation curves for $Ca_v2.2$, $Ca_v2.3$ (left), or $Ca_v1.2$ (right) in BHK cells expressing α_2/δ and β_{4b}. See **Supplementary Table 1** for statistical significance of the difference between vector and RIM1 for $Ca_v2.2$, $Ca_v2.3$, or $Ca_v1.2$. (**e**) RIM1 prolongs the time between first channel opening and last closing within a single-channel trace of $Ca_v2.1$ in BHK cells expressing α_2/δ and β_{4b}. Seven consecutive unitary traces are shown. The mean values for the time of each trace are 184.2 ± 33.3 ms (n = 117 traces) for vector and 502.8 ± 33.3 ms, (n = 101) for RIM1. The time for traces without opening is counted as 0 ms. (**f**) Left: $Ca_v2.1$ currents induced by 100 Hz AP trains for 1 s in BHK cells expressing α_2/δ and β_{1a}. Right: percentage of currents in response to the last stimulus compared to the peak current (n = 6 for vector and n = 4 for RIM1). Data points are mean ± S.E.M. $^{***}P < 0.001$.

Figure 5

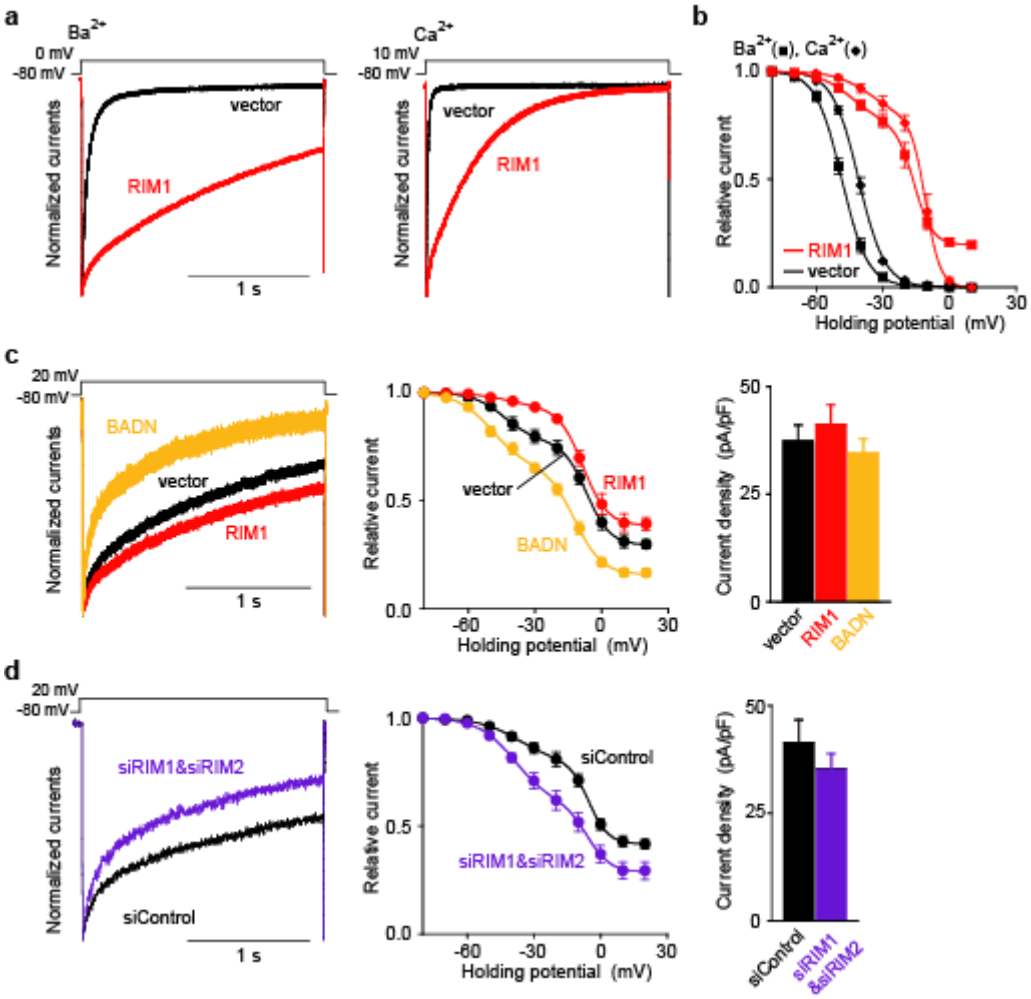
a
Ba2+
0 mV
-80 mV
vector
RIM1
Normalized currents
1 s
Ca2+
10 mV
-80 mV
vector
RIM1
Normalized currents
b
Ba2+(■), Ca2+(●)
Relative current
RIM1
vector
Holding potential (mV)
c
20 mV
-80 mV
BADN
vector
RIM1
Normalized currents
1 s
Relative current
vector
RIM1
BADN
Holding potential (mV)
Current density (pA/pF)
vector
RIM1
BADN
d
20 mV
-80 mV
siRIM1&siRIM2
siControl
Normalized currents
1 s
Relative current
siControl
siRIM1&siRIM2
Holding potential (mV)
Current density (pA/pF)
siControl
siRIM1 &siRIM2

Figure 5 Physiological relevance of effects of RIM1 on inactivation properties of VDCCs.

(**a**) Effects of RIM1 on inactivation time courses of Ba^{2+} and Ca^{2+} currents in HEK cells expressing $Ca_v2.1$, α_2/δ and β_1. For comparison of inactivation time courses before and after expression of RIM1 constructs, the peak amplitudes are normalized for Ba^{2+} (left) and Ca^{2+} currents (right) elicited by 2-s pulses to 0 and 10 mV, respectively, from a V_h of –80 mV. (**b**) Inactivation curves for Ba^{2+} and Ca^{2+} currents in HEK cells expressing $Ca_v2.1$, α_2/δ and β_1. See **Supplementary Table 6** for statistical significance of the differences between vector and RIM1. (**c**) Effects of RIM1 and BADN on the inactivation properties of native VDCCs in PC12 cells maintained for 7-9 culture passages. Left: normalized currents recorded from PC12 cells transfected with vector, RIM1, and BADN. Middle: inactivation curves induced by 2-s holding potential displacement. See **Supplementary Table 7** for statistical significance of the differences among vector, RIM1, and BADN. Right: comparison of current densities at 10 mV (n = 18, 15, and 9 cells for vector, RIM1, and BADN, respectively). (**d**) Acceleration of inactivation by coapplication of siRNAs specific for RIM1 and RIM2 (siRIM1 & siRIM2) in VDCC currents recorded from PC12 cells. PC12 cells were maintained for 2-3 culture passages. Left: normalized currents evoked by step pulses to 20 mV. Middle: inactivation curves induced by 2-s holding potential displacement. See **Supplementary Table 7** for statistical significance of the differences between control GAPDH siRNA (siControl) and siRIM1 & siRIM2. Right: comparison of current densities at 10 mV (n = 6 and 8 cells, for siControl and siRIM1 & siRIM2, respectively). Data points are mean ± S.E.M.

Figure 6

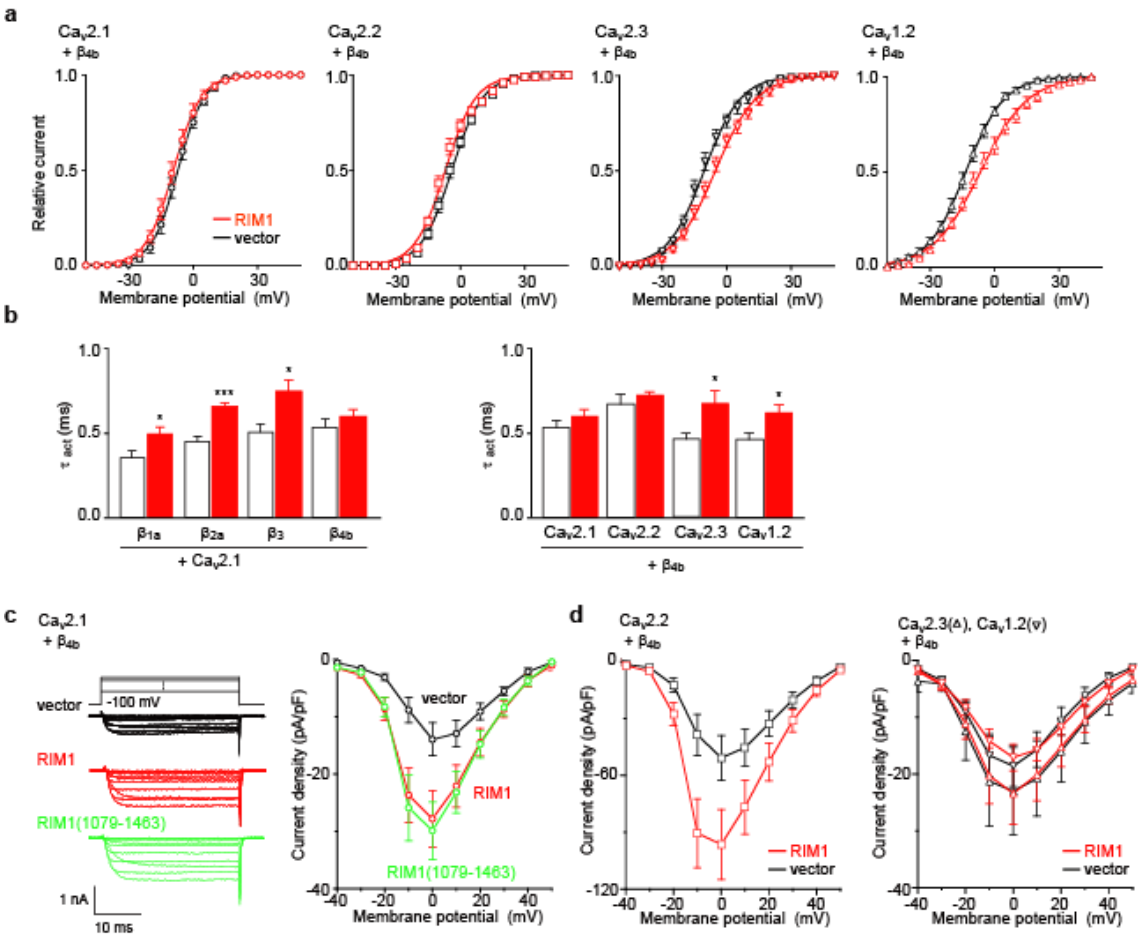
a
Cav2.1 + β4b
Cav2.2 + β4b
Cav2.3 + β4b
Cav1.2 + β4b
Relative current
RIM1
vector
Membrane potential (mV)
b
τ act (ms)
β1a
β2a
β3
β4b
+ Cav2.1
Cav2.1 Cav2.2 Cav2.3 Cav1.2
+ β4b
c
Cav2.1 + β4b
vector
RIM1
RIM1(1079-1463)
-100 mV
1 nA
10 ms
Current density (pA/pF)
d
Cav2.2 + β4b
Cav2.3(Δ), Cav1.2(▽) + β4b

Figure 6 Effects of RIM1 on the activation properties of VDCCs.

(**a**) Effects of RIM1 on activation curves of Ca_v currents elicited in BHK cells expressing α_2/δ and β_{4b}. Tail currents elicited by repolarization to –60 mV after 5-ms test pulse from –50 to 50 mV are used to determine activation curves (see Supplementary Methods for the detail). See **Supplementary Table 1** for statistical significance of the differences between vector and RIM1. (**b**) Left: effects on activation speed of $Ca_v2.1$ channels containing various β-subunits. Time constants are obtained by fitting the activation phase of currents elicited by 5-ms test pulse to 20 mV with a single exponential function. Right: effects of RIM1 on activation speed of Ca_v currents at 20 mV in various VDCC types. $^{*}P < 0.05$ and $^{***}P < 0.001$. (**c**) Effects of RIM1 proteins on P/Q-type $Ca_v2.1$. Left: representative traces for Ba^{2+} currents upon application of test pluses from –40 mV to 50 mV with 10-mV increments in BHK cells expressing α_2/δ and β_{4b}. Right: current density-voltage (*I-V*) relationships of $Ca_v2.1$. The V_h is –100 mV. See **Supplementary Table 2** for statistical significance of the differences between vector and RIM1, or RIM1(1079-1463). (**d**) *I-V* relationships of $Ca_v2.2$ (left) and $Ca_v2.3$ or $Ca_v1.2$ (right) in BHK cells expressing α_2/δ and β_{4b}. The V_h is –100 mV for $Ca_v2.2$ or $Ca_v1.2$, and –110 mV for $Ca_v2.3$. **Supplementary Table 1** for statistical significance of the differences between vector and RIM1 for $Ca_v2.2$.

Figure 7

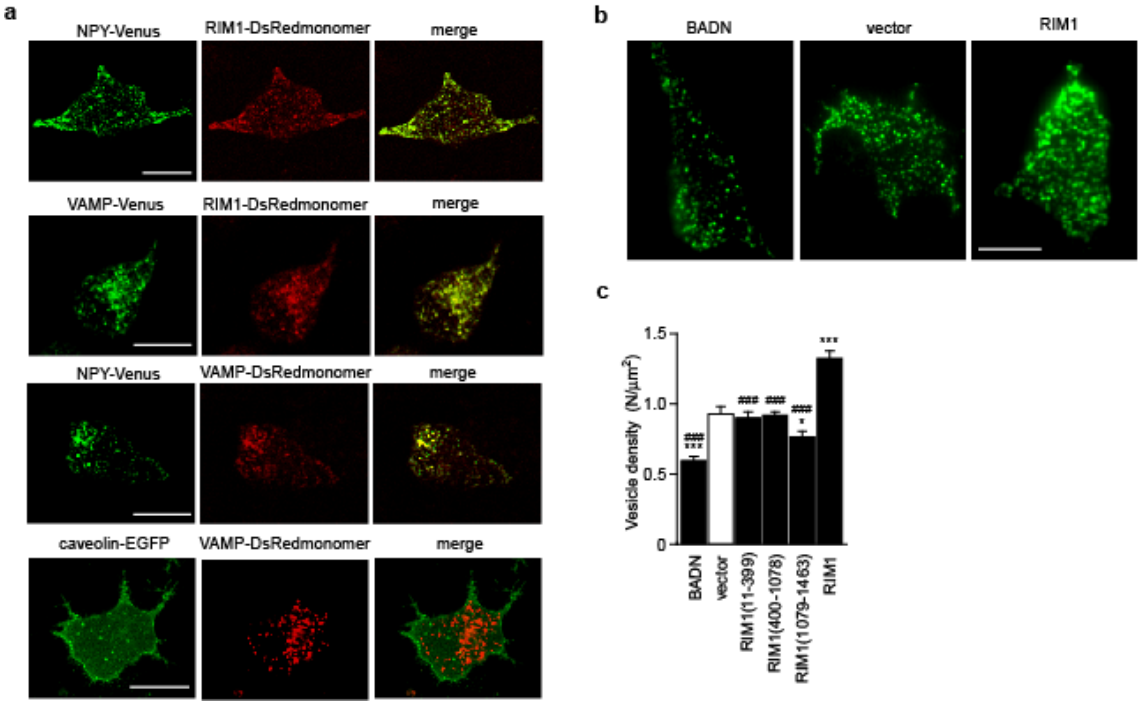

Figure 7 RIM1 and β-subunits associate to anchor neurotransmitter vesicles to VDCCs at the plasma membrane.

(**a**) NPY-containing secretory vesicles are colocalized with RIM1 and VAMP, that is not colocalized with caveolin-1 in PC12 cells. NPY-Venus and RIM1-DsRedmonomer, VAMP-Venus and RIM1-DsRedmonomer, NPY-Venus and VAMP-DsRedmonomer, or caveolin-1-EGFP and VAMP-DsRedmonomer are coexpressed in PC12 cells, and live images of the cells are obtained by confocal microscopy. Scale bar: 10 μm. (**b,c**) Effects of RIM1 constructs and BADN on the density of docked vesicles. In **b**, typical TIRF images of plasma membrane-docked vesicles containing NPY-Venus. Left: BADN-co-transfected PC12 cell. Middle: vector-co-transfected PC12 cell. Right: RIM1-co-transfected PC12 cell. Scale bar: 10 μm. In **c**, the vesicle density is determined by counting the vesicles in each image (n = 20 cells in each). $^{*}P < 0.05$, $^{***}P < 0.001$ vs vector. $^{\#\#\#}P < 0.001$ vs RIM1.

Figure 8

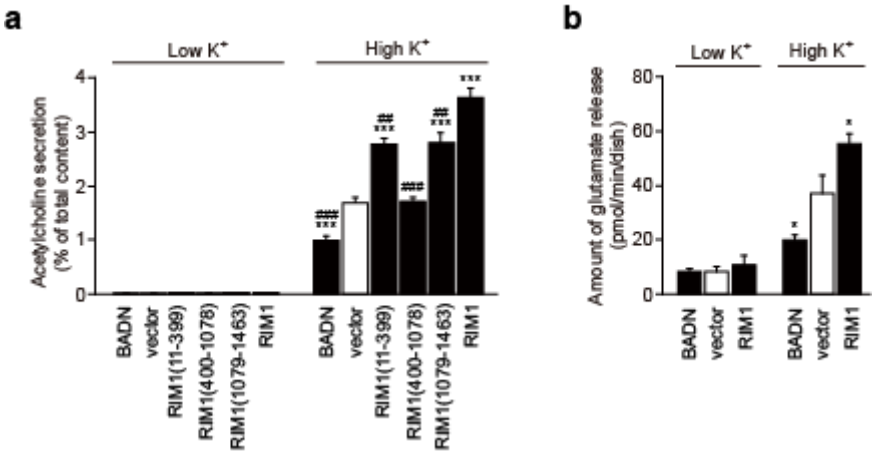

Figure 8 The RIM1-β association enhances neurotransmitter release in PC12 cells and cultured cerebellar neurons.

(**a**) Effects of RIM1 constructs and BADN on depolarization-dependent release of ACh from ChAT-co-transfected PC12 cells. The amount of secreted ACh is determined as a percentage of the cellular content for each dish. $^{***}P < 0.001$ vs vector. $^{\#\#}P < 0.01$, $^{\#\#\#}P < 0.001$ vs RIM1. (**b**) Effects of RIM1 and BADN on depolarization-dependent release of glutamate from cultured cerebellar neurons. $^{*}P < 0.05$.

Supplementary Figure 1

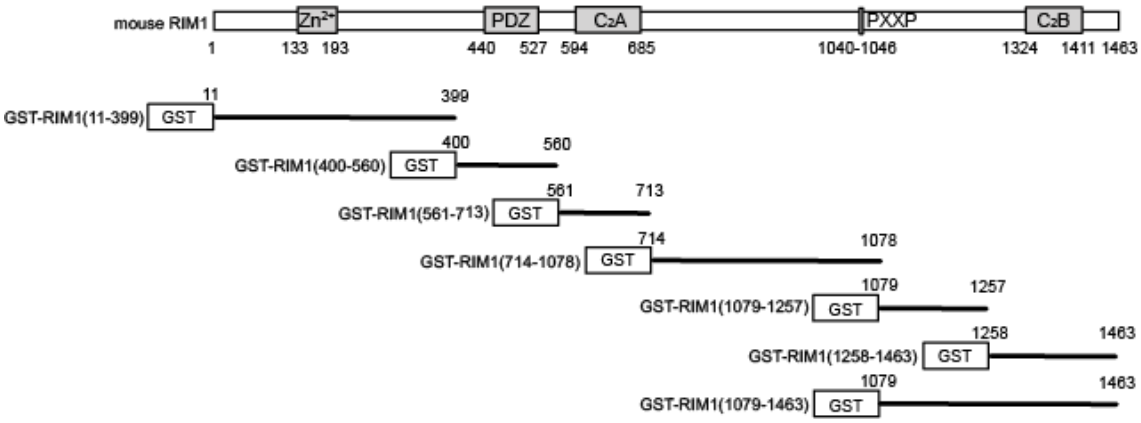

Supplementary Figure 1 Recombinant constructs of GST fusion RIM1 subfragments.

Supplementary Figure 2

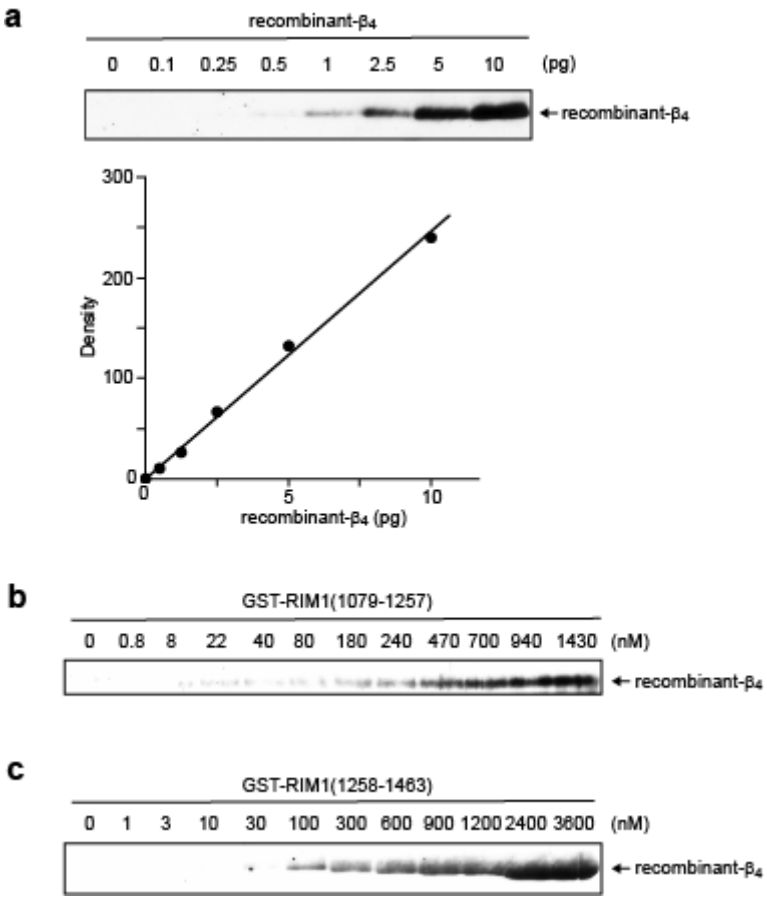

Supplementary Figure 2 *in vitro* binding of the purified RIM1 GST fusion and recombinant β_4 proteins.

(**a**) Intensity of recombinant β_4 detected by enhanced chemiluminescence is proportional to the amount of β_4, supporting that this assay is appropriate for quantitative analyses of RIM1-β_4 binding. (**b**) Dose-dependent binding of GST-RIM11079-1257 to the recombinant β_4-subunit. (**c**) Dose-dependent binding of GST-RIM11258-1463 to the recombinant β_4-subunit.

Supplementary Figure 3

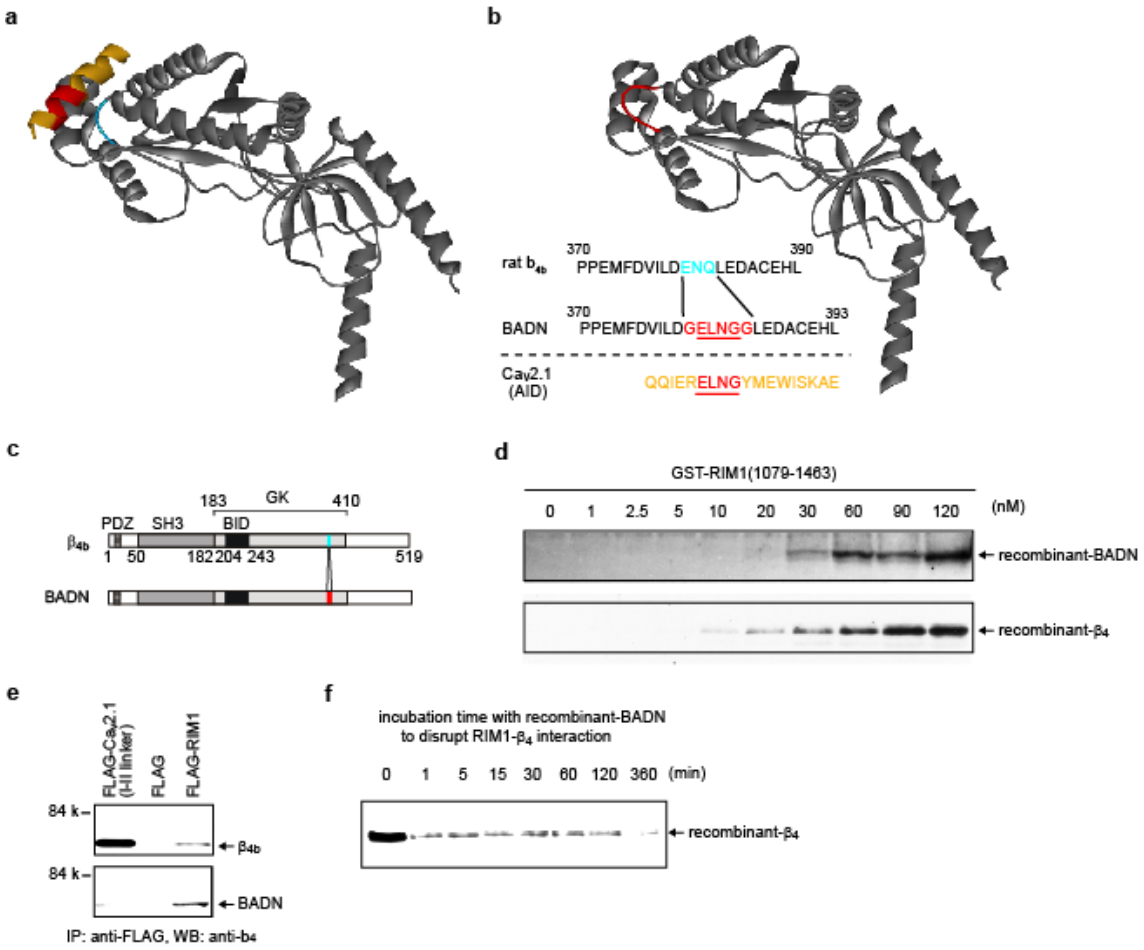

Supplementary Figure 3 Molecular modeling and functional characterization of BADN as a dominant-negative mutant for RIM1 function.

(**a**) X-ray structure of the β subunit and AID (yellow and red) complex adapted from the previous paper by Opatowsky et al[33]. (**b**) Energetically minimized structure of BADN by molecular modeling. BADN is designed to suppress AID binding without destruction of the β subunit 3D structure. Inset indicates the amino acid sequence (370-393) of BADN compared with the sequence of rat β_{4b} and the AID sequence of $Ca_v2.1$. BADN is constructed on the basis of rat β_{4b}, and hexa-peptide (GELNGG (red)) containing the essential region (ELNG) for β subunit binding of AID with flanking glycine residues as spacers replacing the original tri-peptide (ENQ (blue)) to suppress AID binding. (**c**) Domain structure of β_{4b} and BADN. (**d**) Dose-dependent binding of recombinant-BADN to the GST-RIM11079-1463 is shown. This result shows that BADN has affinity to RIM11079-1463 comparable with that of β_4. (**e**) Interaction of recombinant BADN and RIM1 in HEK293 cells. The interaction is evaluated by IP with anti-FLAG antibody, followed by WB with anti- β_4 antibody. Top: HEK293 cells co-transfected with β_{4b} and FLAG-RIM1. FLAG-$Ca_v2.1$(I-II linker) is used as a positive control. Bottom: HEK293 cells co-transfected with BADN and FLAGRIM1. (**f**) Rapid disruption of the RIM1- β_{4b} interaction by BADN. The dissociation is measured in the presence of excessive BADN protein (200 nM). This result suggests that virtually complete disruption of the RIM1- β_{4b} interaction is attained within 6 h of incubation.

Supplementary Figure 4

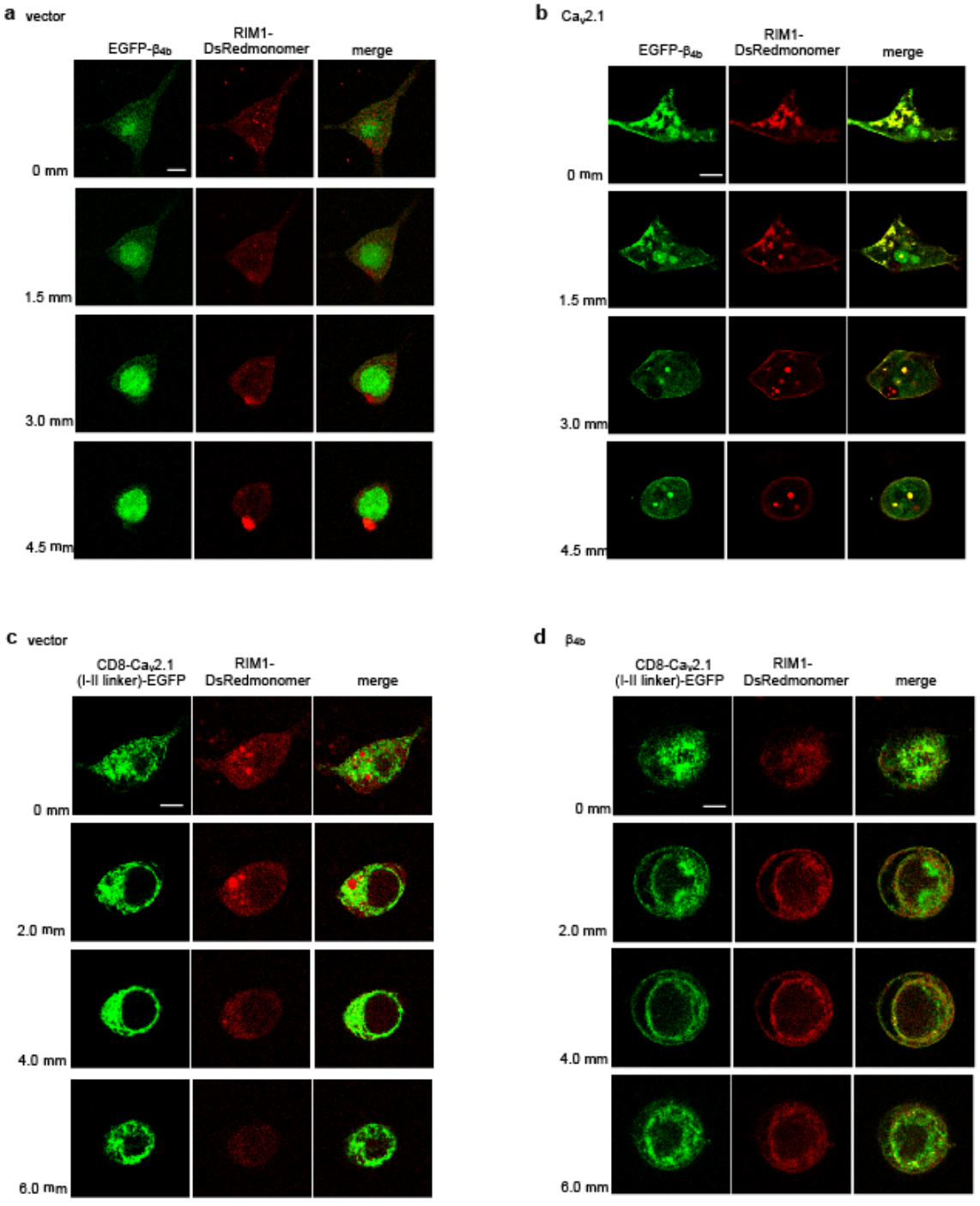

Supplementary Figure 4 Confocal images of RIM1 and β_{4b} colocalization mediated by $Ca_v2.1$ α1-subunit proteins at the plasma membrane.

(**a**) X-Y images at different Z-axis depths in HEK293 cells co-transfected with EGFP-β_{4b} and RIM1-DsRed-monomer in the absence of $Ca_v2.1$. Scale bar: 5 μm. (**b**) X-Y images at different Z-axis depth in of HEK293 cells co-transfected with EGFP-β_{4b} and RIM1-DsRed-monomer in the presence of $Ca_v2.1$. (**c**) X-Y images at different Z-axis depths in HEK293 cells co-transfected with CD8-$Ca_v2.1$(I-II linker)-EGFP and RIM1-DsRed-monomer in the absence of β_{4b}. (**d**) X-Y images at different Z-axis depths in HEK293 cells co-transfected with CD8-$Ca_v2.1$(I-II linker)-EGFP and RIM1-DsRed-monomer in the presence of β_{4b}.

Supplementary Figure 5

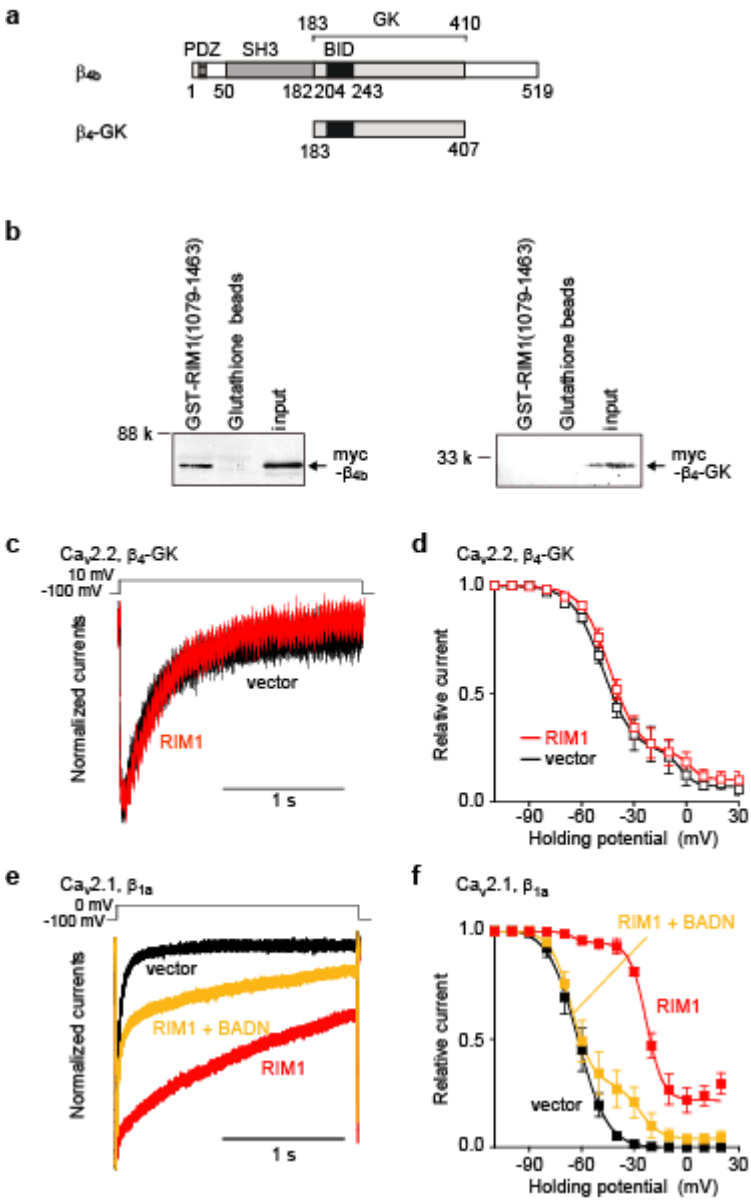

Supplementary Figure 5 Disruption of the RIM1 effects on VDCC inactivation by the β_4 GK domain and BADN.

(**a**) Structure of β_4-GK in comparison with the WT β_{4b}. β_4-GK corresponds to 183-407 of rat β_{4b}. (**b**) Pulldown assay of β_4-GK constructs with RIM11079-1463 GST fusion protein demonstrates that β_4-GK does not interact with RIM11079-1463. cDNA of β_4-GK is subcloned in the expression plasmid pCMV-tag3. GST fusion proteins immobilized on glutathione-Sepharose beads are incubated with cell lysate obtained from myc- β_4-GK-expressing HEK293 cells. Bound proteins are analyzed by WB using anti-myc antibody. (**c**) Inactivation of $Ca_v2.2$ currents in BHK cells expressing α_2/δ and β_4-GK. For comparison of inactivation time courses before and after expression of RIM1 constructs, the peak amplitudes are normalized for Ba^{2+} currents elicited by 2-s pulses to 10 mV from a *V*h of –100 mV. 10 mM Ba^{2+} is used as a charge carrier. (**d**) Inactivation curves of $Ca_v2.2$ currents in BHK cells expressing α_2/δ and β_4-GK. (**e**) Dominant-negative effect of BADN for RIM1 effects on inactivation properties of VDCCs. Inactivation kinetics of $Ca_v2.1$ currents in BHK cells expressing α_2/δ and β_{1a}. (**f**) Inactivation curves of $Ca_v2.1$ in BHK cells expressing α_2/δ and β_{1a}. The differences at > –80 mV between vector and RIM1, or those between RIM1 plus BADN and RIM1 are significant ($P < 0.05$).

Supplementary Figure 6

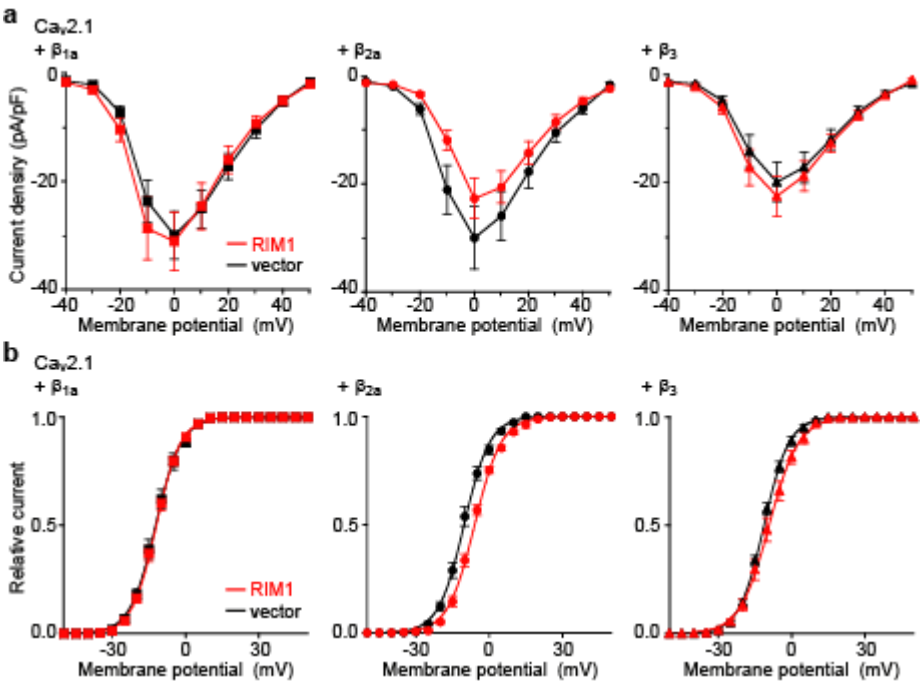

Supplementary Figure 6 Effects of RIM1 on the activation properties of VDCCs.

(**a**) *I-V* relationships of $Ca_v2.1$ channels in BHK cells expressing α2/δ and various β subunits. The *V*h is –100 mV. (**b**) Activation curves. The differences between vector control and RIM1 are significant at membrane potentials from –25 to +5 mV for β_{2a} are significant ($P < 0.05$).

Supplementary Figure 7

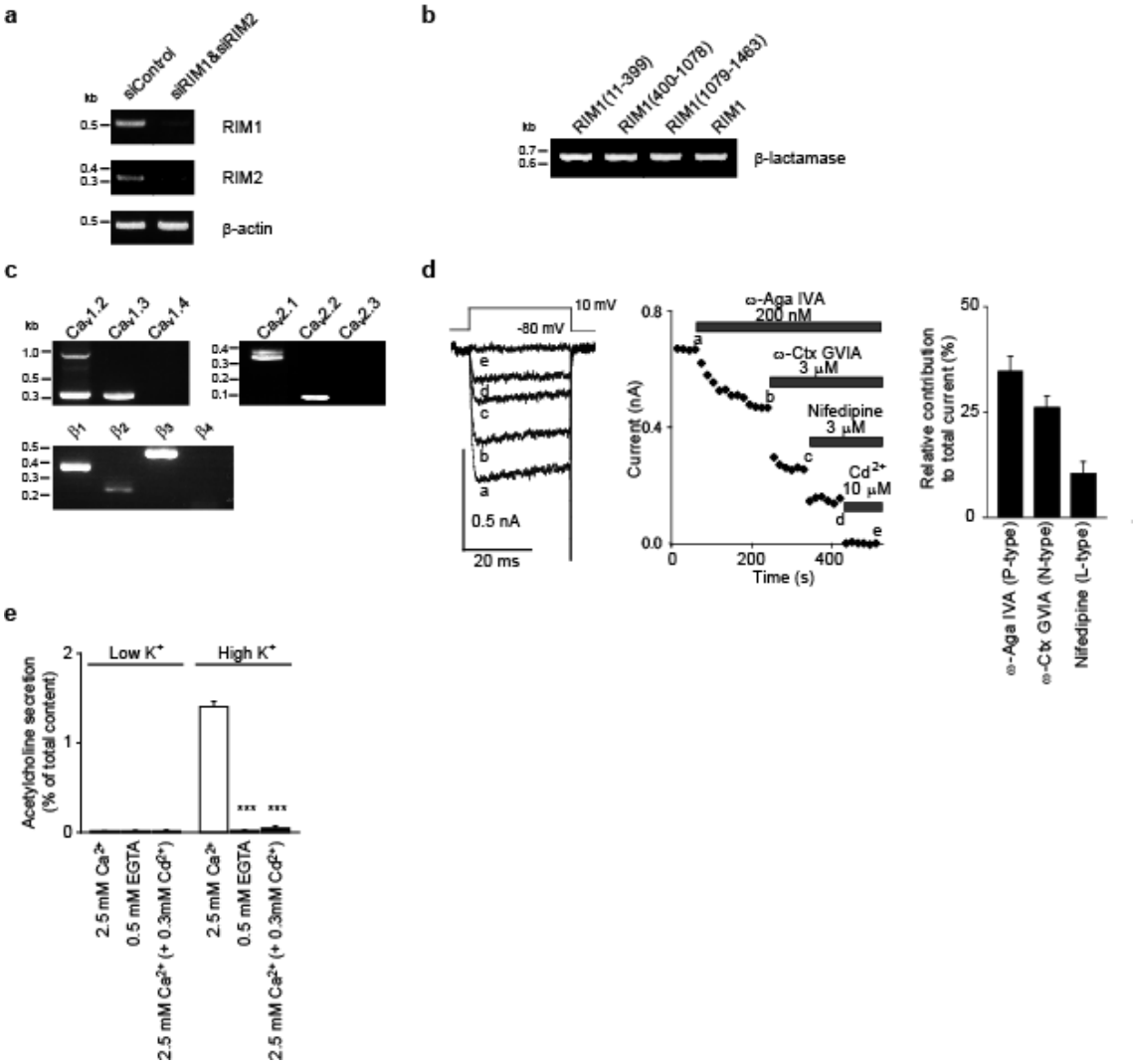

Supplementary Figure 7 Molecular and physiological characterization of PC12 cells.

(**a**) RT-PCR analysis of RIM1 and RIM2 RNA expression in PC12 cells treated with GAPDH siRNA (siControl) and combination of RIM1- and RIM2-specific siRNAs (siRIM1 and siRIM2). Primer sequences are indicated in **Supplementary Table 9**. RT-PCR was performed using LA-PCR kit (TaKaRa), according to the manufacturer's information. (**b**) Transfection levels of cDNAs of RIM constructs are examined using PCR in PC12 cells. Primers are designed to amplify the lactamase gene in the pCI-neo vector (**Supplementary Table 9**). PCR was carried out using LA-PCR kit. (**c**) RNA expression analysis of α_1 and β subunits using RT-PCR in PC12 cells. (**d**) Pharmacological dissection of high voltage-activated Ca^{2+} channel currents in PC12 cells. Left & Middle: time course of blockage of Ca^{2+} current by serial application of 200 nM ω-Aga IVA, 3 μM ω-Ctx GVIA, 3 μM Nifedipine, and 10 μM Cd^{2+} in PC12 cell. Right: summary of relative contributions of each current type. (**e**) Cd^{2+}-sensitive Ca^{2+} influx pathway is responsible for depolarization-dependent ACh release from ChAT-transfected PC12 cells. Cd^{2+} is a selective blocker for high voltage-activated Ca^{2+} channels. ***$P < 0.001$ versus 2.5 mM Ca^{2+}.

Supplementary Figure 8

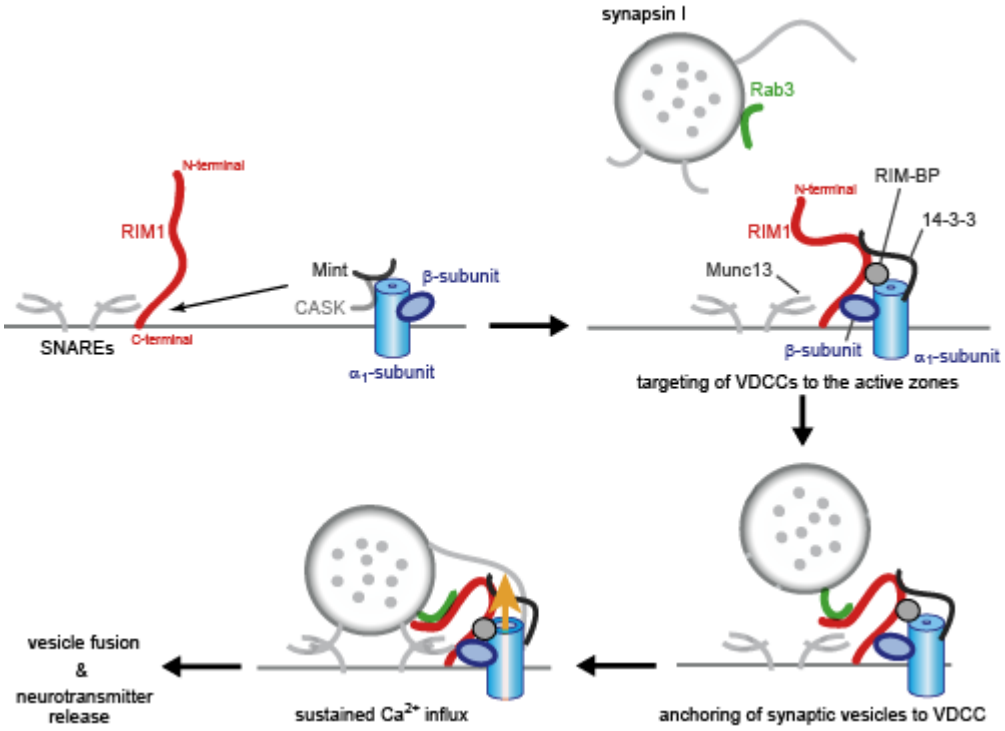

Supplementary Figure 8 A model detailing the putative role of the β subunit-RIM1 interaction at presynaptic AZs.

Synaptic vesicles are anchored to presynaptic AZs through the association of RIM1 with β subunits, Rab3, and Munc13. Also, functional properties of neuronal VDCCs are significantly modulated by RIM1 through physical association with the β subunit, which can efficiently maintain Ca^{2+} influx through VDCC at AZs. These presynaptic processes regulated by the RIM1-β complex can involve other important presynaptic proteins such as RIM-BP in the vesicle anchoring by mediating an indirect association of RIM1 with VDCC α_1. 14-3-3, which regulates VDCC inactivation, may contribute to anchoring via the same mechanism. Mint and CASK regulate presynaptic targeting of VDCCs via their association with α_1.

Supplementary Table 1 Effects of RIM1 constructs on current density, activation, and inactivation of $Ca_v2.1$, $Ca_v2.2$, $Ca_v2.3$, or $Ca_v1.2$ channel in BHK cells expressing α_2/δ and β_{4b}[1].

Subunit combination	Current density (pA / pF)[2]	Activation parameters			Inactivation parameters					
		$V_{0.5}$ (mV)	k (mV)	τ_{act} (ms)[3]	a	$V_{0.5}^{1st}$ (mV)	k^{1st} (mV)	b	$V_{0.5}^{2nd}$ (mV)	k^{2nd} (mV)
$Ca_v2.1$ Vector	−14.0 ± 2.9 (15)	−7.2 ± 1.2 (9)	5.7 ± 0.1 (9)	0.53 ± 0.05 (9)	1.00 ± 0.00 (12)	−45.9 ± 1.8 (12)	−7.5 ± 0.3 (12)			
+ β_{4b} RIM1	−27.8 ± 4.9 (18)*	−9.1 ± 1.6 (13)	5.6 ± 0.2 (13)	0.59 ± 0.04 (13)	0.70 ± 0.04 (6)***	−21.3 ± 1.2 (6)***	−5.6 ± 0.7 (6)			
$Ca_v2.2$ Vector	−50.8 ± 11.9 (12)	−4.1 ± 1.0 (11)	6.8 ± 0.2 (11)	0.67 ± 0.06 (11)	0.91 ± 0.03 (7)	−64.5 ± 1.6 (7)	−7.8 ± 0.5 (7)	0.09 ± 0.04 (7)	−22.4 ± 2.1 (7)	−5.1 ± 1.7 (7)
+ β_{4b} RIM1	−96.4 ± 18.5 (10)*	−7.0 ± 1.0 (7)	6.8 ± 0.4 (7)	0.73 ± 0.02 (7)	0.30 ± 0.06 (5)***	−59.7 ± 1.2 (5)	−7.7 ± 0.7 (5)	0.61 ± 0.06 (5)***	−20.8 ± 1.8 (5)	−4.9 ± 1.0 (5)
$Ca_v2.3$ Vector	−23.0 ± 7.7 (10)	−10.3 ± 1.5 (7)	8.4 ± 0.5 (7)	0.47 ± 0.03 (7)	0.91 ± 0.02 (5)	−78.2 ± 1.3 (5)	−6.7 ± 0.7 (5)	0.08 ± 0.04 (5)	−36.2 ± 3.3 (5)	−6.1 ± 2.9 (5)
+ β_{4b} RIM1	−23.4 ± 5.4 (12)	−5.3 ± 1.4 (6)*	9.4 ± 0.6 (6)	0.67 ± 0.07 (6)*	0.35 ± 0.05 (6)***	−71.0 ± 1.6 (6)**	−9.1 ± 0.9 (6)	0.53 ± 0.05 (6)***	−27.9 ± 2.3 (6)	−7.5 ± 0.4 (6)
$Ca_v1.2$ Vector	−18.6 ± 3.6 (10)	−13.6 ± 1.3(12)	8.4 ± 0.4 (12)	0.46 ± 0.03 (6)	0.93 ± 0.02 (6)	−24.6 ± 3.1 (6)	−8.3 ± 1.3 (6)			
+ β_{4b} RIM1	−17.1 ± 2.3 (13)	−8.0 ± 1.3 (11)**	10.2± 0.3 (11)**	0.62 ± 0.04 (7)*	0.75 ± 0.07 (5)*	−24.7 ± 1.6 (5)	−10.1 ± 0.6 (5)			

1) $^{*}P < 0.05$, $^{**}P < 0.01$, $^{***}P < 0.001$ versus vector.

2) Ba^{2+} currents evoked by depolarizing pulse to 0 mV from a V_h of −100 or −110 mV are divided by capacitance.

3) Activation time constants obtained from currents elicited by 5-ms test pulse to 20 mV. The activation phases are well fitted by a single exponential function.

Supplementary Table 2 Effects of RIM1 constructs on current density, activation, and inactivation of $Ca_v2.1$ channel in BHK cells expressing α_2/δ and various β-subunits[1].

Subunit combination		Current density (pA / pF)[2]	Activation parameters			Inactivation parameters		
			$V_{0.5}$ (mV)	k (mV)	τ_{act} (ms)[3]	a	$V_{0.5}$ (mV)	k (mV)
$Ca_v2.1$	Vector	−30.0 ± 4.4 (11)	−12.3 ± 1.0 (6)	5.0 ± 0.2 (6)	0.35 ± 0.04 (5)	1.00 ± 0.00 (7)	−62.6 ± 1.9 (7)	−7.0 ± 0.3 (7)
+ β_{1a}	RIM1	−31.1 ± 5.5 (7)	−12.0 ± 0.7 (7)	4.9 ± 0.2 (7)	0.49 ± 0.04 (6)*	0.83 ± 0.07 (5)***	−21.6 ± 2.5 (5)***	−6.1 ± 0.9 (5)
+ β_{2a}	Vector	−30.0 ± 5.8 (15)	−10.3 ± 0.9 (8)	5.0 ± 0.2 (8)	0.45 ± 0.03 (8)	1.00 ± 0.00 (13)	−47.4 ± 0.9 (13)	−6.2 ± 0.2 (13)
	RIM1	−22.7 ± 3.7 (6)	−6.0 ± 0.5 (6)***	5.4 ± 0.2 (6)	0.65 ± 0.02 (6)***	0.73 ± 0.05 (6)***	−18.4 ± 1.4 (6)***	−5.3 ± 0.6 (6)**
+ β_3	Vector	−19.9 ± 3.6 (16)	−11.3 ± 0.6 (8)	5.0 ± 0.3 (8)	0.50 ± 0.05 (8)	1.00 ± 0.00 (7)	−67.5 ± 1.4 (7)	−6.8 ± 0.3 (7)
	RIM1	−22.5 ± 3.7 (23)	−9.2 ± 1.3 (9)	5.6 ± 0.2 (9)	0.74 ± 0.07 (7)*	0.66 ± 0.05 (5)***	−13.2 ± 3.3 (5)***	−6.0 ± 0.5 (5)
+ β_{4b}	Vector	−14.0 ± 2.9 (15)	−7.2 ± 1.2 (9)	5.7 ± 0.1 (9)	0.53 ± 0.05 (9)	1.00 ± 0.00 (12)	−45.9 ± 1.8 (12)	−7.5 ± 0.3 (12)
	RIM1	−27.8 ± 4.9 (18)*	−9.1 ± 1.6 (13)	5.6 ± 0.2 (13)	0.59 ± 0.04 (13)	0.70 ± 0.04 (6)***	−21.3 ± 1.2 (6)***	−5.6 ± 0.7 (6)
	$RIM1_{1079–1463}$	−29.9 ± 5.0 (10)**						

1) $^{*}P < 0.05$, $^{**}P<0.01$, $^{***}P < 0.001$ versus vector.

2) Ba^{2+} currents evoked by depolarizing pulse to 0 mV from a V_h of −100 mV are divided by capacitance.

3) Activation time constants obtained from currents elicited by 5-ms test pulse to 20 mV. The activation phases are well fitted by a single exponential function.

Supplementary Table 3 Effects of RIM1 or C-terminal truncated mutants of RIM1 on inactivation of $Ca_v2.1$ channel in BHK cells expressing α_2/δ and β_{1a} [1)2)].

	Inactivation parameters					
	a	$V_{0.5}^{1st}$ (mV)	k^{1st} (mV)	*b*	$V_{0.5}^{2nd}$ (mV)	k^{2nd} (mV)
Vector	1.00 ± 0.00 (7)	−62.6 ± 1.9 (7)	−7.0 ± 0.3 (7)			
RIM1	0.83 ± 0.07 (5)**	−21.6 ± 2.5 (5)***	−6.1 ± 0.9 (5)			
$RIM1_{1079–1257}$	1.00 ± 0.00 (4)#	−58.9 ± 0.7 (4)###	−8.0 ± 0.8 (4)			
$RIM1_{1258–1463}$	0.51 ± 0.03 (6)***###	−55.2 ± 1.5 (6)*###	−9.6 ± 0.9 (6)*##	0.41 ± 0.02 (6)	−22.3 ± 1.0 (6)	−5.1 ± 1.3 (6)
$RIM1_{1079–1463}$	0.70 ± 0.05 (5)***#	−15.8 ± 3.7 (5)***	−5.9 ± 0.9 (5)			

1) $^{*}P < 0.05$, $^{**}P < 0.01$, $^{***}P < 0.001$ versus vector.

2) $^{\#}P < 0.05$, $^{\#\#}P < 0.01$, $^{\#\#\#}P < 0.001$ versus RIM1.

Supplementary Table 4 Effects of RIM1 on inactivation of $Ca_v2.2$ channel in BHK cells expressing α_2/δ and β_4-GK.

	Inactivation parameters					
	a	$V_{0.5}^{1st}$ (mV)	k^{1st} (mV)	*b*	$V_{0.5}^{2nd}$ (mV)	k^{2nd} (mV)
Vector	0.75 ± 0.08 (5)	−48.9 ± 1.5 (5)	−8.1 ± 0.6 (5)	0.20 ± 0.05 (5)	−5.0 ± 2.2 (5)	−3.9 ± 1.0 (5)
RIM1	0.78 ± 0.07 (5)	−44.0 ± 1.8 (5)	−8.1 ± 0.6 (5)	0.11 ± 0.05 (5)	1.4 ± 0.4 (5)	−4.5 ± 0.4 (5)

Supplementary Table 5 Effects of RIM1 or BADN on inactivation of $Ca_v2.1$ channel in BHK cells expressing α_2/δ and β_{1a}[1)2)].

	Inactivation parameters					
	a	$V_{0.5}^{1st}$ (mV)	k^{1st} (mV)	*b*	$V_{0.5}^{2nd}$ (mV)	k^{2nd} (mV)
RIM1	0.06 ± 0.02 (4)***	−64.3 ± 1.9 (4)	−3.8 ± 0.8 (4)**	0.73 ± 0.07 (4)	−22.3 ± 0.9 (4)	−5.1 ± 0.8 (4)
Vector	1.00 ± 0.00 (6)	−62.0 ± 3.1 (6)	−6.7 ± 0.2 (6)			
RIM1 + BADN	0.72 ± 0.07 (5)***###	−64.6 ± 2.4 (5)	−6.0 ± 0.8 (5)#	0.24 ± 0.06 (5)**	−29.2 ± 3.8 (5)	−8.4 ± 2.8 (5)

1) $^{**}P < 0.01$, $^{***}P < 0.001$ versus vector.

2) $^{\#}P < 0.05$, $^{\#\#\#}P < 0.001$ versus RIM1.

Supplementary Table 6 Effects of RIM1 on inactivation of $Ca_v2.1$ channel in HEK cells expressing α_2/δ and β_1[1)].

	Inactivation parameters					
	a	$V_{0.5}^{1st}$ (mV)	k^{1st} (mV)	*b*	$V_{0.5}^{2nd}$ (mV)	k^{2nd} (mV)
Vector (Ca^{2+})	1.00 ± 0.00 (5)	−41.0 ± 0.7 (5)	−5.8 ± 0.3 (5)			
RIM1 (Ca^{2+})	0.22 ± 0.05 (5)***	−35.5 ± 1.7 (5)	−7.4 ± 1.1 (5)	0.79 ± 0.05 (5)	−10.8 ± 1.4 (5)	−3.0 ± 0.2 (5)
Vector (Ba^{2+})	1.00 ± 0.00 (5)	−48.5 ± 1.0 (5)	−5.8 ± 0.3 (5)			
RIM1 (Ba^{2+})	0.23 ± 0.02 (5)***	−45.5 ± 2.4 (5)	−6.4 ± 0.6 (5)	0.58 ± 0.01 (5)	−16.3 ± 1.7 (5)	−4.0 ± 0.6 (5)

1) $^{***}P < 0.001$ versus vector

Supplementary Table 7 Effects of RIM1 or BADN on inactivation of VDCCs in PC12 cells[1)2)].

	Inactivation parameters					
	a	$V_{0.5}^{1st}$ (mV)	k^{1st} (mV)	*b*	$V_{0.5}^{2nd}$ (mV)	k^{2nd} (mV)
Vector	0.23 ± 0.04 (5)	−42.7 ± 0.6 (5)	−7.0 ± 0.9 (5)	0.48 ± 0.04 (5)	−6.9 ± 0.9 (5)	−5.2 ± 0.5 (5)
RIM1	0.07 ± 0.01 (5)**	−40.7 ± 4.5 (5)	−6.4 ± 2.3 (5)	0.54 ± 0.03 (5)	−7.7 ± 1.3 (5)	−5.3 ± 0.4 (5)
BADN	0.36 ± 0.03 (6)**###	−48.5 ± 2.6 (6)	−7.8 ± 0.7 (6)	0.48 ± 0.04 (6)	−11.7 ± 1.3 (6)*#	−5.5 ± 0.6 (6)
siControl	0.21 ± 0.04 (6)	−36.8 ± 1.7 (6)	−7.9 ± 1.4 (6)	0.37 ± 0.04 (6)	−5.3 ± 1.0 (6)	−3.9 ± 0.5 (6)
siRIM1 and RIM2	0.39 ± 0.04 (8)**	−38.6 ± 1.8 (8)	−8.4 ± 0.6 (8)	0.32 ± 0.02 (8)	−6.4 ± 1.5 (8)	−5.1 ± 0.6 (8)

1) $^{*}P < 0.05$, $^{**}P < 0.01$ versus vector.

2) $^{\#}P < 0.05$, $^{\#\#\#}P < 0.001$ versus RIM1.

Supplementary Table 8 Buffer solutions for biochemistry.

Buffer Name	Constituents (final concentration):
NP40 buffer	150 mM NaCl, 50 mM Tris, 1% NP40, protease inhibitors (1 mM PMSF, 10 μg/ml leupeptin), pH 8.0
Buffer I	50 mM Tris, 500 mM NaCl, 1% digitonin, protease inhibitors (0.6 μg/mL pepstatin A, 0.5 μg/mL aprotonin and leupeptin, 0.1 mM PMSF, 0.75 mM benzamidine, 2 μM calpain I inhibitor and calpeptin), pH 7.4
Buffer II	20 mM HEPES, 300 mM NaCl, 0.1% digitonin, protease inhibitors (same as buffer I), pH 7.4
Buffer III	20 mM HEPES, 400 mM NaCl, 0.1% digitonin, protease inhibitors (same as buffer I), pH 7.4
Buffer IV	20 mM HEPES, 700 mM NaCl, 0.1% digitonin, protease inhibitors (same as buffer I), pH 7.4
Buffer V	20 mM HEPES, 0.1% digitonin, protease inhibitors (same as buffer I), pH 7.4
Buffer VI	50 mM Tris, 150 mM NaCl, 0.1% digitonin, protease inhibitors (same as buffer I), 5 – 40% sucrose, pH 7.4

Supplementary Table 9 Antisense and sense PCR primers.

Gene	Orientation	Pair of primers for first PCR (5' to 3')	Pair of primers for nested PCR (5' to 3')
$Ca_v1.2$	Sense	AAGAAGAGAAGGAGAGAAAGAAGCTGGC	GATGCGGAGAGCCTGACCTCTGCCC
	Antisense	CATCCTCTTCACCTGCAGTGTCTGGG	CGGGGGCGTGGGCCCACAGGCATCTCG
$Ca_v1.3$	Sense	TGAGACACAGACCAAGCGAAGC	ACCTTCGACAACTTCCCACAGGCGCTCC
	Antisense	GTTGTCACTGTTGGCTATCTGG	GACCTCTGGTTTGTTGTTTTTTTTGTTTTCTAGG
$Ca_v1.4$	Sense	TCTTCATGCTCTGTGCCT	CCTAACCAGAGATTGGTCTATTCTGGGACCC
	Antisense	AGCCCTGCCTGGTCCTGA	CCTGGGATGGGCAAATCCTCACAACTGCCC
$Ca_v2.1$	Sense	CCAGTCTGTGGAGATGAGAGAAATGGG	CTGATGGCTACTCAGACAGCGAACACTACC
	Antisense	TTTGGAGGGCAGGTCACCCGATTG	CATGCTCAGATCTGTCCCCAGGCC
$Ca_v2.2$	Sense	GCCGTCTCAGCCGCGGCCTTTCT	CAATGCCCTGCTCCAGAAAGAGCCC
	Antisense	CAAAGGTGAGTGTATCCTCAGGC	CCAGACGCTGCCCTAGGTAAGGGTC
$Ca_v2.3$	Sense	ATCTTACTGTGGACCTTCGTGC	GCAGTCCTTTAAGGCTCTCCCCTATG
	Antisense	CTAGCGGTGGTGACATGAGAGTCAGC	CATACATCTCAGTGTAATGGATGCGGCC
β_1	Sense	TCCAGGGACCCTACCTTGTTTCC	GGGACCAGCCGCTGGACCGGG
	Antisense	CCTCCAGCTCATTCTTATTGCGC	GGCCCACCACCCTCCGCACAG
β_2	Sense	TCGGATCCGAAGAAGAACCTTGTCTGG	CCCAACACCGTTCTTCCTCAGCCACACACC
	Antisense	TCGAATTCAGTAGCGATCCTTAGATTTATGC	CCTAGTGCGGTGGCGAGGCTCC
β_3	Sense	GTGGTGTTGGATGCTGAC	GCACAGCTAGCCAAGACCTCACTGG
	Antisense	ATTGTGGTCATGCTCCGA	GGTCATGCCCGTTAGCACTGGG
β_4	Sense	CGTGGGCTCCACAGCTCTCTCACC	CTCTGGACTACAGAGTCAGCGGATGAGGC
	Antisense	CCACCAGAGGGTAGTGATCTCGGCTGTGC	GGAGGACAAGCGGTTCCTACTCTTGCGG
RIM1	Sense	CAGCATCAACAGTTATAGCTCGG	
	Antisense	CATCCAATCACCATGCTGGATAG	
RIM2	Sense	GGATCACAAATCCTTTATGGGAGTGG	
	Antisense	CACAGGATGGCTCTTTATCCCTAGAC	
β-actin	Sense	TTCTACAATGAGCTGCGTGTGGC	
	Antisense	CTCATAGCTCTTCTCCAGGGAGGA	
β-lactamase	Sense	GTTACATCGAACTGGATCTCAACAGC	
	Antisense	CGTGTAGATAACTACGATACGGGAG	

Chaptor 2

Mutation associated with an autosomal dominant cone-rod dystrophy CORD7 modifies RIM1-mediated modulation of voltage-dependent Ca^{2+} channels

Abstract

Genetic analyses have revealed an association between the gene encoding the Rab3A-interacting molecule (RIM1) and the autosomal-dominant cone-rod dystrophy CORD7. However, the pathogenesis of CORD7 remains unclear. We recently revealed that RIM1 regulates voltage-dependent Ca^{2+} channel (VDCC) currents and anchors neurotransmitter-containing vesicles to VDCCs, thereby controlling neurotransmitter release. We demonstrate here that the mouse RIM1 arginine-to-histidine substitution (R655H), which corresponds to the human CORD7 mutation, modifies RIM1 function in regulating VDCC currents elicited by the P/Q-type $Ca_v2.1$ and L-type $Ca_v1.4$ channels. Thus, our data can raise an interesting possibility that CORD7 phenotypes including retinal deficits and enhanced cognition are at least partly due to altered regulation of presynaptic VDCC currents.

Introduction

Originally identified as a putative effector for the synaptic vesicle protein Rab3, RIM1 is expressed in the brain and retinal photoreceptors where it is localized to presynaptic ribbons in ribbon synapses.[1] RIM1 interacts with other presynaptic active-zone protein components, including Munc13, ELKS (also known as CAST), RIM-BP and liprins, to form a protein scaffold in the presynaptic nerve terminal.[2-6] Mouse knockout studies revealed that, in different types of synapses, RIM1 is essential for Ca^{2+}-triggered neurotransmitter release as well as different forms of synaptic plasticity.[5,7,8]

A mutation has been identified for an autosomal dominant cone-rod dystrophy CORD7 in the *RIM1* gene that is localized to chromosome 6q14.[9] A four-generation British family with CORD7 first experienced reduced color vision and visual acuity between the ages of 20 and 40 years. As the disorder progressed, they had difficulty seeing in bright light, and one individual reported visual problems in dim light. At the onset of symptoms, retinal pigmentary changes were already present around the fovea, simulating bull's eye dystrophy, which developed into macular atrophy.[10] Interestingly, the affected individuals also showed significantly enhanced cognitive abilities across a range of domains.[11] Thus, the CORD7 RIM1 mutation is characterized by retinal dystrophy and enhanced brain function. However, the mechanisms underlying these phenotypes are yet to be elucidated.

We recently revealed a previously unknown interaction between two components of the presynaptic active zone, RIM1 and VDCCs,[12] that is essential for Ca^{2+}-triggered neurotransmitter release.[13] RIM1 associates with VDCC β-subunits via the C terminus to markedly suppress voltage-dependent inactivation among different neuronal VDCCs.

In addition, membrane docking of vesicles is also enhanced by RIM1. In pheochromocytoma neuroendocrine PC12 cells and in cultured cerebellar neurons, neurotransmitter release is significantly potentiated by RIM1. Thus, RIM1 association with VDCC β in the presynaptic active zone supports release via two mechanisms: sustaining Ca^{2+} influx through inhibition of channel inactivation, and anchoring neurotransmitter-containing vesicles in the vicinity of VDCCs. Here, we specifically test whether the RIM1 mutation associated with CORD7 affects RIM1 regulation of VDCC current inactivation, in order to gain insight into the molecular mechanisms that underlying the two observed phenotypes in CORD7 patients.

Result and Discussion

A nucleotide (G to A) substitution, that replaces Arg-655 with His in the middle C_2A domain (**Fig. 1A**) reported for its ability to bind to VDCC α_1-subunit,[6] was introduced in the mouse RIM1 cDNA to yield a construct which carries a mutation corresponding to human CORD7 RIM1 mutation R844H.[9] The mouse clone differs from the human clone in having a deletion in the region between the Zn^{2+}-finger-like and PDZ domains. In this region, no specific functional domains have yet been identified. Co-immunoprecipitation experiments suggested an intact interaction between RIM1 mutant R655H and the VDCC β_{4b}-subunit (**Fig. 1B**). To elucidate the functional effects of the RIM1 mutant, we characterized whole-cell Ba^{2+} currents through recombinant VDCCs expressed as $\alpha_1\alpha_2/\delta\beta_{4b}$ complexes containing neuronal α_1-subunits $Ca_v2.1$ of P/Q-type VDCCs or $Ca_v1.4$ of L-type VDCCs. These VDCCs were selected, because P/Q-type $Ca_v2.1$ plays an important role in neurotransmitter release from central neurons,[13] while L-type $Ca_v1.4$ is found at high densities in photoreceptor terminals[14,15] and known for its association with X-linked congenital stationary night blindness.[16] When compared to wild-type RIM1 (WT), R655H significantly increased the non-inactivating component of P/Q-type $Ca_v2.1$ currents (from 0.30 ± 0.04 (n = 6) to 0.43 ± 0.03 (n = 9); $P < 0.01$) (**Fig. 1C**). Inactivation parameters of L-type $Ca_v1.4$ currents were unaffected by R655H RIM1 (**Fig. 1D**) (see Table 1 for the estimated half-inactivation potential and the slope factor). In terms of activation properties, the voltage dependence of P/Q-type ($Ca_v2.1$) current activation was shifted toward negative potentials (see Table 1 for the voltages for half-maximal activation) and activation speed was increased by R655H expression (**Fig. 2A**). Furthermore, RIM1-mediated augmentation of $Ca_v2.1$ current density was significantly enhanced by R655H (Fig. 2B) (see Table 1 for current densities). In contrast to $Ca_v2.1$

currents, the RIM1-mediated hyperpolarizing shift of $Ca_v1.4$ activation was abolished by the mutation (**Fig. 2C**). The effects of R655H on activation speed (**Fig. 2C**) and current density were indistinguishable from those of WT RIM1 for $Ca_v1.4$ channels (**Fig. 2D**).

Here, we demonstrate that the mouse RIM1 mutant R655H, equivalent to the human CORD7 mutation, alters RIM1 function in regulating VDCC currents. For P/Q-type $Ca_v2.1$ VDCC, important in neurotransmitter release at central synapses, the CORD7 mutation accelerated activation, and enhanced the RIM1-mediated suppression of inactivation and augmentation of current density, likely leading to enhanced neurotransmitter release and synaptic transmission. In contrast, for L-type $Ca_v1.4$ VDCC, a prominent player in glutamate release from photoreceptor terminals, the CORD7 mutation abolished the RIM1-mediated hyperpolarization of current activation, likely resulting in impaired synaptic transmission at ribbon synapses of the visual system. The variable effects of the CORD7 mutation on different presynaptic VDCCs may underlie the two reported nervous system phenotypes, retinal dystrophy and enhanced cognitive abilities.

Reference

1. Wang Y, Okamoto M, Schmitz F, Hofmann K, Südhof TC. Rim is a putative Rab3 effector in regulating synaptic-vesicle fusion. *Nature* **388**, 593-598 (1997)
2. Wang Y, Sugita S, Südhof TC. The RIM/NIM family of neuronal C2 domain proteins. *J. Biol. Chem.* **275**, 20033-20044 (2000)
3. Betz A, Thakur P, Junge HJ, Ashery U, Rhee J-S, Scheuss V, Rosenmund C, Rettig V, Brose N. Functional interaction of the active zone proteins Munc13-1 and RIM1 in synaptic vesicle priming. *Neuron* **30**, 183-196 (2001)
4. Ohtsuka T, Takao-Rikitsu E, Inoue E, Inoue M, Takeuchi M, Matsubara K, Deguchi-Tawarada M, Satoh K, Morimoto K, Nakanishi H, Takai Y. CAST: a novel protein of the cytomatrix at the active zone of synapses that forms a ternary complex with RIM1 and Munc13-1. *J. Cell Biol.* **158**, 577-590 (2002)
5. Schoch S, Castillo PE, Jo T, Mukherjee K, Geppert M, Wang Y, Schmitz F, Malenka RC, Südhof TC. RIM1α forms a protein scaffold for regulating neurotransmitter release at the active zone. *Nature* **415**, 321-326 (2002)
6. Coppola T, Magnin-Lüthi S, Perret-Menoud V, Gattesco S, Schiavo G, Regazzi R. Direct interaction of the Rab3 effector RIM with Ca^{2+} channels, SNAP-25, and Synaptotagmin. *J. Biol. Chem.* **276**, 32756-32762 (2001)
7. Castillo PE, Schoch S, Schmitz F, Südhof TC, Malenka RC. RIM1α is required for presynaptic long-term potentiation. *Nature* **415**, 327-330 (2002)
8. Schoch S, Mittelstaedt T, Kaeser PS, Padgett D, Feldmann N, Chevaleyre V, Castillo PE, Hammer RH, Han W, Schmitz F, Lin W, Südhof TC. Redundant functions of RIM1α and RIM2α in Ca^{2+}-triggered neurotransmitter release. *EMBO J.* **25**, 5852-5863 (2006)
9. Johnson S, Halford S, Morris AG, Patel RJ, Wilkie SE, Hardcastle AJ, Moore AT,

Zhang K, Hunt DM. Genomic organization and alternative splicing of human *RIM1*, a gene implicated in autosomal dominant cone-rod dystrophy (CORD7). *Genomics* **81**, 304-314 (2003)

10. Kelsell RE, Gregory-Evans K, Gregory-Evans CY, Holder GE, Jay MR, Weber BHF, Moore AT, Biro AC, Hunt DM. Localization of a Gene (*CORD7*) for a dominant cone-rod dystrophy to chromosome 6q. *Am. J. Hum. Genet.* **63**, 274-279 (1998)
11. Sisodiya S, Thompson P, Need A, Harris S, Weale M, Wilkie S, Michaelides M, Free S, Walley N, Gumb C, Gerrelli D, Ruddle P, Whalley L, Starr J, Hunt D, David G, Deary I, Moore A. Genetic enhancement of cognition in a kindred with cone-rod dystrophy due to RIMS1 mutation. *J. Med. Genet.* **44**, 373-380 (2007)
12. Kiyonaka S, Wakamori M, Miki T, Uriu Y, Nonaka M, Bito H, Beedle AM, Mori E, Hara Y, De Waard M, Kanagawa M, Itakura M, Takahashi M, Campbell KP, Mori Y. RIM1 confers sustained activity and neurotransmitter vesicle anchoring to presynaptic Ca^{2+} channels. *Nat. Neurosci.* **10**, 691-701 (2007)
13. Tsien RW, Ellinor PT, Horne WA. Molecular diversity of voltage-dependent Ca^{2+} channels. *Trens. Pharmacol. Sci.* **12**, 349-354 (1991)
14. Koschak A, Reimer D, Walter D, Hoda J-C, Heinzle T, Grabner M, Striessnig J. $Ca_v1.4\alpha1$ subunits can form slowly inactivating dihydropyridine-sensitive L-type Ca^{2+} channels lacking Ca^{2+}-dependent inactivation. *J. Neurosci.* **23**, 6041-6049 (2003)
15. McRory JE, Hamid J, Doering CJ, Garcia E, Parker R, Hamming K, Chen L, Hildebrand M, Beedle AM, Feldcamp L, Zamponi GW, Snutch TP. The *CACNA1F* gene encodes an L-type calcium channel with unique biophysical properties and tissue distribution. *J. Neurosci.* **24**, 1707-1718 (2004)
16. Bech-Hansen NT, Naylor MJ, Maybaum TA, Pearce WG, Koop B, Fishman GA,

Mets M, Musarella MA, Boycott KM. Loss-of-function mutations in a calcium-channel α_1-subunit gene in Xp11.23 cause incomplete X-linked congenital stationary night blindness. *Nat. Genet.* **19**, 264-267 (1998)

Figure 1

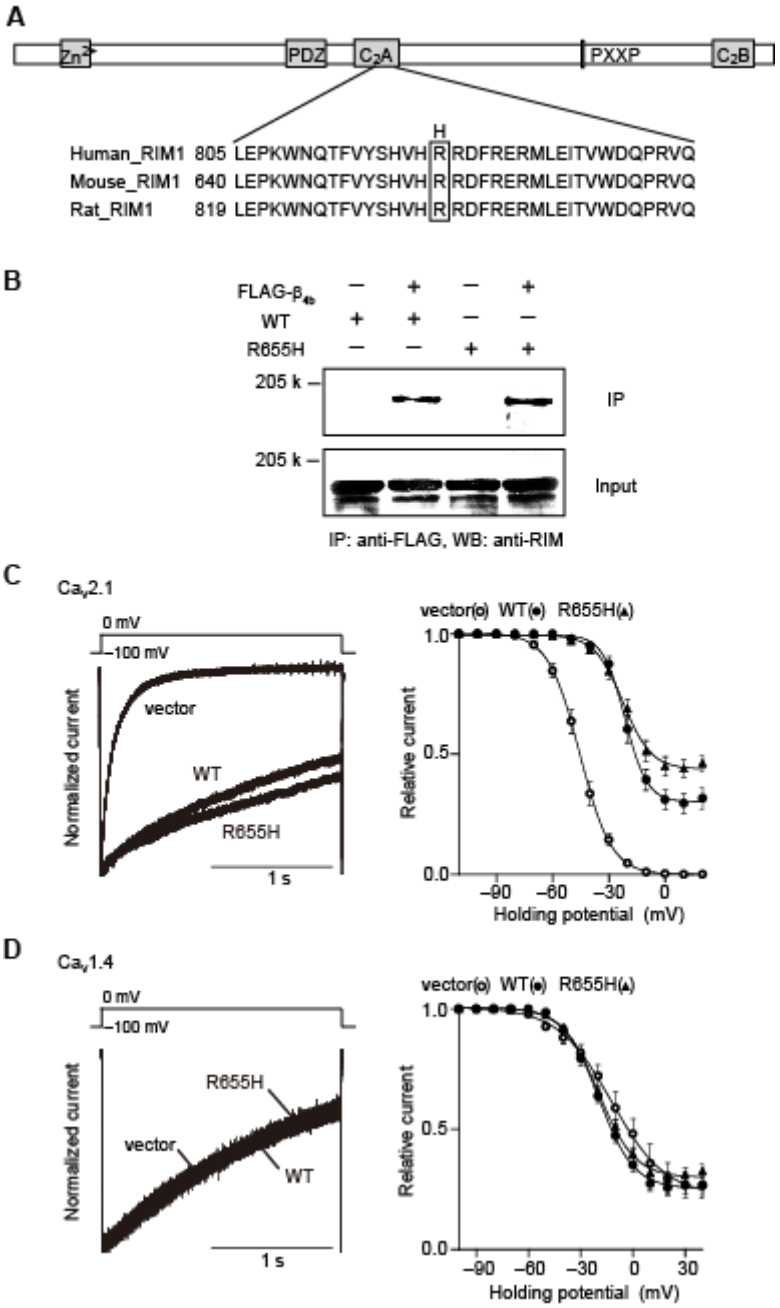
A
Zn
PDZ
C2A
PXXP
C2B
H
Human_RIM1 805 LEPKWNQTFVYSHVH R RDFRERMLEITVWDQPRVQ
Mouse_RIM1 640 LEPKWNQTFVYSHVH R RDFRERMLEITVWDQPRVQ
Rat_RIM1 819 LEPKWNQTFVYSHVH R RDFRERMLEITVWDQPRVQ
B
FLAG-β4b
WT
R655H
205 k
IP
205 k
Input
IP: anti-FLAG, WB: anti-RIM
C
CaV2.1
0 mV
−100 mV
vector
WT
R655H
1 s
Normalized current
vector(o) WT(•) R655H(▲)
Relative current
Holding potential (mV)
D
CaV1.4
0 mV
−100 mV
R655H
vector
WT
1 s
Normalized current
vector(o) WT(•) R655H(▲)
Relative current
Holding potential (mV)

Figure 1 CORD7 mutation R655H affects regulation of $Ca_v2.1$ channel inactivation by RIM1 via β association.

(**A**) Amino acid sequence alignment of C_2A domains of human, mouse and rat RIM1 (GenBank accession number NM_014989, NM_053270 and NM_052829, respectively). The position of the CORD7 substitution (H) is indicated. (**B**) Physical association of recombinant β_{4b} and R655H in HEK293 cells. The interaction is evaluated by immunoprecipitation (IP) with anti-FLAG antibody, followed by western blotting (WB) with anti-RIM antibody. Co-immunoprecipitation of wild-type RIM1 (WT) or R655H with FLAG-β_{4b}. (**C**) Effects of WT and R655H on the inactivation properties of P/Q-type $Ca_v2.1$ currents in BHK cells co-expressing α_2/δ and β_{4b}. Left panel: inactivation of P/Q-type $Ca_v2.1$ currents. The peak amplitudes are normalized for Ba^{2+} currents elicited by 2-s pulses to 0 mV from a holding potential (V_h) of –100 mV before and after expression of WT or R655H. Right panel: inactivation curves of P/Q-type $Ca_v2.1$ currents in BHK cells co-expressing α_2/δ and β_{4b}. The voltage dependence of inactivation, determined by measuring the amplitude of the peak currents evoked by 20-ms test pulses to 0 mV following 2-s prepulses to potentials from −100 to 20 mV with increments of 10 mV from a V_h of −100 mV, was fitted with the Boltzmann's equation. (**D**) Effects of WT and R655H on the inactivation properties of L-type $Ca_v1.4$ currents in BHK cells co-expressing α_2/δ and β_{4b}. Left panel: inactivation of L-type $Ca_v1.4$ currents. Right panel: inactivation curves of L-type $Ca_v1.4$ currents in BHK cells co-expressing α_2/δ and β_{4b}. The voltage dependence of inactivation is determined as in (C) above.

Figure 2

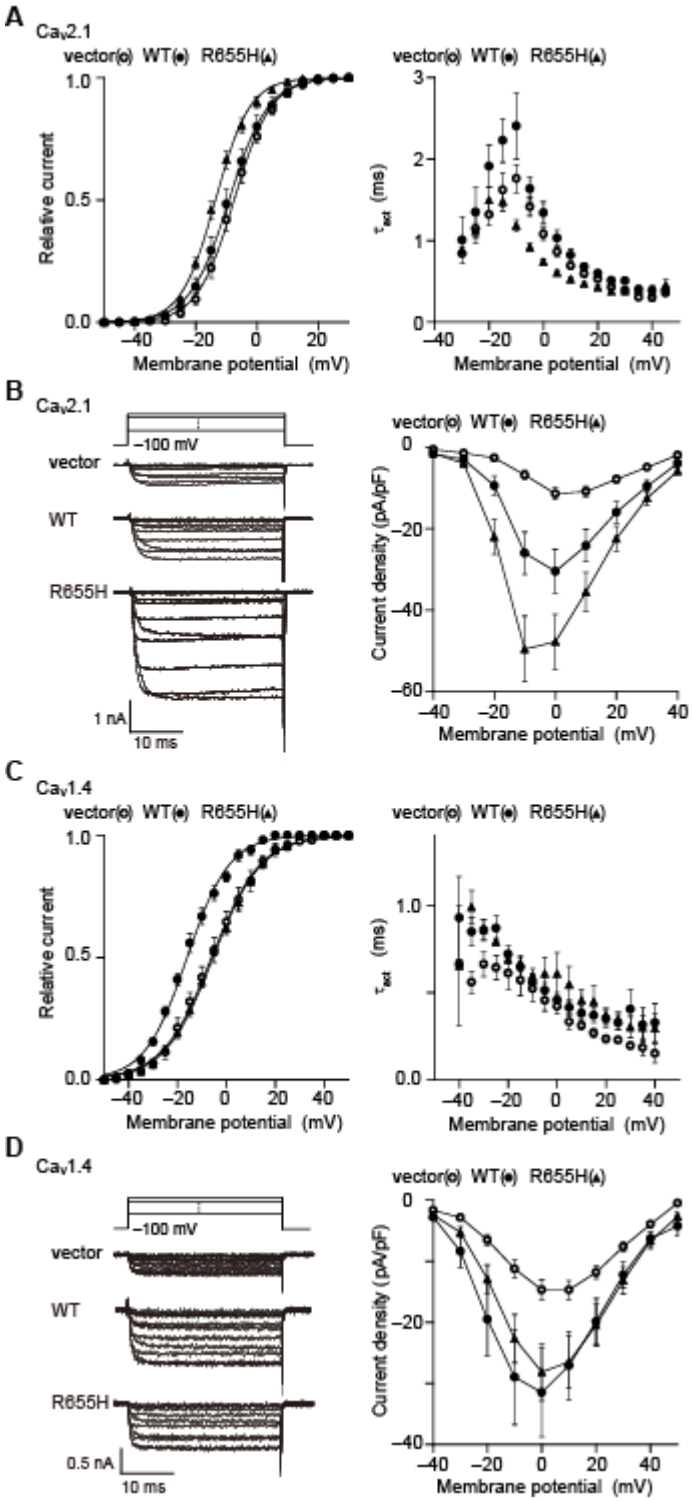
A
Cav2.1
vector(o) WT(•) R655H(▲)
Relative current
Membrane potential (mV)
τact (ms)
B
Cav2.1
−100 mV
vector
WT
R655H
1 nA
10 ms
Current density (pA/pF)
C
Cav1.4
D
Cav1.4
0.5 nA

Figure 2 CORD7 mutation R655H affects regulation of $Ca_v2.1$ and $Ca_v1.4$ channel activation by RIM1 via β association.

(**A**) Effects of WT and R655H on activation properties of $Ca_v2.1$ currents in BHK cells co-expressing α_2/δ and β_{4b}. Left panel: effects of WT and R655H on activation curves of $Ca_v2.1$ currents. Tail currents elicited by repolarization to –60 mV after 5-ms test pulse from –50 to 30 mV are used to determine activation curves. Right panel: effects on activation speed of $Ca_v2.1$ channels. Time constants are obtained by fitting the activation phase of currents elicited by 5-ms test pulse from –30 to 45 mV with a single exponential function. The differences between WT and R655H are significant at membrane potentials from –10 to 25 mV ($P < 0.001$, ANOVA, Fisher's test). (**B**) Effects of WT and R655H on $Ca_v2.1$ current amplitude. Left panel: representative traces for Ba^{2+} currents evoked by test pluses from –40 to 40 mV with 10-mV increments in BHK cells co-expressing α_2/δ and β_{4b}. Right panel: current density-voltage (*I-V*) relationships of $Ca_v2.1$. The V_h is –100 mV. (**C**) Effects of WT and R655H on activation properties of $Ca_v1.4$ currents in BHK cells co-expressing α_2/δ and β_{4b}. Left panel: effects of WT and R655H on activation curves of $Ca_v1.4$ currents. Right panel: effects on activation speed of $Ca_v1.4$ channels. (**D**) Effects of WT and R655H on $Ca_v1.4$ current amplitude. Left panel: representative traces for Ba^{2+} currents evoked by test pluses from –40 to 50 mV with 10-mV increments in BHK cells co-expressing α_2/δ and β_{4b}. Right panel: *I-V* relationships of $Ca_v1.4$. The V_h is –100 mV.

Chaptor 3

A novel protein Caprin complex is crucial for dendritic translocation of voltage-dependent Ca^{2+} channels and dendritic morphology

Abstract

Activity-dependent regulation of dendritic morphology is important for the formation of functional neuronal network in brain. Voltage-dependent Ca^{2+} channel (VDCC) is a most prominent molecule of sensing neuronal activity and raising intracellular Ca^{2+} concentration in neurons for dendritic morphology. However, the mechanism of the localization of VDCC in dendrite has been unknown. Here, we identify a novel protein Caprin, directly associated with VDCC β subunit. Interestingly, Caprin has two β binding regions; Caprin262-437, competes α_1 with binding to β, and Caprin505-580. The formation of VDCC-Caprin complex depends on the interaction of Carin262-437 with SCLIP, stathmin family, in vitro binding assay. In HEK293 cells, Caprin significantly promotes to translocate VDCC β to plasma membrane, and colocalizes VDCC complex at plasma membrane. In cultured hippocampal neurons, the expression of Caprin, regulated by neuronal activity-dependent signaling, induce the colocarization of VDCC-Caprin-SCLIP complex at dendritic protrusion, and axon. The transient expression of Caprin in neuron elaborates filopodia-like structures of dendritic arbor and spine in neuron, however the β binding region deletion construct of Caprin does not. Thus, these results suggest that activity-dependent Caprin association with VDCC complex via β subunit

supports the localization of VDCC at the dendritic protrusion, resulting in elongation of filopodia-like protrusions and spines.

Introduction

Proper dendritic arborization is a critical process for accurate development of neuronal circuits and for activity-dependent plasticity in mature neurons[1-3]. Indeed, dendritic abnormalities are the most consistent pathologic correlate of mental retardation including Down's syndrome[4,5], Fragile X syndrome[6], and fetal alcohol syndromes. Especially, the role of dendritic spines in cognition is suggested by the fact that several forms of mental retardation exhibit a reduction in spine density as well as a predominance of very long, thin filopodia at the expense of mature mushroom-shaped spines[7,8].

In dendritic shafts and spines, depolarization, mediated by glutamate receptors, activates voltage-dependent Ca^{2+} channels (VDCC), contributing additional depolarization and augmenting Ca^{2+} entry[9]. Ca^{2+}-depedent pathway activated by neuronal activity is essential for dendritic outgrowth, and formation of shaft filopodia, may become dendritic spines, through stimulating various signalings[10-12]. Calcium influx via VDCC influences dendritic morphology under basal activity conditions of neurons[11].

Neurons are highly polarized cells: the structural, functional, and molecular differences between their axonal, somate, and dendritic domains underlie their ability to receive, process, and transmit information. Cellular and molecular mechanisms involved in targeting of neuronal proteins have been elucidated recently. However, the molecular mechanisms that regulate the localization and activation of VDCC in dendritic spines and shafts have remained unknown.

VDCCs are heteromultimeric protein complexes composed of the pore-forming α_1, designated as Ca_v, and auxiliary subunits α_2/δ, β and γ (ref. 13). VDCC complexes are associated, primarily via interactions with the α_1 subunit, with neuronal trafficking

proteins including tectex-1, CASK and Mint[14-16]. The α_1 and β subunits interact to enhance functional channel trafficking to the plasma membrane[17,18] and to modify multiple kinetic properties[19]; the β subunit interacts with other proteins and was phosphorylated[20-23]. In the neurons from β_3 or β_4 subunits deficient mice electrophysiological studies revealed no alteration of the Ca^{2+} current density, suggesting the unknown important roles of β subunits[24,25]. Recently, we have demonstrated that RIM1-β complexes target VDCC complexes to the machinery of neurotransmitter release at presynaptic active zone[26]. Therefore, it is intriguing to investigate whether β subunits are involved in targeting VDCC complexes to specific subcellular region of dendrites for dendritic morphology.

Stathmin family phosphoproteins including stathmin, SCG10, SCLIP, and RB3, have been proposed to play specific and complementary roles in the formation of the nervous system[27-30]. SCLIP, enriched goigi apparatus, axon and dendrite in nervous system, controls the early phases of Purkinje cell dendritic differentiation during cerebellum development, and axonal branching in hippocampal neurons[31,32].

Here, we identify that the unknown protein, Caprin, are interacted with VDCC β subunits. The transmembrane protein, Carpin, targets β subunits to dendritic protrusion and plasma membrane in neurons. *In vitro* binding assay, Caprin-β complex is swiched to Caprin-VDCC complex by the interaction of SCLIP. In neurons, VDCC-Caprin-SCLIP complex is promoted to localize at dendritic protrusion and shaft by activity-dependent enhancement of Caprin expression, resulting in elongation of dendritic filopodia-like protrusion and immature spine. Thus, Caprin protein regulates the localization of VDCC and developmental spinogenesis in brains.

Results

Identification of calcium channel processing protein (Caprin)

To identify β subunit-interacting proteins that regulate β subunit and VDCC, we performed yeast two-hybrid screening with a mouse brain complementary DNA library using the full-length rat β_{4b} subunit or rabbit β_{2a} subunit as a bait. The β_4 and β_{2a} subunit were chosen because spontaneous β_4 mutant *Cacnb4*^{lh} (lethargic) mice have clear neurological defects[24] and β_4 and β_{2a} distribute in clusters and localize to synapse[33], suggesting that β_4 or β_{2a}-containing VDCCs are physiologically significant in the brain. We identified 41 clone encoding downstream of stk11, which is unknown protein, and named the encoded protein 'calcium channel processing protein (Caprin)'. Figure 1A shows the amino acid sequence of the mouse Caprin deduced from the open reading frame of the corresponding cDNA sequence. The translation initiation codon is assigned to the first in-frame methionine codon downstream of a stop codon. Caprin is composed of 692 amino acid residues with a hydropathy profile revealing one hydrophobic segment in N-termini (**Fig.1B**). Sufficient length of hydrophobic regions to span the membrane, together with a hydrophobic N-terminal sequence indicative of the signal sequence, suggests that Caprin is a membrane protein and N- and C-terminal regions disposed on the extra- and intracellular side, respectively. In Caprin protein, there were not functional domains and motifs predicted by database. Figure 1C depicts the phylogenetic tree of the Caprins constructed by the neighbor-joining method[34], based on the sequence alignment carried out by the Clustalw program[35]. For analysis of tissue distribution of Caprin, RNA preparations from different mouse tissues were subjected to northern blot using Caprin cDNA as a specific probe (**Fig. 1D**). Caprin mRNA was exclusively detected in the mouse central nervous system. An intense Caprin signal with size of ~3.5 kb was present in the brain, and a relatively weak

signal was detected in the eye. Developmental change of Caprin mRNA expression in the mouse brain was analyzed by nothern blot (**Fig, 1E**). The level of Caprin mRNA was gradually increased with age, from E16 to P4 and stably expressed from P4 to adult. Subcellular distribution analysis in mouse brain showed that Caprin was concentrated in the crude membrane and synaptic membrane (**Fig. 1F**). Recombinantly expressing Caprin-EGFP localized the plasma membrane in HEK293 cell (**Fig. 1G**). As expected from the targeting construct for generation of Caprin deficient mouse, neurons expressing the Caprin can be detected by β-galactosidase activity in the mutant mice (**sFig. 1**). The regions positive in X-gal staining in brain from mutant were hippocampal pyramidal layer and cerebellar granule layer (**Fig. 1H, and sFig. 2**). These data indicate that Caprin, transmembrane protein, developmentally express in the specific regions of central nervous system.

Neuronal VDCC β subunits directly interact with Caprin at plasma membrane

In vitro pulldown assays using glutathione-S-transferase (GST) fusion constructs and immunoprecipitation assays identified the interaction of Caprin with all β subunit isoforms (**Figs. 2A, and 2B**). Figure 2C shows that two subdomains of Caprin protein, 262-437 and 505-580 amino acid residues, have the ability to bind to β subunits (Caprin262-437: β binding region 1, Caprin505-580: β binding region 2) (**Fig. 2D**). Subsequent two-hybrid assays using β_{4b} mutants showed that β binding region 1 of Caprin interacted with different regions of β subunit from β binding region 2 of Caprin. The β binding region 1 of Caprin required β subunit residues 49-410, containing major structural motifs such as the Src homology 3 (SH3) domain, the α_1-interacting domain known as BID and the guanylate kinase (GK) domain, while the β binding region 2 required residues 86-410 (**Fig. 2E**). The result of BADN (beta-AID dominant

negative) construct interacted with β binding region 2, but not β binding region 1, suggested that β binding region 1 of Caprin bind to AID binding pocket of β subunit and compete with α_1 for binding to β subunit. An *in vitro* binding assay using purified β_4 and Caprin recombinants revealed a dissociation constant (K_d) of 0.548 nM for Caprin262-692, which was substantially lower than those of Caprin505-580 (4.48 nM) and Caprin262-437 (30.5 nM) (**Fig. 2F**). Scatchard plot analysis of β_4 binding to Caprin protein calculated by Fig. 2F showed that Caprin interacted with β one by one, because the plots were approximated by linear (**Fig. 2G**). Immunoprecipitation analysis of digitonin solubilized sample of mouse brain microsome confirmed that Caprin physically associate with native β subunit in the brains (**Fig. 2H**).

In recombinant HEK293 cells, β_{4b} was concentrated at the plasma membrane when β_4 was coexpressed with Caprin, whereas β_{4b} was diffusively localized throughout the intracellular area in the absence of Caprin (**Fig. 3A**). In cultured hippocampal neurons, Caprin and β_{4b} were concentrated and colocalized at plasma membrane and dendritic protrusion (**Fig. 3B**). These results suggest that two regions of Caprin directly bind to β subunits and targets β subunit to the plasma membrane and dendritic protrusion in neurons.

Caprin β binding region 1 compete with α_1 for binding to β

We designed AID peptide (QQIERELNGYMEWISKAE) to mask the AID binding pocket of β subunit, which is the α_1 interacting region of β subunits[36] (**Fig.4A**). *In vitro* pulldown assay using purified β_4 and GST-fused Caprin constructs revealed that the interactions between Caprin β binding region 1 constructs and β_4 subunits were disrupted by AID peptide, while the interactions between Caprin β binding region 2 contructs and β_4 subunits were not (**Fig. 4B**). And then, *in vitro* immunoprecipitation

analysis showed that Caprin constructs including β binding region 1 disrupted the interactions between α_1 and β_{4b} subunits (**Fig. 4C**). These data suggest that Caprin β binding region 1 bind the AID binding pocket of β subunit, and compete with α_1 subunit for binding to β subunit.

To elucidate the functional significance of direct Caprin-β_4 coupling, we characterized whole-cell Ba^{2+} currents through recombinant voltage-dependent calcium channel (VDCC) expressed as $\alpha_1\alpha_2/\delta\beta$ complexes in BHK cells. The most prominent Caprin effect on VDCC currents was observed on the amplitude of current density. Current density was markedly decreased in VDCC current (**Figs. 5A, 5B, and 5C**). Surface labeling analysis showed that coexpressing Caprin decreased surface expression level of α_1 subunits regulated by β_{4b} (**Fig. 5D**). These data suggest that impairment of the interaction between α_1 and β by Caprin cause the reduction of surface expression level of VDCC and the decrease of VDCC currents. Interestingly, the voltage dependent activation was slightly but significantly shifted to positive in VDCC current, when Caprin was coexpressed with VDCC complex in BHK cells (**Fig. 5E**). The voltage dependent inactivation was not shift (**Fig. 5F**). These results imply that a part of Caprin proteins may associate with α_1-β complex and affect the kinetics of VDCC currents.

Caprin associates with VDCC complex mediated by the β binding region 2

We characterized the association between native VDCCs and Caprin biochemically using VDCC complexes enriched from mouse brains through microsome preparation, KCl wash, solubilization, wheat germ agglutinin (WGA) purification and sucrose density gradient fractionation. Western blot analysis of sucrose gradient fractions showed that a fraction of Caprin was cosedimented with low density fractions

of β_4 and a part of fractions of Caprin was cosedimented with $Ca_v2.2$ and β_4 (**Fig. 6A**). To clarify the cosedimentation results of Caprin and VDCC subunits, the densitometry analysis was performed with these proteins. In the distribution of Caprin, although the first peak overlapped with the small peak of β_4 subunit, the second peak partly overlapped with VDCC complex, suggesting partial cosedimentation of Caprin with VDCC. In Caprin-deficient mouse brain sample, western blot analysis of sucrose gradient fractions showed that the fractions of β_4, which were cosedimented with main fractions of Caprin in wild-type, were diminished (**Fig. 6B**). The densitometry analysis revealed that the small peak of β_4 subunit was significantly reduced, suggesting that partial fractions of β_4 cosedimented with Caprin in wild-type depended on the Caprin proteins.

To examine the possibility of VDCC-Caprin complex, we performed immunoprecipitation assay using HEK293 cells expressing α_1, β_{4b}, and Caprin. Figure 6C showed that Caprin-β_{4b} complexes interacted with α_1 subunits. Further, *in vitro* pulldown assay revealed that the β binding region 2 deletion constructs of Caprin impaired the ternally complexes, suggesting that β binding region 2 associate with VDCC complex (**Fig. 6D, and sFig. 3**). And then, we observed colocalization of VDCC-Caprin complex at plasma membrane in the confocal imaging of CHO cell expressing α_1 and β with Caprin (**Fig. 6E**). These results suggest that although Caprin mainly associate with β subunit, Caprin partially interacts with VDCC complex at plasma membrane (**Fig. 7**).

A novel interacting partner of Caprin, SCLIP, regulate the association of Caprin with VDCC complex

How were the two conformations of Caprin complexes, Caprin-β subunit or

ternally complex, regulated? We speculated the possibility of a protein that switched one conformation of Caprin complexes to another. To identify the protein, we performed yeast-two hybrid screening with a mouse brain complementary DNA library using mouse Caprin 262-692 amino acid residues as a bait. The screening identified two clones encoding the full-length SCLIP, stathmin family which have been identified for their capacity to integrate and relay intracellular signaling pathways, at least in part through tubulin binding and the control of microtubule dynamics[37-42]. We confirmed the interactions of Caprin with all sthathmin family (**sFig. 4**). Immunoprecipitation assay showed that Caprin 262-437 amino acid residues were required for the interaction of Caprin with SCLIP (**Fig. 8A**). The SCLIP binding region of Caprin was consistent with β binding region 1 which competed with α_1 to binding to β (**Fig. 8B**). To investigate the effect of SCLIP on the interaction of Caprin with β, we performed immunoprecipitation assay using the HEK293 cells expressing α_1, β_{4b}, and Caprin constructs with vector or SCLIP. The analysis showed that SCLIP replaced β_4 as a binding partner of Caprin β binding region 2 deletion mutants, while Caprin full-length interacted with both SCLIP and VDCC (**Figs. 8C, and 8D**). These results suggest that SCLIP competed β_4 with binding to Caprin 262-437 and switch β_4-Caprin complex to VDCC-Caprin complex.

Immunoprecipitation analysis using HEK293 cells expressing α_1, β_4, Caprin, and SCLIP revealed that VDCC-Caprin complex associated with SCLIP (**Figs. 8E, and 8F**). To confirm native VDCC-Caprin-SCLIP complex, we performed western blot analysis of sucrose gradient fractions of WGA-purified samples. The analysis showed that a part of fractions of SCLIP cosedimented with VDCC and Caprin proteins (**Figs. 8G, and 8H**). In cultured hippocampal neurons, recombinant expressing Caprin and SCLIP colocalized at golgi apparatus, dendritic protrusion, growth cone, and axonal

varicosity, same as native SCLIP (**Fig. 9**). These results suggest that Caprin-SCLIP complexes at dendritic and axonal plasma membrane may associate with VDCC complex in the neurons.

Activity-dependent Caprin expression induce translocation of VDCC complex to dendritic protrusion and axon

In cultured hippocampal neuron, α_1 and β_4 were concentrated at the dendritic protrusion and axon when they were coexpressed with Caprin, whereas they were mainly localized at golgi appratus in the absence of Caprin (**Figs. 10A, and 10B**). The localizations of VDCC complex in cultured hippocampal neuron expressing Caprin were consistent with the localizations of Caprin-SCLIP complex (**Fig. 9**). These data suggest that Caprin bind VDCC complex by the interaction of SCLIP with Caprin masking the Caprin262-437, multi binding region, and induce translocation of VDCC complex to dendritic protrusion and axon.

We supposed that the expression of Caprin was regulated in neuron, because the changes of expression of Caprin can control the localization of VDCC complex, resulting in the local activity of VDCC at dendritic protrusion and axon. To verify a hypothesis, we stimulated hipocampal neurons with 90 mM KCl or 10 μM glutamate, which was effective in activation VDCCs and NMDA receptor in previous reports[10]. In cultured hippocampal neurons, the expression of Caprin was significantly potentiated by highK^+ membrane depolarization (**Figs. 10B and 10C**). HighK^+-induced enhancement of Caprin expression was diminished in the absence of extracellular Ca^{2+}. And glutamate stimulation also increased expression of Caprin proteins in cultured hippocampal neurons. These results suggest that activity-dependent depolarization in neurons enhance Caprin expression, regulating localization of VDCC.

Caprin play an important role for dendritic morphology in hippocampal neurons

Activity-dependent plasticity and signaling is a critical process for proper dendritic morphology in neurons[1-3]. In previous reports, the activity of VDCCs influences dendritic growth under basal activity conditions[11]. And stathmin family phosphoproteins, including SCLIP, have been proposed to play specific and complementary roles in the formation and maturation of the nervous system[27-30]. The effects of Caprin on neuronal morphology were examined in cultured hippocampal neurons prepared from embryonic day 18 mice, because activity-dependent Caprin expression may regulate the localization and activity of VDCCs. The morphology of individual neuron was visualized by transfection of EGFP and Caprin constructs, or Caprin-EGFP at E18 + 3 or 7 days in vitro (DIV). The confocal imagings of cultured neurons, transfected at 3 DIV followed by observation 9 days post-transfections, reveals that the neuron expressing EGFP and Caprin elaborate abnormal dendrites, increasing filopodia-like protrusions and retracting dendritic arbors (**Fig. 11A**). The abnormal morphology was not detected in the neuron expressing EGFP and Caprin262-692 deletion construct, which did not associate with VDCC complex. To evaluate the effect of Caprin on morphology of mature neurons, we observed the conforcal imaging of cultured hippocampal neurons, transfected at 8 DIV followed by fixed 10 days post-transfections. As shown in Figure 11B, the neuron, transfected Caprin-EGFP, elaborated filopodia-like spines and formed synapse at the shaft of dendrite, while the dendrite of neuron transfected EGFP had mushroom- and stump-shapes of spines and formed synapses on the spine heads (**Figs. 11B and 11C**). In contrast, compared with cultured neuron from wild-type mouse, the filopodia-like protrusions and spines were reduced in Caprin-deficient cultured hippocampal neuron (**Fig. 11D**). These results

suggest that VDCC-Caprin-SCLIP complexes may play an important role for elaboration of filopodia-like structure and synapse formation in cultured hippocampal neurons.

Discussion

The present investigation reveals the physiological role of a novel protein, Caprin, for regulation of VDCC dynamics mediated by VDCC-Caprin-SCLIP complex. The results of yeast two-hybrid assays, in vitro binding assays and coimmunoprecipitation experiments have identified two interaction regions of Caprin, 262-437 and 505-580 amino acid residues, with β subunits (**Fig. 2**). Caprin262-437, β binding region 1 and SCLIP binding region, compete α_1 with binding to β, while Caprin505-580, β binding region 2, associate with α_1-β complex. SCLIP competed β with binding to Caprin262-437 and switch β-Caprin complex to VDCC-Caprin complex (**Fig. 8**). The alteration of complex is understandable because the association of Caprin262-437 with β is relatively weak (K_d = 30.5 nM) (**Figs. 2H and 2G**). In neuron, the acitivity-dependent enhancement of Caprin expression induces translocation of VDCC-Caprin complex to dendritic protrusion and shaft, resulting in elongation of filopodia-like protrusions and spines (**Figs. 10 and 11**). The disruption of such localization and complex formation by the β binding region deletion mutant of Caprin support a physiological role of Caprin complex for dendritic morphology (**Fig. 11A**).

The Caprin-β association enables Caprin to have a physiological function in activity-dependent dendritic morphology. The transient expression of Caprin induces dynamic change of dendritic morphology, increasing filopodia-like structure. Previous report showed that filopodia in dendritic growth cones were involved in dendritic growth and branching in an activity-independent manner, whereas shaft filopodia were responsible for activity-dependent synaptogenesis by using two-photon imaging of mouse cortical pyramidal neurons[43]. Thus, Caprin may most prominent modify the formation of shaft filopodia, because of activity dependency of Caprin expression. Indeed, in mature neurons expressing Caprin-EGFP, we observe the increase of shaft

filopodia (**Fig. 11B**).

The morphological abnormality induced by transient expression of Caprin is similar to the dendritic abnormalities associated with cognitive impairment, as in Fragile X syndrome and other disorder[44,45]. In previous reports, dendritic or synaptic protein synthesis, including the Fragile X mental retardation protein (FMRP), could provide the specificity and speed necessary for spine morphogenesis[46]. Weiler et al.[47] showed that stimulation of metabotropic glutamate receptors (mGluRs) triggers rapid aggregation of polyribosomes, observed near synapses during peak developmental synaptogenesis[48], and translation of protein (including FMRP), resulting in elongation of dendritic spines[49]. Failure to synthesize specific proteins profoundly affect synapse morphology in patients with Fragile X syndrome (characterized by the absence of FMRP) and FMRP-deficient mice[45,50-52]. It is possible that deregulation or mutation of Caprin may cause a neurological disorder, Fragile X syndrome, because the increase of Caprin expression, affected dendritic morphology, was triggered by glutamate stimulation, same as the translation of FMRP.

Regarding the expression of Caprin and SCLIP in dendrite and axon, Carpin-SCLIP complex may be also important role for targeting VDCC complex to axon (**Fig. 9**). Previous reports demonstrated the mechanisms of targeting VDCC complex to axon mediated by the interactions of tctex-1, or CAST and Mint with α_1 (ref. 14-16). However they did not investigate whether these mechanisms depend on neuronal activities or not. Thus, the targeting mechanism mediated by Caprin-SCLIP complex may be an activity dependent matter in all VDCC targeting mechanisms, previously reported.

In this study, we indicate that Caprin exchange global to local signaling in neurons. In fact, global activity-dependent Caprin expression induces translocation of

VDCC to local region, dendritic protrusion and axon. The activities of VDCC at local region are very important for neuronal development and morphology, as previously reported[9].

Regarding the sucrose gradient experiments by using WGA-purified brain microsome samples, Caprin-β complexes without α_1 distributed at plasma membrane in the brains (**Figs. 6A, and B**). Previous report showed that exogenously expressed Cavβ_{4b} and Cavβ_{2a} subunits distributed in clusters, localized to synapses and attached to the plasma membrane, whereas Cavβ_{1b} and Cavβ_3 were homogenously distributed, similar as our observation in the binding properties and distribution of Caprin-β complexes[33] (**Figs. 2B and 3B**). Thus, it is possible that the Caprin-β complexes may play important physiological roles in the neurons; 1) the complexes disturb the formations of VDCC complexes, resulting in endocytosis or degradation of α_1 subunits and reduction of VDCC currents (**Fig. 5**). 2) the complexes target β to plasma membrane for scaffolding other β binding proteins (**Fig. 3**). As β subunits associate with various kinds of proteins (unpublished data), Caprin may contribute to change the binding partner of β from VDCC complex to other complex.

Materials and Methods

Yeast two-hybrid screening and β-galactosidase assay.

We use pGBK-T7-rat β_{4b}, pGBK-T7-rabbit β_{2a} or pGBK-T7-mouse Caprin as a bait to screen a mouse brain pACT2 library in the yeast strain AH109 (Clontech). We plated transformants (5.0×10^6 for β_{4b}, 3.0×10^6 for β_{2a}, and 3.0×10^6 for Caprin) on synthetic medium lacking adenine, histidine, leucine and tryptophan and assayed His^+ colonies for β-galactosidase activity with a filter assay. Of the transformants, 62, 38, and 14 of these were $LacZ^+$, respectively. We isolated 41 prey clones, encoding Caprin, in sum of β_{4b} and β_{2a} $LacZ^+$ clones and 2 prey clones, encoding SCLIP, in Caprin $LacZ^+$ clones.

cDNA cloning and construction of expression vectors

Caprin (downstream of stk11, NM_015761), Stathmin (NM_019641), SCG10 (NM_025285), SCLIP (NM_009133), and RB3 (NM_019675) were cloned from mouse brain Marathon-Ready cDNA (Clontech) using PCR, and were subcloned into pCI-neo (Promega), the FLAG-tagged vector pCMV-tag2 (Stratagene), the myc-tagged vector pCMV-tag3 (Stratagene), the pDsRed-Monomer-N1 (Clontech), and the pIRES2-EGFP (Clontech). GST-Cav2.1(AID) (rabbit Cav2.1 367-480 amino acid) was constructed by PCR using pK4KBI-2. The rat β_{4b} construct, BADN, and $Ca_v2.1$(I-II linker) (1-435) were previously shown[26].

In vitro binding of the purified proteins, GST-pulldown and coimmunoprecipitation experiments.

Caprin-GST fusion proteins at various concentrations were incubated with 50 pM purified recombinant β_4 subunits for 3 h at 4 °C. Proteins were subjected to western blotting with anti-β_4 directed against the C-terminus (ENYHNERARKSRNRLS)[26].

The densities of protein signals, obtained using NIH imaging (National Institute of Mental Health) under the liner relationship with the applied amount of proteins, were normalized to the densities from the maximal binding. For the pulldown assays, the cell lysate was incubated with glutathione-Sepharose beads bound to purified fusion proteins. The proteins were characterized by western blotting with antibody with anti-FLAG M2 monoclonal antibody (Sigma), and the immunocomplexes were characterized by western blotting with antibody for Myc or EGFP.

Biochemistry of native neuronal VDCC complexes.

Brain microsomes were prepared from mouse as described previously. From microsomes, the VDCC complexes were extracted with solubilization buffer containing (in mM) 50 Tris-HCl, pH 7.4, 500 NaCl, a mixture of protease inhibitors, and 1 % digitonin (Biochemica & Synthetica, Staad, Switzerland) by rotating end-over-end at 4 °C for 1 h. After centrifugation at 142000 x g for 37 min, solubilized proteins in the supernatant were diluted to 150 mM NaCl solution. Then, the solubilized proteins were mixed with wheat germ agglutinin (WGA)-agarose beads (Vector Laboratories, Burlingame, CA) and rotated end-over-end at 4 °C overnight. After washing three times with three bed volumes of ice-cold wash buffer (Buffer I containing (in mM) 50 tris-HCl, pH 7.4, 150 NaCl, a mixture of protease inhibitors, and 0.1 % digitonin), WGA-bound proteins were eluted with elution buffer (Buffer I + 0.3 M N-acetyl-D-glucosamine (Sigma)). The WGA eluant was concentrated to 0.3 ml in an Ultrafree-15 centrifugal filter device (Millipore, Bedford, MA), and applied to a 5-40% sucrose density gradient (Buffer I + 5-40% sucrose). The gradients were centrifuged at 215000 x g for 90 min. Fractions (0.35 ml) were collected from the top of the gradients. Western blots band densities (NIH image) were normalized from three

independent experiments.

For immunoprecipitation, partially solubilized proteins were incubated with protein A-agarose coupled to anti-β_4 or anti-Caprin directed against Caprin 61-261 amino acid sequence. Immunoprecipitated proteins were subject to western blotting with anti-Caprin, directed against Caprin 545-558 amino acid peptide or anti-β_4. To disrupt the physiological association of native Caprin with β_4, partially solubilized proteins were incubated with 200 nM GST-BADN and GST-Caprin$_{262\text{-}437,\ 505\text{-}580}$ for 2 h at 4 °C before immunoprecipitation.

Confocal imaging.

At 32 h after transfection, HEK293 cells or CHO cells were plated on poly-L-lysine-coated glass coverslips. The imaging was performed in modified Ringer's buffer that contained 140 mM NaCl, 5 mM KCl, 2 mM $CaCl_2$, 1 mM $MgCl_2$, 10 mM glucose, and 10 mM HEPES (pH 7.4). Fluorescence images were acquired with a confocal laser scanning microscope (FV500, Olympus).

Immunostaining of cultured hippocampal neurons.

We prepared primary cultures of hippocampal neurons from either ICR mice, purchased from Japan SLC (Shizuoka, Japan). The primary cultures from 18-day-old embryonic mouse hippocampus or postnatal days 0 to 1 mouse hippocampus was performed. Briefly, hippocampus were dissected and dissociated with 0.2% trypsin in phosphate-buffer saline (PBS). Dissociated cell suspensions were plated at 3.0 x 10^5 cells/cm^2 on glass coverslips coated with polyethylenimine, and cultured neurons were fed with the medium (Neurobasal/B27) supplemented with 2 mM glutamine, penicillin, and streptomycin. Cultured neurons were transfected at 3 or 7 d in vitro (DIV) by

Lipofectamine2000 (Invitrogen, Carlsbad, CA), and cell phenotypes were examined at 7, 12 or 18 DIV.

For immunocytochemistry, neurons were fixed in PBS(-) containing 4% paraformaldehyde/4% sucrose. Fixed neurons were quenched in 0.1 M glycine/PBS(-), permeabilized with 0.2% Triton X-100/PBS(-) for 10 min on ice, thoroughly washed with PBS(-), incubated in blocking solution (3% BSA/PBS(-)) for 30 min at room temperature, and then incubated overnight with primary antibodies diluted in the blocking buffer at 4 °C. The next day, the neurons were washed three times with PBS(-) and then were incubated with Alexa Fluor or Cy3-conjugated secondary antibodies at a 1:500 dilution in blocking buffer. The antibody souces and dilutions are as follows: anti-Myc 1:250, anti-SCLIP 1:500, and anti-synaptophysin 1:250.

β-galactosidase staining

For β-galactosidase staining, mice were perfused with a 2% paraformaldehyde solution buffered with 0.12 M sodium phosphate (pH 7.4) under pentocarbital anesthesia, and the brains were immersed immediately in ice-cold 25% sucrose. Frozen coronal sections (40 μm thickness) were stained with the X-Gal reagent[53].

Current recordings.

Whole-cell mode of the patch-clamp technique was performed on BHK cells or PC12 cells at room temperature (22-25 °C) as previously described[26]. Pipette resistance ranged from 2 to 3.5 megohm. The series resistance was electronically compensated, and both the leakage and the remaining capacitance were subtracted by a –P/4 method. Currents were sampled at 100 kHz after low pass filtering at 8.4 kHz (3 db) in the experiments of activation kinetics, otherwise sampled at 10 kHz after low pass filtering

at 2.9 kHz (3 db). An external solution contained 3 mM $BaCl_2$, 155 mM tetraethylammonium chloride (TEA-Cl), 10 mM HEPES, 10 mM glucose (pH adjusted to 7.4 with tetraethylammonium-OH). For current recordings in PC12 cells, an external solution contained 10 mM $BaCl_2$, 153 mM TEA-Cl, 10 mM HEPES, 10 mM glucose (pH adjusted to 7.4 with TEA-OH). The pipette solution contained 95 mM CsOH, 95 mM Aspartate, 40 mM CsCl, 4 mM $MgCl_2$, 5 mM EGTA, 2 mM $ATPNa_2$, 5 mM HEPES, 8 mM creatine phosphate (pH adjusted to 7.2 with CsOH). Details of voltage dependence of inactivation, and voltage dependence of activation were previously described[26].

Generation of mutant mice.

The targeting vector was constructed using the genomic PCR products from 129/SvJ mouse genome DNA, synthetic linkers carrying the loxP sequence[54], the neomycin-resistance gene from pMC1 Neo (Stratagene), the diphtheria toxin gene from pMC1-DT-A, and pBluscriptII SK(-) (Stratagene). J1 ES cells were transfected with the linearized targeting vector and selected using G418. Of ~550 clones isolated, southern blotting analysis identified the clone carrying the homologous mutation. Chimeric mice produced with the ES clones were crossed with C57BL/6J mice and could transmit the mutant gene to the pups. To determine the mouse genotype, PCR with the primer sets of mDos_genoR_Not(+), mDos_genoL_Not2(-), and LacZ_Aat(-) was carried out using genomic DNA from mice; sequences are mDos_genoRNot(+) (5'-GAGCTGAACCTGAGCTGGCTCTATG-3'), mDos_genoL_Not2(-) (5'-GTGGGTGCCGTTGTCCAGATAAGTAG-3'), and LacZ_Aat(-) (5'-CGCTGATTTGTGTAGTCGGTTTATG-3').

Statistical analysis.

All data accumulated under each condition from at least three independent experiments are expressed as means ± s.e.m. Student's t-test, or ANOVA followed by tukey-kramer's test were employed.

References

1. Scott, E.K. & Luo, L. How do dendrites take their shape? *Nat Neurosci* **4**, 359-365 (2001).
2. Yuste, R. & Bonhoeffer, T. Morphological changes in dendritic spines associated with long-term synaptic plasticity. *Annu Rev Neurosci* **24**, 1071-89 (2001).
3. Libersat, F. & Duch, C. Mechanisms of dendritic maturation. *Molecular Neurobiology* **29**, 303-320 (2004).
4. Becker, L.E., Armstrong, D.L. & Chan, F. Dendritic atrophy in children with Down's syndrome. *Ann Neurol* **20**, 520-6 (1986).
5. Benavides-Piccione, R. et al. On dendrites in Down syndrome and DS murine models: a spiny way to learn. *Progress in Neurobiology* **74**, 111-126 (2004).
6. O'Donnell, W.T. & Warren, S.T. A decade of molecular studies of fragile X syndrome. *Annu Rev Neurosci* **25**, 315-38 (2002).
7. Kaufmann, W.E. & Moser, H.W. Dendritic anomalies in disorders associated with mental retardation. *Cereb. Cortex* **10**, 981-991 (2000).
8. van Galen, E.J.M. & Ramakers, G.J.A. Rho proteins, mental retardation and the neurobiological basis of intelligence. *Development, Dynamics and Pathiology of Neuronal Networks: from Molecules to Functional Circuits* **Volume 147**, 295-317 (2005).
9. Higley, M.J. & Sabatini, B.L. Calcium signaling in dendrites and spines: practical and functional considerations. *Neuron* **59**, 902-913 (2008).
10. Bito, H., Deisseroth, K. & Tsien, R.W. CREB phosphorylation and dephosphorylation: a Ca^{2+}- and stimulus duration–dependent switch for hippocampal gene expression. *Cell* **87**, 1203-1214 (1996).
11. Redmond, L., Kashani, A.H. & Ghosh, A. Calcium regulation of dendritic growth

via CaM kinase IV and CREB-mediated transcription. *Neuron* **34**, 999-1010 (2002).

12. Portera-Cailliau, C., Pan, D.T. & Yuste, R. Activity-Regulated dynamic behavior of early dendritic protrusions: evidence for different types of dendritic filopodia. *J. Neurosci.* **23**, 7129-7142 (2003).
13. Ertel, E.A. et al. Nomenclature of voltage-gated calcium channels. *Neuron* **25**, 533-535 (2000).
14. Maximov, A., Südhof, T.C. & Bezprozvanny, I. Association of neuronal calcium channels with modular adaptor proteins. *J Biol Chem* **274**, 24453-6 (1999).
15. Maximov, A. & Bezprozvanny, I. Synaptic Targeting of N-Type calcium Channels in hippocampal neurons. *J. Neurosci.* **22**, 6939-6952 (2002).
16. Lai, M. et al. A tctex1-Ca^{2+} channel complex for selective surface expression of Ca2+ channels in neurons. *Nat Neurosci* **8**, 435-442 (2005).
17. Mori, Y. et al. Primary structure and functional expression from complementary DNA of a brain calcium channel. *Nature* **350**, 398-402 (1991).
18. Bichet, D. et al. The I-II Loop of the Ca^{2+} channel $\alpha 1$ subunit contains an endoplasmic reticulum retention signal antagonized by the β Subunit. *Neuron* **25**, 177-190 (2000).
19. Varadi, G. et al. Acceleration of activation and inactivation by the β subunit of the skeletal muscle calcium channel. *Nature* **352**, 159-162 (1991).
20. Beguin, P. et al. Regulation of Ca^{2+} channel expression at the cell surface by the small G-protein kir/Gem. *Nature* **411**, 701-706 (2001).
21. Hibino, H. et al. Direct interaction with a nuclear protein and regulation of gene silencing by a variant of the Ca^{2+}-channel β4 subunit. *Proc Natl Acad Sci U S A.* **100**, 307–312 (2003).
22. Viard, P. et al. PI3K promotes voltage-dependent calcium channel trafficking to the

23. Vendel, A.C. et al. Alternative splicing of the voltage-gated Ca^{2+} channel β4 subunit creates a uniquely folded N-terminal protein binding domain with cell-specific expression in the cerebellar cortex. *J. Neurosci.* **26**, 2635-2644 (2006).

24. Burgess, D.L. et al. β subunit reshuffling modifies N- and P/Q-Type Ca^{2+}channel subunit compositions in Lethargic mouse brain. *Molecular and Cellular Neuroscience* **13**, 293-311 (1999).

25. Jeon, D. et al. Ablation of Ca^{2+} channel β3 subunit leads to enhanced N-Methyl-D-aspartate receptor-dependent long term potentiation and improved long term memory. *J. Biol. Chem.* **283**, 12093-12101 (2008).

26. Kiyonaka, S. et al. RIM1 confers sustained activity and neurotransmitter vesicle anchoring to presynaptic Ca2+ channels. *Nat Neurosci* **10**, 691-701 (2007).

27. Ozon, S., Maucuer, A. & Sobel, A. The Stathmin family. *European Journal of Biochemistry* **248**, 794-806 (1997).

28. Ozon, S. & Byk, T. SCLIP: a Novel SCG10-like protein of the stathmin family expressed in the nervous system. *Journal of Neurochemistry* **70**, 2386-2396 (1998).

29. Ozon, S., Mestikawy, S.E. & Sobel, A. Differential, regional, and cellular expression of the stathmin family transcripts in the adult rat brain. *Journal of Neuroscience Research* **56**, 553-564 (1999).

30. Curmi, P.A. et al. Stathmin and its phosphoprotein family: general properties, biochemical and functional interaction with tubulin. *Cell Struct Funct* **24**, 345-57 (1999).

31. Poulain, F.E. & Sobel, A. The "SCG10-LIke Protein" SCLIP is a novel regulator of axonal branching in hippocampal neurons, unlike SCG10. *Molecular and Cellular Neuroscience* **34**, 137-146 (2007).

32. Poulain, F.E. et al. SCLIP Is Crucial for the formation and development of the purkinje cell dendritic arbor. *J. Neurosci.* **28**, 7387-7398 (2008).

33. Xie, M. et al. Facilitation versus depression in cultured hippocampal neurons determined by targeting of Ca^{2+} channel Cavβ4 versus Cavβ2 subunits to synaptic terminals. *J Cell Biol.* **178**, 489–502 (2007).

34. Saitou, N. & Nei, M. The neighbor-joining method: a new method for reconstructing phylogenetic trees. *Mol Biol Evol* **4**, 406-25 (1987).

35. Thompson, J.D., Higgins, D.G. & Gibson, T.J. CLUSTAL W: improving the sensitivity of progressive multiple sequence alignment through sequence weighting, position-specific gap penalties and weight matrix choice. *Nucleic Acids Res* **22**, 4673-80 (1994).

36. Opatowsky, Y. et al. Structural analysis of the voltage-dependent calcium channel β subunit functional core and its complex with the α1 interaction domain. *Neuron* **42**, 387-399 (2004).

37. Sobel, A. Stathmin: a relay phosphoprotein for multiple signal transduction? *Trends Biochem Sci* **16**, 301-5 (1991).

38. Belmont, L.D. & Mitchison, T.J. Identification of a protein that interacts with tubulin dimers and increases the catastrophe rate of microtubules. *Cell* **84**, 623-631 (1996).

39. Curmi, P.A. et al. The stathmin/tubulin interaction in vitro. *J. Biol. Chem.* **272**, 25029-25036 (1997).

40. Steinmetz, M.O. et al. Op18/stathmin caps a kinked protofilament-like tubulin tetramer. *EMBO J.* **19**, 572–580 (2000).

41. Charbaut, E. et al. Stathmin family proteins display specific molecular and tubulin binding properties. *J. Biol. Chem.* **276**, 16146-16154 (2001).

42. Ravelli, R.B. et al. Insight into tubulin regulation from a complex with colchicine and a stathmin-like domain. *Nature* **428**, 198-202 (2004).

43. Portera-Cailliau, C., Pan, D.T. & Yuste, R. Activity-regulated dynamic behavior of early dendritic protrusions: evidence for different types of dendritic filopodia. *J. Neurosci.* **23**, 7129-7142 (2003).

44. Purpura, D.P. Dendritic spine "dysgenesis" and mental retardation. *Science* **186**, 1126-8 (1974).

45. Hinton, V.J. et al. Analysis of neocortex in three males with the fragile X syndrome. *Am J Med Genet* **41**, 289-94 (1991).

46. Grossman, A.W. et al. Local protein synthesis and spine morphogenesis: Fragile X syndrome and beyond. *J. Neurosci.* **26**, 7151-7155 (2006).

47. Weiler, I.J. et al. Fragile X mental retardation protein is translated near synapses in response to neurotransmitter activation. *Proc Natl Acad Sci U S A.* **94**, 5395–5400 (1997).

48. Steward, O. & Falk, P.M. Protein-synthetic machinery at postsynaptic sites during synaptogenesis: a quantitative study of the association between polyribosomes and developing synapses. *J Neurosci* **6**, 412-23 (1986).

49. Vanderklish, P.W. & Edelman, G.M. Dendritic spines elongate after stimulation of group 1 metabotropic glutamate receptors in cultured hippocampal neurons. *Proc Natl Acad Sci U S A.* **99**, 1639–1644 (2002).

50. Irwin, S.A. et al. Abnormal dendritic spine characteristics in the temporal and visual cortices of patients with fragile-X syndrome: A quantitative examination. *American Journal of Medical Genetics Part A* **98**, 161-167 (2001).

51. Galvez, R. & Greenough, W.T. Sequence of abnormal dendritic spine development in primary somatosensory cortex of a mouse model of the fragile X mental

52. Grossman, A.W. et al. Hippocampal pyramidal cells in adult Fmr1 knockout mice exhibit an immature-appearing profile of dendritic spines. *Brain Research* **1084**, 158-164 (2006).

53. Nishi, M. et al. Unrestrained nociceptive response and disregulation of hearing ability in mice lacking the nociceptin/orphaninFQ receptor. *EMBO J.* **16**, 1858–1864 (1997).

54. Shibata, H. et al. Rapid colorectal adenoma formation initiated by conditional targeting of the Apc gene. *Science* **278**, 120-3 (1997).

Figure 1

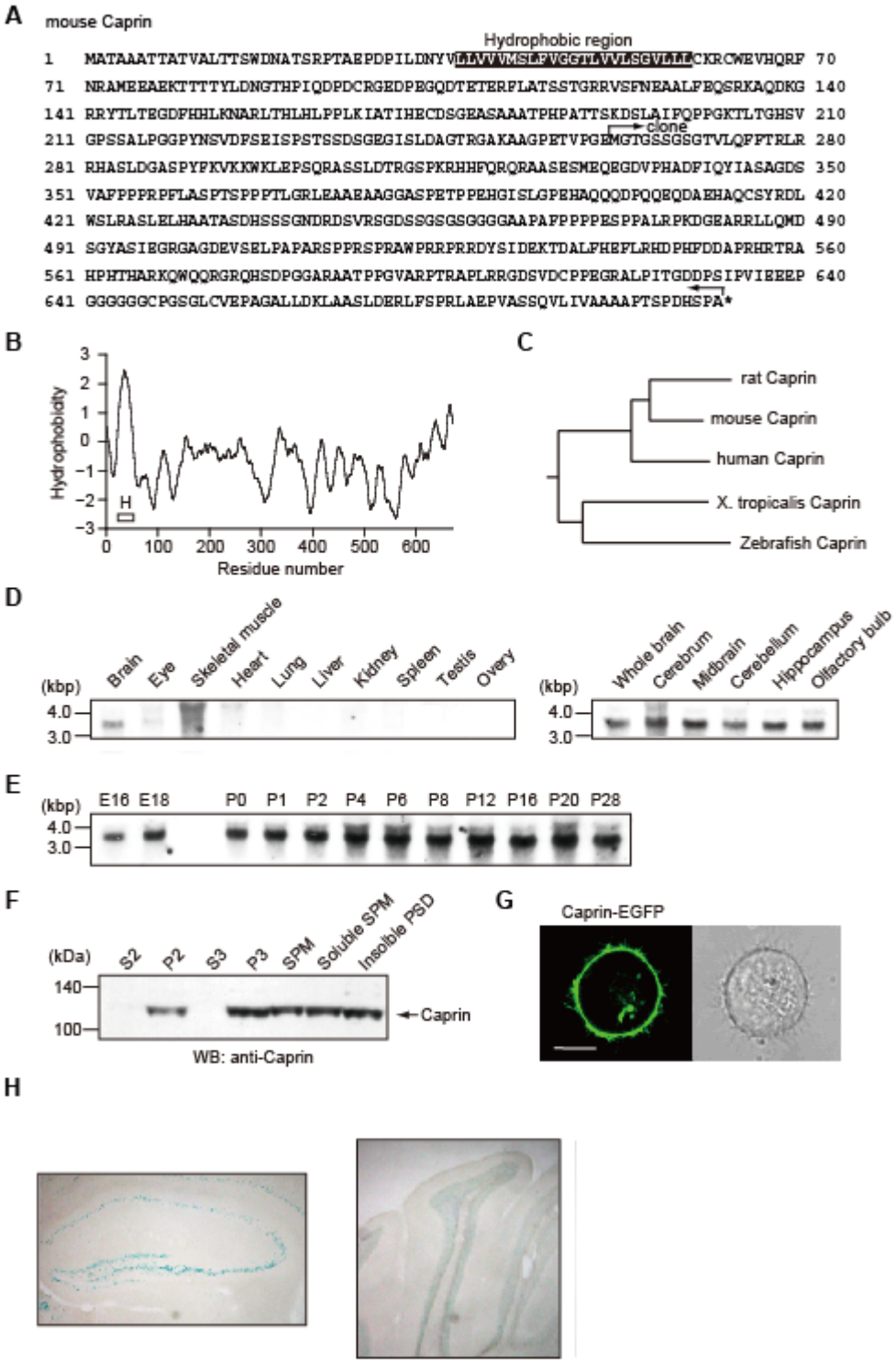
A
mouse Caprin
Hydrophobic region
clone
B
Hydrophobicity
Residue number
C
rat Caprin
mouse Caprin
human Caprin
X. tropicalis Caprin
Zebrafish Caprin
D
(kbp)
Brain
Eye
Skeletal muscle
Heart
Lung
Liver
Kidney
Spleen
Testis
Ovary
Whole brain
Cerebrum
Midbrain
Cerebellum
Hippocampus
Olfactory bulb
E
E16 E18 P0 P1 P2 P4 P6 P8 P12 P16 P20 P28
F
(kDa)
S2 P2 S3 P3 SPM Soluble SPM Insoluble PSD
Caprin
WB: anti-Caprin
G
Caprin-EGFP
H

Figure 1

A, the amino acid sequence of the mouse Caprin deduced from the cDNA sequence. The hydrophobic region (H) is enclosed with block box. The protein region encoded by clone is also indicated. B, the Kyte-Doolittle hydrophobicity profile of mouse Caprin was generated with a window size of 10 amino acids (Kyte J and Doolittle RF 1982). C, the phylogenetic tree for the Caprin family was generated using the Clustalw program. Members of the Caprin family are as follows; rat Caprin (XM_234901), mouse Caprin (NM_015761), human Caprin (NM_152769), x. tropicalis Caprin (NM_001102920), zebrafish Caprin (XP_685582). D, northern blot analysis of Caprin RNA distribution in mouse tissues (left) and in mouse brain (right). E, northern blot analysis of Caprin RNA developmental expression in whole brains. F, subcellular distribution of Caprin protein in neurons. G, the confocal imaging of HEK293 cells expressing Caprin-EGFP. Scale bar, 10 μm. H, expression of β-galactosidase activity in hippocampus (top) and cerebellum (bottom) of the Caprin-deficient mouse.

Figure 2

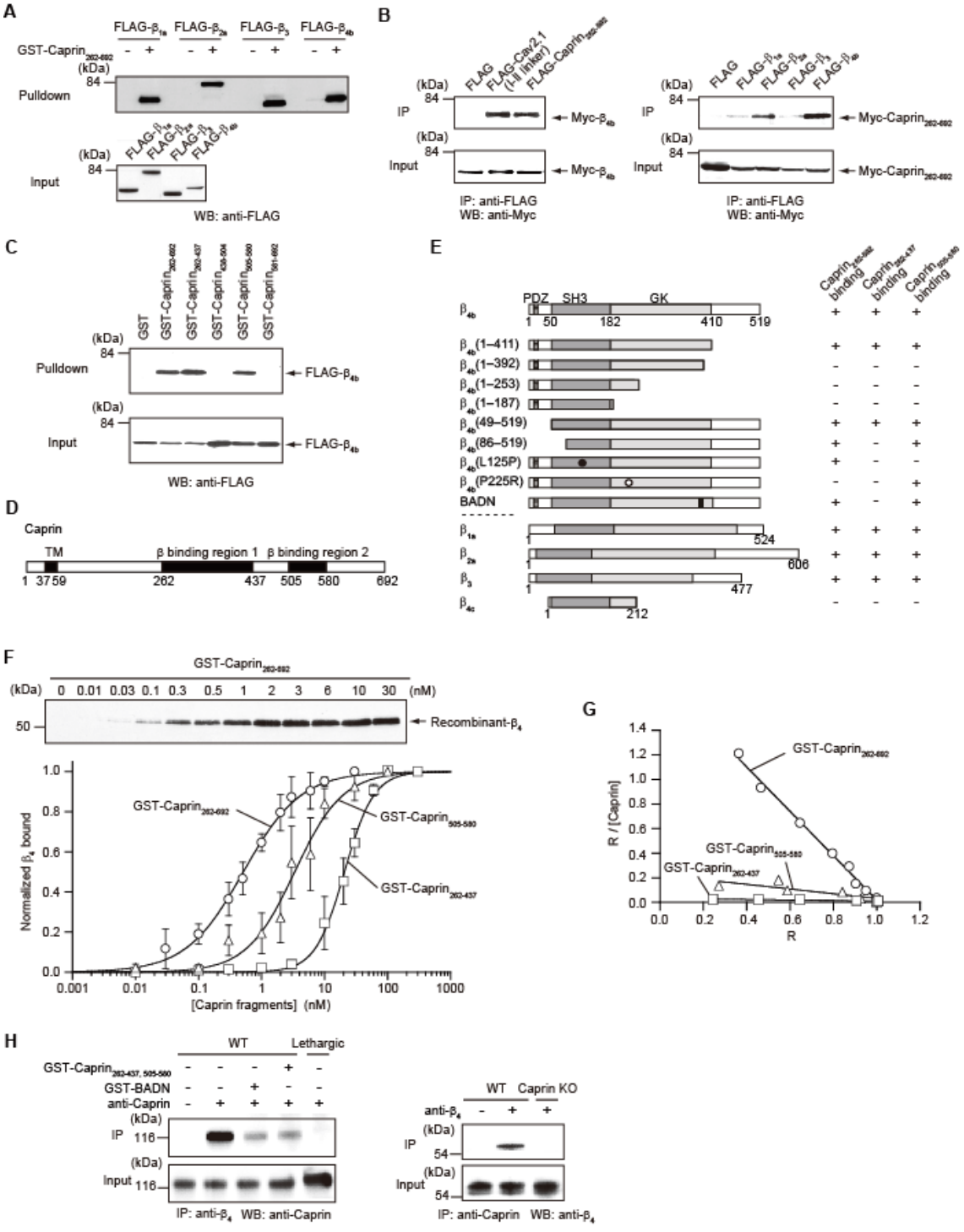
A
FLAG-β1a FLAG-β2a FLAG-β3 FLAG-β4b
GST-Caprin262-692 - + - + - + - +
(kDa)
84
Pulldown
Input
WB: anti-FLAG
B
FLAG
FLAG-Cav2.1 (I-II linker)
FLAG-Caprin262-692
IP
Myc-β4b
Input
IP: anti-FLAG
WB: anti-Myc
Myc-Caprin262-692
C
GST
GST-Caprin263-692
GST-Caprin263-437
GST-Caprin426-504
GST-Caprin505-580
GST-Caprin581-692
FLAG-β4b
D
Caprin
TM
β binding region 1
β binding region 2
1 37 59 262 437 505 580 692
E
PDZ SH3 GK
Caprin262-692 binding
Caprin263-437 binding
Caprin505-580 binding
β4b(1–411)
β4b(1–392)
β4b(1–253)
β4b(1–187)
β4b(49–519)
β4b(86–519)
β4b(L125P)
β4b(P225R)
BADN
β1a
β2a
β3
β4c
F
GST-Caprin262-692
0 0.01 0.03 0.1 0.3 0.5 1 2 3 6 10 30 (nM)
Recombinant-β4
Normalized β4 bound
[Caprin fragments] (nM)
G
R / [Caprin]
R
H
WT
Lethargic
GST-Caprin262-437, 505-580
GST-BADN
anti-Caprin
IP: anti-β4 WB: anti-Caprin
WT Caprin KO
anti-β4
IP: anti-Caprin WB: anti-β4

Figure 2

A, pulldown assay of β_{1a}, β_{2a}, β_3, and β_{4b} with GST fusion Caprin encoded by yeast two hybride clone. GST fusion proteins immobilized on glutathione-Sepharose beads were incubated with cell lysates obtained from FLAG-β-transfected HEK293 cells. Bound proteins were analyzed by western blotting (WB) using antibody for FLAG. B, interaction of recombinant β and Caprin in HEK293 cells. The interaction is evaluated by immunoprecipitation (IP) with antibody for FLAG, followed by WB with antibody for Myc. Left, physical association of Myc- β_{4b} with FLAG-Caprin in comparison with a positive control FLAG-$Ca_v2.1$(I-II linker). Right, physical association of FLAG-β with Myc-Caprin. C, pulldown assay of β_{4b} with GST fusion Caprin muntans. Bound proteins were analyzed by western blotting (WB) using antibody for FLAG. D, domain structure of mouse Caprin. Transmembrane (TM), β-binding region 1, and 2 are shown. E, mapping of Caprin-binding sites on β_{4b} by the yeast two-hybrid assay. β-subunit constructs in bait vectors were tested with Caprin in the prey vector. The interactions were scored by β-galactosidase activity and His^+ prototrophy. F, In vitro association between the purified GST-RIM1 fusion constructs and recombinant β_4 subunit (residues 47-475). GST-Caprin proteins at various concentrations, incubated with β_4 (50 pM), were captured by glutathione-Sepharose beads. Captured β_4 proteins were examined by WB. The bottom panel shows the quantitative densitometric analysis of bands shown in the upper panel. The saturation curves were subjected to the nonlinear least-squares curve-fitting method to evaluate the apparent dissociation constant (K_d). G, scatchard plot analysis of β_4 binding to Caprin proteins calculated by Fig. 2F. H, coimmunoprecipitation of Caprin with the β_4 subunit in the brain. The immunocomplexes were disrupted by GST-BADN or GST-Caprin262-437, 505-580. Immunoprecipitation (IP) using an antibody for β_4 (top) or Caprin (bottom) and

subsequent WB for Caprin (top) or β_4 (bottom) was carried out on digitonin solubilized samples.

Figure 3

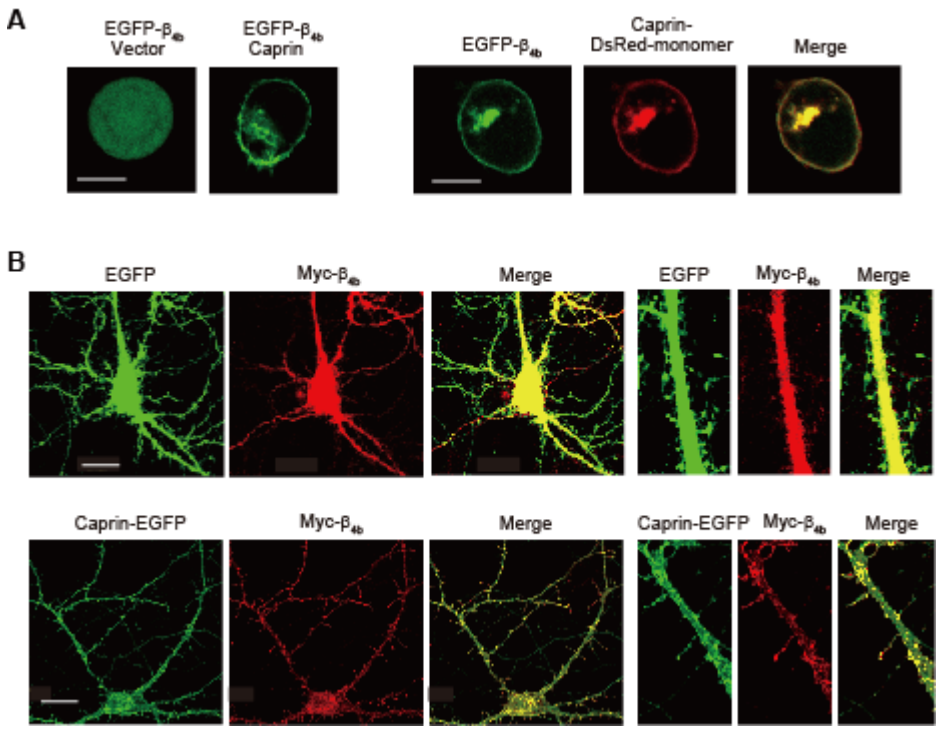

Figure 3

A, Caprin elicited plasma membrane translocation of β_{4b}. Left, confocal imaging of the HEK293 cell expressing EGFP-β_{4b} with vector or Caprin. Right, confocal imaging of the HEK293 cell expressing EGFP-β_{4b} and Caprin-DsRed-monomer. B, confocal imaging of the hippocampal neuron expressing Myc-β_{4b} and EGFP vector (top) or Caprin-EGFP (bottom). Caprin elicited dendritic plasma membrane and protrusion translocation of β_{4b}.

Figure 4

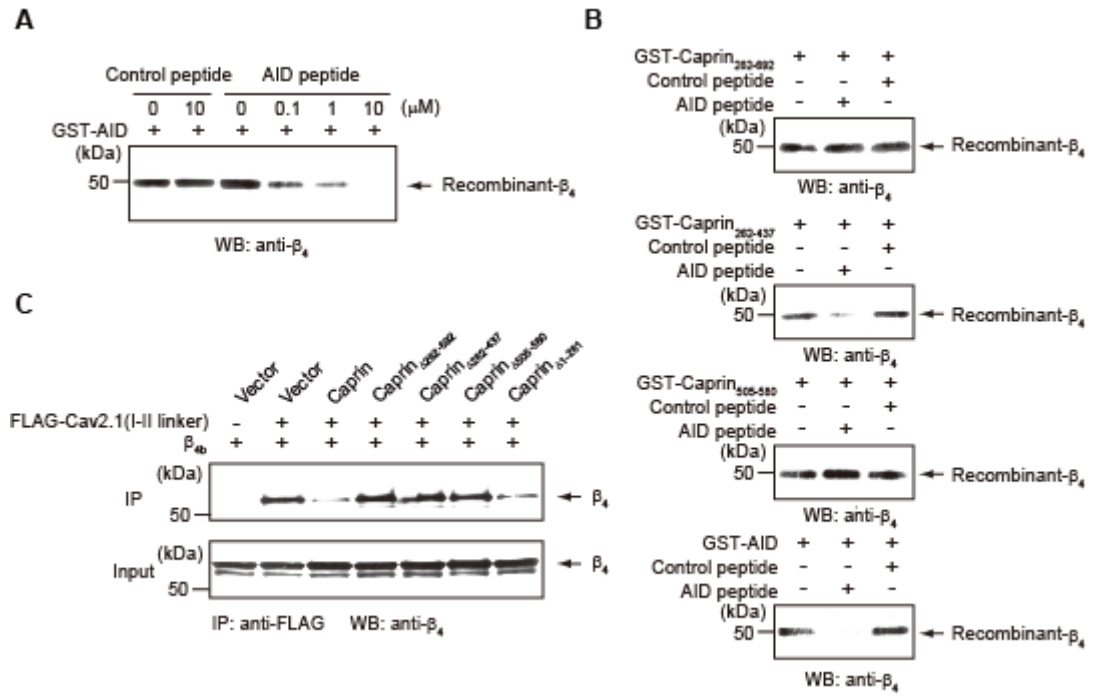

Figure 4

A, *in vitro* association between the purified GST-Ca_v2.1(AID) (residues 367-480) fusion constructs and recombinant β_4 subunit (residues 47-475) was disrupted by AID peptide (QQIERELNGYMEWISKAE). B, *in vitro* association between the purified GST-Caprin mutants fusion constructs and recombinant β_4 subunit. The association between $Caprin_{262-437}$ and recombinant β_4 was disrupted by AID peptide. C, the interaction between Cav2.1 I-II linker and β_{4b} was disrupted by Caprin constructs. The interaction is evaluated by IP with antibody for FLAG, followed by WB with antibody for β_4.

Figure 5

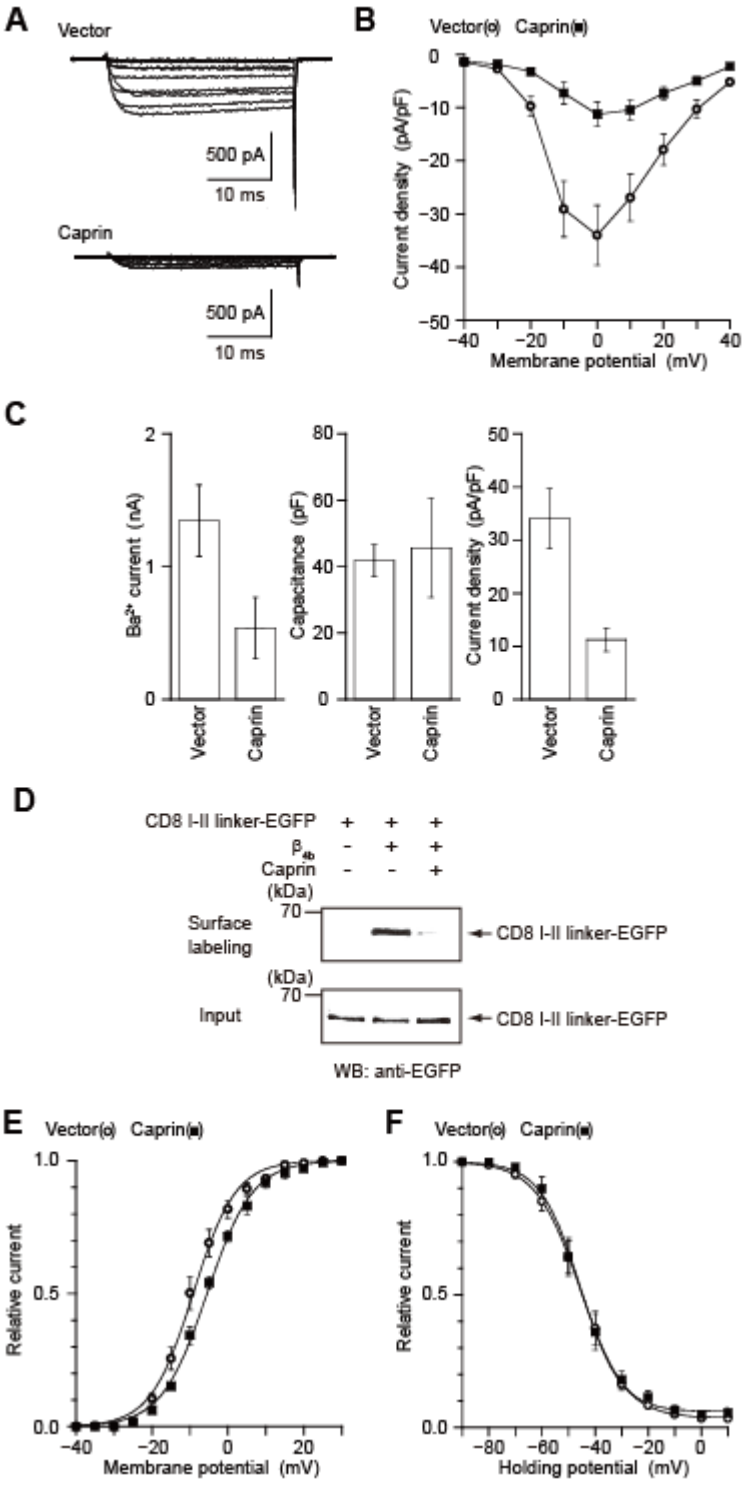
A
Vector
500 pA
10 ms
Caprin
500 pA
10 ms
B
Vector(o) Caprin(■)
Current density (pA/pF)
Membrane potential (mV)
C
Ba2+ current (nA)
Capacitance (pF)
Current density (pA/pF)
Vector
Caprin
D
CD8 I-II linker-EGFP
β4b
Caprin
(kDa)
70
Surface labeling
CD8 I-II linker-EGFP
Input
WB: anti-EGFP
E
Vector(o) Caprin(■)
Relative current
Membrane potential (mV)
F
Vector(o) Caprin(■)
Relative current
Holding potential (mV)

Figure 5 Effects of Caprin proteins on P/Q-type $Ca_v2.1$.

A, representative traces for Ba^{2+} currents (with β_{4b}) on application of test pulses from –40 mV to 40 mV with 10-increments. B, current density-voltage (*I*-*V*) relationships of $Ca_v2.1$. The V_h is –100 mV. C, distribution of peak current amplitude (left), cell capacitance (middle), and current density (right). D, cell surface expression of $Ca_v2.1$ constructs. The cell lysate prepared after exposure to NHS-SS-biotin was incubated with streptavidin-agarose, and the obtained surface proteins were analyzed by WB with anti-EGFP antibody. E, activation curves. Amplitudes of tail currents were normalized to the maximal tail current amplitude. The mean values were plotted against test pulse potentials and fitted to the Boltzmann equation. F, inactivation curves. Amplitudes of currents evoked by the test pulses were normalized to the current amplitude induced by the test pulse after a 2-sec V_h replacement of –100 mV. The mean values were plotted as a function of potentials of the 2-sec V_h displacement, and were fitted to the Boltzmann equation.

Figure 6

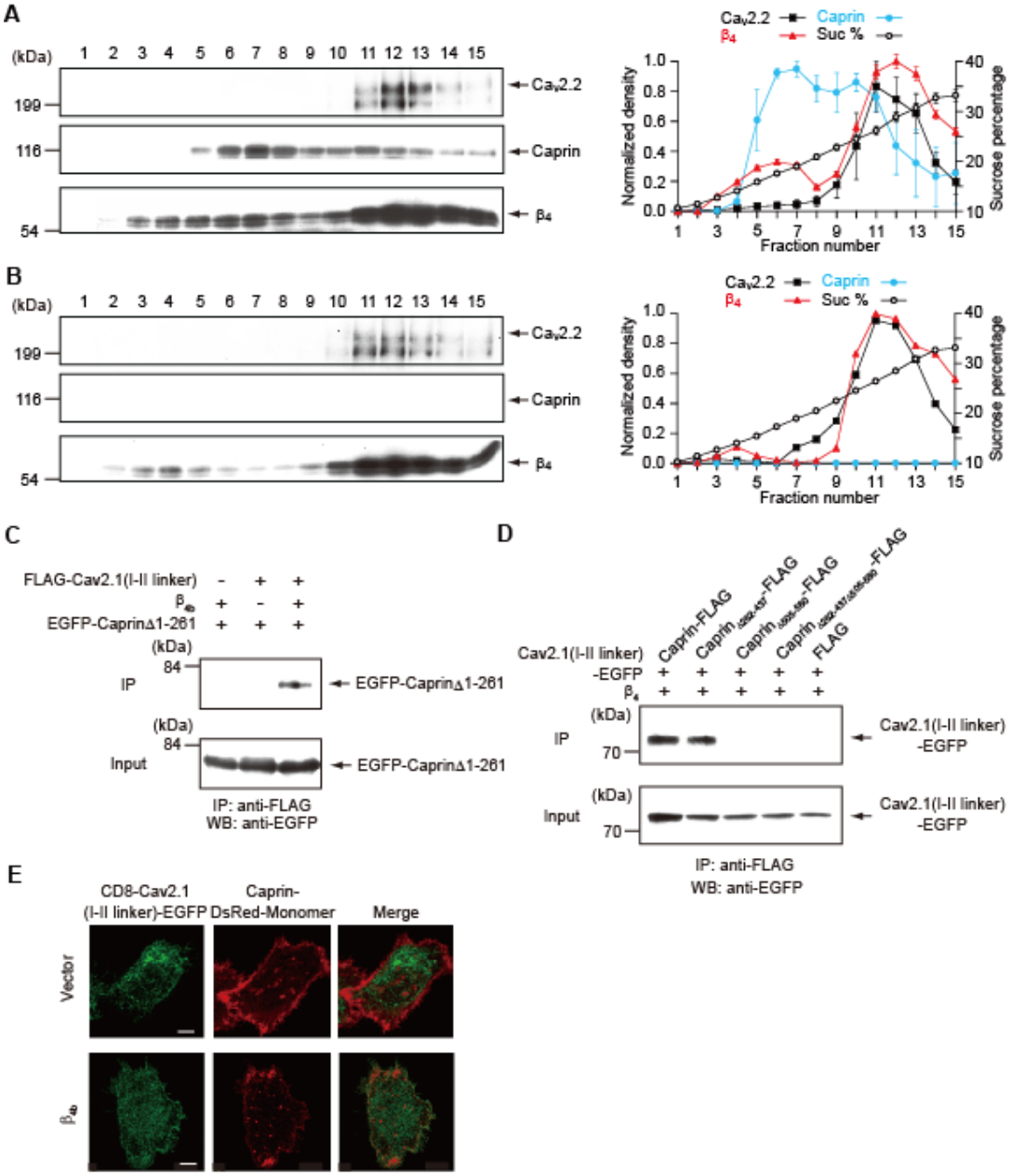
A
(kDa)
1 2 3 4 5 6 7 8 9 10 11 12 13 14 15
199
116
54
Cav2.2
Caprin
β4
Cav2.2 Caprin
β4 Suc %
Normalized density
Sucrose percentage
Fraction number
B
C
FLAG-Cav2.1(I-II linker)
β4b
EGFP-CaprinΔ1-261
84
IP
Input
EGFP-CaprinΔ1-261
IP: anti-FLAG
WB: anti-EGFP
D
Cav2.1(I-II linker)
-EGFP
β4
Caprin-FLAG
FLAG
70
Cav2.1(I-II linker)
-EGFP
IP: anti-FLAG
WB: anti-EGFP
E
CD8-Cav2.1
(I-II linker)-EGFP
Caprin-
DsRed-Monomer
Merge
Vector
β4b

Figure 6

Sucrose gradient fractionation of neuronal VDCC compleses from wild-type (WT) (A) or Caprin knockout mouse (CaprinKO) (B) brains and subsequent WB showed cosedimentation of Caprin with β_4 and with VDCC complex. densitometry of $Ca_v2.1$, β_4 and Caprin from western blots of sucrose gradient fractions. The normalized density of each protein is plotted as a function of the sucrose density fraction number. C, coimmunoprecipitation of recombinant VDCC subunits with Caprin in HEK293 cells. The interaction is evaluated by IP with antibody for FLAG followed by WB with antibody for EGFP. D, interactions of recombinant VDCC subunits and Caprin mutants in HEK293 cells. The interaction is evaluated by IP with antibody for FLAG, followed by WB with antibody for EGFP. E, β_{4b} elicited plasma membrane colocalization of $Ca_v2.1$(I-II linker) and Caprin. Confocal imaging of CHO cells expressing CD8-$Ca_v2.1$(I-II linker)-EGFP and Caprin-DsRed-Monomer with vector or β_{4b}.

Figure 7　a model of Caprin-VDCC complex.

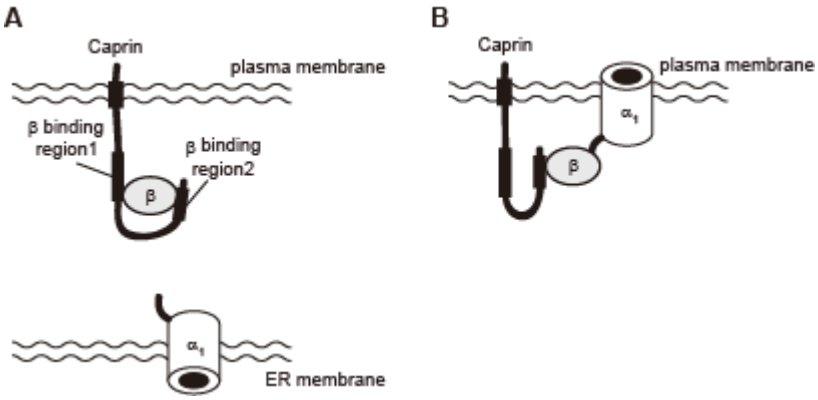

Figure 7　a model of Caprin-VDCC complex.

A, Caprin interacts with β subunit mediated by β binding region 1 and 2 of Caprin. Because Caprin β binding region 1 and α1 competitively bind to β subunits, mainly Caprin disrupts the interaction between α1 and β subunits in vitro.　B, Caprin have the ability to bind with VDCC complex.　Partially, Caprin interacts with VDCC-β complex in mouse brain.

Figure 8

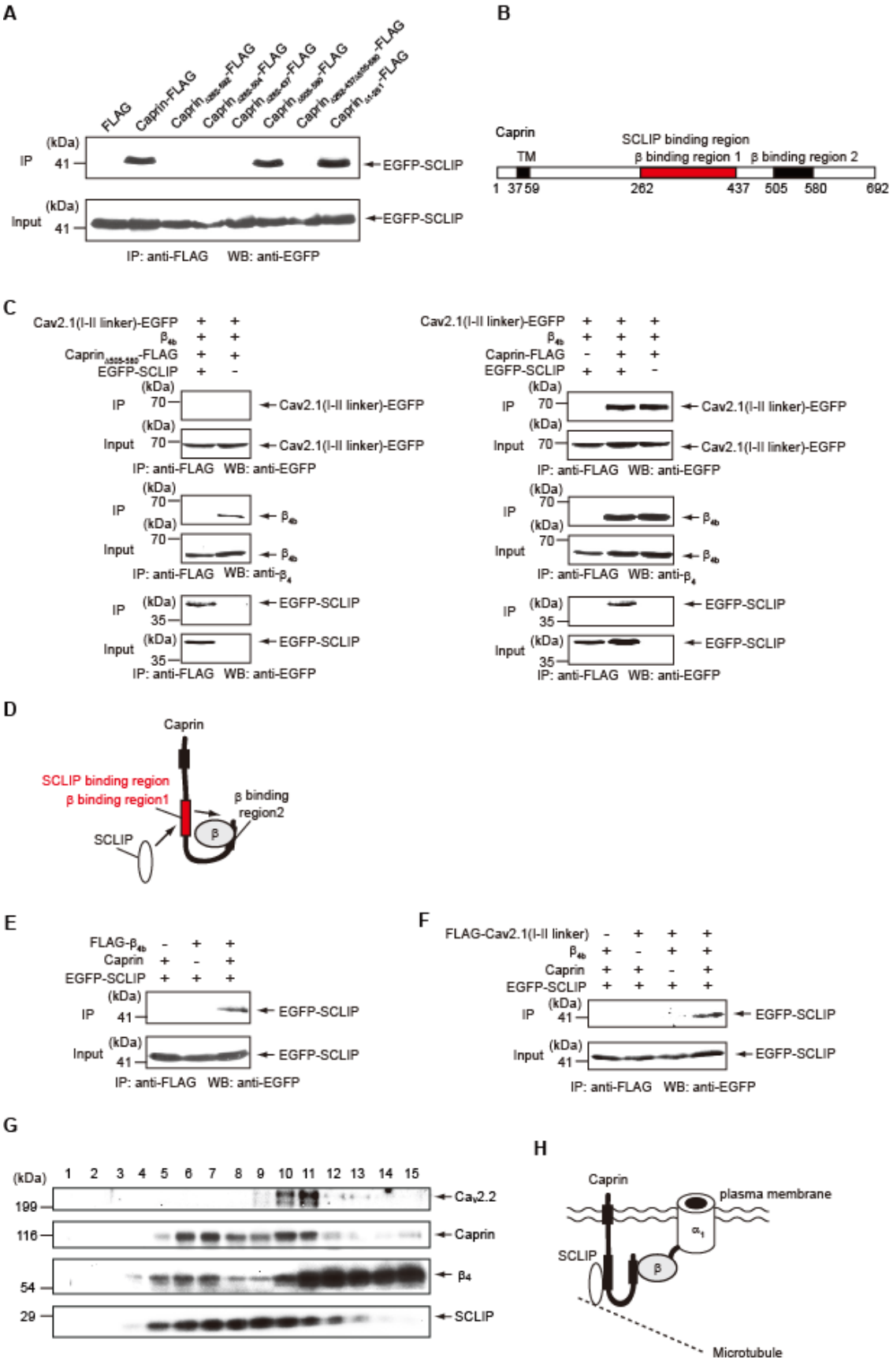
A
FLAG
Caprin-FLAG
IP
(kDa)
41
EGFP-SCLIP
Input
IP: anti-FLAG WB: anti-EGFP
B
Caprin
TM
SCLIP binding region
β binding region 1
β binding region 2
1 37 59 262 437 505 580 692
C
Cav2.1(I-II linker)-EGFP
β4b
Caprin-FLAG
EGFP-SCLIP
70
Cav2.1(I-II linker)-EGFP
IP: anti-FLAG WB: anti-EGFP
IP: anti-FLAG WB: anti-β4
35
EGFP-SCLIP
D
Caprin
SCLIP binding region
β binding region1
β binding region2
SCLIP
β
E
FLAG-β4b
Caprin
EGFP-SCLIP
F
FLAG-Cav2.1(I-II linker)
G
1 2 3 4 5 6 7 8 9 10 11 12 13 14 15
199
116
54
29
CaV2.2
Caprin
β4
SCLIP
H
Caprin
plasma membrane
α1
β
SCLIP
Microtubule

Figure 8

A, immunoprecipitation assay of SCLIP with FLAG tagged Caprin mutants. The interaction is evaluated by IP with antibody for FLAG followed by WB with antibody for EGFP. B, domain structure of mouse Caprin. Transmembrane (TM), β-binding region 1, 2, and SCLIP binding region are shown. C, immunoprecipitation assay of recombinant VDCC subunits and Caprin constructs with vector or SCLIP. The interaction is evaluated by IP with antibody for FLAG followed by WB with antibody for EGFP or β_4. D, a model of β subunit-Caprin-SCLIP complex. Because β subunit and SCLIP competitively bind to Caprin262-437 in vitro, SCLIP have the ability to switch the mode of the interaction between Caprin and β subunit. E, coimmunoprecipitation of recombinant β_{4b}-Caprin complexes with SCLIP in HEK293 cells. The interaction is evaluated by IP with antibody for FLAG followed by WB with antibody for EGFP. F, coimmunoprecipitation of recombinant VDCC subunits-Caprin complexes with SCLIP in HEK293 cells. The interaction is evaluated by IP with antibody for FLAG followed by WB with antibody for EGFP. G, sucrose gradient fractionation of neuronal VDCC compleses from mouse brains and subsequent WB showed cosedimentation of SCLIP with VDCC-Caprin complex. H, a model of VDCC-Caprin-SCLIP complex.

Figure 9

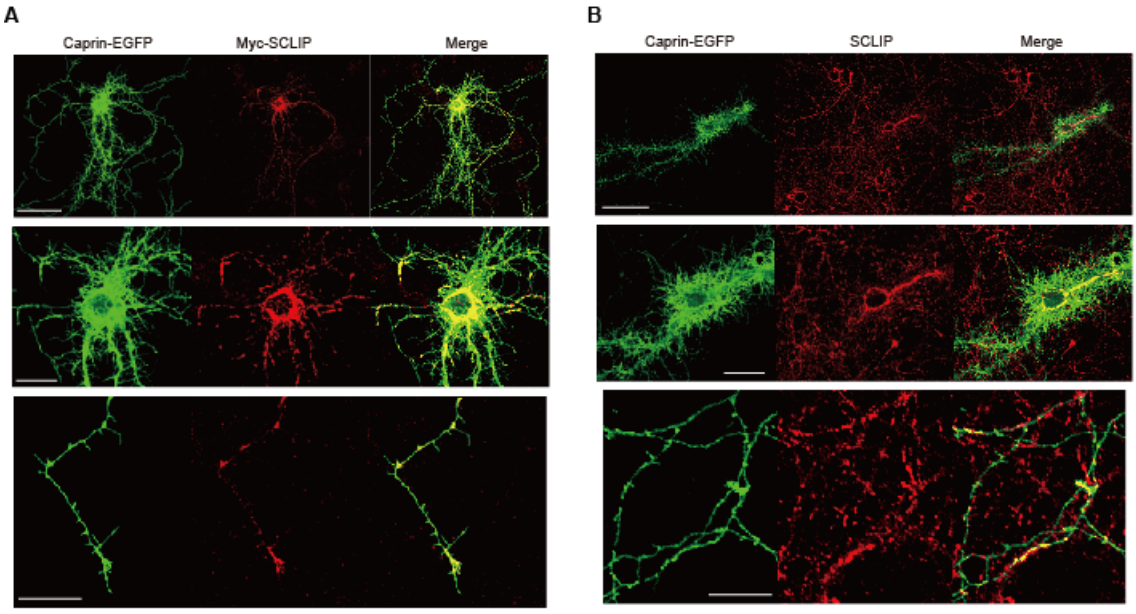

Figure 9

A, immunolocalization of recombinant SCLIP and Caprin in cultured hippocampal neuron. Confocal imaging of the hippocampal neuron expressing Myc-SCLIP and Caprin-EGFP. Scale bar, 50 μm (top), 20 μm (middle), and 10 μm (bottom).

Figure 10

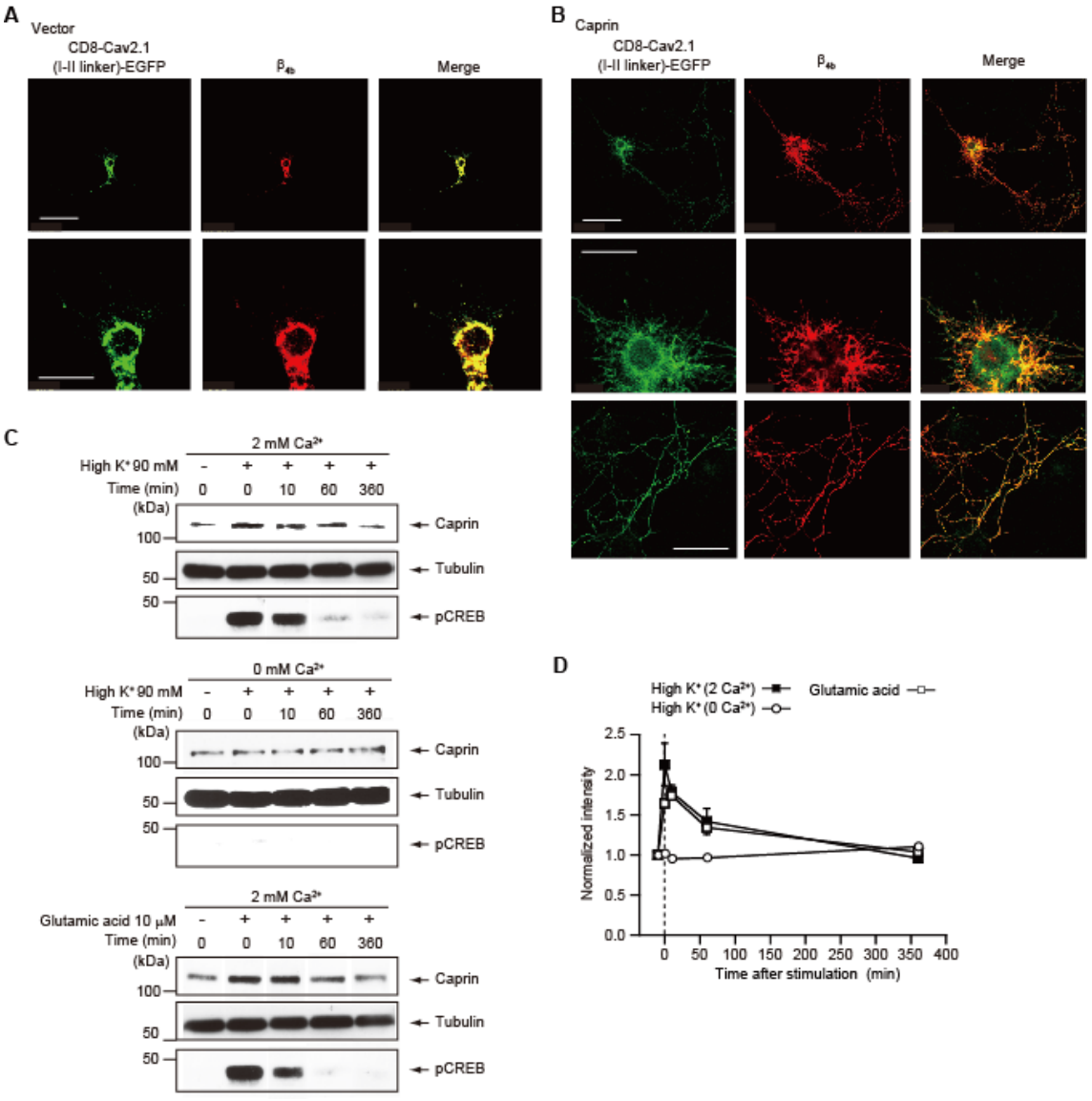
A
Vector
CD8-Cav2.1
(I-II linker)-EGFP
β4b
Merge
B
Caprin
CD8-Cav2.1
(I-II linker)-EGFP
β4b
Merge
C
2 mM Ca2+
High K+ 90 mM - + + + +
Time (min) 0 0 10 60 360
(kDa)
100
50
50
Caprin
Tubulin
pCREB
0 mM Ca2+
High K+ 90 mM - + + + +
Time (min) 0 0 10 60 360
(kDa)
100
50
50
Caprin
Tubulin
pCREB
2 mM Ca2+
Glutamic acid 10 μM - + + + +
Time (min) 0 0 10 60 360
(kDa)
100
50
50
Caprin
Tubulin
pCREB
D
High K+ (2 Ca2+)
High K+ (0 Ca2+)
Glutamic acid
Normalized intensity
2.5
2.0
1.5
1.0
0.5
0.0
0 50 100 150 200 250 300 350 400
Time after stimulation (min)

Figure 10

A, immunolocalization of native SCLIP and recombinant Caprin in cultured hippocampal neuron. Confocal imaging of the hippocampal neuron expressing Caprin-EGFP. Scale bar, 50 μm (top), 20 μm (middle), and 10 μm (bottom). B, Caprin elicited plasma membrane and protrusion translocation of VDCC subunits in cultured hippocampal neurons. Confocal imaging of hippocampal neurons expressing CD8-$Ca_v2.1$(I-II linker)-EGFP and β_{4b} with vector (left) or Caprin (right). C, the expression of Caprin induced by 2 mM Ca^{2+} high K^+ (top), 0 mM Ca^{2+} high K^+ (middle) or 2 mM Ca^{2+} glutamic acid stimuration (bottom) in cultured hippocampal neurons is assessed at indicated time point by western blot. D, The graph depicts the time course of the normalized intensity of caprin protein detected in C.

Figure 11

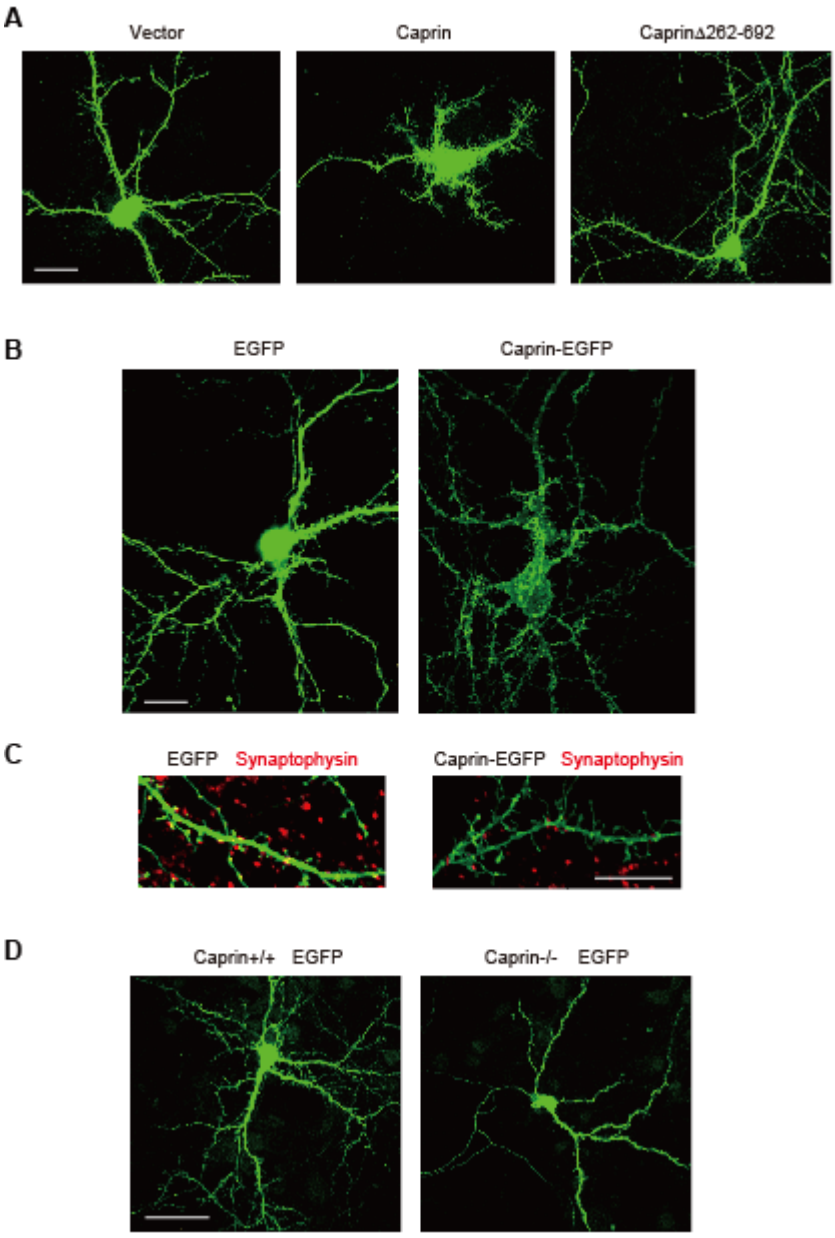
A
Vector
Caprin
CaprinΔ262-692
B
EGFP
Caprin-EGFP
C
EGFP Synaptophysin
Caprin-EGFP Synaptophysin
D
Caprin+/+ EGFP
Caprin-/- EGFP

Figure 11

A, Caprin regulate dendritic morphogenesis in cultured hippocampal neurons. Confocal imaging of the hippocampal neurons expressing EGFP and vector, Caprin, or CaprinΔ262-692. Scale bar, 20 μm. B, the confocal imaging of cultured hippocampal neurons expressing Caprin-EGFP. Scale bar, 20 μm. C, the confocal imaging of the dendrites of cultured hippocampal neurons expressing EGFP (left) or Caprin-EGFP (right). Scale bar, 10 μm. D, the confocal imaging of cultured hippocampal neurons in wild-type (left) or Caprin knockout mouse (right). Scale bar, 50 μm.

Supplementary Figure 1

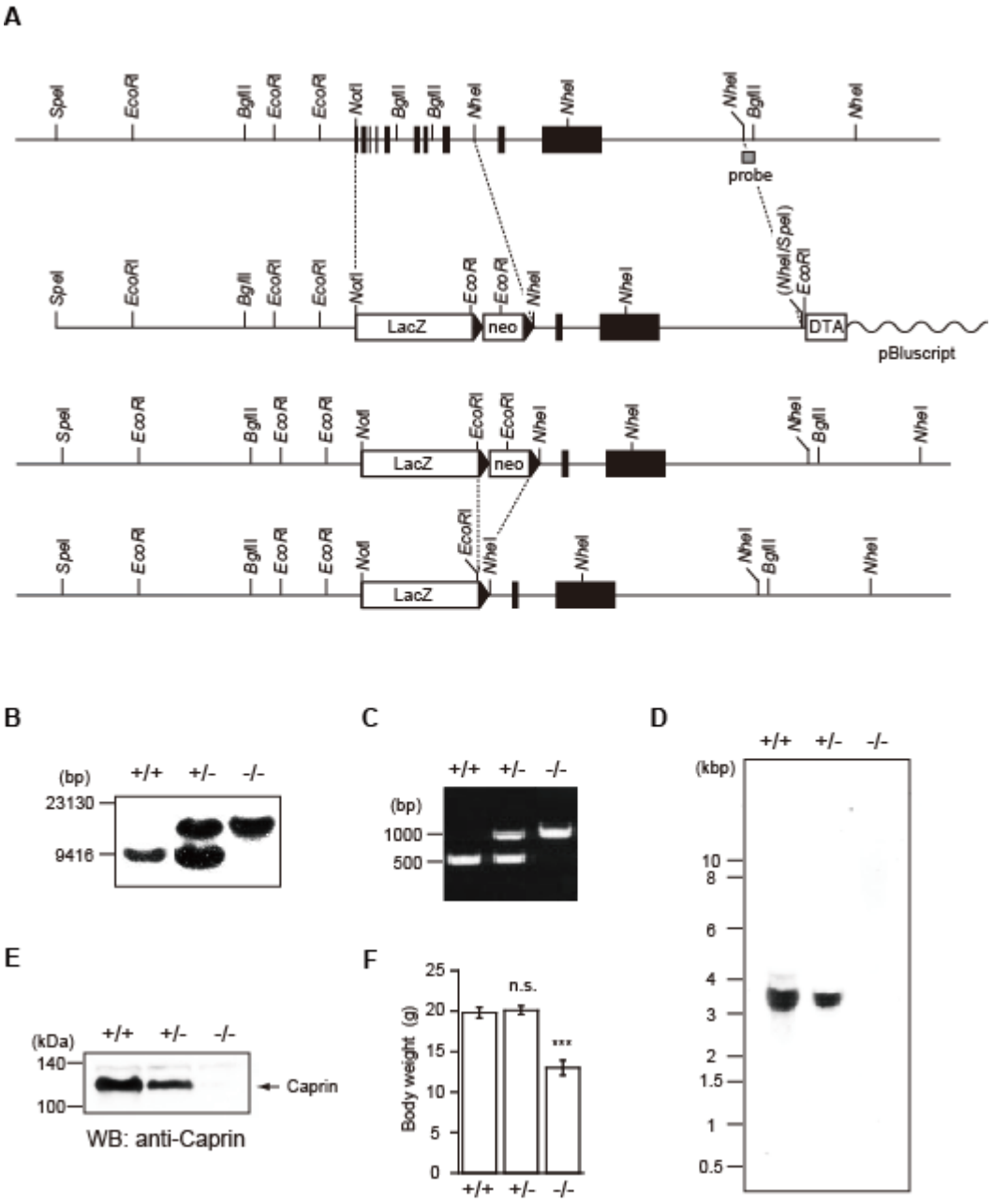

Supplementary Figure 1

A, restriction enzyme maps of the wild-type allele, targeting vector, expected targeted allele, and recombinated targeted allele. B, southern blot analysis of DNAs from Caprin+/+, Caprin+/-, and Caprin-/- mouse. The DNAs were digested with BglII and analysed. The hybridization probe used are shown in A. The expected sizes of the restriction fragments from Caprin+/+, Caprin+/-, and Caprin-/- are 8.9, 8.9 and 16.2, and 16.2 kbp, respectively. C, genomic PCR analysis of DNAs from Caprin+/+, Caprin+/-, and Caprin-/- mouse. The expected sizes of the restriction fragments from Caprin+/+, Caprin+/-, and Caprin-/- are 541, 541 and 1013, and 1013 bp, respectively. D, northern blot analysis of Caprin RNAs from Caprin+/+, Caprin+/-, and Caprin-/- mouse. E, western blot analysis of Caprin proteins form Caprin+/+, Caprin+/-, and Caprin-/- mouse brain. F, comparison of body weights of Caprin+/+, Caprin+/-, and Caprin-/- mice (n = 5, 18, and 10, respectively). Error bars indicate mean ± s.e.m.

Supplementary Figure 2

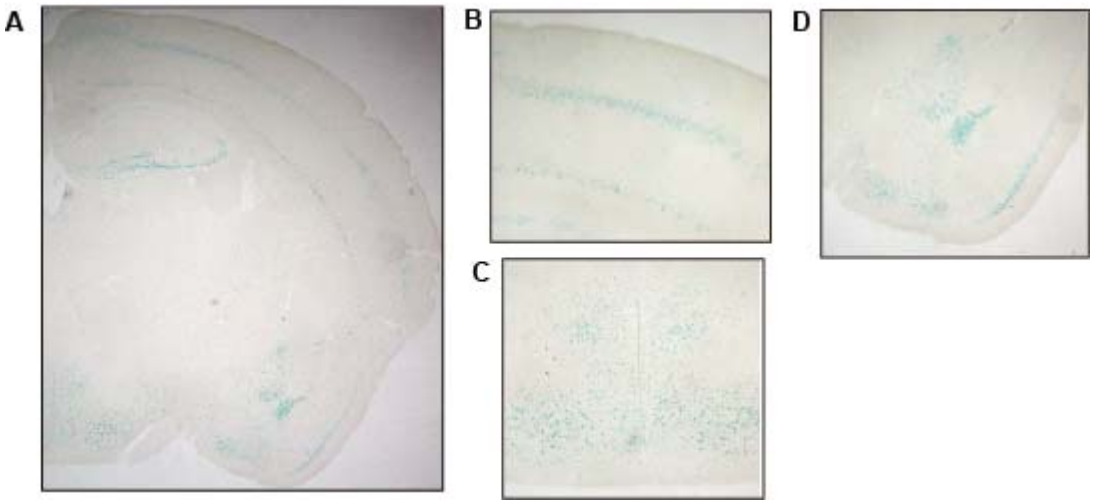

Supplementary Figure 2

Expression of β-galactosidase activity in forebrain (A), cortex (B), thalamus (C), and amygdale (D) of the Caprin-deficient mouse.

Supplementary Figure 3

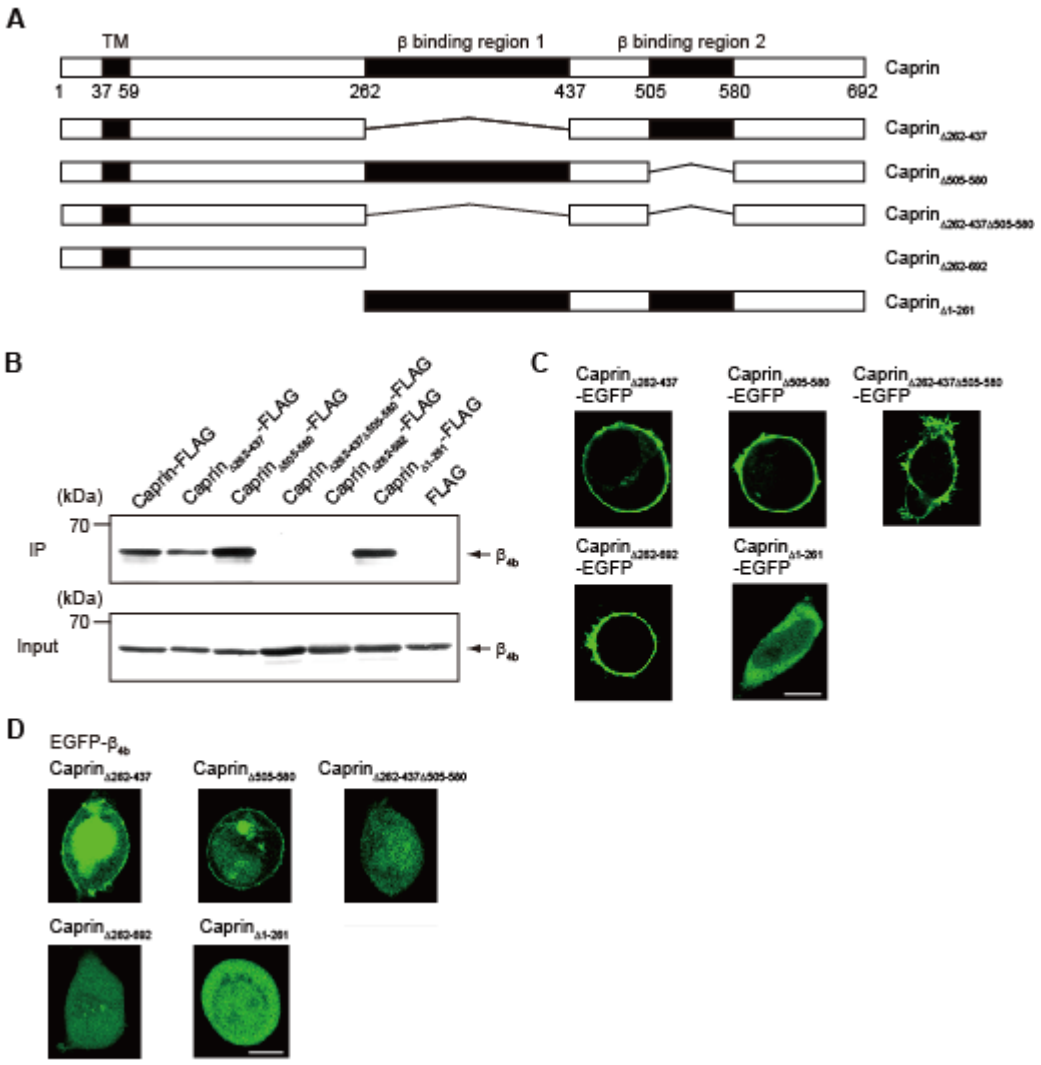

Supplementary Figure 3

A, recombinant constructs of Caprin mutants. B, interaction of recombinant β and Caprin in HEK293 cells. The interaction is evaluated by immunoprecipitation (IP) with antibody for FLAG, followed by WB with antibody for β_4. C, the confocal imaging of HEK293 cells expressing EGFP-fused Caprin constructs. Scale bar, 10 μm. D, the confocal imaging of the HEK293 cell expressing EGFP-β_{4b} with Caprin constructs.

Supplementary Figure 4

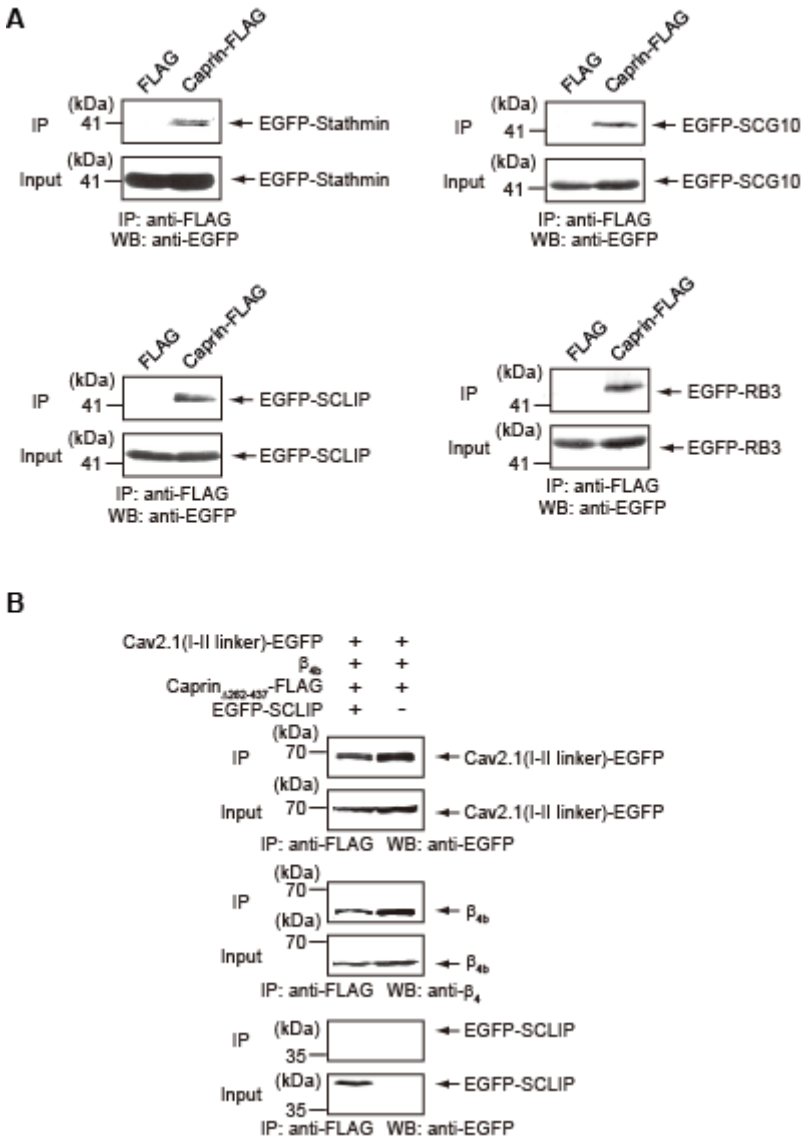

Supplementary Figure 4

A, interaction of recombinant Caprin with sthathmine family in HEK293 cells. The interaction is evaluated by IP with antibody for FLAG followed by WB with antibody for EGFP. B, immunoprecipitation assay of recombinant VDCC subunits and Caprin constructs with vector or SCLIP. The interaction is evaluated by IP with antibody for FLAG followed by WB with antibody for EGFP or β_4.

Chaptor 4

Two novel alleles of tottering with distinct $Ca_v2.1$ calcium channel neuropathologies

Abstract

The calcium channel *CACNA1A* gene encodes the pore-forming, voltage-sensitive subunit of the voltage-dependent calcium $Ca_v2.1$ type channel. Mutations in this gene have been linked to several human disorders, including familial hemiplegic migraine, episodic ataxia 2 and spinocerebellar ataxia type 6. The mouse homologue, *Cacna1a*, is associated with the tottering, $Cacna1a^{tg}$, mutant series. Here we describe two new missense mutant alleles, $Cacna1a^{tg\text{-}4J}$ and $Cacna1a^{Tg\text{-}5J}$. The $Cacna1a^{tg\text{-}4J}$ mutation is a valine to alanine mutation at amino acid 581, in segment S5 of domain II. The recessive $Cacna1a^{tg\text{-}4J}$ mutant exhibited the ataxia, paroxysmal dyskinesia and absence seizures reminiscent of the original tottering mouse. The $Cacna1a^{tg\text{-}4J}$ mutant also showed altered activation and inactivation kinetics of the $Ca_v2.1$ channel, not previously reported for other tottering alleles. The semi-dominant $Cacna1a^{Tg\text{-}5J}$ mutation changed a conserved arginine residue to glutamine at amino acid 1252 within segment S4 of domain III. The heterozygous mouse was ataxic and homozygotes rarely survived. The $Cacna1a^{Tg\text{-}5J}$ mutation caused a shift in both voltage activation and inactivation to lower voltages, showing that this arginine residue is critical for sensing $Ca_v2.1$ voltage changes. These two tottering mouse models illustrate how novel allelic variants can contribute to functional studies of the $Ca_v2.1$ calcium channel.

Introduction

Voltage-dependent calcium channels allow the entry of calcium ions into the cell when the membrane is depolarized, triggering multiple downstream events including synaptic vesicle activation, neuronal plasticity and gene transcription[1]. Electrophysiological and pharmacological studies have defined several types of calcium channels in neurons, including the $Ca_v2.1$ or P/Q-type channels. The major structural alpha subunit of this calcium channel includes the voltage-sensing and ion-gating functions encoded by the *CACNA1A* gene. The $Ca_v2.1$ channel predominantly functions in neurotransmitter release at central synapses[2-4] and neuromuscular junctions[5].

Mutations in the *CACNA1A* gene in humans have been associated with familial hemiplegic migraine with aura (FHM)[6,7], episodic ataxia type 2 (EA2)[8-10], spinocerebellar ataxia type 6 (SCA6)[11-14] and epilepsy[15,16]. SCA6 often arises from a triplet expansion in the glutamate repeat at the carboxy terminus, whereas the EA2 mutations range from missense, nonsense, splice site or deletion mutations[17,18]. Reduced or absent $Ca_v2.1$ channel activity is often associated with EA2 mutations[8,9,19]. FHM mutations arise from missense mutations; in *most* cases the $Ca_v2.1$ channels are activated at more hyperpolarized potentials[6,20,21] and sometimes a reduced density of calcium channels is observed[22,23]. From studies of the mouse mutations tottering (*Cacna1a*^{tg} or *tg*), leaner (*Cacna1a*$^{tg\text{-}la}$)[24] and a mouse strain carrying a human FHM mutation[25], the CACNA1A gene has also been implicated in cortical spreading depression (CSD). CSD is believed to underlie the aura symptoms associated with migraine.

The FHM and EA2 human mutations are inherited in a dominant manner. In contrast, the rodent models with mutations in the *Cacna1a* gene are predominantly recessive, with only one dominant mutation recently described in the wobbly mouse[26].

The tottering and leaner mutants were the first *Cacna1a* mouse mutants to be characterized. The tottering mouse is relatively mildly affected with ataxia, paroxysmal dyskinesia and absence seizures[27,28], whereas the leaner mouse is far more severe; the mice are runted with cell loss in the cerebellum and early death[29]. The two *Cacna1a* targeted mutations are phenotypically similar to the leaner mutation[30,31], and additional missense mutations, including rolling Nagoya[32] and rocker[33], all show the ataxia observed in the tottering mouse. A newly described ataxic model in rats, groggy, is also a recessive mutant[34].

We describe here the histology and neurophysiology of two new spontaneous mutations in the *Cacna1a* gene; the semi-dominant mutation in *Tg-5J* and a recessive mutation in the *tg-4J* allele. These two mutations illustrate how novel missense mutations can validate and further define functional regions within large ion channel subunits like the CACNA1A protein.

Results

Genetic analysis of two new spontaneous mouse mutants with ataxia

A spontaneous mouse mutant with an ataxic gait arose in the C3H/HeJ colony. The phenotype was recessive and, along with the associated dyskinesia, was reminiscent of the previously described tottering (*Cacna1a*^{tg}) mouse. A complementation cross to tottering mice confirmed that this mutant was a new allele of tottering and it was renamed *Cacna1a*$^{tg\text{-}4J}$ (referred to as *tg-4J* throughout this paper).

A second ataxic mouse mutant arose in the B10.M-H2^{f}/nMob Fmn1$^{ld\text{-}2J}$/J colony. The ataxia appeared to be inherited in a dominant fashion. To genetically map this mutation, affected mice from this strain were backcrossed to CAST/EiJ mice to produce the second backcrossed (N2) generation. Analysis of 124 N2 animals revealed tight linkage of the mutant locus to markers on Chromosome 8, including the *Cacna1a* locus. A complementation test between the heterozygous animals and heterozygous leaner (*Cacna1a*$^{+/tg\text{-}la}$) animals showed that the putative compound heterozygote animals is ataxic and had a tendency to lean to one side. This result indicated that this new mutation was indeed allelic with leaner. The new mutation is known as *Cacna1a*$^{Tg\text{-}5J}$ (referred to as *Tg-5J*).

Identification of the 2 missense mutations

From analysis of the RNA and DNA from the *tg-4J* mutant, a single nucleotide change distinguished *tg-4J* from the chromosome of origin (C3H/HeJ); a T-to-C transition at nucleotide residue 1742 (**Fig. 1**). This alteration predicts a conservative amino acid substitution, changing valine to alanine at position 581 (Val581Ala). This valine is located in the transmembrane region S5 in the second homologous domain (**Fig. 1**). Likewise, sequence analysis from the *Tg-5J* strain revealed a single nucleotide change

(G3755A) in domain III that encodes a charge-neutralizing amino acid substitution (Arg1252Gln) (**Fig. 1**). Importantly, the mutated arginine is one of the highly conserved positively charged amino acids located at every third position in the voltage-sensing region S4 in many ion-gating channels, including many voltage-dependent calcium channels as well as low voltage calcium and sodium channels as illustrated in Fig. 2. Interestingly, the only other dominant mouse mutation, wobbly, that has been reported also has a missense mutation in a nearby arginine residue, three amino acids downstream at position 1255, in the same S4 segment of domain III[26].

Behavior and viability of the new tottering mice

Both the homozygous *tg-4J* and heterozygous *Tg-5J* mutants displayed an ataxic gait, suggestive of cerebellar dysfunction. However the ataxia in *Tg-5J* was subtly different from the uncoordinated gait in tottering and *tg-4J* mice. Both of these mutants had an ataxic gait with pronounced high-stepping, waggling movements. In the heterozygous *Tg-5J* mutant, the hind limbs were splayed laterally from the body and the gait was noticeably shakier than tottering. Additionally, the paroxysmal dyskinesia phenotype was observed in the *tg-4J* homozygote but not the *Tg-5J* heterozygote mutants. The *Tg-5J* allele is semi-dominant as the heterozygous *Tg-5J* mice were less affected than the *Tg-5J* homozygotes.

In contrast to the recessive *tg-4J* homozygotes that had a normal lifespan and were able to breed, the *Tg-5J* homozygotes were runted, severely ataxic, and died before 6 weeks of age. This was particularly noticeable for the *Tg-5J* mutants on the B10 isogenic background where, in order to maintain the mutation, heterozygous (het) to wild-type matings were favored as most het by het matings produced no offspring. We also established crosses between the B10.*Tg-5J* and the BALB/cByJ inbred strain.

First generation hybrids routinely show increased vigor, and this proved to be true for the *Tg-5J* mutants. B6:BALB het by het *Tg-5J* matings successfully produced litters, but only 3% of the offspring could be confirmed as being homozygous for the *Tg-5J* mutation. These pups also did not survive beyond 6 weeks of age.

To maintain background uniformity, all the *tg-4J* results presented here came from mice on the B6 background and all the *Tg-5J* results were from the B10 background, with one exception for the green fluorescent protein studies.

Brain cytoarchitecture and cerebellar morphology appear grossly normal

Our initial pathology studies of the *tg-4J* homozygotes and *Tg-5J* heterozygote mice involved gross histological examination of the central nervous system, with serial sagittal sections through the whole brain. The cytoarchitecture of the mutant brains appeared normal at 2- 4 months of age. We further examined the hippocampus and the cerebral cortex in these mice by cresyl violet staining and Golgi impregnations. Both areas were indistinguishable from wild-type animals.

We investigated the cerebellum more closely to explain the ataxia observed in these mutants. We found a normal cerebellar morphology and cytoarchitecture in the *tg-4J* homozygotes, *Tg-5J* heterozygotes and even the *Tg-5J* homozygotes compared to wild type. Measurements of the molecular layer width and total area revealed no significant difference between affected and non-affected littermates. Particular attention was paid to the anterior vermis of the cerebellum where severe Purkinje cell loss has been noted in leaner mice[29]. Western analysis showed no reduction in the amount of CACNA1A protein in brains from either mutant (results not shown).

Calbindin staining and tyrosine hydroxylase expression reveal cerebellar defects

We examined cerebellar sections of *tg-4J* homozygotes, *Tg-5J* heterozygotes and littermate control animals. No reduction in the calbindin staining was observed in the cerebellums from *tg-4J* homozygote and *Tg-5J* heterozygote mice, and no gaps in the Purkinje cell layer were evident (**Fig. 3A, B, and C**). However we did observe axonal swellings in the Purkinje cells of the mutants, reminiscent of other tottering alleles (Fig. 3)[35,36].

Tyrosine hydroxylase (TH) is a key enzyme in the noradrenergic biosynthesis pathway. TH expression is normally expressed transiently in a subset of cerebellar Purkinje cells and is not detected after postnatal day 40. Previous studies of tottering, Wobbly and leaner mutant mice have shown persistent expression of TH[26,37]. We examined normal *tg-4J* homozygotes and *Tg-5J* heterozygotes at 3 months of age and observed expression of TH in both mutants (**Fig. 4C, D, E, and F**).

Aberrant branching of the Purkinje cells in the Tg-5J mutant

We further investigated the architecture of the Purkinje cells. To study the homozygous *Tg-5J* mutation, we intercrossed *Tg-5J* heterozygous mice (from the B10xBALB cross) with the B20 strain carrying a transgene expressing the green fluorescent protein (GFP) gene[38]. Confocal microscopy revealed that the GFP-stained Purkinje cells in the F2 homozygous mutant showed considerably less branching than the control littermate at the same age (**Fig. 5**). The primary branches had novel, GFP negatively-stained vacuoles that did not impede cytoplasmic flow as we detected GFP protein staining throughout the arbor (**Fig. 5B and C**). Vacuoles have previously been reported in the Purkinje cell bodies of SCA1 transgenic mice[39], but this is the first report of vacuoles in dendritic branches.

We turned to Golgi impregnation to evaluate both *tg-4J* homozygous and *Tg-5J*

heterozygous mice at over a year old. Previous studies of older rocker (*Cacna1a*^{rkr}) mutants revealed a process of Purkinje cell dendritic atrophy that resulted in a thinning of the dendritic mass with unusual terminal dendritic extensions[33]. These extensions often turned and grew back towards the Purkinje cell layer giving the dendritic arbor a weeping willow appearance. During normal aging, the controls in our study underwent a slight reduction in the branching complexity of the Purkinje cell dendritic arbor (**Fig. 6A and B**). By contrast, age-matched *Tg-5J* heterozygote animals displayed a Purkinje cell arbor that was significantly reduced in complexity and overall dendritic mass (**Fig. 6E and F**). In addition, we observed an abnormal serpentine-like appearance in the tips of the distal dendrites (**Fig. 6E arrow**). The shafts of main Purkinje dendrites also show a thickening in the upper molecular layer. In contrast, the *tg-4J* homozygote appeared to have a slight thickening of the secondary dendrites but no other histopathology (**Fig. 6C and D**).

Only *tg-4J* showed absence seizures

Another phenotype associated with tottering is absence seizures, observed as characteristic 5-7 Hz spike wave discharges in electroencephalographic (EEG) recordings. EEG studies revealed spike wave discharges, accompanied by behavioral arrest, in *tg-4J* homozygous mice, lasting up to 1.8 seconds in duration and occurring on average 4 times per hour (n = 9, total recording time 18.3 h). This is a less profound seizure phenotype than the original tottering mouse with seizures lasting as long as 10 seconds and recurring hundreds of times per day[27]. The *tg-4J* mutant seizures were abolished by treatment with the anti-epileptic drug, ethosuximide. We were unable to test *Tg-5J* homozygotes because of their early lethality, but the *Tg-5J* heterozygous animals showed no spike wave discharge activity (n = 4).

Calcium channel electrophysiology is altered in both mutations

To determine the functional impact of the mutations on calcium channel activity we initially analyzed recombinant protein transiently expressed in BHK cells. We introduced the T1742C (*tg-4J*) and G3755A (*Tg-5J*) mutations at the corresponding sites of the rabbit *CACNA1A* cDNA[40]. The control wild-type and mutant cDNAs were inserted in the pK4K plasmid[41] and were transiently expressed in the BHK6 cells, which stably express the CACNA2D and CACNB1b subunits[42]. When membrane potential was stepped from a holding potential (V_h) of –100 mV to a test pulse of 0 or 10 mV the average peak current densities for the *Tg-5J* and *tg-4J* channels were not significantly different from the wild-type channel in a solution containing 3 mM Ba^{2+} (**Fig.7A**). Current-voltage (I–V) relationships for the wild-type and mutant Ba^{2+} currents indicated that the wild-type and mutant channels were activated by step depolarization above -50 mV (*Tg-5J*) or –40 mV (*tg-4J*, wt) from a V_h of –100 mV (**Fig. 7A**). The current amplitude increased with increments of depolarization, reaching peaks in the I–V relationships around 0 (*tg-4J*, wt) and -10 mV (*Tg-5J*) (**Fig. 7B**). Current amplitudes and densities were not significantly different among wild-type and mutant channels (**Fig. 7C**) and the capacitance-current relationships were directly proportional.

The activation curves, obtained by fitting peak of tail currents at the fixed potential of –60 mV after 5 msec step depolarization from –50 to 35 mV with 5 mV increments with a single Boltzmann function, showed different voltage dependences between the wild type and mutant channels (**Fig. 8A and B**). Specifically, the midpoint of the activation was –27.3 ± 0.6 mV for *Tg-5J* (n = 7, $p = 4.83^{-7}$ v. wt), –14.5 ± 1.0 mV for wt (n = 5) and – 7.0 ± 1.6 mV for *tg-4J* (n = 6, $p = 0.0051$ v. wt) (**Table 1**). Furthermore, the slope factor (k) was significantly different for 4J: 7.7 ± 0.4 mV for

tg-4J and 5.1 ± 0.5 mV for wt (P = 0.0016). Activation time constants were obtained from single-exponential fits of the activation phase during 5 msec depolarizing steps (**Fig. 8B**). *tg-4J* channels showed significantly different τ_a at –25 and –20 mV. Thus, *Tg-5J* has a significant hyperpolarizing shift in voltage dependence indicating that these channels required weaker depolarization for activation compared to the control (**Table 1**). In contrast, in the *tg-4J* Ca^{2+} channel the activation curve was significantly shifted to depolarizing direction and showed reduction of slope (**Fig. 8A and Table 1**). Furthermore, the *tg-4J* channel showed accelerated activation speed, unlike the *Tg-5J* channel whose kinetic properties were similar to those of wild-type channel (**Fig. 8B**).

The voltage dependence of inactivation was determined by the use of 2 sec prepulses to a series of different potentials (–120 to 10 mV), followed by a 20 msec test pulse to 0 (*tg-4J*, wt) or –10 mV (*Tg-5J*). Test current amplitudes were normalized to the peak current amplitude induced by the test pulse of –120 mV and were plotted against the prepulse potentials (**Fig. 9A**). The inactivation potential midpoint and the slope factor of the inactivation curves fitted by a Boltzmann equation were –63.1 ± 1.9 mV and 6.3 ± 0.6 mV (n = 6) for wt, –79 ± 1.8 mV (n = 5, P = 0.00017) and 8.6 ± 0.6 mV (P = 0.026) for *Tg-5J* and –61 ± 2.9 mV and 7.7 ± 0.3 mV (n = 5) for *tg-4J* (**Fig. 9A**). The *Tg-5J* channels required weaker depolarization for inactivation, but the *tg-4J* inactivation curve was indistinguishable from the control (**Table 1**).

The mean inactivation time currents, τ_{fast} and τ_{slow}, were derived by fitting a sum of two exponential functions to the current decay and were plotted as a function of test potentials from –20 to 0 mV (**Fig. 9B**). *tg-4J* showed significantly different τ_{fast} at –20 and –10 mV. The fraction of current for each component (fast, slow, and sustained) was plotted as a function of the test potential (for –20 to –10 mV) (**Fig. 9C**). Overall, the *tg-4J* channel significantly differed from control in inactivation kinetics: the

fast component of current decay showed increased fraction but reduced speed in the *tg-4J* channel (**Fig. 9B and C**).

In previous studies it has been suggested that results from transfected BHK cells may be unreliable due to the aberrant expression of the transgene[25] and the reconstruction of calcium channel activity with regulatory subunits that may not reflect the *in vivo* situation. To address these concerns, we investigated $Ca_v2.1$ recordings from dissociated Purkinje cells from the mutants and wild-type mice (**Fig. 10, and Table 1**). Unfortunately we were unable to include the *Tg-5J*/ *Tg-5J* homozygotes in this analysis because of their poor viability.

There is a shift of both the $Ca_v2.1$ *Tg-5J*/+ and *tg-4J /tg-4J* activation curves (**Fig. 10D, and Table 1**). From the inactivation curve, the *Tg-5J* heterozygote also shows a shift to lower voltages (**Fig. 10E**). Both of these shifts are significantly less pronounced in the Purkinje cells from the Tg-5J/+ heterozygotes compared to the BHK results (**Table 1**). This is expected as the BHK cells have only the *Tg-5J* mutant form of the CACNA1A protein, whereas the Purkinje cells are derived from the *Tg-5J* heterozygous mice that retain one normal copy of the *Cacna1a* gene.

Noticeably both the current amplitude and capacitance are reduced in the *tg-4J /tg-4J* homozygote Purkinje cells (**Fig. 10C**). These differences are attributable to the smaller size of the *tg-4J /tg-4J* Purkinje neuron cell bodies compared to the controls, indicating that the *tg-4J* mutation disrupts not only the function of the $Ca_v2.1$ channels but also the cellular development of Purkinje cells. Similar results were observed in the tottering rolling Nagoya allele[32]. However in contrast to rolling Nagoya, the current density for the *tg-4J* homozygote was not reduced in either the Purkinje or BHK cells (**Fig. 7, and 10**).

Discussion

These two new spontaneous alleles of tottering reveal an intriguing contrast between the underlying mutations and the phenotypic expression. The *Tg-5J* mutation is due to the loss of a highly conserved arginine residue in a critical voltage-sensing region, with predictably severe consequences. The mutation is semi-dominant, resembling the many human mutations on the CACNA1A gene and the wobbly mouse mutation, with accompanying changes in both the activation and inactivation kinetics of the $Ca_v2.1$ channel. In contrast the *tg-4J* mutation is a relatively benign valine to alanine change in the transmembrane S5 region of domain II; one that would not have been predicted to result in a phenotype as pronounced as the previously described recessive tottering alleles.

The *tg-4J* mutation is phenotypically very similar to the original tottering mutation, with ataxia, paroxsymal dyskinesia and absence seizures. The mutant also showed continued tyrosine hydroxylase expression and Purkinje cell axon swelling. Many of the tottering alleles, including *tg-4J*, are recessive as the heterozygous mice are overtly normal. In contrast, the *Tg-5J* allele is semi-dominant with an ataxic gait, but lacking the dyskinesia and absence seizures of the other tottering alleles. Although the *Tg-5J* homozygote rarely survived to 6 weeks of age, we were able to observe a significant reduction in Purkinje cell dendritic branching in these mice on a mixed genetic background. Persistent tyrosine hydroxylase activity, Purkinje cell axon swelling and branching defects were also observed in the more robust *Tg-5J* heterozygote.

The *Tg-5J* mutation changes a highly conserved arginine residue in S4 of domain III to a glutamine. The arginine is one of 3 in a repeated triplet motif, found not only in the voltage-sensor paddle of calcium channels but also sodium and potassium

ion-gated channels[43]. Missense mutations that replace the arginine residues have been shown to alter calcium channel function; illustrated by two studies of FHM mutations, one involving the arginine to glutamine mutation in domain I (R192Q) and the second, the R583Q missense mutation in domain II of the *CACNA1A* gene. The R192Q mutation was first reported to cause an increase in calcium current density[22], whereas the R583Q mutation showed a shift to more negative potentials for both calcium channel activation and inactivation[18]. The R192Q mutation was further studied in a Knock-in mouse strain expressing this human mutation in place of the normal *Cacna1a* mouse gene[25]. Unlike the many tottering alleles including *tg-4J* and *Tg-5J*, the Knock-in mouse had a normal gait[44]. This strain also showed increased susceptibility to cortical spreading depression (CSD), associated with the neurological aura symptoms of migraines. A shift in the calcium channel activation to lower voltages was observed with this mutant that would predictably lead to an increased action potential-evoked calcium influx and increased glutamate release, triggering the CSD response[25].

The hyperpolarizing shifts observed in the R192Q and R583Q mutations mirrored our *Tg-5J* results of a negative shift in the calcium channel activation curve. Furthermore we found that *Tg-5J* also had a more hyperpolarized inactivation response. From these results we conclude that this mutation represents a dominant gain-of-function, and we predict that *Tg-5J* will show enhanced $Ca_v2.1$ channel activity and increased intracellular calcium concentration in response to depolarizing potentials. However, this enhancement may occur only when the membrane is depolarized from sufficiently hyperpolarized resting potential, since the voltage dependence of inactivation is also shifted to hyperpolarizing potentials by the *Tg-5J* mutation.

The *tg-4J* mutation shifted the voltage dependence of activation of $Ca_v2.1$ channels toward more depolarized potentials, which may lead to loss of calcium channel

activity. A similar depolarizing shift is reported for $Ca_v2.1$ channels in leaner[42] and rolling Nagoya mouse neurons[32]. However, the changes in *tg-4J* activation and inactivation kinetics appear to be unique to this particular tottering mutation. Finally, there was no profound change in the calcium current density in *tg-4J* or *Tg-5J*, unlike many of the mouse tottering mutations, including leaner[45,46] rolling Nagoya[32] and the two targeted alleles[30,31].

The voltage activation changes for the *tg-4J* homozygote from both the BHK transfected cells and the dissociated Purkinje cells show that both approaches can yield comparable results. Although we saw a similar trend in the *Tg-5J* heterozygote results, we were unable to complete this analysis by looking at the *Tg-5J* homozygotes because of their poor viability on the B10 background. Future studies using more robust homozygotes from the B10;BALB cross can potentially confirm the BHK results, hopefully without introducing confounding problems arising from the modified strain background. These two new tottering mouse models with altered calcium channel electrophysiology provide further opportunities to understand how perturbations in the $Ca_v2.1$ calcium channel regulate neuronal excitation and its underlying association with the human disorders.

Method

Identification of the spontaneous ataxic strains

The *Cacna1a*$^{tg\text{-}4J}$ mutant was first detected in the C3H/HeJ colony of Dr. Edward Birkenmeier at The Jackson Laboratory in 1996. It is now maintained as a congenic B6.C3H-*Cacna1a*$^{tg\text{-}4J}$ (*tg-4J*) strain. The *Cacna1a*$^{Tg\text{-}5J}$ (*Tg-5J*) strain arose in the B10.M-*H2*^{f}/nMob *Fmn1*$^{ld\text{-}2J}$/J strain in 1995 and is now on the C57BL/10 (B10) background and on a mixed background between B10 and BALB/cByJ. All animals are housed at The Jackson Laboratory (Bar Harbor, ME), regulated by the Animal Care and Use Committee. The mice were provided a commercial diet and water *ad libitum* under conventional conditions with controlled temperature, humidity, and lighting.

cDNA cloning and sequence analysis

cDNAs encoding the CACNA1A subunit were isolated by reverse transcriptase-polymerase chain reaction methods (RT-PCR) using the random primer DNA labeling system (Life Technologies, Grand Island, NY) and total RNA isolated from mouse brain. PCR primers were designed according to the published sequence data[28] such that the entire 6495 bp sequence was covered. RT-PCR products were subcloned using the TOPO TA Cloning Kit (Life Technologies, Grand Island, NY), and sequenced using an automated sequencer (ABI prism model 377; Applied Biosystems, Foster City, CA). Sequence information was obtained separately from four mutants and three background control mice for each allele studied. The results were confirmed by genomic DNA sequencing.

Immunohistochemistry

Animals were deeply anesthetized with tribromoethanol and transcardially perfused

with 4% paraformaldehyde in 0.1M phosphate buffer (pH 7.5). The brains were immediately removed from the cranium and fixed for an additional 4 hr at 4°C. The brains were then cryoprotected in 18% (w/v) sucrose in PBS at 4°C overnight. Samples were embedded in OCT, 10 micron cryostat sections were cut and allowed to air dry on gelatin coated slides.

Tissue were processed for immunohistochemistry with the anti-tyrosine hydroxylase and calbindin antibodies, as previously described[33]. To evaluate the immunostaining between animals, digital images were captured at defined exposure times.

Green Fluorescent protein (GFP) labeling of Purkinje cells

Tg-5J heterozygous mice from the mixed B10;BALB background were intercrossed to a B6 mouse strain carrying a transgene with the parvalbumin promoter fused to the green fluorescent protein (GFP) gene (strain # B20)[38]. Brains from F2 homozygous *Tg-5J* and controls were dissected at 24 days of age for fixation in Z-fix buffer (Anatech, MI) for 3-4 hours. Vibrotome sagittal sections (60-100um) were mounted onto slides with Clear-mount (Zymed, CA). The sections were viewed using a Leica SP5 AOBS spectral confocal microscope, with a 63X, 1.3 NA glycerol immersion objective. Excitation was at 488nm, with emission collection optimized for green fluorescence detection.

Golgi-Cox

Mutant and control animals were euthanized by carbon dioxide asphyxiation and their brains removed and immersed in fixative (10 mg/ml potassium dichromate, 10 mg/ml mercuric chloride, and 4.5 mg/ml potassium chromate; any precipitate was cleared by

acidification with 0.1N HCl). The brains were stored in the dark undisturbed for 6-8 weeks before dehydration, infiltration with low viscosity nitrocellulose celloidin/parlodion (Fisher, PA) and hardened with chloroform vapors[33]. The blocks were sectioned and mounted onto slides as previously described[33].

Electrocorticographic Recordings

Silver wire electrodes (0.125 mm diameter) soldered to a microminiature connector were implanted bilaterally into the subdural space over frontal and parietal cortex of anesthetized mice several days prior to recording[27]. Cortical activity was recorded from mutants and controls moving freely in the test cage for prolonged periods. Ethosuximide (Sigma, MO), an inhibitor of absence seizure activity, was injected (150 mg/kg, i.p.) to confirm that the seizure activity was suppressed.

Construction of expression plasmids encoding Ca2+ channel CACNA1A subunit with Tg-5J or tg-4J mutations

For construction of expression cDNA encoding the *Tg-5J -CACNA1A* (BI-2**)** subunit mutant, a PCR fragment was amplified using pSPCBI-2[40] as a template, a primer BIPMI(+) (5'-ACCACACCGTGGTCCAAGTGAACAAAAATG-3') (sense) and a primer 5J(-) (5'-GTAGCACCTGGAGCACTCGGAGGGATTTG-3') (antisense). A PCR fragment amplified using pSPCBI-2, and a primer 5J(+)(5'-CAAATCCCTCCGAGTGCTCCAGGGTGCTAC-3') (sense) and a primer BIAcI(-)(5'-GAAGTAGACCACGTAGAAGATGGACATCTC-5') (antisense), were combined with the primers BIPMI(+) and BIAcI(-) in the subsequent PCR. The PCR product was digested with *Pfl*MI and *Acc*I, and the yielded mouse fragment was substituted for the corresponding *Pfl*MI (3574)/*Acc*I (4506) sequence of the rabbit

CACNA1A (BI-2) cDNA in the recombinant plasmid pK4KBI-2[41] to obtain pK4KBI-*Tg-5J*.

The construction of expression cDNA encoding the *tg-4J -CACNA1A* (BI-2) subunit mutant started with the PCR fragment amplified using pSPCBI-2 as a template, a primer BIXhI(+) (5'-GTGCCAAGCTGGAGAACTCGAGTTTTTTCC-3')(sense) and a primer 4J(-) (5'-CCCCAGAAGTGCAAAGGCAACGATAAACAG-3')(antisense). A PCR fragment amplified using pSPCBI-2, and a primer 4J(+) (5'-CTGTTTATCGTTGCCTTTGCACTTCTGGGG-3') (sense) and a primer BIHnIII(-) (5'-CTTCTGCAGGGCAAGCTTTTGATTGACGGC-5') (antisense), were combined with the primers BIXhI(+) and BIHnIII(-) in the subsequent PCR. The PCR product was digested with *Xho*I and *Hin*dIII, and the yielded mouse fragment was substituted for the corresponding *Xho*I (1396)/ *Hin*dIII (2210) sequence of the rabbit *CACNA1A* (BI-2) cDNA in the recombinant plasmid pK4KBI-2[41] to obtain pK4KBI-tg-4J .

Expression of recombinant CACNA1A $Ca2^+$ channels with Tg-5J or tg-4J mutations in BHK cells

BHK cells were transfected with the pAGS-3 recombinant plasmid pAGS-3a2[47] and pCABE[41] using the CaPO4 protocol[48], and were cultured in Dulbecco's modified Eagle medium (DMEM) containing G-418 (600 μg/ml) (Gibco BRL, Gaithersberg, MD), to first establish a BHK line, BHK6, with stable expression of the CACNB1b and CACNA2D subunits. To transiently express the wild-type CACNA1A channel, the *Tg-5J* mutant CACNA1A channel or the *tg-4J* mutant CACNA1A channel, BHK6 cells were transfected with the recombinant plasmid pK4KBI-2, pK4KBI-*Tg-5J* or pK4KBI-

tg-4J, plus pH3-CD8 containing the cDNA of the T-cell antigen CD8[49]. Transfection was carried out using Effectene Transfection Reagent (QIAGEN, Hilden, Germany). Cells were trypsinized, diluted with Dulbecco's modified Eagle's medium (DMEM) containing10% fetal bovine serum (FBS), 30 units/ml penicillin, and 30 μg/ml streptomycin, and plated onto culture dishes (Primaria #3801, Nippon Becton Dickinson, Tokyo, Japan) 18 h after transfection. Then cells were subjected to measurements 48-66 h after the plating. Cells expressing $Ca_v2.1$ channels were selected through detection of CD8 coexpression using polystyrene microspheres precoated with antibody to CD8 (Dynabeads M-450 CD8;DYNAL, Oslo, Norway).

Preparation of dissociated Purkinje cells

Purkinje cells were freshly dissociated from 14- to 26-day old mice. The procedure for obtaining dissociated cells from mice is similar to that described elsewhere[50]. Coronal slices (350-μm-thick) of cerebellum were prepared using a microslicer (Leica, Nussloch, Germany; VT-1000S). After preincubation in Krebs' solution for 46 min at 31 C, the slices were digested: first in Krebs' solution containing 0.025% pronase (Calbiochem-Nocabiochem, La Jolla, CA) for 23 min at 31 C and then in solution containing 0.025% thermolysin (type X; Sigma, MO) for 23 min at 31 C. The Krebs' solution used for preincubation and digestion contained the following (in mM): 124 NaCl, 5 KCl, 1.2 KH_2PO_4, 2.4 $CaCl_2$, 1.3 $MgSO_4$, 26 $NaHCO_3$, and 10 glucose. The solution was continuously oxygenated with 95% O_2 and 5% CO_2. Then the brain slices were punched out and dissociated mechanically by the use of fine glass pipettes having a tip diameter of 100-200 μm. Dissociated cells settled on tissue culture dishes (Primaria #3801; Nippon Becton Dickinson, Tokyo, Japan) within 30 min. Purkinje cells were identified by their large diameter and characteristic pear shape because of the

stump of the apical dendrite. To make a sufficient space-clamp of the Purkinje cell body, Purkinje cells lacking most of dendrites were used throughout the present experiments.

Whole-cell recordings

Electrophysiological measurements were performed on BHK and Purkinje cells. Currents were recorded at room temperature (22 - 25 °C) using whole-cell mode of the patch-clamp technique[51] with an EPC-9 patch-clamp amplifier (HEKA, Darmstadt, Germany). Patch pipettes were made from borosilicate glass capillaries (1.5mm outer diameter; Hilgenberg, Malsfeld, Germany) using a model P-87 Flaming-Brown micropipette puller (Sutter Instrument Co., San Rafael, CA). The patch electrodes were fire-polished. Pipette resistance ranged from 2 to 4 MOhm when filled with the pipette solutions described below. The series resistance was electronically compensated to >50 % and both the leakage and the remaining capacitance were subtracted by –P/4 method. Currents were sampled at 100 kHz after low pass filtering at 8.4 kHz in the experiments of activation kinetics, otherwise sampled at 20 kHz after low pass filtering at 2.9 kHz. Stimulation and data acquisition were performed using the PULSE program (version 7.5, HEKA Elektronik, Lambrecht, Germany). Ba^{2+} currents were recorded in an external solution that contained (in mM): 3 $BaCl_2$, 155 tetraethylammonium chloride (TEA-Cl), 10 HEPES, 10 glucose (pH adjusted to 7.4 with TEA-OH). The pipette solution contained (in mM): 85 Cs-aspartate, 40 CsCl, 2 $MgCl_2$, 5 EGTA, 2 ATPMg, 5 HEPES, 10 creatine-phosphate (pH adjusted to 7.2 with CsOH).

Statistical comparison between normal and mutant channels was performed by Student's t test (*, $P < 0.05$; **, $P < 0.01$; ***, $P < 0.001$).

References

1. Catterall WA. Structure and regulation of voltage-gated Ca2+ channels. *Annu. Rev. Cell Dev. Biol.* **16**, 521-555 (2000).

2. Wheeler DB, Randall A, Tsien RW. Roles of N-type and Q-type Ca2+ channels in supporting hippocampal synaptic transmission. *Science* **264**, 107-111 (1994).

3. Wu LG, Westenbroek RE, Borst JG, Catterall WA, Sakmann B. Calcium channel types with distinct presynaptic localization couple differentially to transmitter release in single calyx-type synapses. *J Neurosci* **19**, 726-736 (1999).

4. Qian J, Noebels JL. Presynaptic Ca(2+) influx at a mouse central synapse with Ca(2+) channel subunit mutations. *J. Neurosci.* **20**, 163-170 (2000).

5. Uchitel OD, Protti DA, Sanchez V, Cherksey BD, Sugimori M, Llinás R. P-type voltage-dependent calcium channel mediates presynaptic calcium influx and transmitter release in mammalian synapses. *Proc. Natl. Acad. Sci. USA* **89**, 3330-3333 (1992).

6. Pietrobon D, Striessnig J. Neurobiology of migraine. *Nat. Rev. Neurosci.* **4**, 386-398 (2003).

7. Alonso I, Barros J, Tuna A, Seixas A, Coutinho P, Sequeiros J, Silveira I. A novel R1347Q mutation in the predicted voltage sensor segment of the P/Q-type calcium-channel alpha-subunit in a family with progressive cerebellar ataxia and hemiplegic migraine. *Clin. Genet.* **65**, 70-72 (2004).

8. Guida S, Trettel F, Pagnutti S, Mantuano E, Tottene A, Veneziano L, Fellin T, Spadaro M, Stauderman K, Williams M, Volsen S, Ophoff R, Frants R, Jodice C, Frontali M, Pietrobon D. Complete loss of P/Q calcium channel activity caused by a CACNA1A missense mutation carried by patients with episodic ataxia type 2. Am. J. Hum. Genet. **68**, 759-764 (2001).

9. Spacey SD, Hildebrand ME, Materek LA, Bird TD, Snutch TP. Functional implications of a novel EA2 mutation in the P/Q-type calcium channel. *Ann. Neurol.* **56**, 213-220 (2004).

10. Cricchi F, Di Lorenzo C, Grieco GS, Rengo C, Cardinale A, Racaniello M, Santorelli FM, Nappi G, Pierelli F, Casali C. Early-onset progressive ataxia associated with the first CACNA1A mutation identified within the I-II loop. *J. Neurol. Sci.* **254**, 69-71 (2007).

11. Zhuchenko O, Bailey J, Bonnen P, Ashizawa T, Stockton DW, Amos C, Dobyns WB, Subramony SH, Zoghbi HY, Lee CC. Autosomal dominant cerebellar ataxia (SCA6) associated with small polyglutamine expansions in the α_{1A}-voltage-dependent calcium channel. *Nat. Genet.* **15**, 62-69 (1997).

12. Shimazaki H, Takiyama Y, Sakoe K, Amaike M, Nagaki H, Namekawa M, Sasaki H, Nakano I, Nishizawa M. Meiotic instability of the CAG repeats in the SCA6/CACNA1A gene in two Japanese SCA6 families. *J. Neurol. Sci.* **185**, 101-107 (2001).

13. Pulst SM, Santos N, Wang D, Yang H, Huynh D, Velazquez L, Figueroa KP. Spinocerebellar ataxia type 2: polyQ repeat variation in the CACNA1A calcium channel modifies age of onset. *Brain* **128**, 2297-2303 (2005).

14. Lindquist SG, Norremolle A, Hjermind LE, Hasholt L, Nielsen JE. Meiotic CAG repeat instability in spinocerebellar ataxia type 6: maternally transmitted elongation in a presumed sporadic case. *J. Neurol. Sci.* **241**, 95-98 (2006).

15. Jouvenceau A, Eunson LH, Spauschus A, Ramesh V, Zuberi SM, Kullmann DM, Hanna MG. Human epilepsy associated with dysfunction of the brain P/Q-type calcium channel. *Lancet* **358**, 801-807 (2001).

16. Beauvais K, Cave-Riant F, De Barace C, Tardieu M, Tournier-Lasserve E, Furby A.

New CACNA1A gene mutation in a case of familial hemiplegic migraine with status epilepticus. *Eur. Neurol.* **52**, 58-61 (2004).

17. Ophoff RA, Terwindt GM, Vergouwe MN, van Eijk R, Oefner PJ, Hoffman SMG, Lamerdin JE, Mohrenweiser HW, Bulman DE, Ferrari M, Haan J, Lindhout D, B. vOG-J, Hofker MH, Ferrari MD, Frants RR. Familial hemiplegic migraine and episodic ataxia type-2 are caused by mutations in the Ca^{2+} channel gene CACNL1A4. *Cell* **87**, 543-552 (1996).
18. Kraus RL, Sinnegger MJ, Koschak A, Glossmann H, Stenirri S, Carrera P, Striessnig J Three new familial hemiplegic migraine mutants affect P/Q-type Ca(2+) channel kinetics. *J. Biol. Chem.* **275**, 9239-9243 (2000).
19. Jeng CJ, Sun MC, Chen YW, Tang CY. Dominant-negative effects of episodic ataxia type 2 mutations involve disruption of membrane trafficking of human P/Q-type Ca2+ channels. *J. Cell Physiol.* **214**, 422-433 (2008).
20. Tottene A, Fellin T, Pagnutti S, Luvisetto S, Striessnig J, Fletcher C, Pietrobon D. Familial hemiplegic migraine mutations increase Ca(2+) influx through single human CaV2.1 channels and decrease maximal CaV2.1 current density in neurons. *Proc. Natl. Acad. Sci. U S A* **99**, 13284-13289 (2002).
21. Mullner C, Broos LA, van den Maagdenberg AM, Striessnig J. Familial hemiplegic migraine type 1 mutations K1336E, W1684R, and V1696I alter Cav2.1 Ca2+ channel gating: evidence for beta-subunit isoform-specific effects. *J. Biol. Chem.* **279**, 51844-51850 (2004).
22. Hans M, Luvisetto S, Williams ME, Spagnolo M, Urrutia A, Tottene A, Brust PF, Johnson EC, Harpold MM, Stauderman KA, Pietrobon D. Functional consequences of mutations in the human alpha1A calcium channel subunit linked to familial hemiplegic migraine. *J. Neurosci.* **19**, 1610-1619 (1999).

23. Barrett CF, Cao YQ, Tsien RW. Gating deficiency in a familial hemiplegic migraine type 1 mutant P/Q-type calcium channel. *J. Biol. Chem.* **280**, 24064-24071 (2005).

24. Ayata C, Shimizu-Sasamata M, Lo EH, Noebels JL, Moskowitz MA. Impaired neurotransmitter release and elevated threshold for cortical spreading depression in mice with mutations in the alpha1A subunit of P/Q type calcium channels. *Neuroscience* **95**, 639-645 (2000).

25. van den Maagdenberg AM, Pietrobon D, Pizzorusso T, Kaja S, Broos LA, Cesetti T, van de Ven RC, Tottene A, van der Kaa J, Plomp JJ, Frants RR, Ferrari MD. A Cacna1a knockin migraine mouse model with increased susceptibility to cortical spreading depression. *Neuron* **41**, 701-710 (2004).

26. Xie G, Clapcote SJ, Nieman BJ, Tallerico T, Huang Y, Vukobradovic I, Cordes SP, Osborne LR, Rossant J, Sled JG, Henderson JT, Roder JC. Forward genetic screen of mouse reveals dominant missense mutation in the P/Q-type voltage-dependent calcium channel, CACNA1A. *Genes Brain Behav.* **6**, 717-727 (2007).

27. Noebels JL, Sidman RL. Inherited epilepsy: spike-wave and focal motor seizures in the mutant mouse tottering. *Science* **204**, 1334-1336 (1979).

28. Fletcher CF, Lutz CM, O'Sullivan TN, Shaughnessy JD, Hawkes R, Frankel WN, Copeland NG, Jenkins NA. Absence epilepsy in tottering mutant mice is associated with calcuim channel defects. *Cell* **87**, 607-617 (1996).

29. Herrup K, Wilczynski SL Cerebellar cell degeneration in the leaner mutant mouse. *Neuroscience* **7**, 2185-2196 (1982).

30. Jun K, Piedras-Renteria ES, Smith SM, Wheeler DB, Lee SB, Lee TG, Chin H, Adams ME, Scheller RH, Tsien RW, Shin HS Ablation of P/Q-type Ca(2+) channel currents, altered synaptic transmission, and progressive ataxia in mice lacking the alpha(1A)-subunit. *Proc. Natl. Acad. Sci. U S A* **96**, 15245-15250 (1999).

31. Fletcher CF, Tottene A, Lennon VA, Wilson SM, Dubel SJ, Paylor R, Hosford DA, Tessarollo L, McEnery MW, Pietrobon D, Copeland NG, Jenkins NA. Dystonia and cerebellar atrophy in Cacna1a null mice lacking P/Q calcium channel activity. *FASEB J.* **15**, 1288-1290 (2001).

32. Mori Y, Wakamori M, Oda S, Fletcher CF, Sekiguchi N, Mori E, Copeland NG, Jenkins NA, Matsushita K, Matsuyama Z, Imoto K. Reduced voltage sensitivity of activation of P/Q-type Ca2+ channels is associated with the ataxic mouse mutation rolling Nagoya (tg(rol)). *J. Neurosci.* **20**, 5654-5662 (2000).

33. Zwingman TA, Neumann PE, Noebels JL, Herrup K. Rocker is a new variant of the voltage-dependent calcium channel gene Cacna1a. *J. Neurosci.* **21**, 1169-1178 (2001).

34. Tokuda S, Kuramoto T, Tanaka K, Kaneko S, Takeuchi IK, Sasa M, Serikawa T. The ataxic groggy rat has a missense mutation in the P/Q-type voltage-gated Ca2+ channel alpha1A subunit gene and exhibits absence seizures. *Brain Res.* **1133**, 168-177 (2007).

35. Rhyu IJ, Abbott LC, Walker DB, Sotelo C. An ultrastructural study of granule cell/Purkinje cell synapses in tottering (tg/tg), leaner (tg(la)/tg(la)) and compound heterozygous tottering/leaner (tg/tg(la)) mice. *Neuroscience* **90**, 717-728 (1999).

36. Rhyu IJ, Oda S, Uhm CS, Kim H, Suh YS, Abbott LC. Morphologic investigation of rolling mouse Nagoya (tg(rol)/tg(rol)) cerebellar Purkinje cells: an ataxic mutant, revisited. *Neurosci. Lett.* **266**, 49-52 (1999).

37. Austin MC, Schultzberg M, Abbott LC, Montpied P, Evers JR, Paul SM, Crawley JN. Expression of tyrosine hydroxylase in cerebellar Purkinje neurons of the mutant tottering and leaner mouse. *Brain Res. Mol. Brain Res.* **15**, 227-240 (1992).

38. Chattopadhyaya B, Di Cristo G, Higashiyama H, Knott GW, Kuhlman SJ, Welker E,

Huang ZJ. Experience and activity-dependent maturation of perisomatic GABAergic innervation in primary visual cortex during a postnatal critical period. *J. Neurosci.* **24**, 9598-9611 (2004).

39. Clark HB, Burright EN, Yunis WS, Larson S, Wilcox C, Hartman B, Matilla A, Zoghbi HY, Orr HT. Purkinje cell expression of a mutant allele of SCA1 in transgenic mice leads to disparate effects on motor behaviors, followed by a progressive cerebellar dysfunction and histological alterations. *J. Neurosci.* 17, 7385-7395 (1997).
40. Mori Y, Friedrich T, Kim MS, Mikami A, Nakai J, Ruth P, Bosse E, Hofmann F, Flockerzi V, Furuichi T, et al. Primary structure and functional expression from complementary DNA of a brain calcium channel. *Nature* **350**, 398-402 (1991).
41. Niidome T, Teramoto T, Murata Y, Tanaka I, Seto T, Sawada K, Mori Y, Katayama K. Stable expression of the neuronal BI (class A) calcium channel in baby hamster kidney cells. *Biochem. Biophys. Res. Commun.* **203**, 1821-1827 (1994).
42. Wakamori M, Yamazaki K, Matsunodaira H, Teramoto T, Tanaka I, Niidome T, Sawada K, Nishizawa Y, Sekiguchi N, Mori E, Mori Y, Imoto K. Single tottering mutations responsible for the neuropathic phenotype of the P-type calcium channel. *J. Biol. Chem.* **273**, 34857-34867 (1998).
43. Ruta V, Chen J, MacKinnon R. Calibrated measurement of gating-charge arginine displacement in the KvAP voltage-dependent K+ channel. *Cell* **123**, 463-475 (2005).
44. Kaja S, van de Ven RC, Broos LA, Veldman H, van Dijk JG, Verschuuren JJ, Frants RR, Ferrari MD, van den Maagdenberg AM, Plomp JJ. Gene dosage-dependent transmitter release changes at neuromuscular synapses of CACNA1A R192Q knockin mice are non-progressive and do not lead to morphological changes or muscle weakness. *Neuroscience* **135**, 81-95 (2005).

45. Dove LS, Abbott LC, Griffith WH. Whole-cell and single-channel analysis of P-type calcium currents in cerebellar Purkinje cells of leaner mutant mice. *J. Neurosci.* **18**, 7687-7699 (1998).

46. Lorenzon NM, Lutz CM, Frankel WN, Beam KG.. Altered calcium channel currents in Purkinje cells of the neurological mutant mouse leaner. *J. Neurosci.* **18**, 4482-4489 (1998).

47. Klöckner U, Mikala G, Varadi M, Varadi G, Schwartz A. Involvement of the carboxyl-terminal region of the a_1 subunit in voltage-dependent inactivation of the cardiac calcium channels. *J. Biol. Chem.* **270**, 17306-17310 (1995).

48. Chen C, Okayama H High-efficiency transformation of mammalian cells by plasmid DNA. *Mol. Cell Biol.* **7**, 2745-2752 (1987).

49. Jurman ME, Boland LM, Liu Y, Yellen G. Visual identification of individual transfected cells for electrophysiology using antibody-coated beads. *Biotechniques* **17**, 876-881 (1994).

50. Wakamori M, Hidaka H, Akaike N. Hyperpolarizing muscarinic responses of freshly dissociated rat hippocampal CA1 neurones. *J. Physiol.* **463**, 585-604 (1993).

51. Hamill OP, Marty A, Neher E, Sakmann B, Sigworth FJ. Improved patch-clamp techniques for high-resolution current recording from cells and cell-free membrane patches. *Pflugers Arch.* **391**, 85-100 (1981).

Figure 1

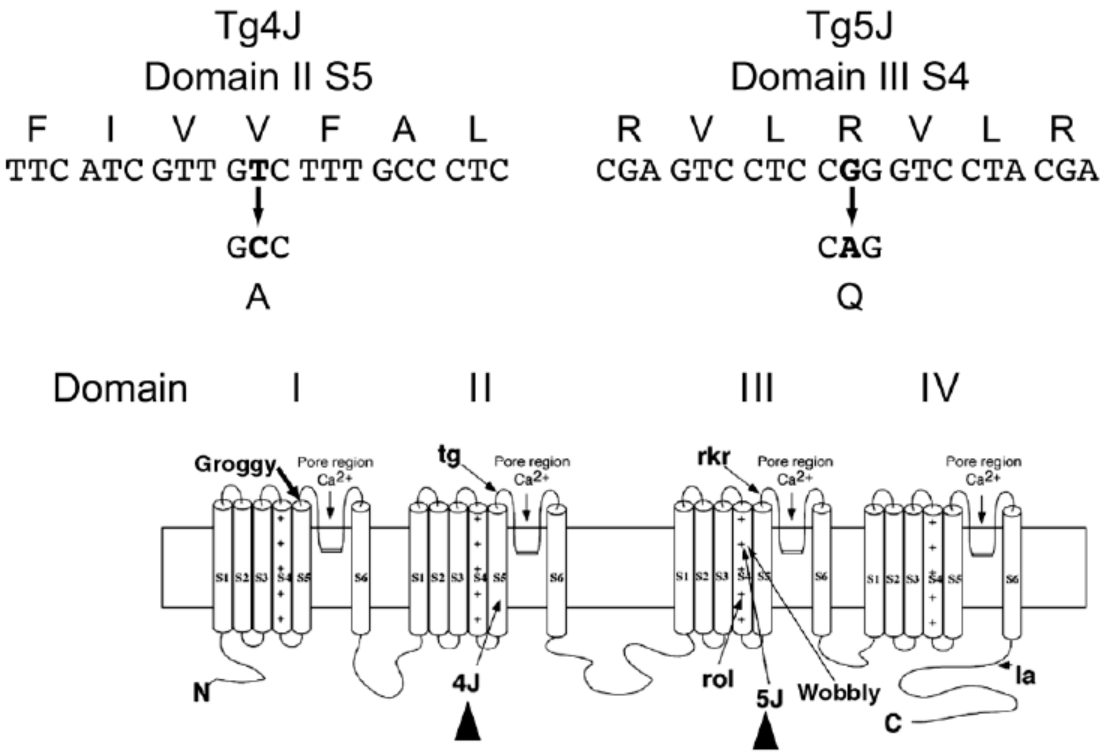

Figure 1 The *tg-4J* and *Tg-5J* mutations.

The *tg-4J* had a thymine (T) to cytosine (C) transition at nucleotide position 1742, resulting in a valine (V)-to-alanine (A) switch. *Tg-5J* showed a guanine (G) to adenine (A) change at nucleotide 3755, changing an arginine (R)-to-glutamine (Q).

Below is the proposed transmembrane topography of the CACNA1A protein and the sites of the recessive mouse alleles, *Cacna1a*^{tg} (tottering), *Cacna1a*$^{tg\text{-}la}$ (leaner), *Cacna1a*^{rol} (rolling Nagoya), and *Cacna1a*^{rkr} (rocker). The dominant wobbly mouse and the recessive groggy rat mutation sites are also included. Triangles highlight the position of the *tg-4J* and *Tg-5J* mutations.

Figure 2

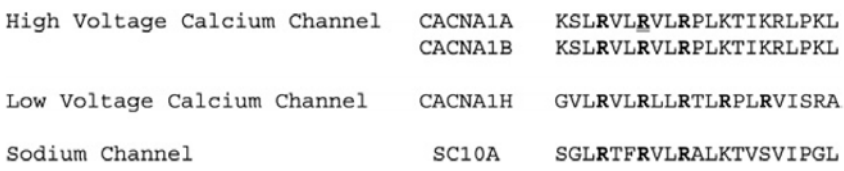

Figure 2 Conserved sequence with the arginine motif in ion-gated channels.

Examples from ion-gated channels showing the conserved arginine motifs in bold. The sequence shown from each channel is identical between human, rat and mouse. The underlined R represents the arginine mutated in *Tg-5J*.

Figure 3

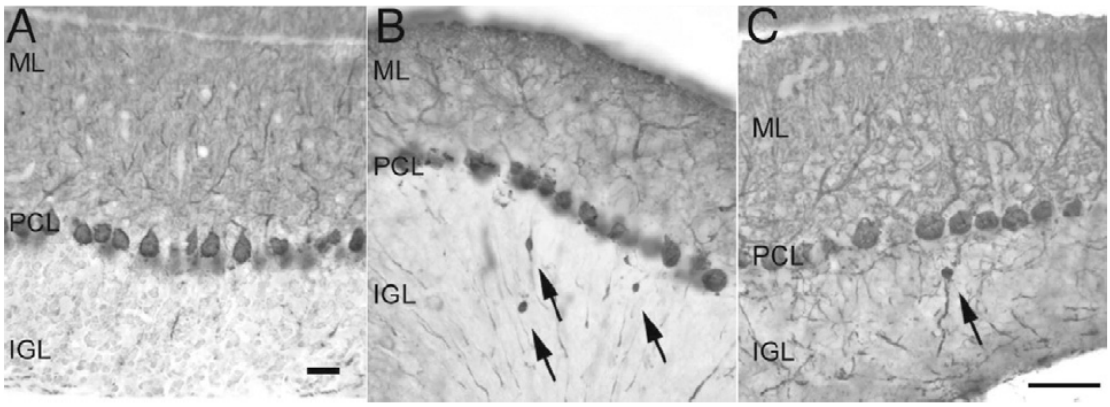

Figure 3 Calbindin staining in adult cerebellum.

Calbindin staining in adult wild-type (A), *tg-4J* homozygous (B) and *Tg-5J* heterozygous (C) cerebellum reveals axonal swellings of the Purkinje cell axons (arrows) in the internal granule cell layer of the *tg-4J* and *Tg-5J* mutants. Scale bars 25μM.

Figure 4

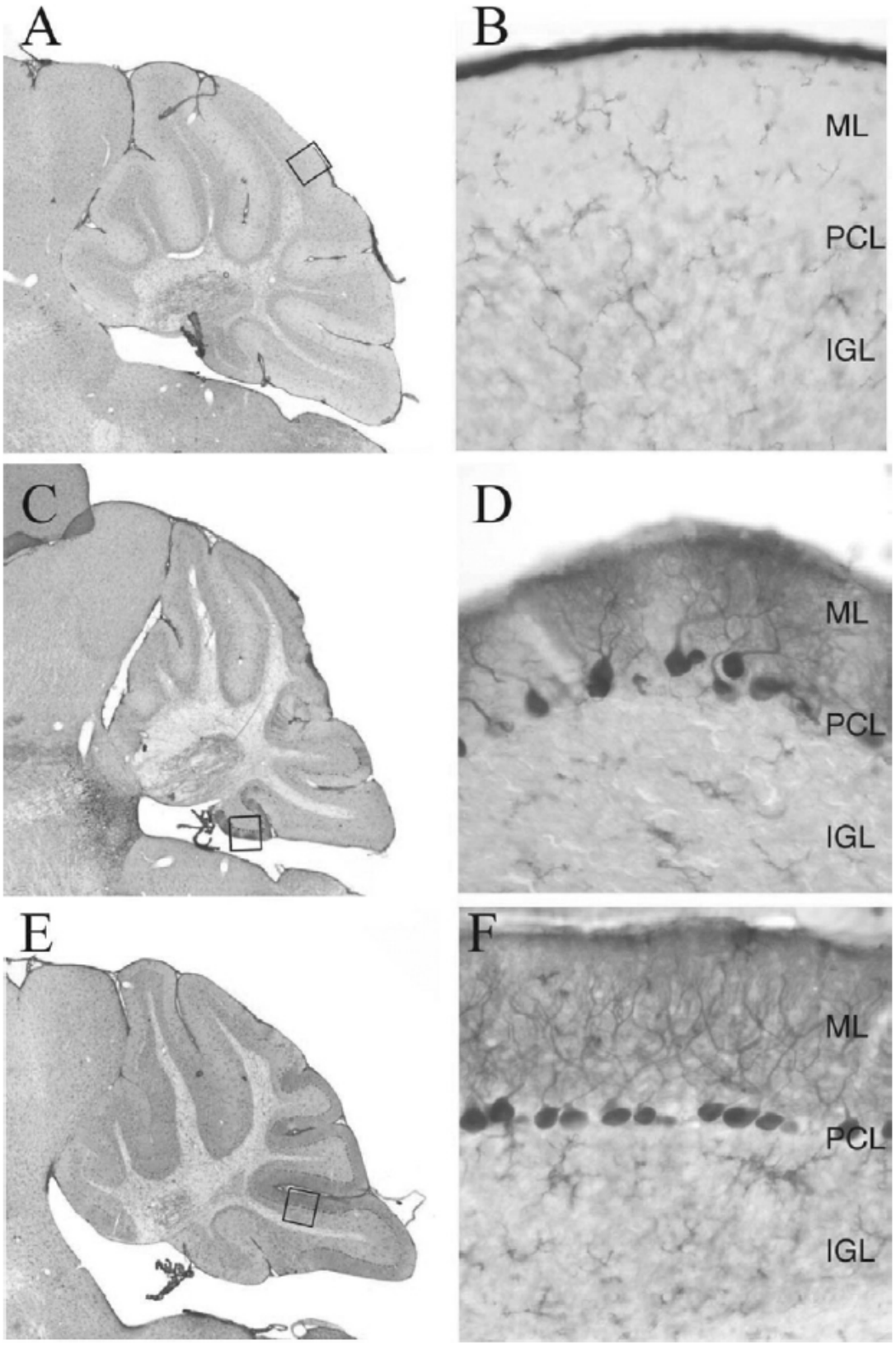

Figure 4 Tyrosine hydroxylase expression in the cerebellum.

Tyrosine hydroxylase staining in the cerebellum from control (A,B), *tg-4J* (C,D) and *Tg-5J* het. (E,F) adult animals reveal persistent TH expression in subpopulations of Purkinje cells from both the *tg-4J* and *Tg-5J* animals. Abbreviations: Purkinje (PCL), molecular (ML), internal granule cell layer (IGL) (Location of higher magnification pictures shown as dashed box).

Figure 5

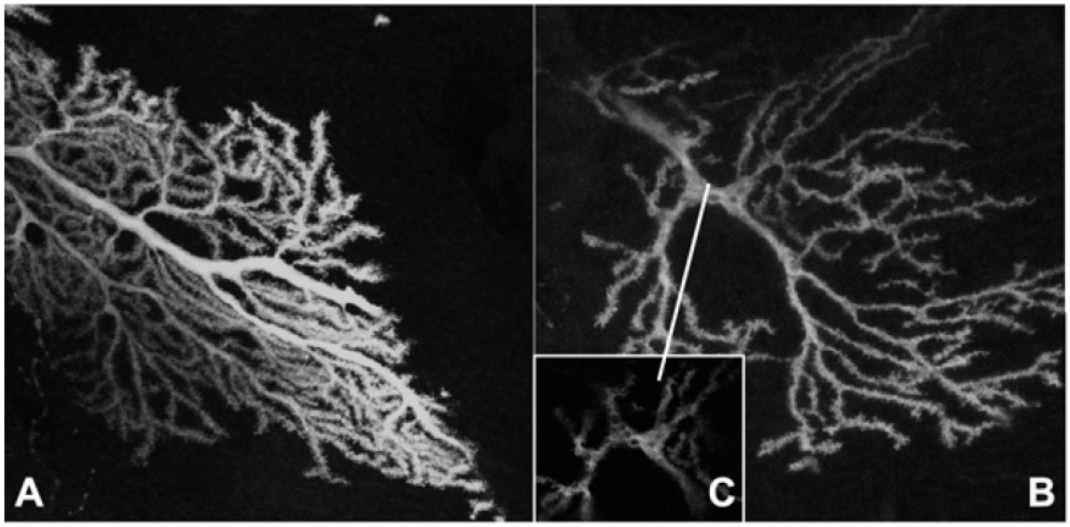

Figure 5 Green Fluorescent protein labeling of Purkinje cells from the *Tg-5J* homozygote.

Confocal microscopy of a GFP labeled Purkinje cell from (A) control aged 24 days and (B) *Tg-5J* homozygote at 24 days. Panel C highlights the abnormal vacuoles observed within the primary branch of the *Tg-5J* mutant.

Figure 6

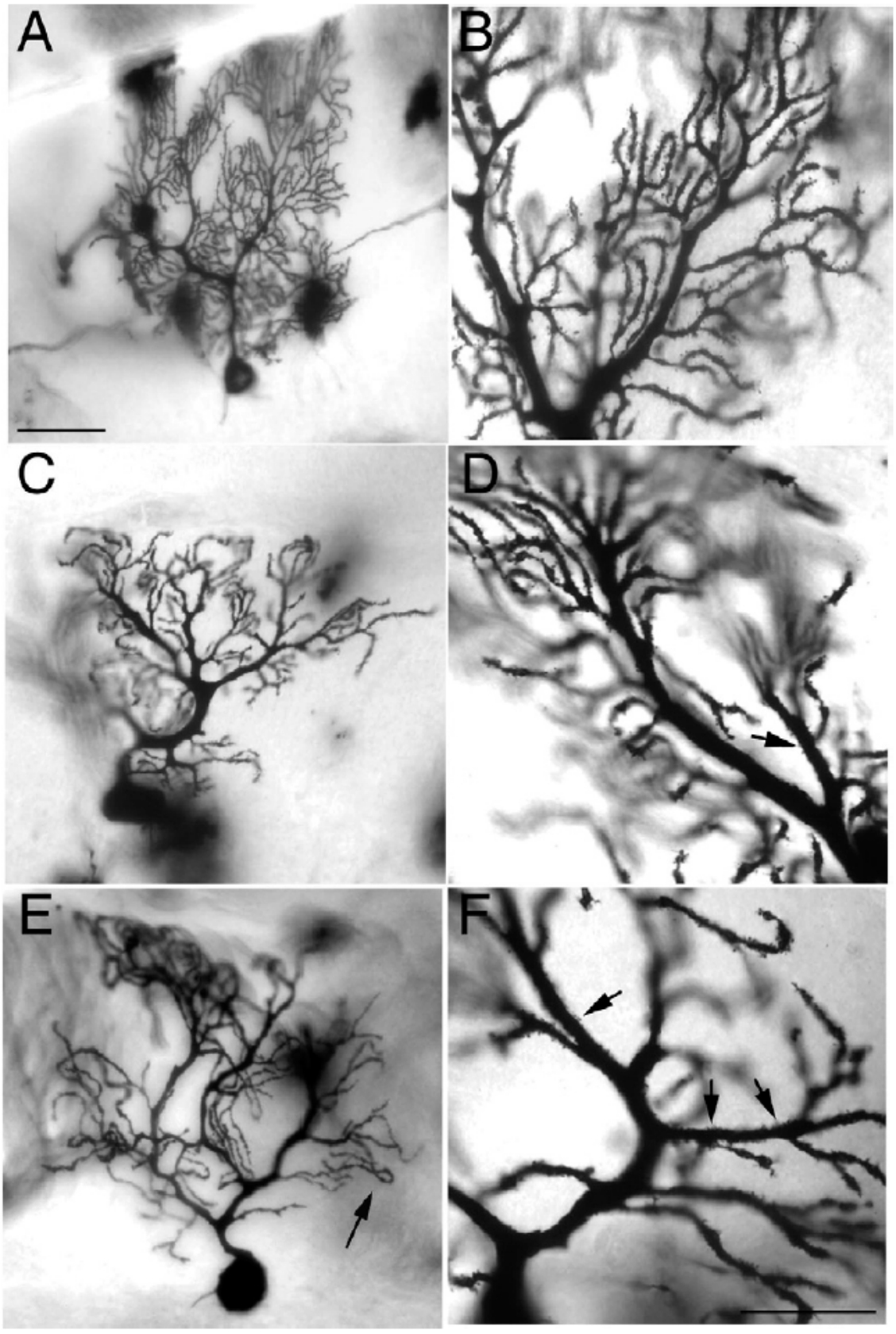

Figure 6 Golgi impregnation of individual cerebellar Purkinje cells shows dendritic abnormalities in adult *tg-4J* and *Tg-5J* mutants of over 1 year of age.

Branching in the wild-type Purkinje cell appears very dense with increasing number of branching points near the distal tips (A, B). In *tg-4J* homozygous mutants a slight thickening of primary dendrites and ectopic spines is observed (C, D). *Tg-5J* heterozygous mutants show a decrease in branching and have down turned distal ends of their dendritic tree and ectopic spines shown by the arrows (E and F). Scale bars 50uM (A, C, and E) and 25uM (B, D, and F).

Figure 7

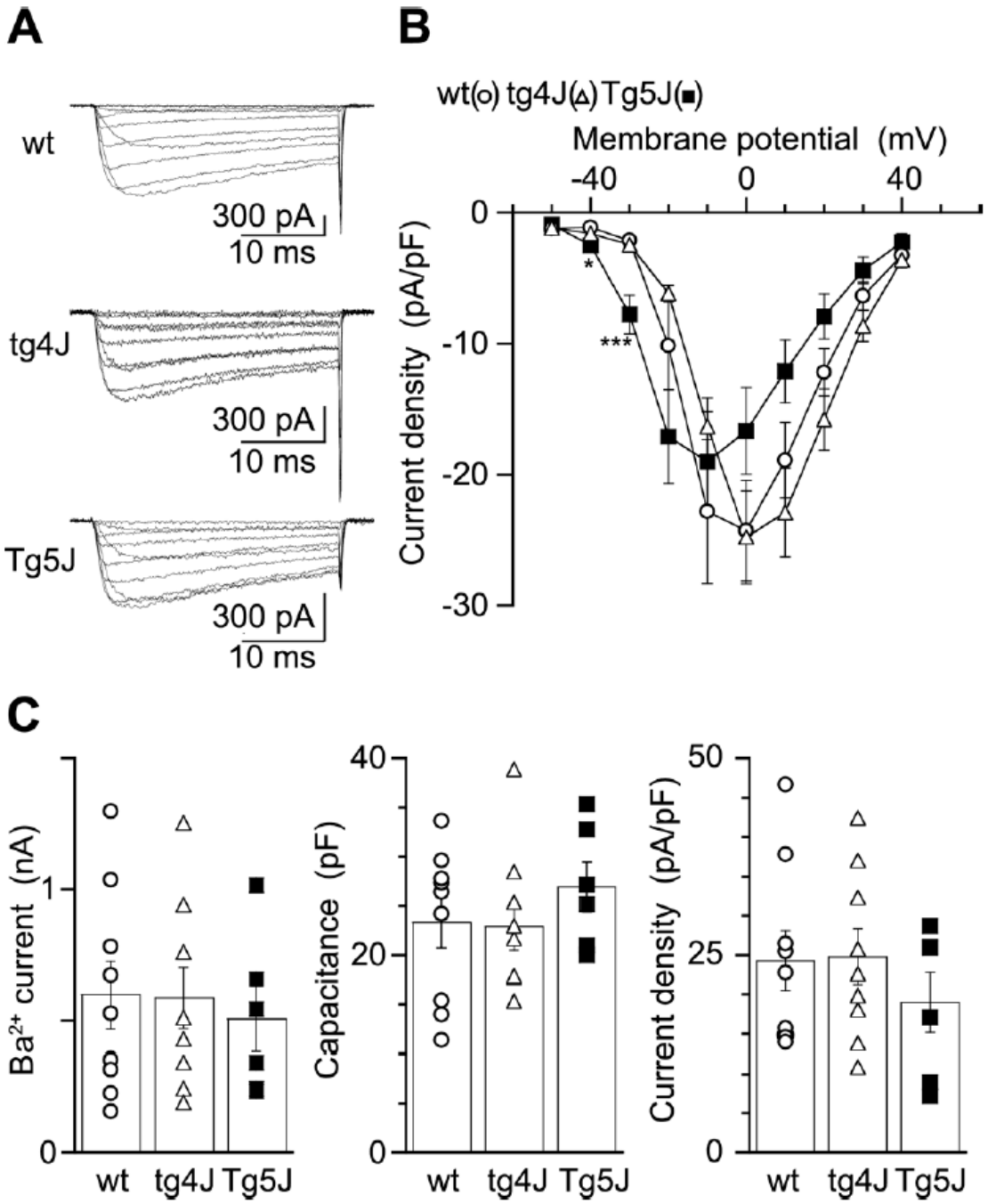
A
wt
300 pA
10 ms
tg4J
300 pA
10 ms
Tg5J
300 pA
10 ms
B
wt(○) tg4J(△) Tg5J(■)
Membrane potential (mV)
-40
0
40
0
-10
-20
-30
Current density (pA/pF)
*
***
C
Ba2+ current (nA)
1
0
wt
tg4J
Tg5J
Capacitance (pF)
40
20
0
wt
tg4J
Tg5J
Current density (pA/pF)
50
25
0
wt
tg4J
Tg5J

Figure 7 Comparison of Ba^{2+} currents in BHK cells expressing the mutant and the wild-type $Ca_v2.1$ channels.

A, Families of Ba^{2+} currents evoked by 30-msec depolarizing pulses from –50 to 40 mV for the wild-type $Ca_v2.1$ channel (top), the *tg-4J* $Ca_v2.1$ channel (middle) and the *Tg-5J* $Ca_v2.1$ channel (bottom) with 10-mV increments from a holding potential (V_h) of –100 mV.

B, Current density was plotted against membrane potential. Each point represents an average value of 8, 9 and 6 BHK cells expressing the wild-type $Ca_v2.1$ channel (open circle), the *tg-4J* $Ca_v2.1$ channel (open triangle) and the *Tg-5J* $Ca_v2.1$ channel (filled square), respectively.

C, Distribution of peak current amplitude (left), cell capacitance (middle), and current density (right). Individual values of Ca^{2+} channel currents in the wt, the *tg-4J* mutant and the *Tg-5J* mutant $Ca_v2.1$ channels and their means (open box) ± S.E. are shown. Error bars indicate mean ± S.E. if they are larger than symbols. $*P < 0.05$ and $***P < 0.001$ versus wt.

Figure 8

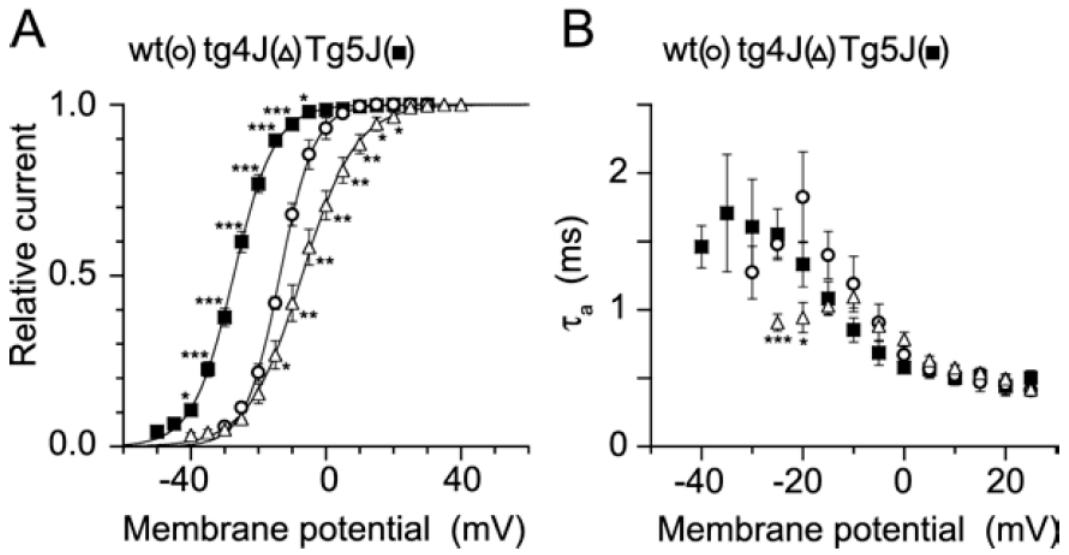

Figure 8 $Ca_v2.1$ activation currents in wild-type, *tg-4J* and *Tg-5J*.

A, Amplitudes of tail currents were normalized to the maximal tail current amplitude. The mean values from 5 BHK cells of the wild-type $Ca_v2.1$ channel, 7 BHK cells of the *Tg-5J* $Ca_v2.1$ channel and 6 BHK cells of the *tg-4J* $Ca_v2.1$ channel were plotted against test pulse potentials and fitted to the Boltzmann equation with a midpoint ($V_{0.5}$) of –14.5 mV and a slope factor (k) of 5.1 mV for the wild-type $Ca_v2.1$ channel (open circle), and a $V_{0.5}$ of –27.3 mV and a k of 6.1 mV for the *Tg-5J* $Ca_v2.1$ channel (filled square) and a $V_{0.5}$ of –7.0 mV and a k of 7.8 mV for the *tg-4J* $Ca_v2.1$ channel (open triangle).

B, Comparison of activation kinetics. Activation time constants were obtained from single-exponential fits of activation phase during 5-msec depolarizing steps. Data are expressed as mean ± SE of 6, 5 and 5 BHK cells expressing the wild-type, the *Tg-5J* and the *tg-4J* $Ca_v2.1$ channels, respectively.

Figure 9

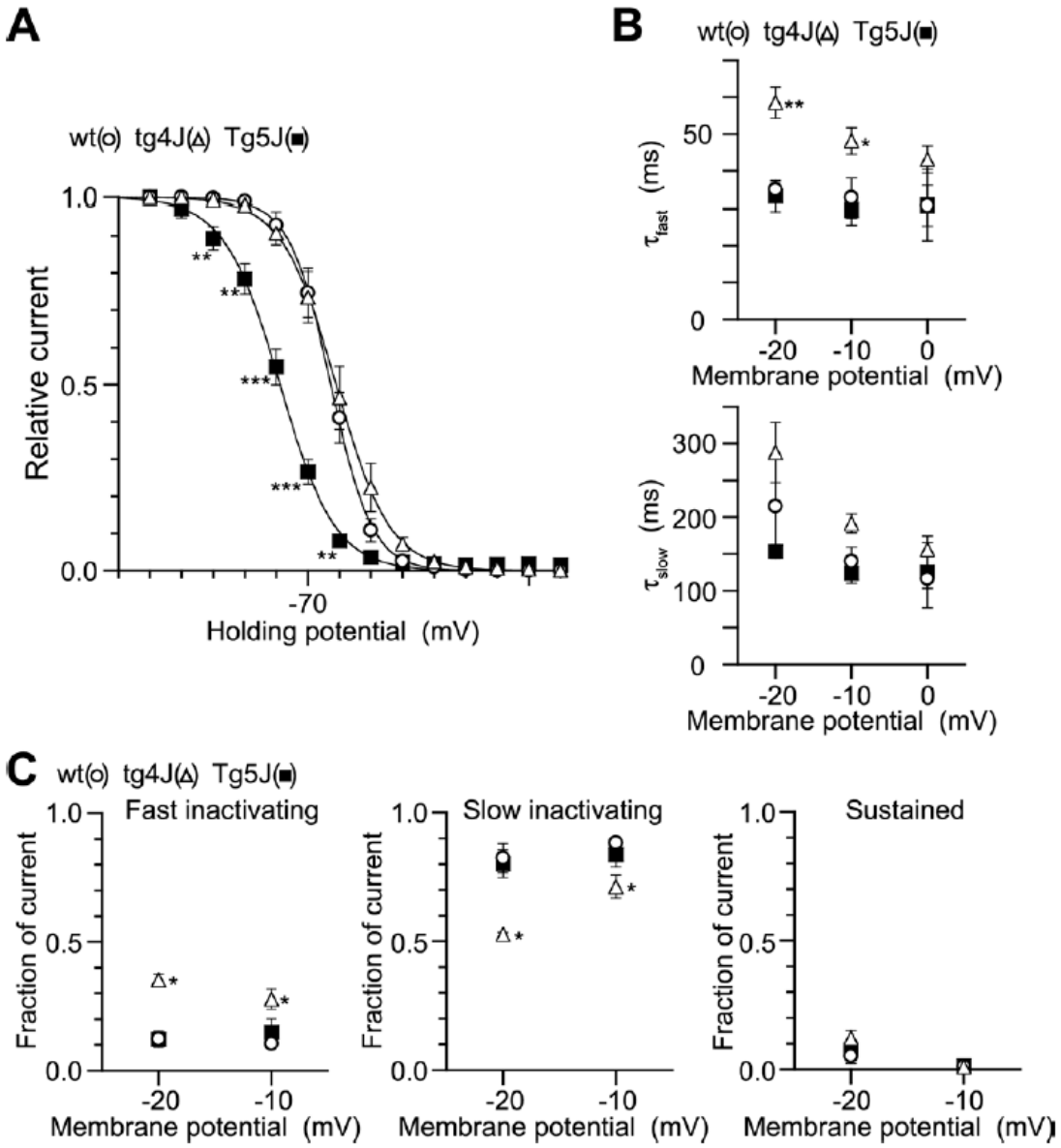
A
wt(o) tg4J(Δ) Tg5J(■)
Relative current
1.0
0.5
0.0
-70
Holding potential (mV)
B
wt(o) tg4J(Δ) Tg5J(■)
τfast (ms)
50
0
-20 -10 0
Membrane potential (mV)
τslow (ms)
300
200
100
0
-20 -10 0
Membrane potential (mV)
C
wt(o) tg4J(Δ) Tg5J(■)
Fast inactivating
Slow inactivating
Sustained
Fraction of current
1.0
0.5
0.0
-20 -10
Membrane potential (mV)

Figure 9 $Ca_v2.1$ inactivation curves in wild-type, *tg-4J* and *Tg-5J*.

A, Amplitudes of currents evoked by the test pulses were normalized to the current amplitude induced by the test pulse after a 2-sec V_h replacement of –120 mV. The mean values from 6 BHK cells expressing the wild-type $Ca_v2.1$ channel (open circle), 5 BHK cells expressing the *Tg-5J* channel (filled square) and 5 BHK cells expressing the *tg-4J* channel (open triangle) were plotted as a function of potentials of the 2-sec V_h displacement, and were fitted to the Boltzmann equation. $V_{0.5}$ and k were –63.1 and 6.3 mV for the wild-type α_{1A} channel, –79.0 and 8.6 mV for the *Tg-5J* channel and –61.2 and 7.7mV for the *tg-4J* channel, respectively.

B and C, Current decay was fitted by a sum of two exponential functions. The mean inactivation time constants, τ_{fast} (top) and τ_{slow} (bottom), were plotted as a function of test potentials from –20 to 0 mV. The fractions of the components, fast (left), slow inactivation (middle), and sustained components (right), were plotted against test potentials. Data are expressed as mean ± SE of 3, 6 and 3 BHK cells expressing the wild-type, the *Tg-5J* and the *tg-4J* $Ca_v2.1$ channels, respectively. Error bars indicate mean ± SE if they are larger than symbols.

Figure 10

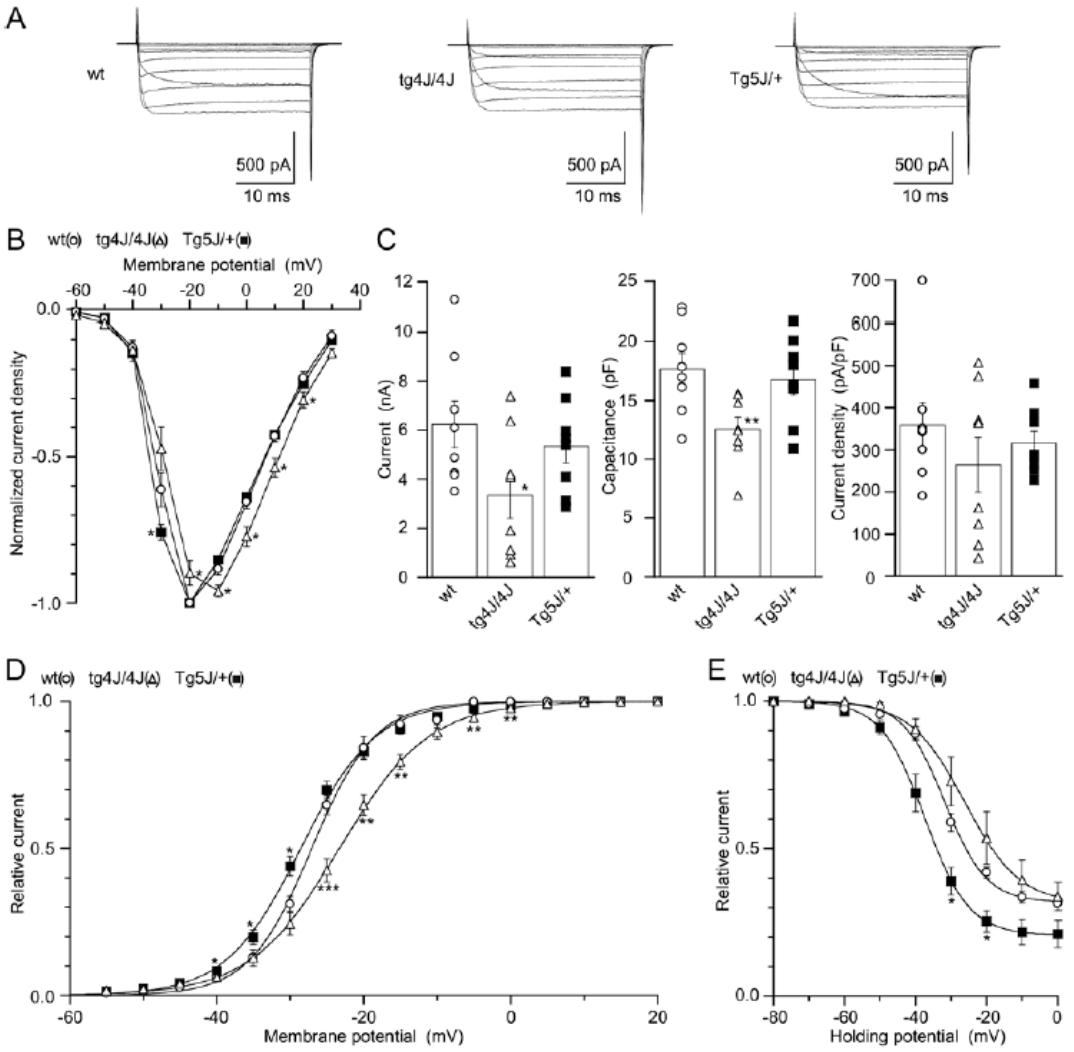
A
wt
tg4J/4J
Tg5J/+
500 pA
10 ms
B
wt(o) tg4J/4J(Δ) Tg5J/+(■)
Membrane potential (mV)
Normalized current density
C
Current (nA)
Capacitance (pF)
Current density (pA/pF)
wt
tg4J/4J
Tg5J/+
D
Relative current
Membrane potential (mV)
E
Holding potential (mV)

Figure 10 Comparison of $Ca_v2.1$ currents recorded in cerebellar Purkinje cells dissociated from wild-type, *tg-4J /tg-4J* homozygotes and *Tg-5J/+* heterozygous mice.

A, Families of Ba^{2+} currents evoked by 30-msec depolarizing pulses from –60 to 30 mV for wt, *tg-4J /4J*, and *Tg-5J/+* mice with 10-mV increments from a V_h of –80 mV. B, Normalized current density was plotted against membrane potential. Each point represents an average value of 8 Purkinje cells from the wt (open circle), *tg-4J /4J* (filled triangle) and *Tg-5J/+* (open square), respectively.

C, Distribution of peak current amplitude (left), cell capacitance (middle), and current density (right). Individual values of Ca^{2+} channel currents in wt, *tg-4J /4J* and *Tg-5J/+* Purkinje cells and their means (open box) ± S.E. are shown.

D, Activation curves. Amplitudes of tail currents were normalized to the maximal tail current amplitude. The mean values from 7 wt, 7 *tg-4J /4J*, and 8 *Tg-5J/+* Purkinje cells were plotted against test pulse potentials and fitted to the Boltzmann equation.

E, Inactivation curves. Amplitudes of currents evoked by the test pulses were normalized to the current amplitude induced by the test pulse after a 2-sec V_h replacement of –80 mV. The mean values from 3 wt, 3 *tg-4J /4J*, and 6 *Tg-5J/+* were plotted as a function of potentials of the 2-sec V_h displacement, and were fitted to the Boltzmann equation. Error bars indicate mean ± S.E. if they are larger than symbols. $*P < 0.05$, $**P < 0.01$ and $***P < 0.001$ versus wt.

Table 1. Activation and inactivation parameters of Ca(v)2.1 channels in BHK cells and dissociated Purkinje cell neurons

BHK cells	Activation parameters				Inactivation parameters			
	$V_{0.5}$	S.E.	k	S.E.	$V_{0.5}$	S.E.	k	S.E.
wt	−14.49	1.01	5.06	0.46	−63.05	1.85	−6.27	0.63
tg4J	−7.03	1.63**	7.67	0.37**	−61.16	2.86	−7.66	0.25
Tg5J	−27.29	0.63***	6.07	0.38**	−79	1.75***	−8.56	0.57

Purkinje neurons	Activation parameters				Inactivation parameters					
	$V_{0.5}$	S.E.	k	S.E.	a	S.E.	$V_{0.5}$	S.E.	k	S.E.
wt	−26.86	0.69	4.31	0.35	0.68	0.01	−31.79	0.84	−5.81	0.15
tg4J/4J	−23.35	1.03*	5.95	0.27***	0.69	0.03	−25.45	3.72	−7.27	0.85
Tg5J/+	−28.48	0.61	5.03	0.44	0.79	0.05	−37.3	1.24*	−5.74	0.67

k, slope factor; $V_{0.5}$, half-maximal activation; $V_{0.5}$, half-maximal inactivation; a, rate of inactivating component; $V_{0.5}$, half-inactivation potential.
* $P<0.05$ versus wt.
** $P<0.01$ versus wt.
*** $P<0.001$ versus wt.

Chaptor 5

Cholinergic induced oscillation in hippocampus of *tottering* Ca^{2+} channel mutant mice.

Abstract

Neurological mutant mice serve as useful *in vivo* models to investigate channel functions in neural activity. *tottering* (*tg*) mouse is a well known epilepsy model that has mutations in the P/Q-type Ca^{2+} channels α_{1A} subunit gene. While functional abnormalities of *tg* mutant Ca^{2+} channels have been revealed at the molecular level, important impacts of these mutant channels in controlling network activities and behaviors have been poorly understood. The present studies investigate influences of altered properties of mutant Ca^{2+} channels on cholinergic oscillation in hippocampus, using multi-channel recording system (MED64 system), to understand mechanism underlying epileptic phenotype in *tg* mutant mice at the network level. High frequency patterns of oscillation elicited by acetylcholine agonist, carbachol, are more frequently observed in *tg* hippocampus. The further pharmacological studies revealed that the contribution of inhibitory circuits to cholinergic oscillation in *tg* mice differs from that in wild type, caused by the different expression pattern of $GABA_A$ receptor subunits. These results suggest that mutant Ca^{2+} channel in *tg* induced the epileptiform activity of neuronal network mediated by the abnormality of $GABA_A$ receptor expression.

Introduction

The mutant mice which have a nerve disease are very useful model for investigation of channel properties in neural activity. Especially *tottering* (*tg*) locus on mouse chromosome 8 is well known epileptic mouse mutation that indicates a delayed-onset, recessive disorder consisting of ataxia, paroxysmal dyskinesia, and behavioral absence seizures resembling petit mal epilepsy[1,2]. The *tg* mutation in the gene encoding the pore-forming α_{1A} subunit of the P- and Q-type Ca^{2+} channels have been found[1]. Recent genetic and molecular biological analyses have revealed many forms of inherited channelopathies. Although *in situ* hybridization revealed no difference in the levels of α_{1A} subunit mRNA in *tg* mice compared to wild-type[1], the number of functional channels appears to be reduced in the mutants, as whole-cell current density in dissociated Perkinje neurons of *tg* mice is decreased[3]. The decrease in presynaptic P- and Q-type Ca^{2+} currents that led to an increased dependence on N-type channels, ensuring normal excitatory transmission, was revealed at hippocampal Schaffer collateral synapses[4]. Fundamental properties of excitatory synaptic transmission in the cerebellum and the role of Ca^{2+} channel subtypes therein were investigated in *tg* mice[5]. Although the amplitude of the parallel fiber-mediated EPSC was only mildly decreased in young non-ataxic *tg* mice, it was drastically diminished in adult ataxic *tg* mice of postnatal day 28-35, showing a good correlation to manifestation of ataxia. However, although the critical role of mutant Ca^{2+} channels for transmitter release has been revealed, the roles of these mutant channels in contribution for network activities and abnormal behaviors have been poorly understood.

One of the brain regions that most readily exhibit oscillations is the hippocampus. With regard to extrinsic inputs, results from several studies indicate that ascending cholinergic projections promote endogenous oscillations. Although a pioneering

study[6] showed that applying cholinergic blockers or septal lesions had no obvious effect on the oscillations, subsequent studies demonstrated that fast waves (30 –60 Hz) in freely moving rats are enhanced by a cholinesterase inhibitor, physostigmine, and substantially reduced by cholinergic antagonists[7]. Application of cholinergic agonist to hippocampal or entorhinal slices has been reported to induce seconds-long episodes of theta-like activity[8-11], but recently it is shown that faster frequency rhythms (20 –40 Hz) are also triggered[12-14]. Although the evidence is not extensive, the combination of in vivo and in vitro results points to the conclusion that the cholinergic inputs play an important role in generating oscillatory synchronous activity in the hippocampus and cerebral cortex.

The present studies investigated influences of altered properties of mutant Ca^{2+} channels on cholinergic oscillation in hippocampus, to understand mechanism underlying epileptic phenotype in *tg* mutant mice at the network level. Additional pharmacological and physiological studies were then conducted to test ideas about the circuitries and transmitters underlying the oscillations.

Results

Cholinergic induced oscillation in hippocampus

Figure 1A contains a micrograph of a hippocampal slice and underlying 64-electrode array with 150 μm between recording positions (the "broad array"). The electrode array was established to analyze two-demensional current source density of brain slices[14,15]. Infusion of 50 μM carbachol, an analog of acetyl choline, was followed by a gradually developing rhythmic activity in the pyramidal cell fields (**Fig. 1B**). The rhythmic activity included two kinds of waves, big (> 0.1 mV, θ rhythm 4-8 Hz) and small (< 0.1 mV, β and γ rhythm 8~ Hz) (**Fig. 1C**). The big wave composed more 50 msec of firing time and more 230 msec of afterhyperpolarization time, suggesting synchronous oscillation of many neurons firing in hippocampus. This burst, big oscillation induced by carbachol, closely resemble interictal crusts recorded in hippocampal slices in a variety of in vitro models of epileptiform activity[11,16,17]. To investigate the origin of the synchronous oscillation, we performed the measurement of calbachol-induced oscillation in entire hippocampus slice by using 64-electrode array with 450 μm between recording positions. Continuous two-dimensional current source density analysis showed that the synchronous firing occuerd at CA3 region and difuse to CA1 and DG regions (**Fig. 2A**). And we found that carbachol elicited oscillatory behavior in CA3 when it is isolated from the hippocampus (**Fig. 2B**). These data suggested that CA1 and DG cannot support carbachol oscillations in the 4-8 Hz range on its own but requires oscillations generated in CA3 to be propagated synaptically to CA1(ref. 11).

Cholinergic oscillation patterns in tottering mice

We compared the cholinergic oscillation in wild-type (wt) and tottering mice (*tg*), which

display a delayed-onset, recessive disorder consisting of ataxia, motor seizure, and absence seizure resembling petit mal epilepsy, because the oscillation, we observed, was resemble epileptiform activity. Notably, the patterns of oscillation induced by 50 μM carbachol in hippocampal slice from tottering mice, was different from those in wt. In wt mice, the waves of low frequency were constantly occurred, while in *tg* mice the cluster of high frequency burst were occurred every 5-15 sec (**Fig. 3A**). To compare the oscillation in wt and *tg*, the number of waves or the percentage of occupation time of wavs was plotted by the frequency of waves in the cholinergic oscillation from wild-type and tottering (**Fig. 3B and 3C**). Figure 3B showed that the number of high frequency wavs was significantly increased and the number of low frequency waves was significantly decreased in *tg*. In the analysis of the occupation time of waves, the occupation of the low frequency renge (0.8-1.25 Hz) was decreased and the occupation time of the high frequency renge (6-10 Hz) was increased in *tg* mice (**Fig. 3C**). In Figure 3D, the waveforms normalized peak time to 0 and averaged in *tg* have faster rise time than the ones in wild mice (wild: 18.26 ± 1.62 msec, *tg/tg*: 13.65 ± 0.90 msec; $p < 0.05$), but in the case of duration at half amplitude there is not difference. Spatiotemporal patterns of carbachol induced bursting oscillations showed the delay time at the peak point between CA3 and CA1 in *tg* mutant mice was smaller than that in wt mice (wild: 8.26 ± 0.72 msec (n = 4), *tg/tg*: 5.27 ± 0.94 msec (n = 4); $p < 0.05$) (**Fig. 4**). These results of cholinergic induced oscillation observed in *tg* mutant mice suggest that the activities of neurons induced by carbachol were enhanced and more synchronous firing was occured.

Pharmacological analysis of cholinergic induced oscillation in wt and *tg*

To investigate the different pattern of oscillation in *tg*, we performed pharmacological

analysis. The antagonists of muscarnic receptor, M1 receptor, and AMPA receptor (1 μM atropine, 1 μM prenzepine, and 20 μM CNQX, respectively) diminished or inhibited the cholinergic oscillation in *tg*, same as in wt (data not shown). The data suggest that cholinergic oscillation was majorly produced by M1 receptors and AMPA receptors. 50 μM AP5, NMDA receptor antagonist, enhanced the number of the low frequency bursts of cholinergic oscillation in wt and *tg*, suggesting the inhibition of low frequency bursts by the activity of NMDA recptor (data not shown).

In presence of $GABA_A$ receptor antagonist, picrotoxin 20 μM, the occupation time of the low frequency (< 1 Hz) was shifted to middle renge (1-4 Hz) in wt, while the occupation time of the high frequency (> 4 Hz) was shifted to middle renge (1-4 Hz) in *tg* (**Fig. 5A**). Thus, the pattern of the occupation time in *tg* were very similar as that in wt (**Fig. 5B**). The data suggest that the effects of inhibitory transmission on neuronal network activity induced by carbachol may be different between wt and *tg*. The further pharmacological study showed that diazepam, enhancer of $GABA_A$ receptor, induce the enhancement of the high frequency burst in *tg*, whereas diazepam did not affect the frequency pattern in wt (**Fig. 6A, and 6B**). In *tg* mutant mice, the number of pulse per cluster and duration time of cluster were significantly increased in presence of diazepam (**Fig. 6C**), suggesting that the activity of $GABA_A$ receptor affected the high frequency burst in tg, but not in wt.

The analysis of inhibitory transmission in *tg* mutant mice.

What induces the different activity of $GABA_A$ receptor between in wt and tg? Next, we performed the analysis of the number and the distribution of inhibitory neurons. The immunocytochemical analysis showed that inhibitory neurons and inhibitory synapses in hippocampus were detected by GAD65, 67 antibodies (**Fig. 7**). However

the number and the distribution of inhibitory neurons in hippocampus from *tg* mutant mice were not different from wt (**Fig. 8**). In the brain, there were various combinations of subunits composed $GABA_A$ receptor and the expression patterns of subunits were developmentaly changed. Aberrent $GABA_A$ receptor expression in the cerebral cortex, and cerebellum of *tg* has been reported previously[18-22], leading us to speculate that $GABA_A$ receptor expression in the hippocampus of *tg* may also be compromised. The comparison of the expression pattern of $GABA_A$ receptor in wt and *tg* showed that α subunits slightly inceased, while β subunits slightly decreased in *tg* (**Fig. 9**). These results suggest that the abnormality component of $GABA_A$ receptor induced the different activity of inhibitory transmission in *tg*.

Discussion

In this study, we observed the cholinergic-induced oscillation of hippocampal slice by using multi-electrode array (MED system). The large amplitude oscillation in hippocampus occuered at CA3 and conducted to CA1 and DG. The comparison of the oscillation pattern in wt and *tg* showed that carbachol induced the abnormal burst, which is clustering wave and high frequency in *tg*. The pharmacological analysis revealed that the activities of inhibitory transmission in *tg* were different from that in wt. In *tg* mutant mice, the number and the distribution of inhibitory neurons were not different, however the expression patterns of $GABA_A$ receptor were slightly different from wt. These results suggest that mutant Ca^{2+} channel in *tg* induced the abnormal burst of neuronal network mediated by the abnormality of $GABA_A$ receptor expression.

Previous reports showed various kinds of cholinergic-induced oscillation in hippocampus in vitro[8,11,13,14]. In pharmacological properties of the oscillation, the large oscillation we focused on was similar to the oscillation reported by Williams and Kauer[11]. Investigation of the oscillation in tg mutant mice, known as absence epilepsy model mice, is very important for understanding the abnormal neuronal network activity because the oscillation is similar to the epileptiform oscillation, previously reported[11].

In cholinergic induced oscillation of *tg*, we found 1) the high frequency oscillation, 2) the decrease of rise time, the average time from baseline to peak of one wave, and 3) the decrease of delay time, the averge time conducting from CA3 to CA1. In pharmacological analysis, picrotoxin induced the same frequency pattern in *tg* as in wt, suggesting the abnormal activity of inhibitory transmission in *tg*. Previous reports showed that a gene-linked alteration in synaptic inhibition, characterized by a net reduction in the hyperpolarizing IPSP and a positive shift of the $GABA_A$-dependent synaptic equilibrium potential, may contribute to the prolongation of the K^+-induced

paroxysmal depolarizing shift (PDS) during synchronous network bursting in CA3 pyramidal neurons of the epileptic *tg* mutant[18]. The alteration of rise time of waves showed the activity of neurons in *tg* was more synchronous than that in wt, suggesting enhancement of the carbachol sensitivity. It is possible that the resting potential in *tg* may be shifted to positive, resulting in the firing of neurons induced by small depolarizing stimulation. In previous reports, the expression of muscarnic receptors was not alter or reduced in *tg* mutant mice[23,24], and the current density of low voltage-activated Ca^{2+} channel were increased in thalamic relay neuron from *tg* mutant mice[25]. It is possible that the enhancement of the low voltage-activated Ca^{2+} channel activity in hippocampus may induce the depolarizing shift of resting potential of neurons and more synchronous firing of neurons in *tg*.

The decrease of the delay time may be caused by the alteration of 1) the efficiency of conducting, 2) the output of CA3, and 3) input of CA1. The prevous report revealed that compensatory molecular mechanisms in the regulation of presynaptic Ca^{2+} entry and neurontransmitter release in *tg*, suggesting the efficiency of conducting was not alter. In this study, we showd that the more synchronous firing in *tg*, suggesting the transient output of CA3 region was enhanced. And it is possible that in CA1, the resting potential were shifted to positive, same as CA3. These results suggest that the alteration of the output of CA3 and the input of CA1 caused the decrease of the delay times. However the previous report indicated that impared neurontransmitter release and elevated threshold for cortical spreading depression in *t*g mutant mice. Thus, we may observe the brain region specific abnormality in *tg* mutant mice.

We analyzed the number of inhibitory neurons, and the $GABA_A$ receptor expression. These results indicated that the number was not altered, but $GABA_A$

receptor expression slightly was altered. The alteration of $GABA_A$ receptor expression was reported in the cortex and cerebellum of *tg* mutant mice, and the brain of other epileptic model animals, for example temporal lobe epilepsy model[19-22,26-28].

In further studies, we investigate other possibilities cause the alteration of neuronal network activity in *tg* mutant mice, for example the chlolide ion concentration of intracellular and the neurogenesis in hippocampus, were dependent on Ca^{2+} influx via voltage-gated calcium channels as previously reported[29-31].

Materials and Methods

Animals

The C57BL/6J-*tg* strain of *tg* mice was introduced from the Jackson Laboratory (Bar Harbor, ME). The *tg* and *tgrol* mice were provided with a commercial diet (CE-2, Nihon Clea, Tokyo, Japan) and water *ad libitum* under conventional conditions with controlled temperature, humidity, and lighting (22 ± 2 ˚C, 55 ± 5%, and 12 hr light/dark cycle with lights on at 7 A.M.). These strains were maintained and propagated by mating between heterozygous mice in the Center for Experimental Animal, Okazaki National Research Institutes. Genotyping of *tg* mice was performed using PCR-restriction fragment length polymorphism (PCR-RFLP). A PCR fragment was obtained using a pair of primers, 5'GGAAACCAGAAGCTGAACCA-3' (sense) and 5'-GAAATGGAGGAATTCAGGG-3' (antisense) and genomic DNA as a template. Digestion of the fragment with *Aci*I yielded the following fragments: 295 bp in *tg*/*tg*, 127 and 168 bp in +/+, and 127, 168, and 295 bp in *tg*/+ (Wakamori et al., 1998).

Slice preparation

Wild and *tg* mutant mice at postnatal days 27 – 36 were killed by decapitation after anesthesia, in accordance of institutional guideline for animal experiments. The brain was immediately soaked in ice-cold, oxygenated preparation artificial cerebrospinal fluid (aCSF) of the following composition (in mM): 124 NaCl, 26 $NaHCO_3$, 10 glucose, 3 KCl, 1.25 KH_2PO_4, 2 $CaCl_2$, 2 $MgSO_4$, for approximately 2 min. The hippocampus was dissected free, placed on the ice-cold stage of a vibrating tissue slicer (Leica: VT-1000S) and sections taken at 300 μm. Sections were soaked in the oxygenated preparation buffer for 1 h at room temperature.

Electrophysiological experiments with multi-electrode array

Procedures for the preparation of the Multi-Electrode Dish (Alpha MED Sciences Co., LTD.: MED probe) are described in previous reports[14,15]. The device has an array of 64 planar microelectrodes, arranged in an 8 x 8 pattern with interelectrode spacing of 150 μm (MED-P510P). The slices positioned to cover the 8 x 8 array on the MED probe were placed in a small CO_2 incubator at 32 ˚C and responses were collected in recording aCSF (in mM: 124 NaCl, 26 $NaHCO_3$, 10 glucose, 3 KCl, 1.25 KH_2PO_4, 2 $CaCl_2$, 0.75 $MgSO_4$). Oxygenated, fresh recording aCSF was infused at 1.5 ml/min. Spontaneous field potentials at all 64 sites were simultaneously hardware filtered through a 1–10 kHz bandpass filter and recorded with the multi-channel recording system at a 20 kHz sampling rate.

Drugs were purchased from Sigma (pirenzepine, methoctramine, picrotoxin, APV, CNQX, diazepam) and Wako (all other compounds). All drugs were bath applied at known concentrations and were prepared daily from compound or frozen aliquots.

Data analysis

The frequency of oscillation response was calculated by interburst interval that was measured as the time between the start of one burst and the start of the next. All data are presented as mean ± S.E.M. One-way analysis of variance (ANOVA) was employed for statistical analysis.

Procedures for CSD analysis of two-dimensional multi-electrode data are described by Shimono et al (2000). The data were low pass filtered at 200 Hz, and then spatially smoothed by a 3 x 3

kernel (0 1/8 0, 1/8 1/2 1/8, 0 1/8 0). The result was convoluted with a 3 x 3 Laplacian kernel (0 1 0, 1 -4 1, 0) to produce a discrete approximation of the second spatial

derivative. The medium was considered ohmic with homogeneous conductance. Current vs. time plots for single points in the slice were obtained by computing the 8 x 8 current source density for each time step, and calculating the value at the desired location via spline interpolation.

RT-PCR

Total RNA, eluted from hippocampus of 28-35 days old mice, WT and *tg*, were reverse-transcripted by using TAKARA RNA LA PCR kit ver1.1. From reverse-transcripted cDNA, the fragments of target protein sequences were amplificated by PCR (Table 1). The intensities of the bands, detected by the electrophoresis analysis of the PCR products, calculated by image J. All values are normalized by internal control, GAPDH.

Real-time PCR

Total RNA, eluted from hippocampus of 28-35 days old mice, WT and *tg*, were reverse-transcripted by using TAKARA RNA LA PCR kit ver1.1. From reverse-transcripted cDNA, the fragments of target protein sequences were amplificated by Real time PCR (Roche: Lightcycler-DNA FastStart DNA Master SYBR Green) (Table 1). All values are normalized by internal control, GAPDH.

Histological procedure

For immunohistochemistry, wt and *tg* mice aged P28-33 were anesthetized with 75 mg/kg pentobarbital and perfused intracardially with 4% paraformaldehyde and 0.2% picric acid in 0.1M sodium phosphate buffer (PB) for 12 min. Brains were removed and fixed overnight at 4 °C and subsequently incubated in PB containing 10, 20, and

30% sucrose for overnight each. The tissue was sliced at 40 μm along the coronal section by a microtome (SM2000R; Leica). Tissue slices were washed in 0.05 M Tris-buffered saline (TBS) before incubation in 1% H_2O_2 for 1 h. Slices were washed three times in TBS and incubated with a rabbit polyclonal antibody against glutamic acid decarboxylase (GAD) (1:5000; Chemicon, Temecula, CA) in TBS containing 10% normal goat serum and 2% bovine serum albumin for two overnights at 4 °C. the tissues were washed three times in TBS and incubated 3 h at room temperature in biolinylated anti-rabbit IgG (Vector Laboratories, Burlingame, CA) using a 1:200 final dilution including normal goat serum and TBS. After rinses, the tissues were incubated with avidin-biotin-peroxidase complex (ABC Elit kit; Vector Laboratories) in TBS for 30 min. After washing in TBS, the tissues were reacted with DAB (0.05%) and H_2O_2 (0.002%) in TBS. Immunostaining clearly stained the somate of GABAergic neurons, sparing their nuclei, as previously reported[33].

References

1. Fletcher, C.F. et al. Absence Epilepsy in Tottering Mutant Mice Is Associated with Calcium Channel Defects. *Cell* **87**, 607-617 (1996).
2. Doyle, J. et al. Mutations in the Cacnl1a4 calcium channel gene are associated with seizures, cerebellar degeneration, and ataxia in tottering and leaner mutant mice. *Mammalian Genome* **8**, 113-120 (1997).
3. Wakamori, M. et al. Single Tottering Mutations Responsible for the Neuropathic Phenotype of the P-type Calcium Channel. *J. Biol. Chem.* **273**, 34857-34867 (1998).
4. Qian, J. & Noebels, J.L. Presynaptic Ca2+ Influx at a Mouse Central Synapse with Ca2+ Channel Subunit Mutations. *J. Neurosci.* **20**, 163-170 (2000).
5. Matsushita, K. et al. Bidirectional Alterations in Cerebellar Synaptic Transmission of tottering and rolling Ca2+ Channel Mutant Mice. *J. Neurosci.* **22**, 4388-4398 (2002).
6. Stumpf, C. Drug action on the electrical activity of the hippocampus. *Int Rev Neurobiol* **8**, 77-138 (1965).
7. Leung, L.W. Spectral analysis of hippocampal EEG in the freely moving rat: effects of centrally active drugs and relations to evoked potentials. *Electroencephalogr Clin Neurophysiol* **60**, 65-77 (1985).
8. Konopacki, J., MacIver, M.B., Bland, B.H., & Roth, S.H. Carbachol-induced EEG 'theta' activity in hippocampal brain slices. *Brain Res*. **405**, 196-198 (1987)
9. MacVicar, B.A. & Tse, F.W. Local neuronal circuitry underlying cholinergic rhythmical slow activity in CA3 area of rat hippocampal slices. *J Physiol.* **417**, 197–212 (1989).
10. Dickson, C.T. & Alonso, A. Muscarinic Induction of Synchronous Population Activity in the Entorhinal Cortex. *J. Neurosci.* **17**, 6729-6744 (1997).

11. Williams, J.H. & Kauer, J.A. Properties of Carbachol-Induced Oscillatory Activity in Rat Hippocampus. *J Neurophysiol* **78**, 2631-2640 (1997).
12. Boddeke, H.W., Best, R. & Boeijinga, P.H. Synchronous 20 Hz rhythmic activity in hippocampal networks induced by activation of metabotropic glutamate receptors in vitro. *Neuroscience* **76**, 653-8 (1997).
13. Fisahn, A. et al. Cholinergic induction of network oscillations at 40[thinsp]Hz in the hippocampus in vitro. *Nature* **394**, 186-189 (1998).
14. Shimono, K. et al. Origins and Distribution of Cholinergically Induced beta Rhythms in Hippocampal Slices. *J. Neurosci.* **20**, 8462-8473 (2000).
15. Oka, H. et al. A new planar multielectrode array for extracellular recording: application to hippocampal acute slice. *Journal of Neuroscience Methods* **93**, 61-67 (1999).
16. Swann, J.W., Smith, K.L. & Brady, R.J. Localized excitatory synaptic interactions mediate the sustained depolarization of electrographic seizures in developing hippocampus. *J Neurosci* **13**, 4680-9 (1993).
17. Traub, R.D. & Wong, R.K. Cellular mechanism of neuronal synchronization in epilepsy. *Science* **216**, 745-7 (1982).
18. Helekar, S.A. & Noebels, J.L. Analysis of voltage-gated and synaptic conductances contributing to network excitability defects in the mutant mouse tottering. *J Neurophysiol* **71**, 1-10 (1994).
19. Jalilian Tehrani, M.H. & Barnes, E.M. Reduced function of [gamma]-aminobutyric acidA receptors in tottering mouse brain: Role of cAMP-dependent protein kinase. *Epilepsy Research* **22**, 13-21 (1995).
20. Tehrani, M.H.J. et al. Aberrant expression of GABAA receptor subunits in the tottering mouse: an animal model for absence seizures. *Epilepsy Research* **28**,

213-223 (1997).

21. Ayata, C. et al. Impaired neurotransmitter release and elevated threshold for cortical spreading depression in mice with mutations in the α1A subunit of P/Q type calcium channels. *Neuroscience* **95**, 639-645 (1999).
22. Kaja, S. et al. Aberrant cerebellar granule cell-specific GABAA receptor expression in the epileptic and ataxic mouse mutant, Tottering. *Neuroscience* **148**, 115-125 (2007).
23. Liles, W.C. et al. Decreased muscarinic acetylcholine receptor number in the central nervous system of the tottering (tg/tg) mouse. *J Neurochem* **46**, 977-82 (1986).
24. Dusser, A.E. & Peroutka, S.J. Neurotransmitter receptors in adult tottering (tg/tg) mice. *Epilepsia* **31**, 378-81 (1990)
25. Zhang, Y. et al. Mutations in High-Voltage-Activated Calcium Channel Genes Stimulate Low-Voltage-Activated Currents in Mouse Thalamic Relay Neurons. *J. Neurosci.* **22**, 6362-6371 (2002).
26. Poulter, M.O. et al. Differential Expression of alpha 1, alpha 2, alpha 3, and alpha 5 GABAA Receptor Subunits in Seizure-Prone and Seizure-Resistant Rat Models of Temporal Lobe Epilepsy. *J. Neurosci.* **19**, 4654-4661 (1999).
27. Loup, F. et al. Selective Alterations in GABAA Receptor Subtypes in Human Temporal Lobe Epilepsy. *J. Neurosci.* **20**, 5401-5419 (2000).
28. Peng, Z. et al. Altered Expression of the {delta} Subunit of the GABAA Receptor in a Mouse Model of Temporal Lobe Epilepsy. *J. Neurosci.* **24**, 8629-8639 (2004).
29. Eriksson, P.S. et al. Neurogenesis in the adult human hippocampus. *Nat Med* **4**, 1313-1317 (1998).
30. Ganguly, K. et al. GABA Itself Promotes the Developmental Switch of Neuronal GABAergic Responses from Excitation to Inhibition. *Cell* **105**, 521-532 (2001).

31. Ben-Ari, Y. Excitatory actions of gaba during development: the nature of the nurture. *Nat Rev Neurosci* **3**, 728-39 (2002).
32. Tozuka, Y. et al. GABAergic Excitation Promotes Neuronal Differentiation in Adult Hippocampal Progenitor Cells. *Neuron* **47**, 803-815 (2005).
33. Sasaki, S. et al. Impaired Feedforward Inhibition of the Thalamocortical Projection in Epileptic Ca2+ Channel Mutant Mice, tottering. *J. Neurosci.* **26**, 3056-3065 (2006).

Figure 1

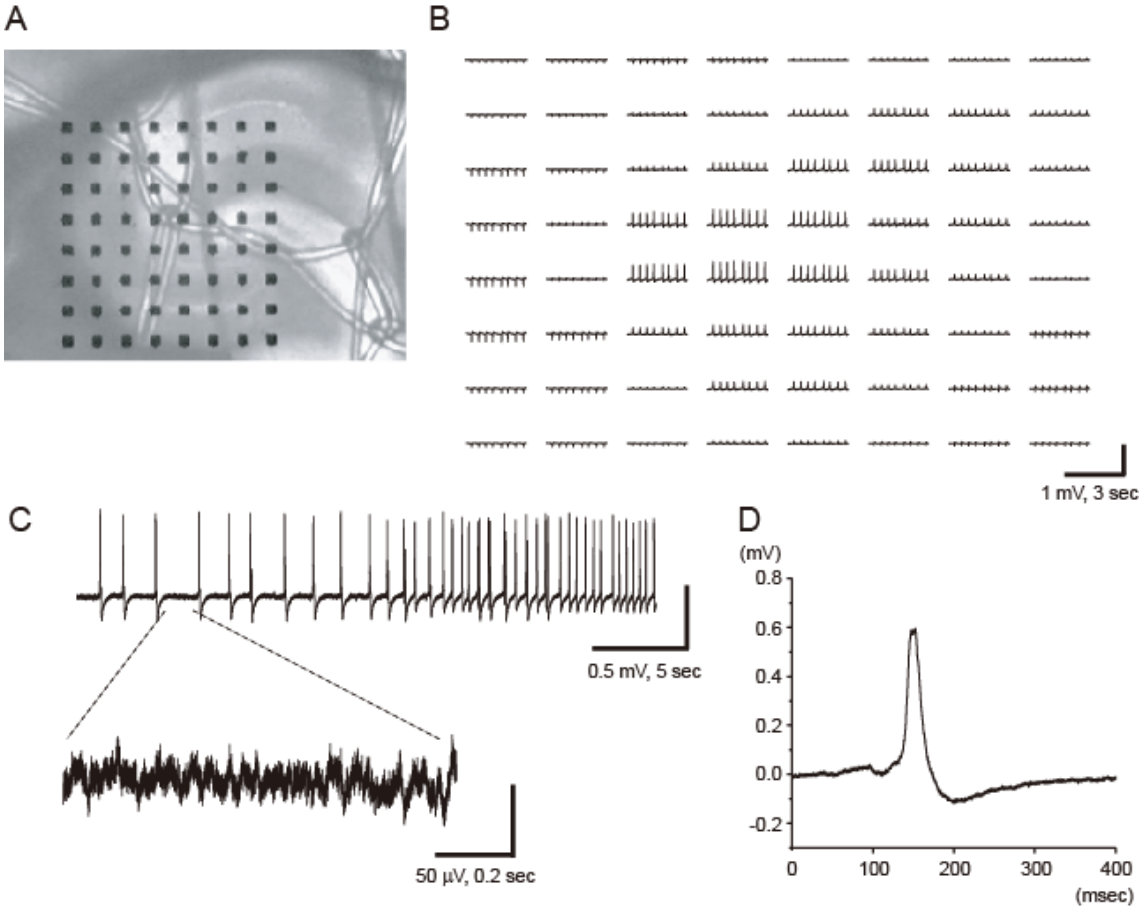

Figure 1 Distribution of carbachol-induced bursting oscillations

Panel A shows a micrograph of hippocampal slice on MED probe (spacing: 150 μm). Epileptic bursting oscillations happened after infusion of 50 μM carbachol and low Mg (0.75 mM) solution (Panel B). A sharp gradient between bursting oscillation versus low-intensity activity exists along the proximoapical axis in CA3. The polarity of the responses is reversed across the cell body layer boundary. Cholinergic burst consists of two components. Bursting responses appeared with lower frequency (~1 Hz, Panel C, top). Small fast oscillation (~20Hz) also can be detected between δ bursts (Panel C, bottom). Each bursting response has about 50 ms duration (Panel D).

Figure 2

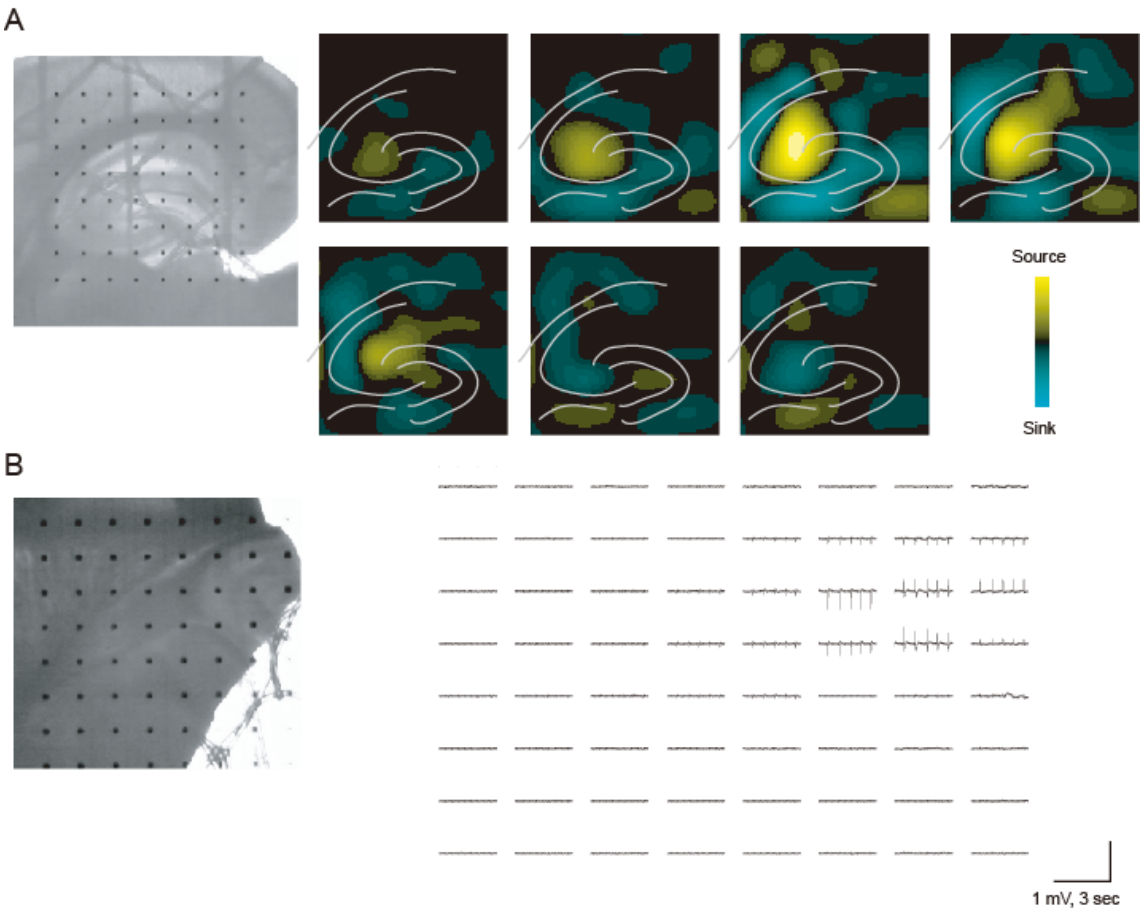

Figure 2 Origin of cholinergic bursting oscillations

Panel A investigated where is main source of bursting response. Each frame shows computed current source density in the region of the electrode array (300 μm spacing). These frames picked up around one burst every 5 msec. Yellow stands for source component and blues stand for sink component. Gray lines indicate cell body layer and boundary of hippocampus and DG. Source was localized in apical dendric area of CA3. To make sure if this activities really come from CA3 area, only CA3 area was incubated on MED probe (Panel B). After slicing hippocampus, put knife to remain only CA3 area. Even in this situation, some bursting response happened with carbachol (30 μM) and low Mg^{2+} solution.

Figure 3

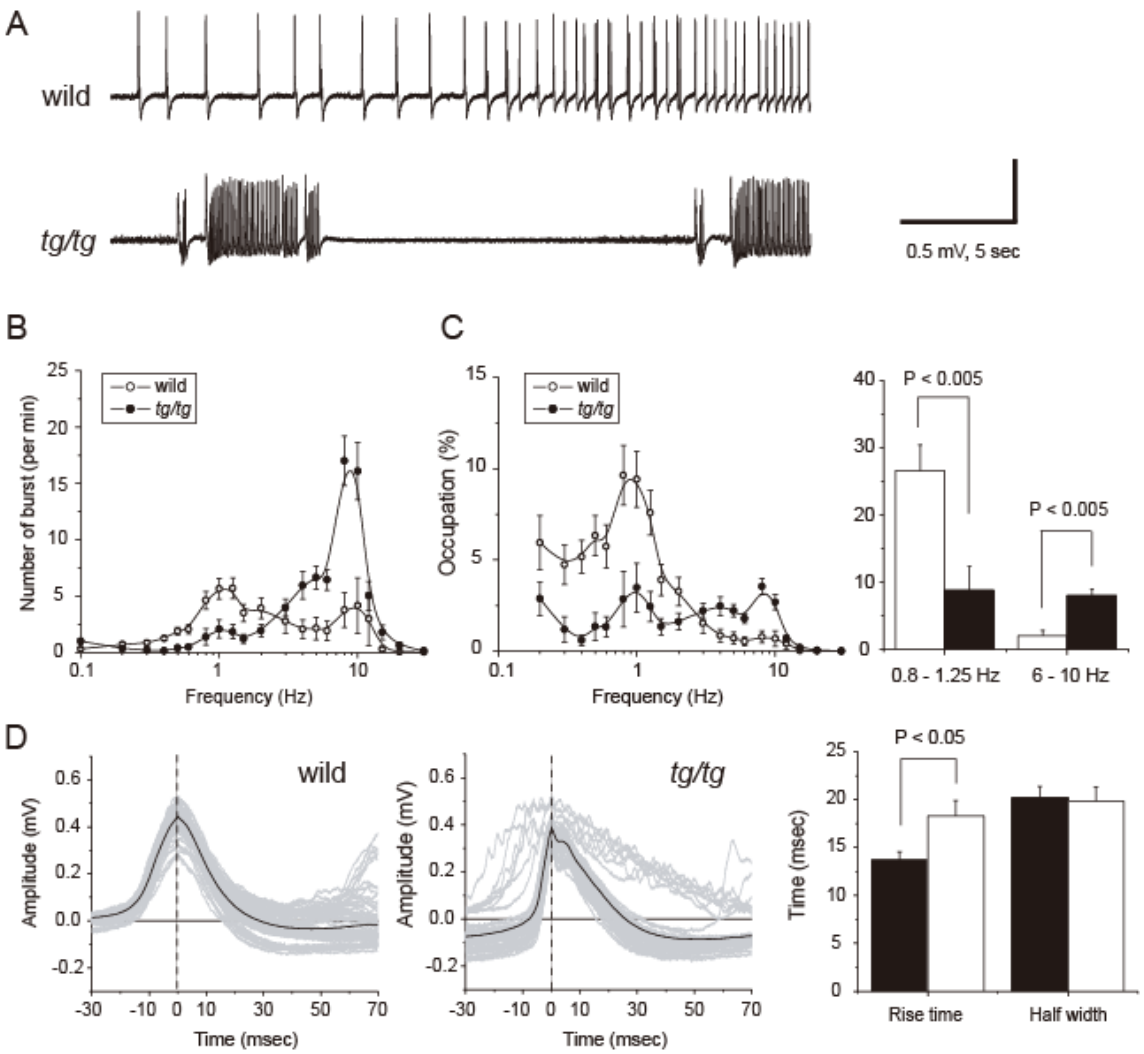
A
wild
tg/tg
0.5 mV, 5 sec
B
wild
tg/tg
Number of burst (per min)
Frequency (Hz)
C
wild
tg/tg
Occupation (%)
Frequency (Hz)
P < 0.005
P < 0.005
0.8 - 1.25 Hz
6 - 10 Hz
D
wild
tg/tg
Amplitude (mV)
Time (msec)
P < 0.05
Time (msec)
Rise time
Half width

Figure 3 Different epileptic patterns between wild and *tottering* (*tg*) mutant mice

Panel A shows a typical patterns of bursting oscillations on wild and *tg* mutant mice. In wild mice, most of bursting responses appeared with lower frequency (~1 Hz). In *tg* mice, bursting responses make a cluster, which consists of higher frequency oscillations. Panel B right shows averaged histogram of interburst intervals (CCh 50 μM, wild: n=18, *tg/tg*: n=14). The bursting oscillation in wild mice has significantly more components than that in *tg* mice in lower frequency. In contrast, bursting oscillation in *tg* mice has more higher frequency pattern than that in wild type. Panel C shows the occupation of each frequency component. The right graph compared the occupation at lower (0.8 – 1.25 Hz) and higher frequency (6 – 10 Hz). The lower frequency bursts in wild type occupy significantly more than that in *tg* (wild: 26.62 ± 3.80 % vs. *tg/tg*: 8.77 ± 3.76 %, $P < 0.005$). The higher frequency in wild type occupy significantly less than that in tg type (wild: 2.01 ± 0.80 % vs. *tg/tg*: 8.02 ± 0.90 %, $P<0.005$). Panel D shows comparison of the burst shape between wild and *tg* mutant mice. The left and central graphs show burst components picked up from figure 2A's data (black: averaged burst, gray: overlaid bursts). The right graph shows summary of burst shape. Bursts in *tg* mutant mice have faster rise time than the ones in wild mice (wild: 18.26 ± 1.62 msec, *tg/tg*: 13.65 ± 0.90 msec; $p < 0.05$), but in the case of duration at half amplitude there is not difference.

Figure 4

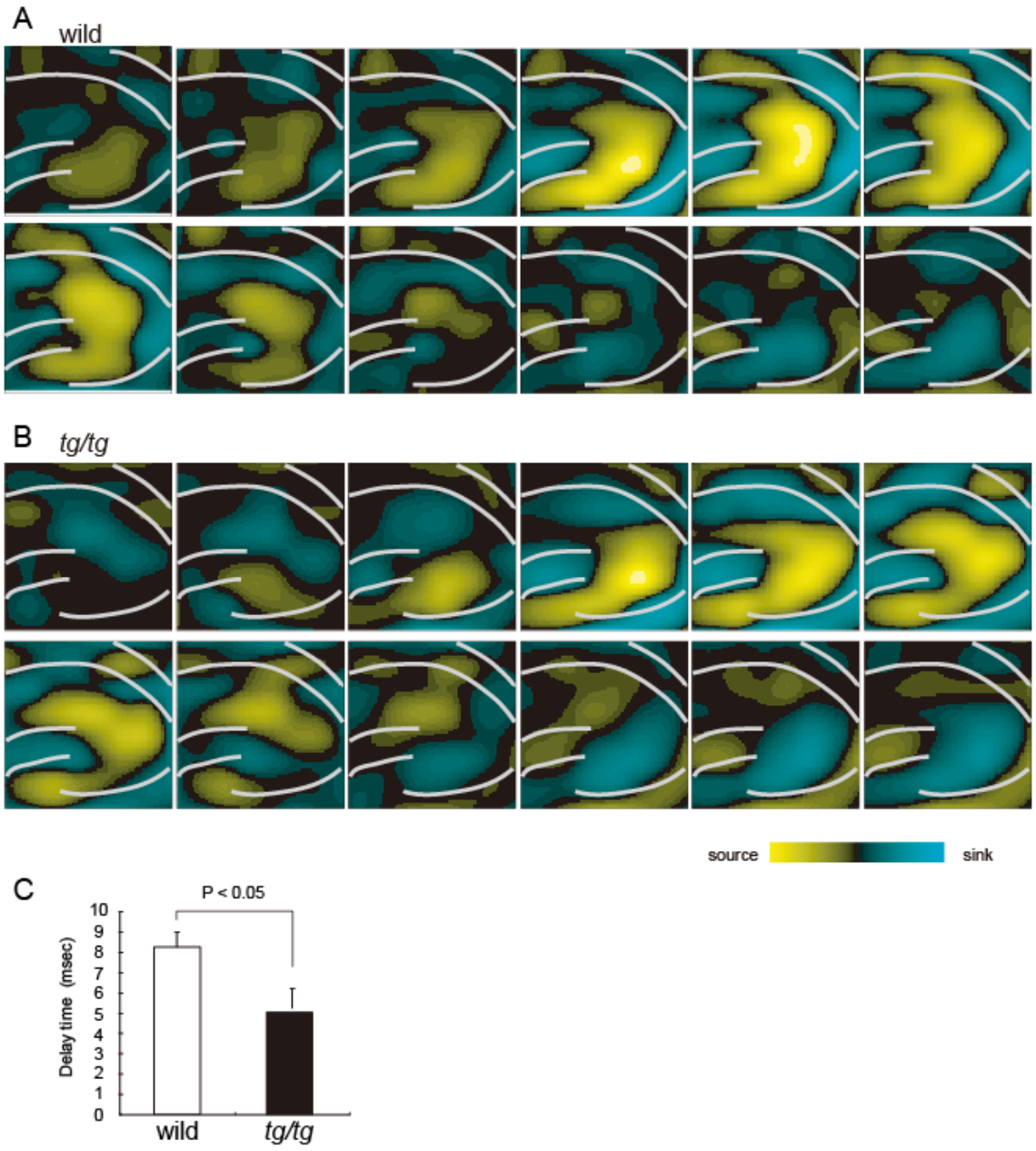
A
wild
B
tg/tg
source
sink
C
P < 0.05
Delay time (msec)
10
9
8
7
6
5
4
3
2
1
0
wild
tg/tg

Figure 4 Spatiotemporal patterns of carbachol induced bursting oscillations

This figure compared spatial pattern of cholinergic bursting oscillation in between wild (Panel A) and *tg* (Panel B) mouse hippocampus. Each frame shows computed current source density in the region of the electrode array. These frames picked up around one burst every 3 msec. Yellow stands for source component and blue stands for sink component. Gray lines indicate cell body layer. Panel C indicates the delay time at the peak point between CA3 and CA1. The phase delay in *tg* mutant mice has more than that in wild mice (wild: 8.26 ± 0.72 msec (n = 4), *tg/tg*: 5.27 ± 0.94 msec (n = 4); $p < 0.05$).

Figure 5

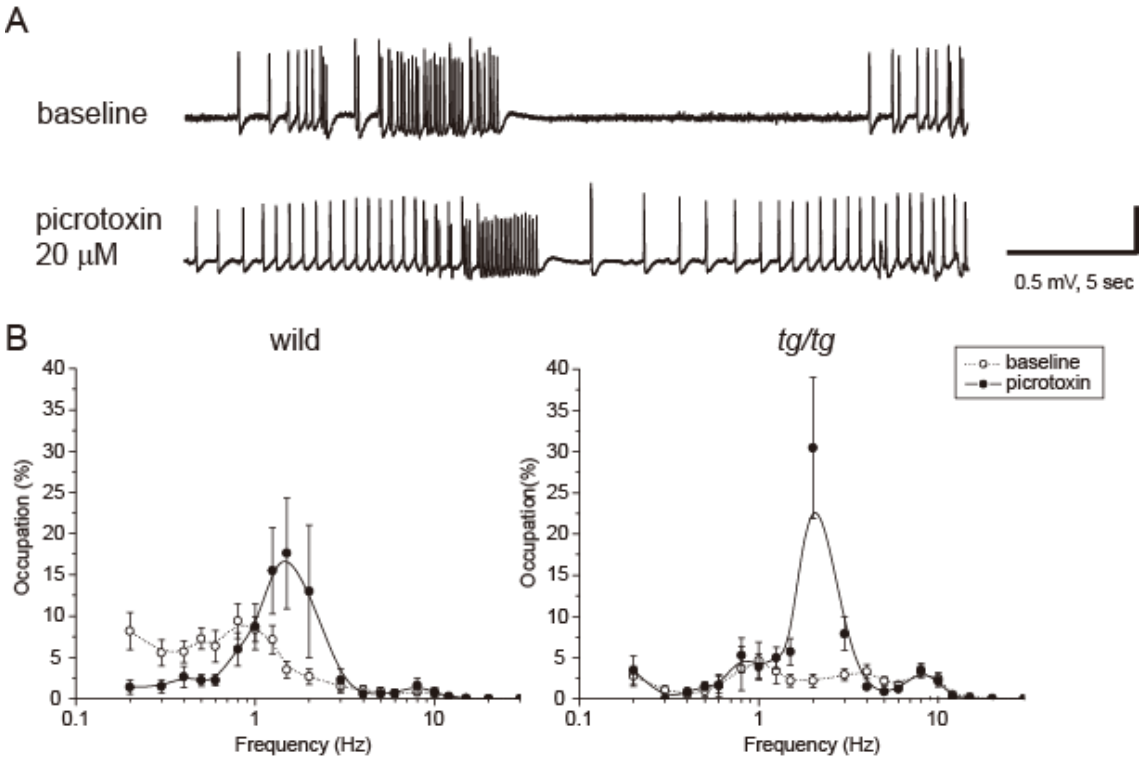

Figure 5

Inhibitor of GABAergic transmission, picrotoxin, induced the low frequency of oscillation in wild-type and *tg* (panel A). Averaged histogram of interburst intervals in the absence and presence of picrotoxin (panel B). In the presence of picrotoxin, oscillation patterns in *tg* are similar as those in wild-type.

Figure 6

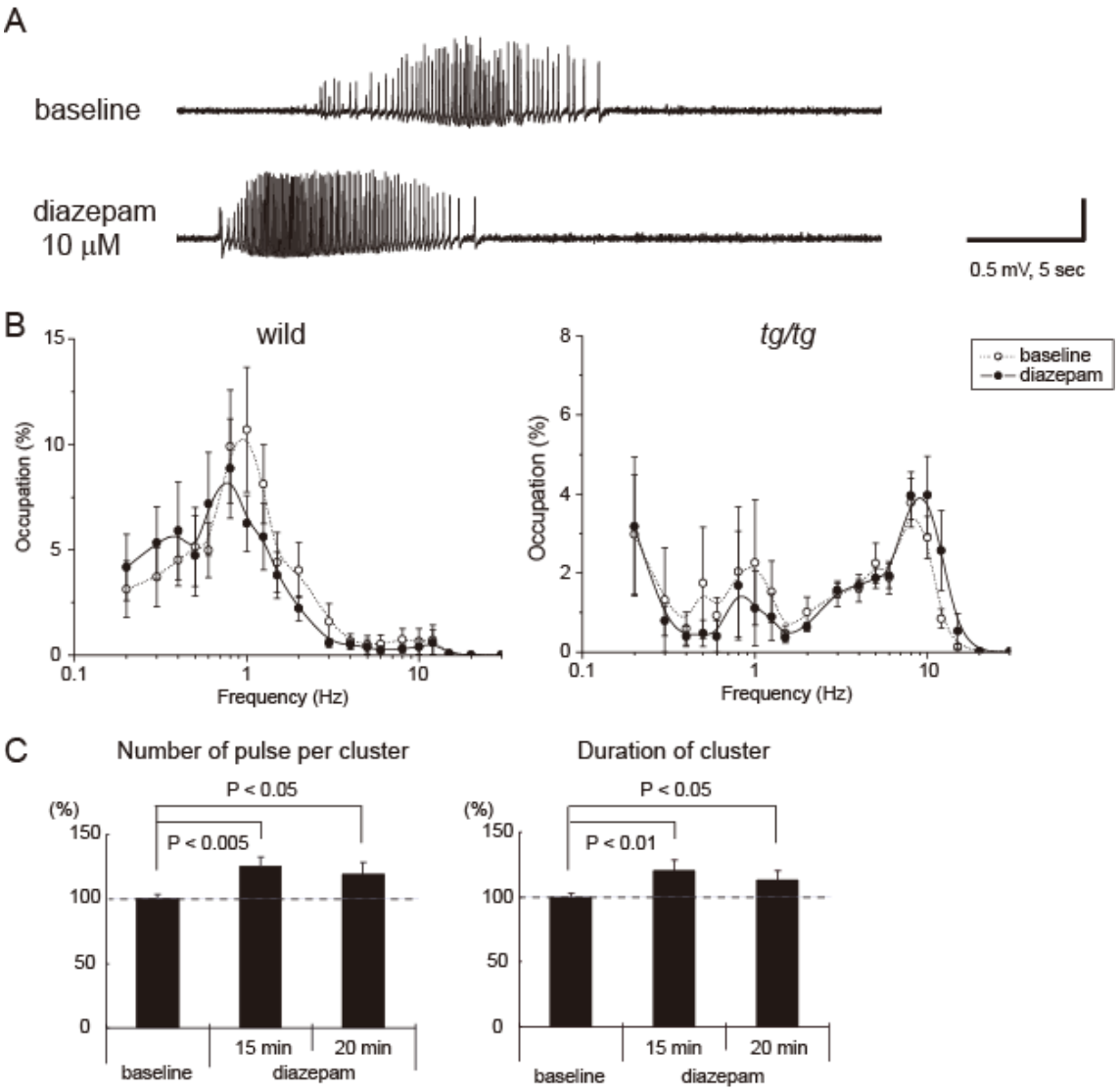
A
baseline
diazepam
10 μM
0.5 mV, 5 sec
B
wild
tg/tg
baseline
diazepam
Occupation (%)
Frequency (Hz)
C
Number of pulse per cluster
Duration of cluster
P < 0.05
P < 0.005
P < 0.01
(%)
150
100
50
0
baseline
15 min
20 min
diazepam

Figure 6 Transmitter systems involved in cholinergic oscillations of tg mutation

Positive modulator of GABAergic transmission, diazepam, enhanced the frequency of fast bursting oscillation only in *tg* mice (Panel A). Each bursting cluster had more bursts in the presence of 10 μM diazepam. Panel B shows averaged histogram of interburst intervals in the absence and presence of diazepam (wild: n=4, *tg*: n=5). Only in *tg* mice, fast components increased in the presence of diazepam (baseline: 28.03 ± 6.75, diazepam: 57.13 ± 13.27; $p < 0.1$). Panel C shows number of pulse per cluster and duration of cluster normalized by the values of baseline.

Figure 7

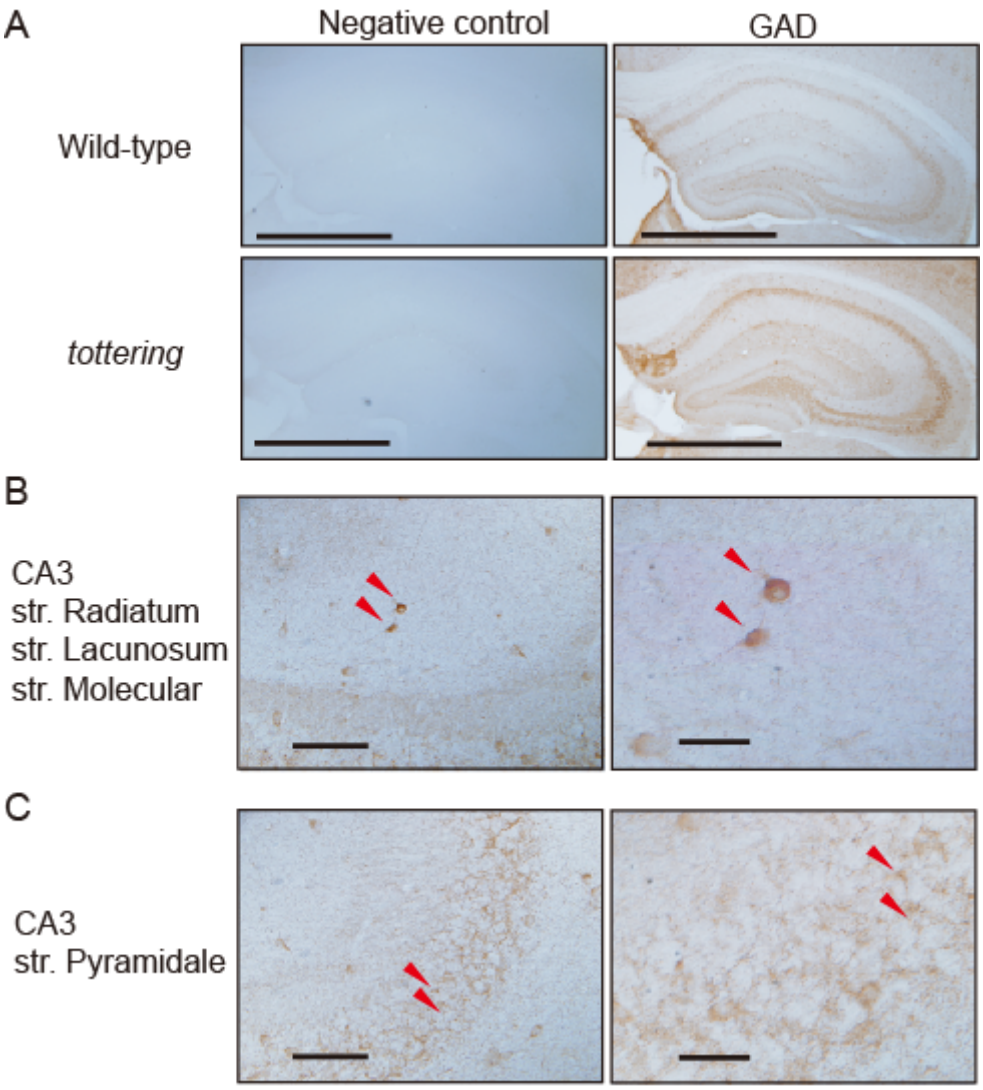

Figure 7 immunocytochemical analysis of GABAergic neuron in hippocampus

Panel A shows the imaging of hippocampal slices immunostained by GAD65 and 67 antibody. Scale bar is 1 mm. The cell bodies (panel B) and inhibitory synapses (panel C) are detected in hippocampal slice from wild-type mice. Scale bars of right panel are 100 μm, and those of left panel are 50 μm.

Figure 8

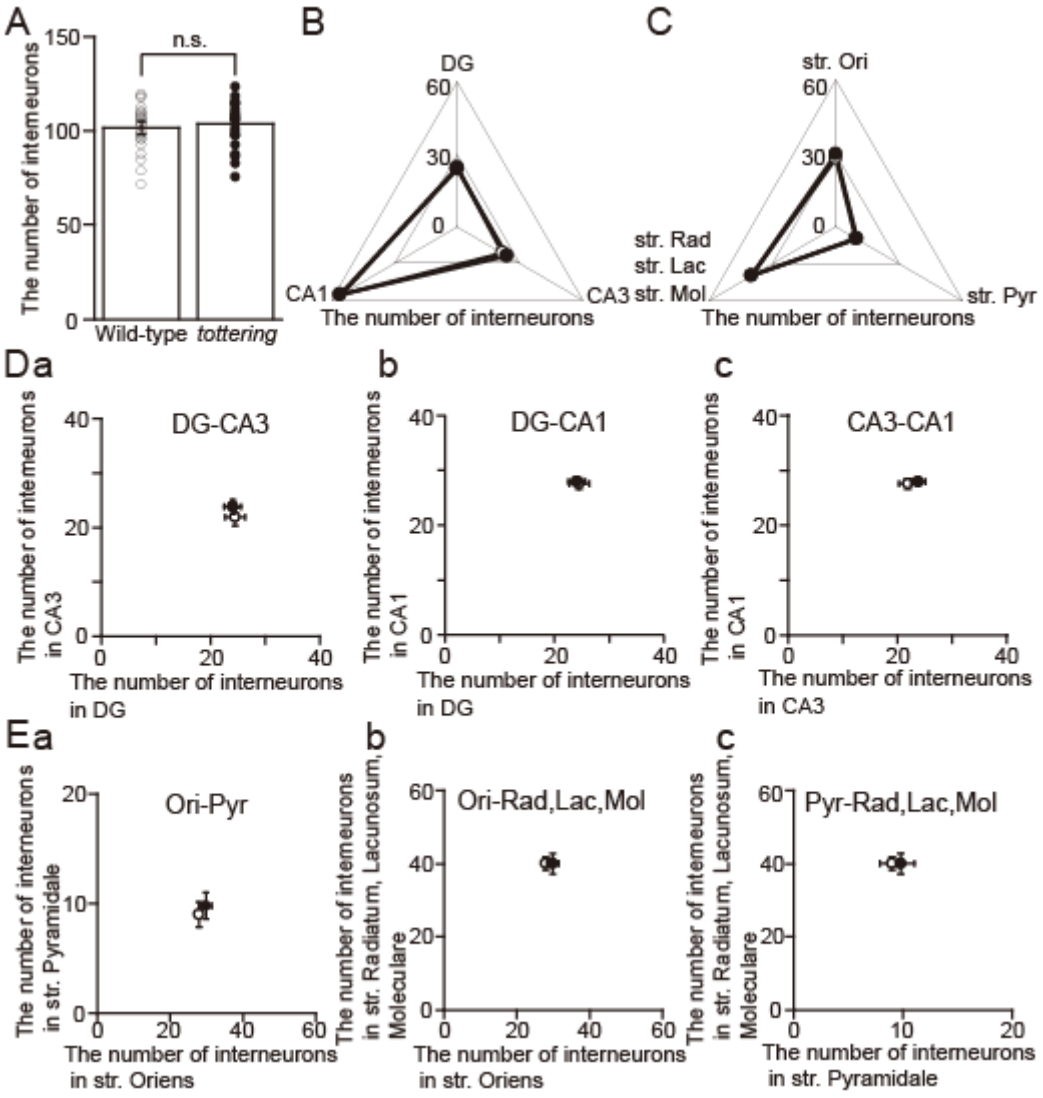

Figure 8 the analysis of the number of inhibitory neuron in WT and *tg*.

Panel A shows the comparison of the number of inhibitory neuron in WT and tg hippocampus (WT: n = 23, *tg*: n = 21). The distributions of inhibitory neurons in regions (CA1, CA3, and DG) (panel B) and stratums (str. Oriens, str. Pyramidale, and str. Radiatum+Lacunosum+Moleculare) (panel C) in hippocampus slice form WT and *tg*. The relationships of each region (panel D) or each stratum (panel E) in hippocampal slice are analized by the number of inhibitory neurons in WT and *tg*.

Figure 9

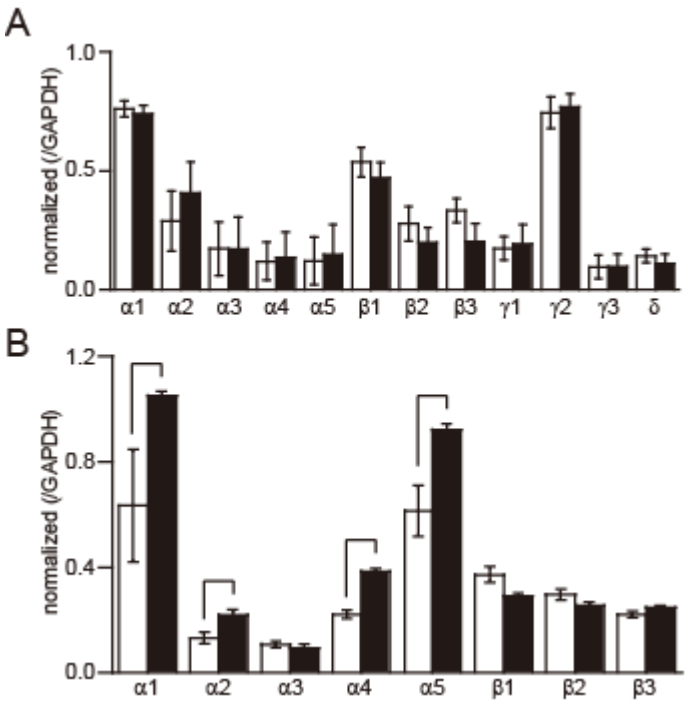

Figure 9 the expression of the subunits composed $GABA_A$ receptors in WT and *tg*. Panel A shows the comparison of the expression of $GABA_A$ receptors in WT and *tg* by using RT-PCR analysis (white, WT; black, *tg*) (α1-α5: n = 2, β1-β3: n = 4, γ1-γ3: n = 4, and δ: n = 4). Each values are calculated by image J and normalized by the intensity of GAPDH expression. Panel B shows the comparison of the expression of $GABA_A$ receptors in WT and *tg* by using Real time-PCR analysis (white, WT; black, *tg*) (α1-α5: n = 2, β1-β3: n = 2, γ1-γ3: n = 2, and δ: n = 2).

Table 1 the lists of primer for PCR.

		size (bp)	primer
$GABA_A$	α1	576	5'-ATCTTTGGGCCTGGACCCTCATTCT-3'
			5'-CTGGCTCTCTGGTCCACTCATAG-3'
	α2	445	5'-TCTTCTGGTGTGGGACCCAGTCA-3'
			5'-GGCTTGGACTGTAAGCCTCATGG-3'
	α3	363	5'-TGGGCTTGGGAAGGCAAGAAGGT-3'
			5'-GCCCTTGATAGCTGATTCCCGGT-3'
	α4	206	5'-TGTCACCAGCTTTGGGCCCGTTT-3'
			5'-GGAGCTGTCATGTTATGTGAGAC-3'
	α5	161	5'-GACGAGACCAATGACAACATCAC-3'
			5'-TCCATTTCCGTGTCAGACACTGG-3'
	β1	334	5'-GGGGCTTCTCTCTTTTCCCGTGA-3'
			5'-GGTGTCTGGTACCCAGAGTTGGT-3'
	β2	495	5'-CAACTCTGGGTGCCTGACACCTA-3'
			5'-TCCTAATGCAACCCGTGCAGCAG-3'
	β3	389	5'-GGTTTGCTGCGCTCAGAGCGTAA-3'
			5'-TACAGCACTGTCCCATCAGGGT-3'
	γ1	234	5'-GTAGCTGATCCTAAGTACTGGAG-3'
			5'-GGATGTTCTAGCAGGTACTGCATC-3'
	γ2	331	5'-GGTGGAGTATGGCACCCTGCATT-3'
			5'-AGGCGGTAGGGAAGAAGATCCGA-3'
	γ3	591	5'-TGCTCGGTCCAGGAGGGTAGA-3'
			5'-CTGATCAGCTGCCTCAACTGAATTTTT-3'
	δ	398	5'-GACTACGTGGGCTCCAACCTGGA-3'
			5'-ACTGTGGAGGTGATGCGGATGCT-3'
GAPDH		602	5'-TGCTGAGTATGTCGTGGAGTCTA-3'
			5'-AGTGGGAGTTGCTGTTGAAGTCG-3'

List of Publication

1. Kiyonaka, S., Wakamroi, M., Miki, T., Uriu, Y., Nonaka, M., Bito, H., Beedle, A.M., Mori, E., Hara, Y., De Waard, M., Kanagawa, M., Itakura, M., Takahashi, M., Campbell, K.P., & Mori, Y. RIM1 confers sustained activity and neurotransmitter vesicle anchoring to presynaptic Ca^{2+} channels. *Nat. Neurosci.* **10**, 691-701 (2007)

2. Miki, T., Kiyonaka, S., Uriu, Y., De Waard, M., Wakamori, M., Campbell, K.P., & Mori, Y. Mutation associated with an autosomal dominant cone-rod dystrophy CORD7 modifies RIM1-mediated modulation of voltage-dependent Ca^{2+} channels. *Channels* **1**, 144-147 (2007)

3. Yamaji, N., Sugase, K., Nakajima, T., Miki, T., Wakamori, M., Mori, Y., & Iwashita, T. Solution structure of agelenin, an insecticidal peptide isolated from the spider *Agelena opulenta*, and its structural similarities to insect-specific calcium channel inhibitors. *FEBS Lett.* **581**, 3789-3794 (2007)

3. Miki, T., Zwingman, T.A., Wakamori, M., Letz, C.M., Cook, S., Hosford, D., Herrup, K., Fletcher, D.F., Mori, Y., Frankel, W.N., and Letts, V.A. Two novel alleles of tottering with distinct Ca(v)2.1 calcium channel neuropathologies. *Neuroscience* **155**, 31-44 (2008)

4. Ohmori, I., Ouchida, M., Miki, T., Mimaki, N., Kiyonaka, S., Nishiki, T., Tomizawa, K., Mori, Y., and Matsui, H. A CACNB4 mutation shows that altered $Ca_v2.1$ function may be a genetic modifier of severe myoclonic epilepsy in infancy. *Neurobiol. Dis.* **32**, 349-354 (2008)